PhD Dissertation

International Doctorate School in
Information and Communication Technologies

DISI - University of Trento

Advanced Methods for the Analysis of Radar Sounder and VHR SAR Signals

Adamo Ferro

Advisor:

Prof. Lorenzo Bruzzone

University of Trento

December 2011

A mia nonna,
che sapeva già tutto

Hai visto mai
che un piede poi basti
a cambiare la vita
se solo toccherà la Luna

Abstract

In the last decade the interest in radar systems for the exploration of planetary bodies and for Earth Observation (EO) from orbit increased considerably. In this context, the main goal of this thesis is to present novel methods for the automatic analysis of planetary radar sounder (RS) signals and very high resolution (VHR) synthetic aperture radar (SAR) images acquired on the Earth. Both planetary RSs and VHR SAR systems are instruments based on relatively recent technology which make it possible to acquire from orbit new types of data that before were available only in limited areas from airborne acquisitions. The use of orbiting platforms allows the acquisition of a huge amount of data on large areas. This calls for the development of effective and automatic methods for the extraction of information tuned on the characteristics of these new systems. The work has been organized in two parts.

The first part is focused on the automatic analysis of data acquired by planetary RSs. RS signals are currently mostly analyzed by means of manual investigations and the topic of automatic analysis of such data has been only marginally addressed in the literature. In this thesis we provide three main novel contributions to the state of the art on this topic. First, we present a theoretical and empirical statistical study of the properties of RS signals. Such a study drives the development of two novel automatic methods for the generation of subsurface feature maps and for the detection of basal returns. The second contribution is a method for the extraction of subsurface layering in icy environments, which is capable to detect linear features with sub-pixel accuracy. Moreover, measures for the analysis of the properties of the detected layers are proposed. Finally, the third contribution is a technique for the detection of surface clutter returns in radargrams. The proposed method is based on the automatic matching between real and clutter data generated according to a simulator developed in this thesis.

The second part of this dissertation is devoted to the analysis of VHR SAR images, with special focus on urban areas. New VHR SAR sensors allow the analysis of such areas at building level from space. This is a relatively recent topic, which is especially relevant for crisis management and damage assessment. In this context, we describe in detail an empirical and theoretical study carried out on the relation between the double-bounce effect of buildings and their orientation angle. Then, a novel approach to the automatic detection and reconstruction of building radar footprints from VHR SAR images is presented. Unlike most of the methods presented in the literature, the developed method can extract and reconstruct building radar footprints from single VHR SAR images. The technique is based on the detection and combination of primitive features in the image, and introduces the concept of semantic meaning of the primitives.

Qualitative and quantitative experimental results obtained on real planetary RS and spaceborne VHR SAR data confirm the effectiveness of the proposed methods.

Keywords
Radar sounder, ground penetrating radar, synthetic aperture radar, very high resolution images, building detection, signal processing, remote sensing, planetary exploration.

Acknowledgments

This thesis is the result of more than three years of work. In this period I had the opportunity to learn, travel, present my work in international conferences, meet and know people. I had the opportunity to participate to international projects, to contribute in the writing of proposals. I had the opportunity to work and stay where the space probes I was dreaming on when I was a kid were built. So "opportunity" is probably the word I can use to describe my PhD, and I think I fully exploited my opportunities and gained a lot from them. For all these opportunities I am deeply grateful to Lorenzo. He took the risk to bet on me since the very beginning. As a result, I started to leave the Earth even before starting the PhD (but my heart in the end never left the lovely city of Dorsten). His scientific guidance and experience have been fundamental to move my steps in a field which was basically unexplored, and his confidence has been invaluable to learn the ropes of research. Although after this experience doing research will not be my official job, I hope we can somehow continue to collaborate.

Regarding the period in California, I thank all the JPLers who spent some time with me. In particular, a special mention goes to Essam Heggy for personally managing my staying at JPL, for his enthusiasm, his suggestions and for the meals at Zankou Chicken. I am also grateful to my house-owner-mate Myriam, who daily contributed to remind me that the real world was on the Earth (OK, maybe not in California...). Finally, I want to say muchas gracias to the Party and his (now) wife Aglae for picking me up at Pasadena and travel over three states together.

During the activities related to radar sounders I had fruitful discussions and help from many people. I want to thank all the people I met working on MARSIS and SHARAD data, from different countries and institutions. Special mention goes to the guys of the SHARAD Operating Center (SHOC) in Rome, Italy, and Nathaniel E. Putzig from the Southwest Research Institute, Boulder, CO, USA, who always answered to my doubts and provided me with some datasets. I thank also the Italian Space Agency (ASI), for partially supporting my work.

Regarding the part of my work related to SAR, I thank Franziska Greßler from Infoterra, Germany, for providing the TerraSAR-X data used in this thesis.

Much of my work benefitted from open source libraries and software. Therefore, I want to express my gratitude to all the people behind the Orfeo Toolbox[1] (OTB), the Insight Toolkit[2] (ITK), the Java Parallel Processing Framework[3] (JPPF), Drools[4], and

[1] http://www.orfeo-toolbox.org
[2] http://www.itk.org
[3] http://www.jppf.org
[4] http://www.jboss.org/drools

the Matlab Radar Toolbox[5].

Work does not mean only code, but also colleagues. Hence, I cannot forget to thank all the people who shared the RSLab-experience with me in the last three years. I would like to especially thank Dominik for introducing me to this world since my master thesis, for reviewing this dissertation and for his hints on coding, software tools, parallel programming, CPU, GPU, GPGPU, BMW, HB, Cannstatter Volksfest, Schweinshaxe and tagliere tipico bavarese. Furthermore, I am thankful to Alain for helping in the development and testing of the clutter detection technique during his master thesis. His availability to discuss future developments by mobile phone when he will be the director of the Vodafone call center has been also much appreciated. Another special mention goes to Ana-Maria, for proofreading this document and for her commitment to understand whatever problem she had to face, and learn from it. It has been a pleasure to supervise her work, and I wish her a brilliant PhD. As ex-co-advisor, I only retain the right to be automatically invited whenever she tastes some Montenegro. Last but not least, I am also especially grateful to Claudia for forcing me to parallelize her WW1 Matlab codes. Starting from this spontaneous collaboration, she had the merit to succeed in what nobody did in more than three years: make me have breaks. Although I still have many things to learn about the functioning of coffee machines, the experience gained in the last weeks of my PhD will probably be very helpful in my future job. However, I will also probably break this new habit very soon again, as I will hardly find new colleagues having at the same time both her love-or-hate irreverence and sensitiveness.

During this PhD my family also played a very important role. I thus want to thank my parents for their continuous and unconditioned support. In these years they have always been a reference point, and helped me with enthusiasm whenever I asked for help (or not). I am sorry but this is probably (hopefully) the last title I get. It is now time to hang up new pictures on the wall. . . :)

Finally, I want to express my profound gratefulness to Sara. In the last nine years she has always been crucial for all my choices, and pushed me whenever I had any doubt. She has always believed in me more than myself, and accepted to live in the instability and uncertainty that comes along with a PhD. Now that this experience is ended and a completely new one is starting, I am convinced that also this time everything will go in the right direction as long as she is with me.

[5]http://www.radarworks.com

Contents

List of Figures

List of Tables

List of Abbreviations

ALSE	Apollo Lunar Sounder Experiment
ASDC	ASI's Science Data Center
ASI	Italian Space Agency
AWGN	Additive white Gaussian noise
BR	*Basal returns* class
CALTECH	California Institute of Technology
DEM	Digital elevation model
DInSAR	Differential InSAR
EJSM	Europa Jupiter System Mission
EO	Earth Observation
ESA	European Space Agency
GLACIES	Glaciers and Icy Environments Sounding
GO	Geometric Optics
GPR	Ground penetrating radar
HS	High-resolution SpotLight
InSAR	Interferometric SAR
ISAR	Inverse SAR
JAXA	Japan Aerospace Exploration Agency
JGO	Jupiter Ganymede Orbiter
JPL	Jet Propulsion Laboratory
KL	Kullback-Leibler divergence
L-BFGS-B	Limited-memory bound-constrained Broyden-Fletcher-Goldfarb-Shanno optimizer
LR	*Low returns* class
LRS	Lunar Radar Sounder
MAE	Mean absolute error
MAP	Maximum *a posteriori*
MARSIS	Mars Advanced Radar for Subsurface and Ionosphere Sounding
MF	Membership function
ML	Maximum likelihood
MOLA	Mars Orbiter Laser Altimeter
MRO	Mars Reconnaissance Orbiter
NASA	National Aeronautics and Space Administration
NPLD	North Pole Layered Deposits

NT	*No target* class
OASIS	Orbiting Arid Subsurface and Ice Sheet Sounder
pdf	Probability density function
PDS	NASA's Planetary Data System
PO	Physical Optics
PolSAR	Polarimetric SAR
PRF	Pulse repetition frequency
PRI	Pulse repetition interval
PS	Persistent Scatterers
PSO	Particle Swarm Optimization
RADAR	Radio Detection And Ranging
RAR	Real aperture radar
RCS	Radar cross section
RDR	Reduced data records
RGB	Red-Green-Blue composition
RMSE	Root mean square error
RS	Radar sounder
SAR	Synthetic aperture radar
SC	ScanSAR
SCR	Signal-to-Clutter Ratio
SHARAD	Shallow Radar
SL	*Strong layers* class
SM	StripMap
SNR	Signal-to-Noise Ratio
SP	SpotLight
SPM	Small Perturbation Method
SSR	Sub-Surface Radar
TSSM	Titan Saturn System Mission
UTM	Universal Transverse Mercator
UXO	Unexploded ordnance
VHR	Very high resolution
WL	*Weak layers* class

List of Symbols

f_c	Radar central frequency
B_w	Radar signal bandwidth
P_r	Received power
P_t	Transmitted power
η_{ant}	Antenna gain
λ_c	Wavelength
R	Range between radar and target
η_{loss}	Medium losses (one way)
σ_s	Radar cross section
η_{radar}	Radar system parameter constant
σ_0	Target backscattering coefficient
$k_B \approx 1.38 \cdot 10^{-23}$ Ws/K	Boltzmann constant
T_N	Noise temperature
t_{pulse}	Pulse duration
Q	Number of scatterers in a resolution cell
ξ	Amplitude of radar signal
φ	Phase of radar signal
t_i	Integration time
L_s	Synthetic aperture length
$\theta_{3\text{dB}}$	Antenna 3 dB aperture
V_s	Velocity of the radar
(x_0, y_0, h_0)	Position of the RS at a generic time instant
$\eta_{\text{loss,fact}}$	Attenuation factor
ω	Angular frequency
$\mu = \mu_0 \cdot \mu_r$	Magnetic permeability of a material
$\varepsilon = \varepsilon_0 \cdot \varepsilon_r = \varepsilon' - i\varepsilon''$	Dielectric permittivity of a material
$\varepsilon_0 = 8.85 \cdot 10^{12}$ Fm^{-1}	Dielectric permittivity of vacuum
ε_r	Material relative permittivity
ρ	Reflection coefficient
τ	Transmission coefficient
ν	Velocity of propagation in dielectric media
$\nu_{\text{light}} \approx 3 \cdot 10^8$ m/s	Speed of light
$\mu_0 = 4\pi \cdot 10^{-7}$ Vs/Am	Magnetic permeability of vacuum
μ_r	Material relative permeability
z	Depth

t	Time delay
δ_{alt}	RS along-track resolution
δ_{act}	RS across-track resolution and SAR ground-range resolution
δ_z	Range resolution
η_z	Range compression factor
B_D	Total Doppler bandwidth
D_F	Diameter of the first Fresnel zone
n_{echo}	Number of echoes processed during SAR focusing
η_{alt}	Along-track compression factor
D_{pl}	First pulse-limited resolution cell
(x, y, h)	Position of a generic ground point
θ	Incidence angle
w_x, w_y	Axes parallel and orthogonal to flight trajectory
L_a, L_e	Antenna sizes
δ_{slr}	Slant-range resolution
θ_{alt}	Angular aperture in azimuth direction of SAR
I	Number of radargram frames
J	Number of radargram samples
X	Radargram image
$p_R(\xi)$	Rayleigh pdf
μ_{ξ^2}	Signal mean power
$p_N(\xi)$	Nakagami pdf
v_N	Shape parameter of the Nakagami pdf
$\Gamma(.)$	Gamma function
v_Γ	Shape parameter of the Gamma pdf
$p_K(\xi)$	K pdf
$K_v(.)$	Modified Bessel function of the second kind of order v
v_K	Shape parameter of the K pdf
n_{smp}	Number of samples per class used in the statistical analysis
$l_{n_{\text{smp}}}(v_K, \mu_{\xi^2}; \xi_1, \xi_2, \ldots, \xi_{n_{\text{smp}}})$	Likelihood function of the K distribution
S	Histogram of the local samples
N	Theoretical noise distribution
$\text{KL}_{SN} = \text{KL}(S, N)$	Kullback-Leibler divergence between S and N
$j_0(i)$	First return position of the frame i
μ_N	Estimated frame noise mean amplitude
s_N	Estimated frame noise amplitude standard deviation
R_{fs}	Free space region
w_G	Guard interval
$w_a \times w_r$	Size of the window used for the calculation of KL_{SN}
$\delta w_a \times \delta w_r$	Step of the window used for the calculation of KL_{SN}
R_s	Shallow subsurface region
$P(i, j)$	Propagation term
ϑ	Curvature term
γ_p	Linear feature

w	Local width of a linear feature
c	Local contrast of a linear feature
Φ_p	Representation of γ_p in the image reference system
$\Omega_{\gamma_p}(i,j)$	Line local width operator
$C_{\gamma_p}(i,j)$	Line local contrast operator
$r(j,s,w,c)$	Steger filter response in the 1D case
$a_s(j)$	1D Gaussian convolution kernel
Λ	Set of detected linear features
$\bar{j}_{ss}(\gamma_p)$	Mean depth of the linear feature γ_p
$\mu(\gamma_p)$	Mean intensity of the linear feature γ_p
$\bar{c}_r(\gamma_p)$	Relative mean contrast of the linear feature γ_p
$\bar{c}(\gamma_p)$	Mean contrast of the linear feature γ_p
$n(\Delta I, \Delta J)$	Number of detected linear features in the radargram space $(\Delta I, \Delta J)$
$\Theta(\Delta I, \Delta J)$	Density of detected linear features in the radargram space $(\Delta I, \Delta J)$
$\delta(.)$	Dirac impulse
$g_{i'j'}$	Control points of the B-spline grid
$G = G_I \cdot G_J$	Number of B-spline grid control points
$D(i,j)$	Deformation field of the B-spline transform
$\Upsilon(X_{\text{ref}}, \hat{X}_m^f)$	Similarity measure between X_{ref} and $\hat{X}_m^f$
$\text{MI}(X_{\text{ref}}, X_m)$	Mutual information between X_{ref} and X_m
$H(X)$	Entropy of X
$p_{X_{\text{ref}}}(\xi_{\text{ref}})$	Marginal probability function of ξ_{ref}
$p_{X_{\text{ref}},X_m}(\xi_{\text{ref}}, \xi_m)$	Joint probability function of ξ_{ref} and ξ_m
$hist(\xi_{\text{ref}}, \xi_m)$	Joint histogram of X_{ref} and X_m
Π	Product image
$\pi(i,j)$	Sample of Π at the position (i,j)
Δd	Mean shift error
Δd_{alt}	Mean shift error in the along-track direction
Δd_z	Mean shift error in the range direction
Δd_{RMSE}	Root mean square error
ϕ	Building orientation angle
θ_{roof}	Gable-roof inclination angle
h_{RMS}	Surface RMS height
l_c	Surface correlation length
$\sigma_{\text{DB}} = \sigma_{\text{DB},c} + \sigma_{\text{DB},i}$	Double-bounce RCS
$k = 2\pi/\lambda$	Wave number
h_w	Building wall height
l_w	Building wall length
θ_w	Local incidence angle on the building wall
T	Number of Tupin-filterings
$\Sigma_b(b)$	Sigmoid function
(b_0, b_r)	Parameters of a sigmoid function
$S_{\tilde{h}}$	Footprint hypothesis score

$n_{\tilde{h}}$	Score factor depending on the number of primitives
$\Xi_{\tilde{h}}(p,q)$	Score relative position factor
$M_{\tilde{h}}(p,q)$	Score MF factor
$Z_{\tilde{h}}$	Score shadow factor

Introduction

In this chapter we introduce our PhD thesis work. In particular, an overview of the present radar systems for the observation of the Earth and of other planetary bodies is given. This allows us to highlight and discuss the motivation, the objectives and the novel contributions of this thesis. Finally, the structure of the document is illustrated.

Background

In the last decade the interest in radar systems for the observation of the Earth (EO) and of other planetary bodies from orbit increased considerably. The main reason for this is the capability of radars to overcome the limitations of passive systems (e.g., the dependence on sun illumination and weather conditions [1]) and the intrinsic properties of the transmitted signals, which make it possible to retrieve information also from parts of the targets which are even not visible (e.g., subsurface [2], structure of forest canopy [3]). In this thesis we focus on the development of novel techniques for the automatic analysis of data acquired by two particular types of radar instruments: radar sounders (RSs), and very high resolution (VHR) synthetic aperture imaging radars (SARs). In the following we give some background information on these two systems.

The use of radars for the analysis of the subsurface is a well-known technique exploited for more than forty years on the Earth. Such investigations have been carried out by means of surface-mounted ground penetrating radars (GPRs) and airborne RSs. The main targets have been the Earth icy regions (i.e., Antarctica, Greenland, glaciers) and arid environments (e.g., Sahara desert). The role of GPRs and RSs is very important. Indeed, thanks to their nadir-looking geometry and the long wavelengths employed, these can provide vertical profiles of the subsurface, showing the subsurface stratigraphy with high detail and reaching several kilometers of depth [2, 4, 5]. GPRs and RSs are thus key instruments for the study of the subsurface of icy and arid regions, which are nowadays of high interest as they provide information about the past and present climate of our planet. The characteristics of such instruments are also suited to achieve primary scientific goals of planetary exploration mainly related to the detection and mapping of subsurface water or ice reservoirs that can be indicators of life in the Solar System. Although future missions foreseen the use of GPRs on landers [6], the use of ground-mounted platforms is very difficult in the context of planetary exploration. In this scenario, RSs can be effectively mounted on satellite platforms and probe the subsurface of planetary bodies from orbit. Therefore, in the last six years three orbiting RSs operated at Mars and on the Moon. These are: the Mars Advanced Radar for Subsurface and Ionosphere Sounding (MARSIS), onboard the European Space Agency's (ESA) orbiter Mars Express and operating since August 2005 [7]; the Shallow Radar (SHARAD) mounted on the Mars Reconnaissance Orbiter of the U.S. National Aeronautics and Space Administration (NASA) and active since the end of 2006 [8]; and the Lunar Radar Sounder (LRS) of the Kaguya spacecraft of the Japan Aerospace Exploration Agency (JAXA), which operated between the end of 2007 and the beginning of 2009 [9]. These instruments followed after many years the first orbital RS, the Apollo Lunar Sounder Experiments (ALSE) onboard the Apollo 17 spacecraft [10]. The high quality results obtained by these orbiting RSs further increased the interest on such systems for new planetary exploration missions. In the context of planetary exploration RSs have been proposed for the payload of future missions devoted to the study of the moons of Jupiter and of Titan (which is a moon of Saturn). In particular, one of the missions currently under study (but yet not finally selected for launch) is the Europa Jupiter System Mission (EJSM). Such a mission is devoted to the joint study of Jupiter and its moons using two orbiters, one leaded by ESA and the other by NASA [11]. The payloads of each orbiter include a RS with the goal of probing the subsurface of the icy moons Europa and Ganymede. During the PhD period, we have been involved in the activities related to the definition of the Sub-Surface Radar (SSR) of the ESA-lead Jupiter Ganymede Orbiter (JGO) [12]. Titan is also an interesting target for radar sounding. Another joint ESA/NASA proposal was the Titan Saturn System Mission (TSSM), where both an orbiter and a montgolfière were proposed to carry a RS instrument [13]. The success of the aforementioned planetary RS instruments also pushed for the development of orbital RSs for EO. Although such type of instrument has been already proposed in the past [14, 15], no orbiting RSs have been launched around our planet so far. However, the interest of the scientific community on this type of system increased in the last few years [16]. This is due to the need to answer questions related to the recent climate change and to predict its evolution in the near future. Indeed, an orbital RS can provide important information on the state of Earth polar regions. Moreover, it can probe Earth arid areas from space, thereby giving a new sight on the evolution of such environments and mapping buried aquifers. The main advantages of orbital RSs with respect to airborne and ground-based campaigns is that data acquired from orbit can reveal the subsurface structure of the Earth with unprecedented coverage, sampling and homogeneity. In 2010 we collaborated to the definition of the proposal to ESA of the Glaciers and Icy Environments Sounding mission (GLACIES) [17]. At the time of writing, another mission proposal is the Orbiting Arid Subsurface and Ice Sheet Sounder (OASIS), leaded by the NASA's Jet Propulsion Laboratory (JPL) in collaboration with the Italian Space Agency (ASI) [18]. All the aforementioned missions, both for planetary exploration and EO, provide/will provide a huge amount of data. This poses the problem of the processing of such data, which in most cases is still carried out according to manual visual inspection. In this context, it is mandatory to develop advanced techniques that can automatically analyze and extract information from the data for properly supporting the scientific community.

Another important type of radar system on which the interest has raised in the last decade is the synthetic aperture radar for imaging. SARs have been used extensively for EO since the early 80's using airborne platforms, and then also with orbiting systems (e.g., ERS-1 and 2, ENVISAT-ASAR, RADARSAT-1) [19]. In this scenario, starting from 2007 new generation SARs mounted onboard of satellites and capable to achieve a very high resolution up to less than 1 m became available. These are the Italian COSMO-SkyMed constellation (made up of four satellites) [20] and the German TerraSAR-X satellite [21]. In 2010 another German satellite was launched, TanDEM-X, with the goal of working in pair with TerraSAR-X to create accurate digital elevation models (DEMs) of the Earth [22]. Such systems permit to study the Earth surface with radars at a level of detail which was previously possible only using airborne instruments. In particular, the analysis and monitoring of urban areas benefits from the improved SAR resolution. This allows the study of urban environments at scales smaller than the building size, opening to new applications linked to SAR imagery (e.g., automatic building detection [23, 24], change detection [25, 26] and classification [27] at meter resolution or better). In particular, the capability of SAR systems to acquire data without the need of sun illumination and clear sky makes VHR SAR data extremely important for rapid damage assessment and emergency response after catastrophic events [28, 29]. However, the improved resolution of spaceborne VHR SAR data makes it not feasible the application of data analysis algorithms previously developed for low- and medium-resolution images. This thus calls for the development of novel techniques tailored for such new data.

Objectives and Novel Contributions of the Thesis

The main goal of this thesis is to present novel methods for the automatic analysis of planetary RS signals and VHR SAR images acquired on urban areas. As mentioned above, both planetary RSs and VHR SAR systems are relatively recent instruments. Both provide from orbit new type of data that before were available only in a limited way from ground and airborne acquisitions. Indeed, the use of orbiting platforms allows the acquisition of a huge amount of data having also different properties from those of data acquired by aerial or terrestrial platforms. This calls for the development of methods for the automatic extraction of information tuned on such new data. This is particularly true for RSs. In fact, RS signals acquired by satellites are currently mostly analyzed by means of manual investigations and the topic of automatic analysis of such data has been only marginally addressed in the literature. Manual investigations are subjective and time-consuming tasks, which may limit the scientific return of the data. Therefore, automatic techniques can greatly support the planetary scientific community, ensuring reliable, consistent and fast extraction of information from the data. Moreover, they can be very useful in the perspective of new RS satellite missions for EO. Regarding the analysis of VHR SAR images, as mentioned above one of the most important applications is the extraction of information from urban areas. The development of techniques suited to this goal capable to exploit the new spaceborne VHR SAR data is a recent and topical subject. In particular, the development of methods capable to maximize the information extracted on urban areas from single images can be very relevant for practical applications related to crisis management and damage assessment.

In the framework of the development of automatic methods for the analysis of RS data we mainly focused on the data acquired by the planetary RS instrument SHARAD at

Mars. However, the proposed novel methods can be properly tuned for the analysis of data acquired by other instruments (e.g., MARSIS, airborne and future spaceborne RS data of the Earth). In this thesis we introduce three main novel contributions on this topic:

1. a statistical analysis of RS signals aimed at the development of automatic methods for the detection and characterization of subsurface features;
2. a technique for the automatic extraction and analysis of ice layering;
3. a method for the automatic detection of surface clutter returns through clutter simulation matching.

The part of the thesis related to the analysis of VHR SAR data is mainly focused on information retrieval from built-up areas using the currently operating spaceborne sensors, i.e., COSMO-SkyMed, TerraSAR-X, and TanDEM-X. In particular, in the thesis we introduce two main novel contributions:

1. a study on the relation between the double-bounce effect of buildings and their orientation angle, carried out by means of both empirical and theoretical analyses;
2. an automatic technique for the detection of building radar footprints from single VHR SAR images.

In the following two subsections we describe in greater detail the main novel contributions of the thesis. The former is devoted to the analysis of RS signals, while the latter refers to the contributions regarding the analysis of VHR SAR data.

Analysis of Radar Sounder Signals

The main novel contributions of the thesis related to the analysis of RS signals can be summarized as follows.

Statistical analysis of radar sounder signals for the automatic detection and characterization of subsurface features

As mentioned above, the topic of the automatic analysis of RS signals has not been addressed sufficiently in the literature. In this thesis we thus provide a first contribution to fill this gap by presenting both i) a study of the theoretical statistical properties of RS signals, and ii) two novel techniques for the automatic analysis of sounder radargrams. The main goal of the study is the identification of statistical distributions that can accurately model the amplitude fluctuations of different subsurface targets. This is fundamental for the understanding of signal properties and for the definition of automatic data analysis techniques. The results of such a study drive the development of two novel techniques for i) the generation of subsurface feature maps, and ii) the automatic detection of the deepest scattering areas visible in the radargrams. The former produces for each radargram a map showing which areas have high probability to contain relevant subsurface features. The latter exploits a region-growing approach properly defined for the analysis of radargrams to identify and compose the basal scattering areas. Experimental results obtained on SHARAD data acquired at Mars confirm the effectiveness of the proposed techniques.

Extraction and analysis of ice layering

In the context of planetary exploration of icy environments, the analysis of the structure of the ice stratigraphy is of primary importance for the study of their past history and for the prediction of their evolution. This is a relevant topic for both the present missions at Mars [30,31], and for future missions to other icy bodies [12]. Similarly, the possible launch of Earth orbiting RSs in the future will allow the observation of the ice stratigraphy of Earth's poles, which is very important for the study of such regions [32,33]. In this thesis we propose a novel method for the automatic detection of subsurface linear features from RS data acquired in icy regions showing extended layering. The proposed method allows the estimation of the position of the linear features with sub-pixel accuracy. Moreover, each detected linear interface is treated as a single object which is completely described by the position of its points, the estimated local width and the contrast. This allows the direct measurement of geometrical and radiometric parameters (e.g., slope angle, intensity) without the need of further post-processing steps. In the thesis we also propose some measurements for deriving from the output of the proposed technique important variables that can characterize quantitatively the properties of the detected linear features (e.g., mean depth, mean intensity) and their distribution (e.g., number and density of layers). The proposed method has been tested on several radargrams acquired by the SHARAD instrument on the North Pole of Mars achieving very promising results.

Detection of surface clutter returns through clutter simulation matching

One of the most critical issues that affect the analysis of orbiting RS data is the the presence of spurious surface clutter returns [2]. These are due to off-nadir echoes related to surface topography which may be detected as (or mask) actual subsurface targets. The detection of such returns is usually carried out manually by means of visual comparison between actual radargrams and surface clutter simulations obtained using available DEMs [34, 35]. This is an inherently subjective and time-consuming task that may reduce the scientific return of the data. In this thesis we address this problem by proposing a novel technique for the automatic detection of surface clutter returns in RS data. The proposed method is made up of three steps: i) simulation of surface clutter returns using available DEMs, ii) automatic coregistration of radargrams and simulations, and iii) extraction of surface clutter returns from the coregistered radargrams. The coregistration is performed in two phases: i) a coarse registration based on the detection of the first return line on both the input radargrams, and ii) a fine registration based on B-spline deformation. Such procedure is suited also to the coregistration of multitemporal radargram series. The proposed technique is robust to radargram deformations (e.g., due to ionosphere effects) and allows the generation of different types of outputs (e.g., coregistered simulations, binary clutter maps, false-color compositions) pointing out the presence of clutter in the radargrams. These can both greatly support the scientific community in manual analysis of RS data and drive the development of reliable automatic methods for information extraction. The effectiveness of the proposed method is proven on two datasets acquired on different areas of Mars by the SHARAD instrument.

Analysis of VHR SAR Data

In this subsection we briefly describe the main novel contributions of this thesis regarding the analysis of VHR SAR data.

Study of the relationship between double bounce and orientation of buildings

Among the different scattering contributions present in meter-resolution VHR SAR data from urban areas, the double-bounce effect of buildings (which is caused by the corner reflector assembled by the front wall of the building and its surrounding ground area) is an important scattering characteristic [36,37]. It indicates the presence of a building because it appears as a linear feature in correspondence with its front wall. The double bounce has been often exploited for the development of automatic methods for the detection and reconstruction of buildings from multi-aspect [23] and interferometric SAR (InSAR) data [24]. However, the relation between the double-bounce effect and the SAR illumination conditions, and thus its reliability as a feature for building detection purposes, has not been investigated to a sufficient extent in real VHR SAR images yet. In this thesis we thus extend and refine the findings from [38], presenting a detailed study of the relation between the double-bounce effect and the orientation angle. First, we investigate empirically a set of industrial and residential buildings with two different ground materials (grass and asphalt) in spaceborne meter-resolution TerraSAR-X images. Then we compare these findings with state-of-the-art theoretical models in order to assess to which extent they can predict the double bounce behavior. This is important to properly use these models for information extraction purposes (e.g., building detection and reconstruction). In order to deal with slightly rough surfaces such as asphalt, we developed a novel model for double-bounce scattering based on the Small Perturbation Method (SPM).

Automatic detection and reconstruction of building radar footprints from single VHR SAR images

As mentioned above, automatic information extraction methods are essential for the exploitation of new VHR SAR imagery. Focusing on the analysis of urban areas, which is of prime interest of VHR SAR, in this thesis we present a novel method for the automatic detection of buildings from VHR SAR scenes, which also reconstructs the 2D radar footprints of the detected buildings. Unlike most of the literature methods (see e.g., [23,24]), the proposed approach can be applied to single images. The method is based on the extraction of a set of low-level features from the images and on their composition to more structured primitives using a production system. Then, the concept of semantic meaning of the primitives is introduced and used for both the generation of building candidates and the radar footprint reconstruction. The semantic meaning represents the probability that a primitive belongs to a certain scattering class (e.g., double bounce, roof, facade) and has been defined in order to compensate for the lack of detectable features in single images. Indeed, it allows the selection of the most reliable primitives and footprint hypotheses on the basis of fuzzy membership grades. The efficiency of the proposed method is demonstrated by processing a meter-resolution TerraSAR-X spotbeam scene containing flat- and gable-roof buildings at various settings. The results show that the method has a high overall detection rate and that radar footprints are reconstructed accurately.

Structure of the Thesis

This document is divided into six main chapters. Chapter 1 illustrates the fundamentals and the background notions needed for the understanding of the thesis. The remaining five chapters are divided in two parts.

The first part, which is organized in three chapters, is devoted to the developed novel methods for the analysis of RS signals. Chapter 2 presents a study on the statistical properties of RS signals. Moreover, it also describes two novel automatic methods for the generation of subsurface feature maps, and for the detection of basal returns (both based on the aforementioned statistical analysis). In this chapter we also define the reference system and the notation used throughout this part of the thesis. Chapter 3 illustrates the proposed novel method for the automatic detection of subsurface linear interfaces in icy regions showing extended layering and presents a related set of measures for extracting their properties. Chapter 4 describes the proposed novel technique for the automatic detection of surface clutter returns through clutter simulation matching. In each chapter an introduction to the specific topic and a review of the related state of the art is provided.

The second part of the thesis, which is divided in two chapters, is focused on the work carried out on VHR SAR images. Chapter 5 describes the main scattering contributions present in VHR SAR images of urban areas and reviews the state of the art regarding the modeling of the double-bounce effect. This introduces the study carried out on the relationship between double bounce and the orientation of buildings in VHR SAR images. Chapter 6 presents the state of the art regarding the analysis of VHR SAR images focusing on the study of urban areas, and in particular on building detection and reconstruction techniques. Then, it describes in detail the proposed novel method for the automatic detection and reconstruction of building radar footprints from single VHR SAR images.

Finally, in the last chapter the conclusions of the thesis are drawn along with proposals for future research and developments.

Chapter 1

Fundamentals and Background

In this chapter we review the fundamentals of radar in order to provide the concepts and definitions needed throughout the thesis. In the first section we illustrate the basic principles of radar, while in the following two sections we describe more in detail the peculiarities of RSs and SAR systems.

1.1 Radar Basic Principles

The term *radar* is the acronym of Radio Detection and Ranging. Radars are active systems that transmit electromagnetic pulses towards a target and measure its scattering properties. The central frequency f_c and the bandwidth B_w of the transmitted signals depend on the type of radar and on the considered application. Nowadays radar systems work in the range between few MHz and tens of GHz. The scattering characteristics of a target depend mainly on its geometric and dielectric properties, the working frequency, and the radar acquisition geometry. In the following we will consider only monostatic geometries, i.e., the transmitting and receiving antenna are the same (or their relative distance is negligible). In the next subsections we illustrate general concepts that are relevant for this thesis. More details on specific characteristics of RSs and VHR SAR systems will be provided in the dedicated sections.

1.1.1 Radar Equation

An example of monostatic geometry is shown in Fig. 1.1. The received signal power P_r can be evaluated by using a classical radar equation for monostatic systems that expresses the received power by the radar as a function of the transmitted power P_t, the antenna gain η_{ant}, the wavelength λ_c, the range between the radar and the target R, the one-way medium losses η_{loss} (here losses introduced by the system are neglected), and the radar cross section (RCS) σ_s [39], as follows:

$$P_r = \eta_{\text{radar}} \sigma_s, \tag{1.1}$$

$$\eta_{\text{radar}} = \frac{P_t \lambda_c^2 \eta_{\text{ant}}^2}{(4\pi)^3 R^4 \eta_{\text{loss}}^2}, \tag{1.2}$$

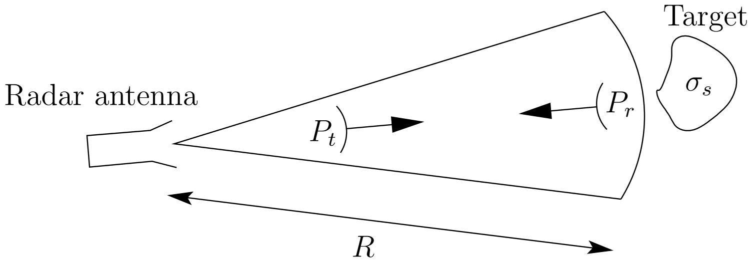

Figure 1.1: Monostatic radar configuration.

where η_{radar} is a constant including the main radar system parameters, and σ_s can be expressed by the product of the target backscattering coefficient σ_0 and its effective area. The target effective area depends on the radar parameters, the target shape and the acquisition geometry.

An important factor for the assessment of the quality of radar measurements is the Signal-to-Noise Ratio (SNR), which is calculated as:

$$\text{SNR} = \frac{P_r \cdot t_{\text{pulse}}}{k_B \cdot T_N}, \tag{1.3}$$

where k_B is the Boltzmann constant, T_N depicts the noise temperature and t_{pulse} is the transmitted pulse duration. The higher the SNR, the better is the performance of the radar, as the signal can be distinguished from the background noise more clearly.

1.1.2 Effects of the Coherent Nature of Radar Signals

The signals transmitted by modern radars are characterized by waveforms described by precise amplitude and phase variations in time, which can be modeled using complex functions. The interaction of such waveforms with targets changes both the amplitude and the phase of the signals [39]. Moreover, the propagation of the signals through dispersive media (e.g., in the case of RSs) also modifies the shape of the transmitted waveforms [2]. All these effects can represent an issue for the interpretation of radar signals. In turn, they can be also exploited for retrieving accurate information on the targets. As an example, Differential InSAR (DInSAR) and Persistent Scatterers (PS) techniques use the small signal phase difference due to the motion of targets to measure precisely their displacement.

One of the main effects due to the coherent nature of radar signals is the so-called *speckle*. As the resolution cell of a radar is large compared to its wavelength, a number Q of targets are present in one cell. Speckle is thus the result of constructive and destructive interferences between the complex returns from such scatterers. Their individual scattering contributions sum up coherently resulting in a single complex value $\xi \cdot e^{i\varphi}$ measured at the sensor (see Fig. 1.2):

$$\xi \cdot e^{i\varphi} = \sum_{q=0}^{Q} \xi_q \cdot e^{i\varphi_q}, \tag{1.4}$$

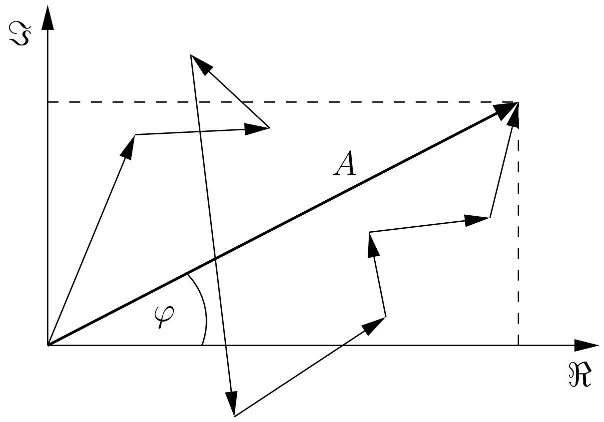

Figure 1.2: Speckle effect. Coherent sum of signals scattered by individual scatterers within a resolution cell represented on the complex plane.

with ξ being the modulus and φ the phase [1]. Although speckle is not random as it depends on the scatterers present in the scene, it is often modeled as random multiplicative noise. It can be reduced by averaging correlated samples implying a reduction of the spatial resolution. In the case of RSs and imaging radars (e.g., SARs) multilooking techniques average samples directly during the formation of the final radar product [1]. Speckle filters have been also developed for the application to processed SAR images [40].

1.1.3 Synthetic Aperture Processing

A very important processing technique that led to the great improvement of the resolution of radar systems is the synthetic aperture processing, or Doppler filtering. Radars exploiting such technique are thus called synthetic aperture radars. However, in the literature the term SAR is usually specifically referred to imaging radars. In this thesis we adopt the same convention. Doppler processing is possible when there is relative motion between the radar and the target and the resolution of the system can be improved only in the motion direction through the analysis of the phase history of the target. As in this thesis we focus on RSs and SARs, here we consider the case in which the target is not moving and the radar is flying on a spaceborne (or airborne) platform. As the radar is moving along its path, an ideal point target on the ground is illuminated by the radar in a time interval t_i called integration time. The space covered by the radar during t_i corresponds to a distance L_s. The considered geometry is illustrated schematically in Fig. 1.3. Ideally, the integration time and the covered distance are given by:

$$t_i = \frac{\theta_{3\mathrm{dB}} R}{V_s}, \tag{1.5}$$

$$L_s = t_i \cdot V_s. \tag{1.6}$$

where $\theta_{3\mathrm{dB}}$ is the 3 dB aperture of the radar antenna in the along-track (or azimuth) direction, and V_s is the velocity of the radar. However, a shorter integration time can be considered in particular cases (see, e.g., the RS case in Sec. 1.2).

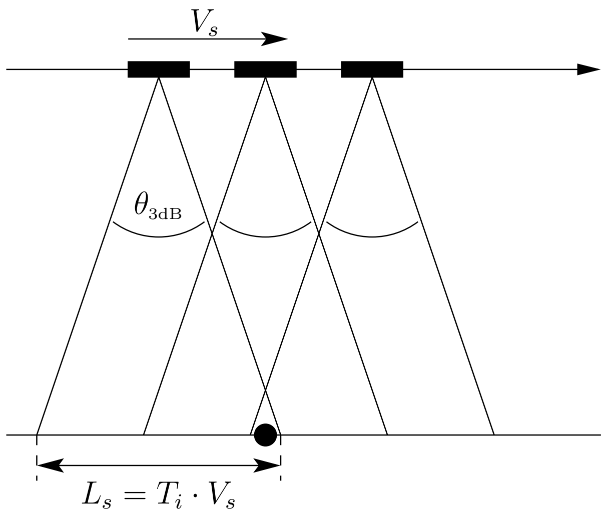

Figure 1.3: Principle of SAR. The point target is illuminated during the integration time t_i, corresponding to a distance L_s which represents the length of the synthetic aperture.

During the integration time the target response shows different Doppler shifts due to the relative motion of the spacecraft with respect to the target. Therefore, although different targets are present in the same antenna footprint, their returns have different Doppler shifts. Coherent radars thus measure and record the phase history of the received signals and this information is then exploited to resolve the ground targets in the Doppler domain using a focusing algorithm, which analyzes the phases of a series of consecutive echoes. As a result, an antenna length longer than the physical one is synthesized. For this reason, the distance L_s is called synthetic aperture length. More details on focusing techniques and on the resolutions achievable by RSs and SARs using Doppler filtering will be given in the next sections.

1.2 Radar Sounder

In this section[1] we review the main characteristics of RSs. After a brief overview on RS systems, the acquisition process and geometry of RSs is illustrated. Then, the relation between RS characteristics and geometrical resolution is described in detail. After this, the concept of surface clutter is introduced. Finally, a description of the SHARAD instrument is reported as an example of planetary RS instrument.

1.2.1 Overview

Radar sounding is a well-known nonintrusive technique which allows the investigation of the structural and dielectric characteristics of the subsurface. This is performed by transmitting waves in the MF, HF or VHF frequency ranges into the subsurface and

[1]Part of this section appears in:
[12] L. Bruzzone, G. Alberti, C. Catallo, A. Ferro, W. Kofman, and R. Orosei, "Subsurface radar sounding of the Jovian Moon Ganymede," *Proc. IEEE*, vol. 99, no. 5, pp. 837–857, 2011.

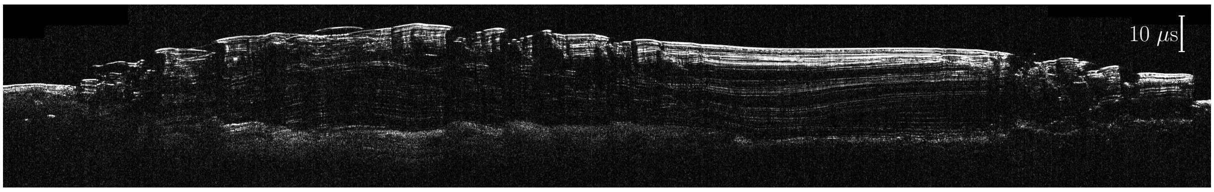

Figure 1.4: SHARAD radargram 1319502 acquired on the North Pole of Mars.

recording the signals scattered back from subsurface structures or dielectric discontinuities [2]. RS data are usually stored as radargrams. Radargrams are 2D images that represent the recorded echo power for a given range position as a function of time (or distance) on one axis, and as a function of the instrument along-track position on the other. Therefore, a radargram shows a sounding profile taken over a certain ground track. As an example, Fig. 1.4 shows a radargram acquired by the SHARAD instrument on the North Pole of Mars.

RSs are usually mounted on flying platforms, such as airplanes or satellites. As ice is the most transparent material in the considered range of frequencies [41], airborne RSs are widely used for the study of Earth's poles and can provide local or regional mapping on areas of interest [42]. Although interest has been shown by the glaciological community for an Earth orbiting sounder [16], at the time of writing spaceborne RSs have been used only for the exploration of other planets or moons. Examples are the Lunar Radar Sounder (LRS) of the Japanese orbiter Kaguya [9], the Mars Advanced Radar for Subsurface and Ionosphere Sounding (MARSIS) on the ESA's Mars Express orbiter [7], and the Shallow Radar (SHARAD) of the Mars Reconnaissance Orbiter of NASA [8]. The latter two instruments are currently operating at Mars and are providing high quality data which allow a detailed study of the subsurface of the Red Planet. In particular, these instruments make it possible to reveal the ice stratigraphy of Mars' poles [30, 31, 43], and to detect fine linear interfaces in other areas of the planet [44]. In this thesis we will use for our experiments data acquired by the SHARAD instrument. Its main characteristics are reported in Sec. 1.2.5. As mentioned in the introduction of the thesis, new planetary RS instruments are planned to be included in the payloads future missions devoted to the study of other bodies, such as the moons of Jupiter [11, 12] and Titan [13]. Activities for the definition of an Earth orbiting sounder are also in progress [17, 18].

1.2.2 Acquisition Process and Geometry

Fig. 1.5 shows the typical acquisition geometry of a RS. A 2D schematic representation is also shown in Fig. 1.6. The instrument is mounted on a platform, which flies at an altitude h_0 from the ground. We denote the nadir-ground point below the radar at a generic time instant with the coordinates (x_0, y_0). The platform altitude depends on the mission profile and can span between several hundreds of meters and several hundreds of kilometers, depending on the type of platform (i.e., airplane or satellite). As an example, the orbital RSs operating at Mars work in an altitude range of 250-300 km for SHARAD [8], and up to 800 km for MARSIS [7].

At the beginning of defined pulse repetition intervals (PRIs), the transmitter emits an

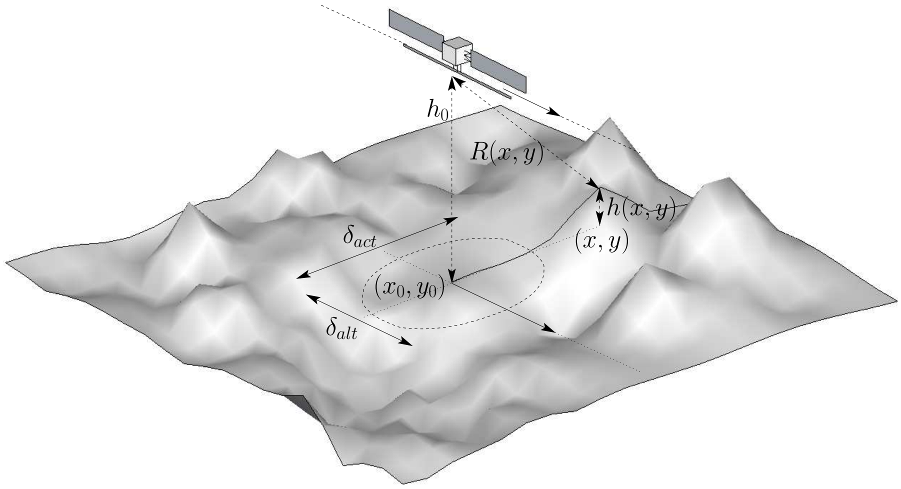

Figure 1.5: Acquisition geometry of a RS instrument. The radar nadir point is denoted with (x_0, y_0). h_0 is the platform height. δ_{alt} and δ_{act} are the along- and across-track resolutions on ground, respectively. The position of a generic ground point is denoted with (x, y) and its elevation is given by $h(x, y)$. The distance between the radar and a ground point is denoted with $R(x, y)$.

electromagnetic pulse which travels from the radar to the surface and then penetrates the subsurface. The pulse is attenuated by the medium and partially reflected from the interior of the subsurface where the complex dielectric permittivity changes. The reflected signals travel back to the receiving antenna and the complex signal is recorded as a function of travel time of the transmitted radar pulse [2]. In the following we describe more in detail the main factors describing the signal propagation in the medium: signal attenuation, reflection and transmission, and wave propagation velocity.

Signal attenuation

The two-way power attenuation present in (1.1) depends on the characteristics of the medium, in terms of dielectric properties (e.g., material, water content) and structure (e.g., porosity) [2]. A simple model suited to the modeling of homogeneous layers considers an exponential relation between attenuation and an attenuation factor $\eta_{\text{loss,fact}}$ according to the following law:

$$\eta^2_{\text{loss}}(z) = e^{4\eta_{\text{loss,fact}} z}, \tag{1.7}$$

where z is the depth in the subsurface. The attenuation factor $\eta_{\text{loss,fact}}$ is given by:

$$\eta_{\text{loss,fact}} = \omega\sqrt{\frac{\mu\varepsilon'}{2}}\sqrt{\sqrt{1+\left(\frac{\varepsilon''}{\varepsilon'}\right)^2}-1}, \tag{1.8}$$

where $\omega = 2\pi f$, μ is the magnetic permeability of the medium, and

$$\varepsilon = \varepsilon_0 \cdot \varepsilon_r = \varepsilon' - i\varepsilon''. \tag{1.9}$$

The term ε represents the dielectric permittivity of the material, which is given by the product of the vacuum permittivity ε_0 and the material relative permittivity ε_r. From

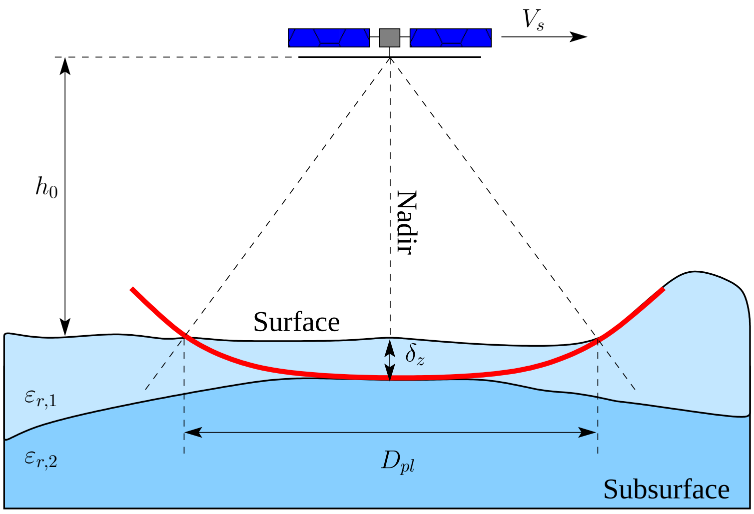

Figure 1.6: 2D representation of the acquisition geometry of a RS instrument.

(1.7) we deduce that attenuation is higher at higher frequencies, thereby resulting in a minor penetration depth.

Reflection and transmission

At each dielectric interface the Snell's law applies. Assuming that the subsurface is characterized by a homogeneous stratigraphy, the reflection coefficient $\rho_{p,p+1}$ between the layer p and the layer $p+1$ is given by:

$$\rho_{p,p+1} = \left| \frac{\sqrt{\varepsilon_{r,p}} - \sqrt{\varepsilon_{r,p+1}}}{\sqrt{\varepsilon_{r,p}} + \sqrt{\varepsilon_{r,p+1}}} \right|^2, \tag{1.10}$$

where $\varepsilon_{r,p}$ is the relative dielectric constant of layer p. Assuming that no absorption loss is generated by the interface, the fraction of energy that is transmitted through the interface is given by the transmission coefficient $\tau_{p,p+1}$, as follows:

$$\tau_{p,p+1} = 1 - \rho_{p,p+1}. \tag{1.11}$$

Wave propagation velocity

The knowledge of the velocity of propagation of the transmitted wave into the medium is important in order to properly translate the recorded signals from the time domain to the depth domain. The velocity of propagation in real dielectric media ν differs from the speed of light ν_{light}. In particular, ν depends on the dielectric properties of the medium, as follows:

$$\nu = \frac{1}{\sqrt{\mu\varepsilon}} = \frac{1}{\sqrt{\mu_0\mu_r\varepsilon_0\varepsilon_r}} = \frac{\nu_{\text{light}}}{\sqrt{\varepsilon_r}}, \tag{1.12}$$

where μ_0 is the magnetic permeability of vacuum and μ_r is the material relative permeability (which can be considered equal to 1). From (1.12) it is possible to note that the propagation velocity of the waves through a real material is always smaller than the speed of the wave propagating in vacuum. Therefore, the higher the dielectric permittivity of the material ε_r, the lower the propagation speed through it.

The permittivity of the medium is thus the only parameter that relates depth z to time delay t, according to the following equation:

$$z = \frac{\nu t}{2}. \tag{1.13}$$

The time delay is computed from the transmission of the wave until its reception. Thus, t is the two-way travel time of a pulse. The factor 2 at the denominator of (1.13) is necessary in order to properly convert time to range.

1.2.3 Geometrical Resolution

The ground resolution in the along-track (across-track) direction describes the capability of the RS to separate two closely spaced scatterers in the direction parallel (perpendicular) to the motion vector of the sensor. These quantities are denoted with δ_{alt} and δ_{act} for the along- and across-track resolution, respectively. The ground resolutions depend on the instrument characteristics (e.g., bandwidth, antenna type and size), the surface roughness, the adopted signal processing techniques, and the operational constraints (e.g., the orbiter altitude) [2]. The range resolution is a function of the signal bandwidth and of the dielectric properties of the subsurface. In the following more details about the calculation of the resolution of a RS instrument will be given.

Range resolution

In most RSs, range resolution is not achieved through the transmission of the shortest possible pulse, but rather through the use of a chirp, i.e., a long pulse linearly modulated in frequency. In this case, thanks to range-compression techniques using matched filters [45] the vertical (range) resolution of a RS δ_z depends on the signal bandwidth B_w and is equal to:

$$\delta_z = \frac{\nu_{\text{light}}}{2B_w\sqrt{\varepsilon_r}}. \tag{1.14}$$

Thus, the effective resolution in the subsurface depends on the material in which the wave is traveling. Usually, weighting is applied during the range compression in order to reduce the sidelobes due to the signal processing [45]. As a result, the effective range resolution worsens by a factor that depends on the applied weighting function (e.g., Hanning, Hamming). It is important to note that the bandwidth of the signal is a key factor also for the gain of the system. Indeed, radar systems using chirp signals can achieve a gain equal to the range compression factor η_z, given by:

$$\eta_z = t_{\text{pulse}} B_w, \tag{1.15}$$

where t_{pulse} represents the chirp duration.

Along-track resolution

In the along-track direction it is possible to exploit the Doppler effect and thus a synthetic aperture to improve the ground resolution. As a result, the surface contributions coming from off-nadir in the along-track direction are reduced, thereby improving the so-called Signal-to-Clutter Ratio (SCR). As described in Sec. 1.1.3, as the RS is moving along its path, an ideal point target on the ground is illuminated by the radar in a time interval t_i called integration time, given by (1.5), in which the target response shows different Doppler shifts. Such shifts can thus be processed in order to improve the along-track resolution. The Doppler processing can be *focused* or *unfocused*. The choice of the focusing strategy has to take into account the processing requirements, the data rate, the SNR gain produced by each strategy, and the power consumption and supplementary mass involved by additional onboard processing. These parameters are critical in the definition of a planetary RS and will compete in a trade-off between the instrument constraints and the scientific goals of the mission. For airborne instruments less strict constraints apply. In the following we give more details on the focused and unfocused processing approaches.

Focused processing In the focused case the phase history of the signal is fully exploited and the maximum theoretical along-track resolution that is achievable is in the order of few meters. The result of the focusing algorithm is the synthesis of a long antenna (i.e., synthetic antenna or synthetic aperture) which length is equal to the space covered by the orbiter during the integration time. As described in Sec. 1.1.3, in general the synthetic antenna length L_s is given by (1.6). This is possible if the Doppler shifts are properly sampled by the instrument. This condition if fulfilled if the pulse repetition frequency (PRF), which is the inverse of the PRI, is greater than the lower limit given by the total Doppler bandwidth B_D, which is equal to [45]:

$$B_D = \frac{2V_s^2}{h_0\lambda_c}t_i. \tag{1.16}$$

The along-track resolution obtained after the focusing δ_{alt}^f can be calculated as follows [45]:

$$\delta_{alt}^f \approx \frac{V_s}{B_D} = \frac{h_0\lambda_c}{2L_s}. \tag{1.17}$$

Equation (1.5) indicates the maximum ideal integration time. However, for spaceborne RSs it is commonly assumed that the coherent scattering from the ground is limited by the first Fresnel zone. The diameter of the Fresnel zone D_F is given by:

$$D_F = \sqrt{2\lambda_c h_0}. \tag{1.18}$$

The integration time can be thus reduced to match a ground surface with a length equal to D_F, obtaining:

$$t_{i,eff}^f = \frac{D_F}{V_s}, \tag{1.19}$$

where $t_{i,eff}^f$ is called effective integration time. From (1.6), this is equivalent to set a synthetic aperture length L_s equal to D_F. The along-track resolution calculated using the effective integration time is thus lower than the maximum value considering the ideal case. The number n_{echo} of echoes that should be processed to obtain the fixed synthetic aperture is:

$$n = t^{f}_{i,eff}\text{PRF}. \tag{1.20}$$

Generally, a PRF much higher than the lower limit imposed by the Doppler bandwidth is used to improve the SNR. Indeed, such echoes are integrated to focus one resolution cell. As a consequence, the SNR of the focused signal increases by a factor n_{echo}. This gain is called along-track compression factor η_{alt}.

Despite the many advantages of the focused Doppler processing, it is highly resource demanding. For this reason it is usually not implemented onboard the RS and it is performed offline after the acquisition process. In the case of a planetary mission profile with very limited downlink bandwidth, onboard focused processing can significantly reduce the amount of data to be transmitted to the Earth (if the needed resources are available). However, this implies that raw data are not available for reprocessing anymore if the focusing algorithm implemented onboard fails, or dedicated processing is required for improving specific results (e.g., in the case of particular surface topography).

Unfocused processing The unfocused Doppler processing permits to reduce the computation effort of the onboard electronics with respect to the focused case at the cost of a reduced along-track resolution. A typical approach is to keep the signal phase variation during a synthetic aperture smaller than $\pi/4$ [7]. The phase compensation of the echoes during the formation of a synthetic aperture is thus simpler and can be also performed onboard in real time, as only a linear phase compensation of the echoes is required. Under such condition, the maximum synthetic antenna aperture is:

$$L_s = \sqrt{\frac{h_0\lambda_c}{2}}, \tag{1.21}$$

which, from (1.6), corresponds to an effective integration time $t^{uf}_{i,eff}$ given by:

$$t^{uf}_{i,eff} = \frac{1}{V_s}\sqrt{\frac{h_0\lambda_c}{2}}. \tag{1.22}$$

Inserting (1.21) in (1.17) shows that the along-track resolution in the unfocused case δ^{uf}_{alt} is equal to the synthetic antenna length L_s. Therefore, the algorithm needs to process only one aperture per resolution cell and subsequent apertures do not overlap. This results in a further reduction of the computation effort for the digital section of the instrument in the case of onboard processing, at the cost of reduced along-track resolution and processing gain.

Across-track resolution

For the across-track direction no Doppler processing is possible. In fact, in the across-track plane the spacecraft has no relative motion with respect to the ground targets and thus the backscattered signals have no Doppler shift. However, although the antenna radiation pattern may be very broad (e.g., in the case of a spaceborne RS using a dipole antenna), the echoes coming from large off-nadir angles can be assumed to be sufficiently weak to not affect the echoes coming from nadir direction when the surface is flat. On the one hand, for smooth surfaces the across-track ground resolution δ_{act} is assumed to be equal to the first Fresnel zone diameter (1.18). On the other hand, for the case of incoherent scattering (rough surface) the ground resolution is commonly approximated with the so-called first pulse-limited resolution cell D_{pl}. The first pulse-limited cell is represented by a circle on the ground centered in the nadir point, which diameter is given by the intersection of the wavefront with the ground surface when the transmitted wave has penetrated into the ground to a depth equal to the range resolution δ_z. The diameter of such a circle is given by:

$$D_{pl} = 2\sqrt{2h_0\delta_z} = 2\sqrt{\frac{h_0 c}{B_w}}. \tag{1.23}$$

1.2.4 Surface Clutter

When relevant topography is present within the ground swath (see Fig. 1.5 and Fig. 1.6), lateral echoes coming from a generic position (x, y) of the surface [characterized by an elevation $h(x, y)$] may appear in the range corresponding to the subsurface as they may be recorded by the instrument at the same time of subsurface returns. The range $R(x, y)$ between the RS instrument [located at (x_0, y_0, h_0)] and a generic position (x, y) of the surface is given by (see Fig. 1.5):

$$R(x, y) = \sqrt{(x - x_0)^2 + (y - y_0)^2 + [h_0 - h(x, y)]^2}. \tag{1.24}$$

Such returns become relevant on irregular (sloped) or rough surfaces, and their strength depends on the system spatial resolution and on the relation between the radar wavelength and the size of the surface irregularities. The presence of strong surface clutter may hamper the correct interpretation of radargrams. In fact, clutter returns may be interpreted as or mask actual subsurface features.

Different techniques have been proposed in the literature to perform surface clutter reduction. On the one hand, surface returns coming from the along-track direction are usually suppressed by means of synthetic aperture processing, which is employed in all the recent orbiting RSs [7–9]. On the other hand, across-track clutter can be reduced only by using directive antennas or more complex techniques exploiting more antennas [7], antenna sub-apertures [5] or different polarizations [46]. However, these solutions imply to increase the complexity of the RS instrument (both in terms of design of the instrument and of the required hardware and mechanical components) and have not yet been applied successfully to planetary RSs due to the strict constraints related to the definition of spaceborne instruments and platforms. As a result, planetary RS data (e.g., acquired at Mars) usually show strong clutter returns which are detected through the comparison of radargrams with clutter simulations (more details on this procedure will be given in Chapter 4).

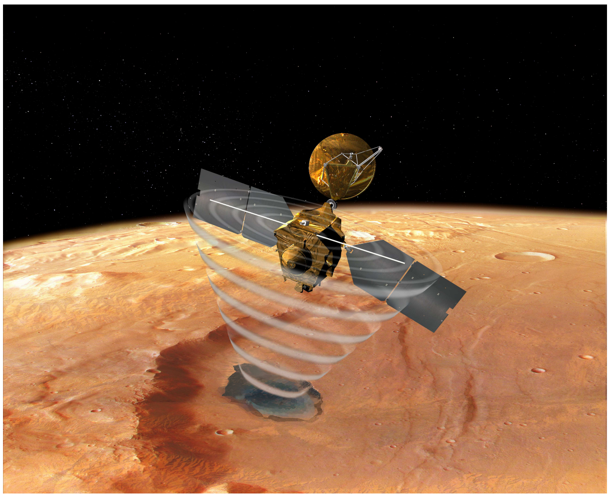

Figure 1.7: Artist's view of MRO and SHARAD at Mars. (© NASA/JPL-Caltech)

1.2.5 The SHARAD Radar Sounder

SHARAD (Shallow Radar) is a facility instrument of the NASA's Mars Reconnaissance Orbiter (MRO) provided by the ASI. MRO was launched in August 2005 and SHARAD became operational in November 2006. An artist's view of MRO and SHARAD is shown in Fig. 1.7. The main goal of SHARAD is to map, in selected areas, dielectric interfaces to several hundred meters depth in the Martian subsurface and to interpret these results in terms of the occurrence and distribution of expected materials, including competent rock, regolith, water and ice. In particular, SHARAD can search for and map liquid or frozen water in the first hundred of meters of the Mars subsurface.

Its main technical characteristics are summarized in Tab. 1.1. SHARAD operates at a central frequency of 20 MHz using a dipole antenna of 10 m. It can achieve a maximum penetration depth of about 1 km in the icy regions of Mars (e.g., the North Pole). The instrument uses chirp waveforms, with a bandwidth of 10 MHz. This gives a range resolution of 15 m in free space, which corresponds to less than 10 m in ice. The maximum along- and across-track resolutions are in the order of 300 m and 3 km, respectively.

SHARAD is designed for performing the minimum amount of processing onboard. The data are focused onground through range and Doppler focusing of the chirp signals. Raw data are processed at the SHARAD Operations Center of Thales Alenia Space in Rome, Italy, under the guidance and control of the SHARAD science team. Data are then distributed to the community from the ASI's Science Data Center in Frascati, Italy [47], and from the Geosciences Node of the Planetary Data System (PDS) at Washington University in St. Louis, USA [48].

Table 1.1: Main parameters of SHARAD.

Orbiter altitude	255 – 320 km
Central frequency	20 MHz
Transmitted bandwidth	10 MHz
Antenna	10 m dipole
Transmitted power	10 W
Pulse length	85 μs
Pulse repetition frequency	700 or 350 Hz
Along-track resolution	0.3 – 1 km
Across-track resolution	3 – 7 km
Penetration depth	$<\sim$1 km
Vertical resolution	15 m (vacuum)

1.3 Synthetic Aperture Radar

In this section the main concepts related to SARs are described. In the first subsection a brief overview of SAR systems is reported. The acquisition geometry and the geometrical resolution of SARs is then illustrated. After a description of the main distortions occurring in SAR imagery due to the acquisition geometry, an overview of the main characteristics of present VHR SAR systems is given.

1.3.1 Overview

SARs represent an evolution of the so-called real aperture radars (RAR). The main difference between RARs and SARs is the much finer along-track (azimuth) resolution of SARs, which is obtained by exploiting synthetic aperture processing (see Sec. 1.1.3). Both systems share the side-looking geometry, which will be described in greater detail in the following subsections. SARs date back to the 50's, when the use of the Doppler analysis as a mean to improve the azimuth resolution of radars was proposed. Since then, SARs became a very important tool for the observation of the Earth. Examples of SAR instruments that operated/are operating from orbit providing valuable images of the Earth surface are ERS-1 and 2, ENVISAT-ASAR, and RADARSAT-1 [19]. As mentioned in the introduction, starting from 2007 new VHR SAR systems achieving geometrical resolutions in the order of 1 m have been launched. These will be described in more detail in Sec. 1.3.5. Future satellite SAR systems are also under development (e.g., ESA's Sentinel [49]). SARs are also operated using airborne platforms. Examples are the German PAMIR [50], and the French SETHI [51]. Airborne systems are usually used to develop new technologies and to perform accurate measurement campaigns on specific areas (e.g., full-polarimetric and/or multi-aspect acquisitions). New airborne systems can achieve geometrical resolutions in the order of few centimeters [50].

All the mentioned SAR systems work in the microwave frequency spectrum. The main frequencies used so far span from L-band to C-band, and X-band for most of the new VHR SAR systems. In this frequency bands microwave signals penetrate cloud coverage, enabling the acquisition of SAR images in almost all weather conditions. Recently, the interest on the development of spaceborne SAR systems working at P-band is increasing.

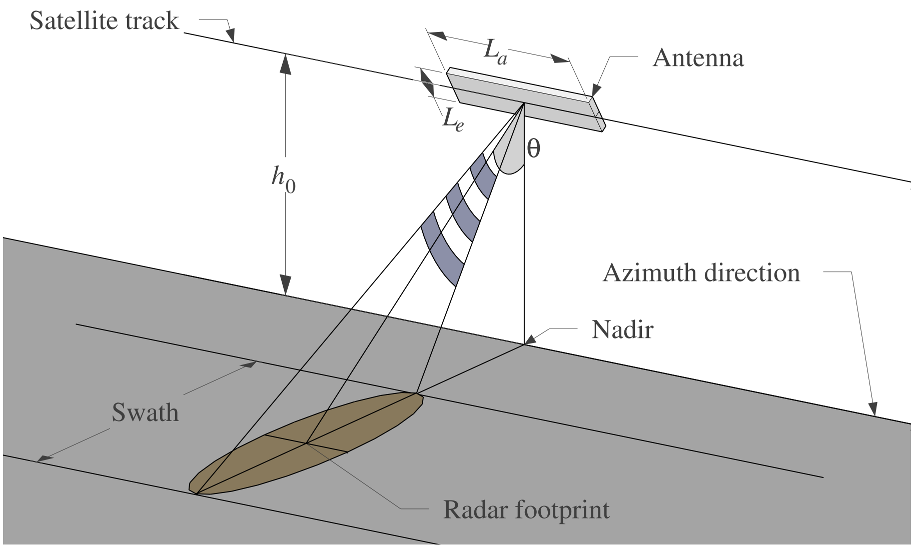

Figure 1.8: Side-looking geometry of SAR systems.

Indeed, such low frequencies allow a detailed study of vegetated areas and biomass [52]. Finally, high-frequency SARs working in the Ku-band have been also developed and proposed for the monitoring of icy environments (see, e.g., [53]).

SAR imagery is used in a very broad field of applications. Thanks to the new generation VHR SAR systems, the monitoring of urban areas particularly benefitted from the improved geometrical resolution. Indeed, urban environments can now be analyzed at building and sub-building level. This allows new applications (e.g., building change detection and classification) and, in combination with the independence of SAR on sun illumination and weather conditions, make VHR SAR imagery an important source of information for the monitoring of critical and emergency scenarios.

1.3.2 Acquisition Geometry

Airborne and spaceborne SAR systems illuminate the scene using a side-looking geometry (see Fig. 1.8). The antenna of the radar system is mounted on a flying platform. Its horizontal and vertical axes are parallel and orthogonal to the azimuth direction, respectively. The angle between nadir and the radar beam direction is called incidence angle and will be denoted with θ. The footprint of the main lobe of the radar beam on the ground can be approximated by an ellipse with the principal axes given by:

$$w_x = R \cdot \theta_{3\mathrm{dB},a} = \frac{h_0 \cdot \theta_{3\mathrm{dB},a}}{\cos(\theta)}, \tag{1.25}$$

$$w_y = \frac{R \cdot \theta_{3\mathrm{dB},e}}{\cos(\theta)} = \frac{h_0 \cdot \theta_{3\mathrm{dB},e}}{\cos^2(\theta)}, \tag{1.26}$$

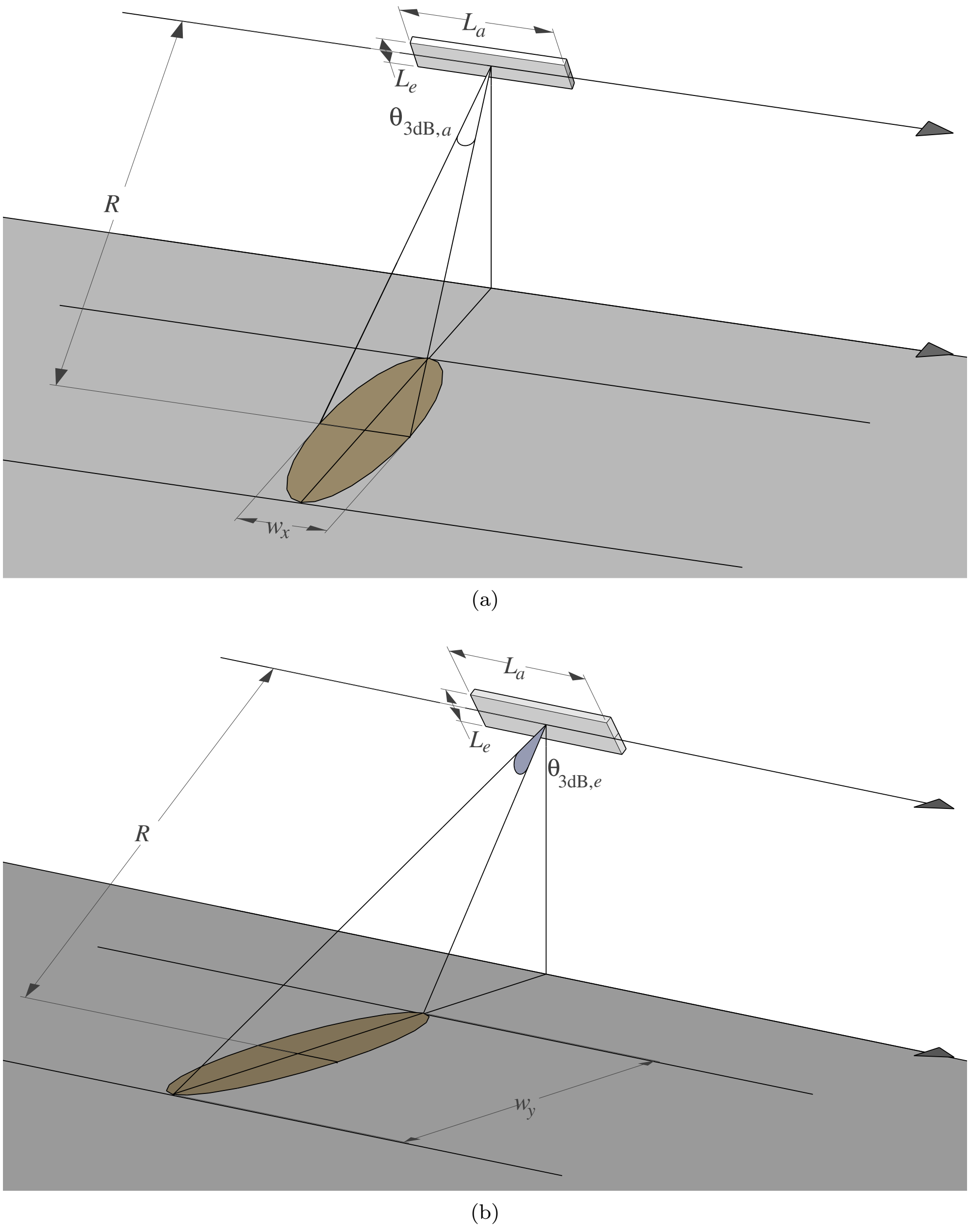

Figure 1.9: Angles and antenna footprint sizes of SAR systems. (a) Azimuth direction, (b) range direction.

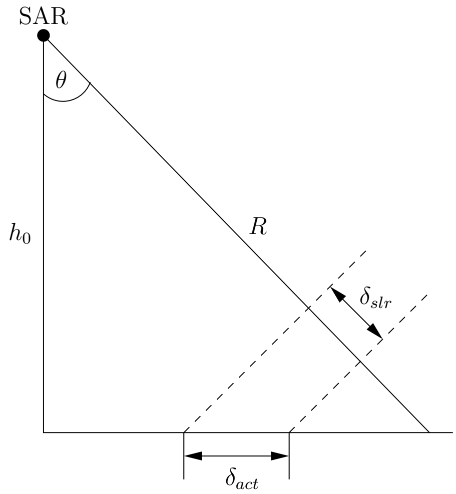

Figure 1.10: Geometry in slant- and ground-range projection.

where

$$\theta_{3\text{dB},a} = \frac{\lambda_c}{L_a}, \tag{1.27}$$

$$\theta_{3\text{dB},e} = \frac{\lambda_c}{L_e}. \tag{1.28}$$

w_x and w_y represent the axes parallel and orthogonal to the flight trajectory, respectively. L_a and L_e are the antenna sizes (see Fig. 1.9).

Regarding the plane perpendicular to the flight direction, two reference systems are usually used to define the position of a point. These are the *slant range* and the *ground range* (see Fig. 1.10). The slant range is the direction identified by the conjunction between a point target and the SAR system. The ground range is the projection of the slant range on the ground (corresponding to the across-track direction of the RS case). Therefore, the ground range depends on the incidence angle and on the surface topography.

1.3.3 Geometric Resolution

In the range direction the definition of resolution follows the same principles explained for the RS range resolution in Sec. 1.2.3. Also for SAR, pulse compression techniques with matched-filter processing are used, achieving high range resolutions and high SNR at the same time. With these techniques the slant-range resolution δ_{slr} and the ground-range resolution δ_{act} are related to the frequency bandwidth B_w of the transmitted radar pulse by:

$$\delta_{slr} = \frac{\nu_{\text{light}}}{2 \cdot B_w}, \tag{1.29}$$

$$\delta_{act} = \frac{\nu_{\text{light}}}{2 \cdot B \cdot \sin(\theta)}. \tag{1.30}$$

As mentioned above, SAR systems can considerably improve the azimuth resolution by processing the phase information of the complex signals (the basic principles of synthetic aperture processing have been discussed in Sec. 1.1.3). Indeed, without the use of synthetic aperture processing, the azimuth resolution of a SAR system would be the same of a RAR sensor, that is equal to the azimuth antenna footprint size given by (1.26). This corresponds to values that can reach the tens of kilometers for spaceborne systems. Following the theory of Sec. 1.1.3, a point target is illuminated by the SAR beam during a time span t_i (integration time) depending on w_x, in which the platform is moving. During this time the SAR system records the phase history of the signal. Under the assumption of fully focused processing, the synthetic aperture thus corresponds to a synthetic antenna length L_s which is the distance traveled by the sensor while illuminating a target with its beam:

$$L_s = w_x = \frac{h_0 \cdot \lambda_c}{L_a \cdot \cos(\theta)}. \tag{1.31}$$

Similarly to the case of (1.17), the angular aperture in the azimuth direction of SARs θ_{alt} is:

$$\theta_{alt} = \frac{\lambda_c}{2 \cdot L_s}. \tag{1.32}$$

The azimuth resolution δ_{alt} of SAR is thus given by:

$$\delta_{alt} \approx R \cdot \theta_{alt} = \frac{\lambda_c \cdot h_0}{2 \cdot L_s \cdot \cos(\theta)} = \frac{L_a}{2}. \tag{1.33}$$

Therefore, the azimuth resolution of a SAR sensor is theoretically only dependent on the length of the actual antenna, but not on the distance between sensor and target.

1.3.4 Geometric Distortions in SAR Imagery

The side-looking geometry of SAR together with non-flat terrain causes geometric distortions, such as foreshortening, and relief displacement. Furthermore, it is source for layover and shadow effects, which are visible as relatively bright and dark regions in SAR imagery, respectively. These effects are visible in SAR images from areas with relevant topography (e.g., mountains). Moreover, they are also visible in VHR SAR images of urban areas (see Chapter 5). In the following, the main geometric distortion effects are described.

Foreshortening In Fig. 1.11a we show the foreshortening phenomenon, which is a dominant effect in mountainous areas. Inclined surfaces, which are oriented towards the sensor, appear shortened in SAR imagery. For instance distance $\overline{AB}$ is much longer than its projection $\overline{A'B'}$ on SAR slant-range image space. The slant-range compression results in a brighter area $\overline{A'B'}$, since it contains the entire energy scattered by the longer $\overline{AB}$ area.

Relief displacement SAR measures the distances between an object and the sensor. Hence, if the inclination of the surface is larger than the incidence angle, the top of the elevated structure is shifted in the image towards the sensor, as shown in Fig. 1.11b.

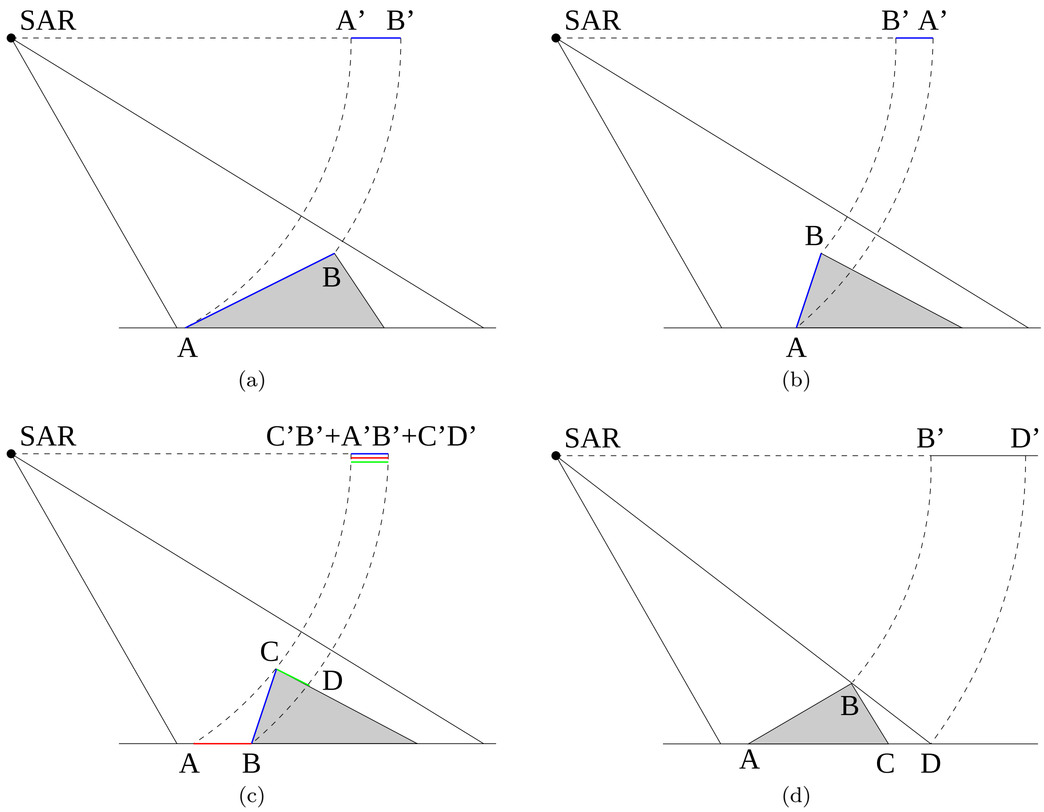

Figure 1.11: Geometric effects of SAR. (a) Foreshortening, (b) relief displacement, (c) layover, (d) shadow.
.

Although A is located on the ground in front of the elevated point B, the projection on the SAR slant range space results in a reversed order, i.e., B' is closer to the sensor than A'.

Layover The layover effect is related to the relief displacement. If a slope is steeper than the radar beam, parts of the ground surface, the slope facing the sensor, and parts of the slope turned away from the sensor are equidistant to the SAR antenna. Therefore, their backscattering return to the sensor at the same time, causing the layover effect, whereas the different signals cannot be separated anymore. For instance, in Fig. 1.11c, the slope $\overline{BC}$ is steeper than the incidence angle of the radar beam so that $\overline{AB}$, $\overline{BC}$, and $\overline{CD}$ are located within the same distance to the sensor. Hence, their backscattering overlays in the area $\overline{C'B'} + \overline{A'B'} + \overline{C'D'}$.

Shadow Shadows are areas where no backscattering is recorded at the sensor, because they are occluded from the radar beam. This occurs when surfaces which are turned away from the sensor are steeper than the SAR illumination, as shown in Fig. 1.11d. The area between $\overline{BD}$ cannot be illuminated by the radar beam, since $\overline{BC}$ is steeper than the radar beam, causing the shadow area $\overline{B'D'}$.

1.3.5 VHR SAR sensors

Until recently, SAR images with resolutions in the order of 1 m could only be obtained by airborne sensors. The first spaceborne VHR SAR sensors became available with the launch of the German TerraSAR-X satellite (Fig. 1.12a) and the Italian COSMO-SkyMed constellation (Fig. 1.12b). TerraSAR-X has been recently complemented by the TanDEM-X mission [22], which supports the acquisition of single pass InSAR data to produce a global DEM according to the HRTI-3 specification. Instead, the COSMO-SkyMed program consists of a constellation of four satellites. All the satellites have been launched successfully so far.

The TerraSAR-X satellite is equipped with a high resolution polarimetric SAR that operates in X-band (9.65 GHz) [21]. It acquires data with single or dual polarization in four acquisition modes: High-resolution SpotLight (HS), SpotLight (SP), StripMap (SM) and ScanSAR (SC). Furthermore, it can acquire fully polarimetric data using an experimental high resolution mode. An overview of the main acquisition parameters of TerraSAR-X is given in Tab. 1.2.

Similar to TerraSAR-X, the COSMO-SkyMed satellite constellation is equipped with X-band sensors which support the SP, SM and SC modes [20]. Another fine SP acquisition mode is dedicated to defense applications. It supports single and dual polarization modes (the latter only in a special SM mode). Since COSMO-SkyMed consists of four satellites it can provide images from the same region with a worst case response time of three days and a short worst case revisit time of 12 hours. The main characteristics of COSMO-SkyMed are summarized in Tab. 1.3.

Table 1.2: Main acquisition characteristics of TerraSAR-X.

Parameter	**HS**	**SP**	**SM**	**SC**
Coverage (azimuth × ground range)	5 km × 10 km	10 km × 10 km	< 1500 km × 30 km	< 1500 km × 100 km
θ	20° - 55°	20° - 55°	20° - 45°	20° - 45°
δ_{alt}	1 m	2 m	3 m	16 m
δ_{act}	1.5 m - 3.5 m	1.5 m - 3.5 m	1.7 m - 3.5 m	1.7 m - 3.5 m

Table 1.3: Main acquisition characteristics of COSMO-SkyMed.

Parameter	**SP**	**SM**	**SC**
Coverage (azimuth × ground range)	10 km × 10 km	30 km - 40 km × 30 km - 40 km	100 km - 200 km × 100 km - 200 km
θ	25° - 50°	25° - 50°	25° - 50°
δ_{alt}	1 m	3 m - 5 m	30 m - 100 m
δ_{act}	1 m	3 m - 5 m	30 m - 100 m

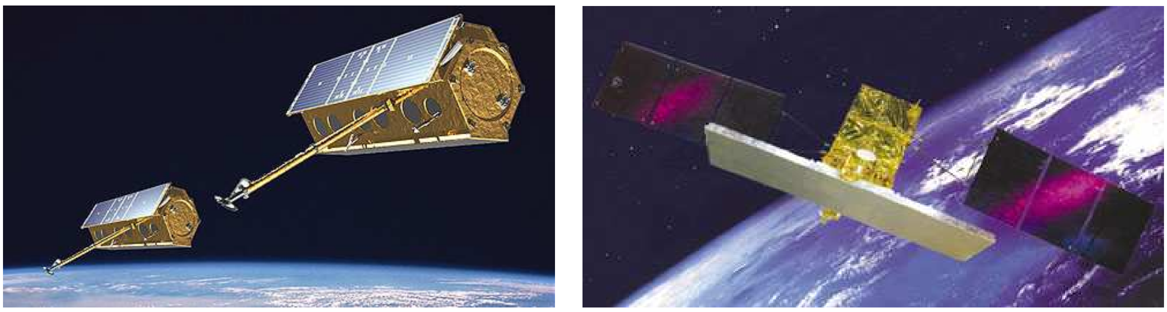

(a) (b)

Figure 1.12: VHR SAR satellites. (a) TanDEM-X constellation (© Astrium). (b) COSMO-SkyMed (© Telespazio.)

Part I

Novel Methods for the Automatic Analysis of Radar Sounder Signals

Chapter 2

Statistical Analysis of Radar Sounder Signals for the Automatic Detection and Characterization of Subsurface Features

In this chapter[1] we present both i) a study of the theoretical statistical properties of RS signals, and ii) two novel techniques for the automatic analysis of sounder radargrams. The main goal of the study is the identification of statistical distributions that can accurately model the amplitude fluctuations of different subsurface targets. This is fundamental for the understanding of signal properties and for the definition of automatic data analysis techniques. The results of such a study then drive the development of two novel techniques for i) the generation of subsurface feature maps, and ii) the automatic detection of the deepest scattering areas visible in the radargrams. The former produces for each radargram a map showing which areas have high probability to contain relevant subsurface features. The latter exploits a region-growing approach properly defined for the analysis of radargrams to identify and compose the basal scattering areas. Experimental results obtained on SHARAD data acquired at Mars confirm the effectiveness of the proposed techniques.

2.1 Introduction on the Automatic Analysis of Radar Sounder Data

As mentioned in the introduction of this thesis, the automatic analysis of planetary RS signals has not yet been addressed in the literature to a sufficient extent. The related works present in the literature regard the analysis of ground-based or airborne GPR and RS signals (e.g., [55, 56]), which operate in different frequency ranges and achieve a better spatial resolution with respect to orbiting RSs. Moreover, Earth campaigns are

[1]Part of this chapter appears in:
[54] A. Ferro and L. Bruzzone, "A novel approach to the automatic detection of subsurface features in planetary radar sounder signals," in *Proc. IEEE Int. Geoscience and Remote Sensing Symp. (IGARSS)*, 2011, pp. 1071–1074.

often reduced to well defined areas with limited extension, for which the interpretation of the radargrams can be performed manually, without the need of automatic techniques. An exception is represented by anti-mines and unexploded ordnance (UXO) detection campaigns, which make extensive use of GPR technology [57]. Different papers in the past decade proposed the use of pattern recognition approaches to the analysis of GPR signals (e.g., [55, 58–60]). However, they are mainly devoted to the detection of specific buried objects, such as mines, pipes or tanks buried at small depths using ground-based GPRs. Such objects present hyperbola-like signatures in the radargrams, which are completely different from the signatures of buried structures present in RS images acquired by orbiting platforms. The radargrams obtained by airborne acquisitions over the Earth's polar areas show similarities with spaceborne RS data acquired on icy bodies. The main features present in such images are subsurface echoes coming from the interfaces present between different subsurface ice layers and basal returns [61]. This is the typical situation shown in the radargrams related to the Mars' Poles [30, 31] and other areas of the Red Planet [44].

Another approach to the analysis of RS measurements is to apply inversion techniques to the signals in order to estimate the dielectric characteristics of the subsurface [62, 63]. In this context, the correct understanding of the radargrams and the development of any information extraction technique need the knowledge of the propagation laws of the radar signal into the matter in order to avoid errors in the physical interpretation of the returns [2]. However, the inversion process is very complex and requires proper assumptions on the investigated domain, e.g., on the ground composition [64].

This chapter provides a first contribution to fill the gap present in the literature on the automatic analysis of planetary RS data by presenting a study of the theoretical statistical properties of RS signals. The goal of this study is the identification of a statistical distribution which can accurately model the amplitude fluctuations of different subsurface targets. On the basis of the results of this study, we then propose two novel techniques for the generation of subsurface feature maps, and the automatic detection of the deepest scattering area visible in the radargrams.

The remaining of the chapter is organized as follows. Sec. 2.2 defines the radargram reference system and the notation used throughout this chapter and also in the other chapters of this part. In Sec. 2.3 we address the problem of the statistical modeling of RS signals. The models presented are then tested on real SHARAD data in Sec. 2.4. Sec. 2.5 presents an automatic technique for the generation of subsurface feature maps. Sec. 2.6 addresses the automatic detection of basal returns and its application to the SHARAD radargrams of the NPLD of Mars. Finally, Sec. 2.7 draws the conclusion of this chapter.

2.2 Radargram Reference System and Notation

In this section we fix the reference system and define the notation used throughout the thesis for what concerns the chapters devoted to the developed techniques for the analysis of RS data.

The acquisition geometry of a RS instrument is described in detail in Sec. 1.2.2. For the sake of completeness, we recall that the RS position projected on the ground at a generic time t has been depicted with (x_0, y_0), while h_0 represents the altitude of the

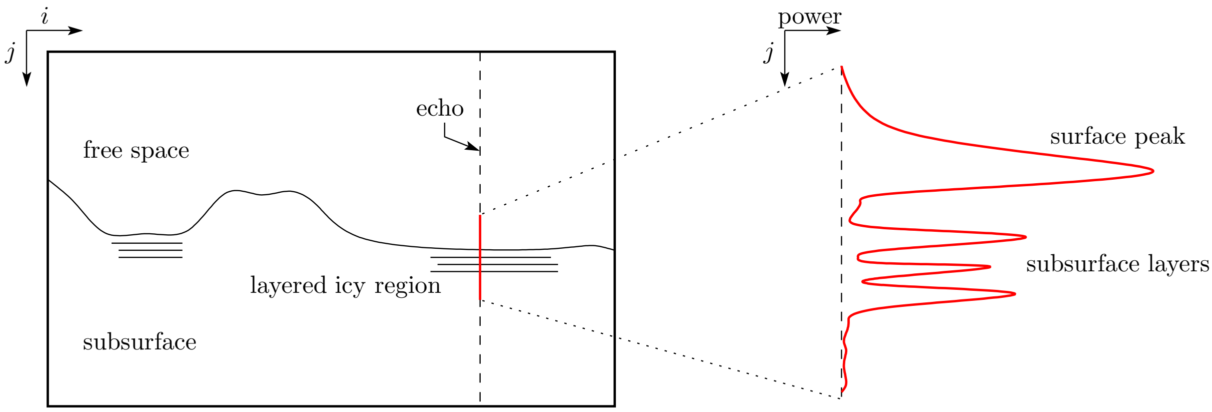

Figure 2.1: Radargram reference system and definition of the notation used in this thesis on a simplified qualitative radargram.

instrument from the ground. Similarly, a generic ground point is located at (x, y), and has a topographic elevation depicted by $h(x, y)$ (see Fig. 1.5).

In this thesis radargrams will be considered as 2D images composed by I columns. Each column i represents a radargram amplitude (or power) echo (or frame) which has been recorded by the RS at a certain position (x_i, y_i) during its receiving time window. Every frame is composed by J samples, which time separation depends on the instrument sampling frequency. The value of the radargram sample (i, j) will be denoted with $\xi(i, j)$ and a radargram image will be identified with X. Fig. 2.1 shows the defined reference system and notation on a simplified qualitative radargram. The spatial relation between radargram frames and geographical locations can be reconstructed by matching the coordinates i and (x_i, y_i). The translation of the range coordinates j into actual distances is more complex. Indeed, such a process needs the knowledge of the dielectric properties of the subsurface in order to properly convert time to depth [2]. It is noteworthy that the time position of surface clutter returns does not depend on the subsurface dielectric properties as the echoes generated by the surface propagate only in the free space.

2.3 Statistical Modeling of Radar Sounder Signals

In order to develop effective information extraction techniques from RS data, a precise knowledge of the statistics of the analyzed signals is necessary. In this section we review the main characteristics of the sounder signals and select three statistical models which are likely to be appropriate to model the signal fluctuations. The validity of such models will be tested on real SHARAD data in Sec. 2.4.

2.3.1 Background and Motivation

The analysis of radar signals is historically linked to statistics. This is due to the coherent nature of the radar signals which makes the RCS of targets fluctuate when even slightly changes in the viewing configuration or in the target orientation occur [1]. The effects of clutter and noise also greatly contribute to the fluctuations of the RCS. Radar signals are thus modeled using probability density functions (pfd) under the assumption that the signal amplitude (or intensity) is the realization of a random variable within each radar resolution cell. Many statistical models have been developed in order to fit the radar signals related to different target types. Such statistical models are based on theoretical descriptions of the scattering effects, or on empirical fitting to sample data. Examples of theoretical pdf commonly used in the analysis of radar signals are the Rayleigh, Rice, negative exponential, Gamma and K distributions. The most important empirical pdf are the Weibull and log-normal distributions [1].

The statistical approach has been extensively used in the analysis of SAR images for the characterization of distributed targets such as agriculture fields, forests or water surfaces. For this type of targets a single resolution cell does not provide sufficient information about the scattering characteristics of the surface under investigation due to the signal fluctuations, which depend on intrinsic fluctuations of the target RCS and on speckle. In order to characterize the analyzed surface it is thus necessary to calculate statistical parameters of the distribution of the radar signals coming from the area of interest.

In this context, statistical tools can be also exploited for the analysis of RS signals for the detection and characterization of different types of subsurface features. This can support the analysis of the radargrams, by automatically detecting the regions of interest and extracting information which can drive subsequent feature extraction algorithms. The goal of this section is thus to define a reference theoretical framework which can be used for a reliable statistical analysis of the signals, taking into account the physical characteristics of the targets.

2.3.2 Statistical Models

In order to perform an analysis of RS signals, it is necessary to describe the signal statistical properties taking into account the physical processes involved in the scattering from subsurface features for a typical RS instrument mounted onboard an aerial or satellite platform. Our goal is to describe statistically the distribution of the signals coming from the subsurface by considering groups of adjacent samples in a predefined neighborhood system extended both in range (vertical) and azimuth directions. As mentioned previously, each radargram can be seen as a 2D image defined in the range and azimuth directions. The signals measured by the radar during each acquisition window (frames) correspond to the columns of the 2D image. Thus, pixels in the same neighborhood system describe the geologic features in a given position of the subsurface. According to this modeling, we can analyze radargrams with a 2D signal processing approach; this is important given that most of the subsurface features detected by a RS are not spot features but show a certain extension, especially in the azimuth direction.

As a reference, Tab. 2.1 reports the main characteristics of the two RSs currently operating at Mars: MARSIS [7] and SHARAD [8]. The resolutions of the radars are comparable with the diameter of the corresponding Fresnel zone, from which the returns are supposed to be coherent. However, the surface and especially the subsurface, which is the target of our investigation, are far from being flat and always present a certain amount of roughness, which introduces a significant non-coherent component in the scattering [65].

Table 2.1: Main characteristics of the MARSIS and SHARAD RSs operating at Mars.

Instrument	f_c	λ_c $(\varepsilon_r = 4)$	B_w	δ_z $(\varepsilon_r = 4)$	δ_{alt}	δ_{act}	D_F
MARSIS	1.8-5 MHz	83-30 m	1 MHz	75 m	5-10 km	10-30 km	∼10 km
SHARAD	20 MHz	7.5 m	10 MHz	7.5 m	0.3-1 km	3-7 km	∼3 km

Indeed, the amount of roughness drives the across-track resolution, which, for MARSIS and SHARAD, is controlled only by their dipole antenna pattern as no synthetic aperture processing is possible in the across-track direction. It is thus possible to consider the radar footprints sufficiently wide to assume that many different independent scatterers contribute to the scattering for each resolution cell.

In the following, we will focus on the statistical distribution of amplitude signals. The analysis of amplitude data is preferred here with respect to intensity data due to the large dynamic that characterize RS acquisitions, which is much more amplified in intensity data and may affect the stability of the analysis.

Rayleigh pdf

The simplest pdf that describes the amplitude ξ of the returns from a large number Q of independent scatterers is the Rayleigh distribution:

$$p_R(\xi) = \frac{2\xi}{\mu_{\xi^2}} \exp\left[-\frac{\xi^2}{\mu_{\xi^2}}\right], \tag{2.1}$$

where ξ^2 indicates the signal power, and μ_{ξ^2} is the only parameter of the distribution and represents the mean power of the signal [1]. Eq. (2.1) is valid for $\xi \geq 0$ (this also holds for the other pdfs which will be presented in the following) and the mean value of ξ is given by $\mu_\xi = \sqrt{\pi\mu_{\xi^2}}/2$. The corresponding distribution in the power (intensity) domain is the negative exponential distribution. It is worth noting that the Rayleigh distribution is also the ideal theoretical model for the amplitude when a zero mean additive white Gaussian noise (AWGN) affects the in-phase and quadrature signals received by the radar in areas of no subsurface scattering.

Nakagami pdf

The second model that we consider is the Nakagami pdf, which is a two-parameter function given by [66]:

$$p_N(\xi) = 2\left(\frac{v_N}{\mu_{\xi^2}}\right)^{v_N} \frac{\xi^{2v_N-1}}{\Gamma(v_N)} \exp\left[-\frac{v_N\xi^2}{\mu_{\xi^2}}\right], \tag{2.2}$$

where v_N is called *shape* or *order parameter* and $\Gamma(.)$ depicts the gamma function. The validity range of v_N is $(0; +\infty)$. The Nakagami pdf for amplitude data corresponds in the intensity domain to the Gamma pdf described by the shape parameter $v_\Gamma = v_N$ and the mean intensity μ_{ξ^2} [66]. The Gamma pdf has been widely used for the modeling of radar signals and is a generalization of other well-known distributions, such as the negative exponential and chi-square [67]. In particular, when v_Γ is an integer value, the Gamma pdf can be derived as the sum of v_Γ identical independent exponentially distributed random variables. Similarly, in the amplitude domain the Nakagami pdf is a generalization of the Rayleigh pdf, which can be obtained by setting $v_N = 1$ in (2.2).

K pdf

The last distribution that we consider is the K distribution, defined as [1]:

$$p_K(\xi) = \frac{4}{\Gamma(v_K)} \left(\frac{v_K}{\mu_{\xi^2}}\right)^{(v_K+1)/2} \xi^{v_K} K_{v_K-1}\left[2\xi\sqrt{\frac{v_K}{\mu_{\xi^2}}}\right], \tag{2.3}$$

where $K_{v_K-1}(.)$ is the modified Bessel function of the second kind of order $v_K - 1$. The parameter v_K is also called shape (or order parameter), and its validity range is $(0; +\infty)$. The K distribution has also been used for modeling sea clutter and distributed targets of different types in SAR images. It is derived by assuming that the number of scatterers within a resolution cell Q fluctuates being controlled by a birth-death-immigration process, i.e., Q is a random variable that follows a negative binomial distribution [1]. The assumption that the number of scatterers varies between different resolution cells is in agreement with the scenario represented by a RS acquisition, where within each single radargram frame a different number of scatterers (e.g., subsurface interfaces) may contribute to the scattering measured in different time samples.

The K distribution is also obtained by modeling the radar intensity ξ^2 as a compound pdf, also referred to as *product model*. This formulation expresses the radar intensity as the product of two uncorrelated processes with different spatial scales: an underlying RCS and a multiplicative speckle contribution. The mathematical representation of this formulation is:

$$p_K(\xi^2) = \int_0^\infty p_1(\xi^2/u)p_2(u)du, \tag{2.4}$$

where $p_2(u)$ represents the pdf of the underlying RCS (which only depends on the physical characteristics of the scatterers) and $p_1(\xi^2/u)$ is the speckle contribution, which arises as a consequence of their random distribution and orientation. By assuming an underlying RCS which is Gamma distributed and a speckle contribution modeled by a negative exponential pdf, both the signal intensity and amplitude result K distributed [1].

The product model is thus suited to the modeling of spatially non-homogeneous targets. As proposed in [68] and [69], $p_1(\xi^2/u)$ can be interpreted as the density of the returns from an incremental area of a surface which reflectivity varies spatially with mean u, while $p_2(u)$ describes the bunching of scatterers in terms of spatial variations of the underlying RCS, which are on a much larger scale than the variations described by $p_1(\xi^2/u)$. Such a formulation has been effectively used to model sea clutter, where scatterers are bunched by swell structure [69]. This situation to a certain extent resembles the measurements performed by a RS in presence of subsurface layer stratigraphy, where the returns are bunched at each interface. The K distribution has thus physical basis which are in agreement with the characteristics of RS acquisitions.

Fig. 2.2 shows a comparison between the Rayleigh, Nakagami and K distributions for a fixed μ_{ξ^2} and varying shape parameters.

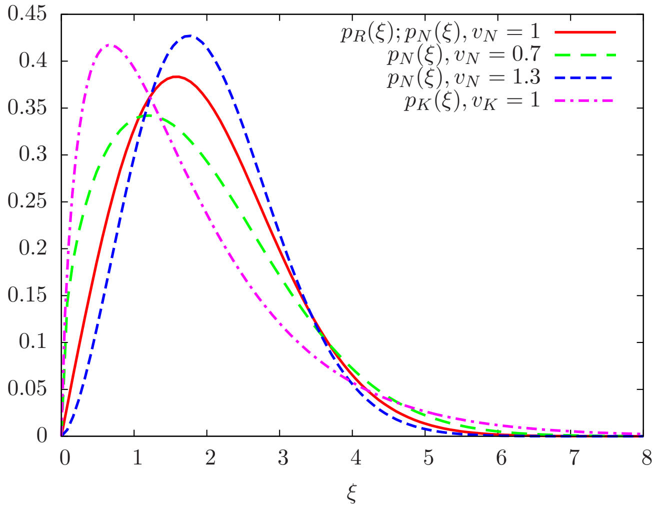

Figure 2.2: Examples of pdf curves obtained using the models presented in Sec. 2.3. For all the curves $\mu_{\xi^2} = 5$.

Other pdfs can be used to model radar data, e.g., Rice, log-normal, Weibull [1]. In particular, for the analysis of RS signals, the Rice distribution is suited to the modeling of surface returns from flat surfaces, allowing the estimation of the coherent scattering for inversion purposes [70]. However, the pdfs selected for the analysis reported in this dissertation cover the most important classes of theoretical distributions which are used for the modeling of radar data, and have the advantage to allow us to describe the scattering from subsurface features with a physical-based approach. As such, they represent generalizations or approximations of many other distributions proposed in the literature. It is worth noting that the research of the absolute best fitting pdf for RS signals is out of the scope of this work.

2.4 Empirical Analysis of the Statistical Models on SHARAD Radargrams

With the goal of studying the statistical distribution of real data, we analyzed different subsurface target types and studied the statistical distributions of their returns by fitting the theoretical pdfs described in Sec. 2.3 to the data. We selected as test data a set of SHARAD radargrams of the North Pole Layered Deposits (NPLD) of Mars. Such radargrams show different target types, from very strong scattering linear interfaces (due to ice stratigraphy) to smooth returns from the base of the NPLD. An example of SHARAD radargram of the NPLD of Mars and its ground track overlayed on a DEM obtained from Mars Orbiter Laser Altimeter (MOLA) [71] data are reported in Fig. 2.3.

2.4.1 Definition of Target Classes and Dataset Description

The target classes that we investigated are the following: *no target* (NT), *strong layers* (SL), *weak layers* (WL), *low returns* (LR), *basal returns* (BR). The class *no target* cor-

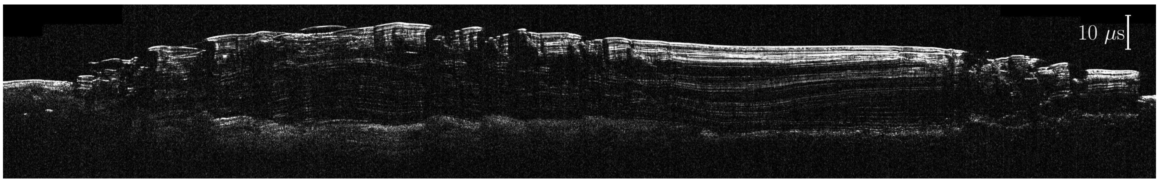

(a)

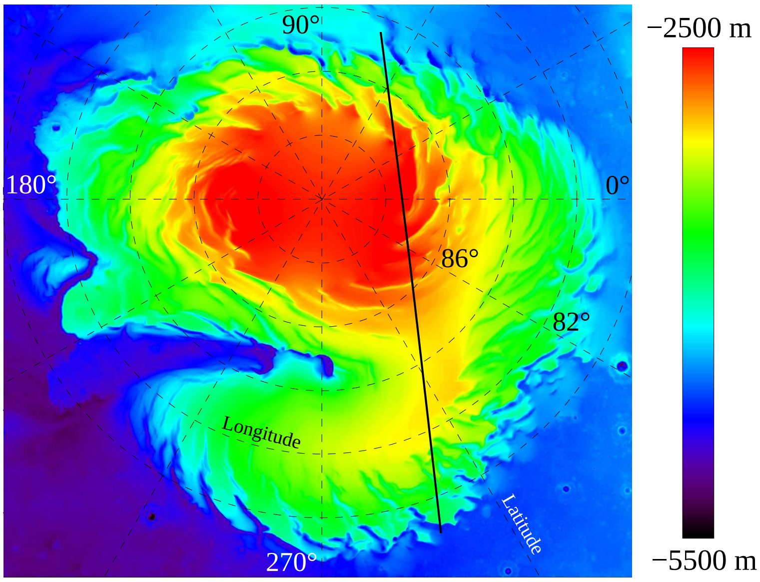

(b)

Figure 2.3: (a) Portion of the SHARAD radargram 1319502, and (b) its acquisition track highlighted on an altimetric map of the NPLD of Mars derived from MOLA data. The radargram corresponds to the solid line.

responds to areas of the radargram where no scattering is present. These are the upper part of the radargram, before any surface return, and the areas in the subsurface where no interfaces are detected. We define *strong layers* the areas of the radargram where dense and strong scattering layering is present. This corresponds generally to areas in the upper subsurface of the NPLD. The class *weak layers* corresponds to the subsurface scattering related to less dense and less strong scattering layering, which usually occurs below the areas described by the class *strong layers*. The class *low returns* includes the areas of the radargram containing very weak scattering coming from deep structures. When these are present, they are usually located between the areas of *weak layers* and *basal returns*. Finally, the class *basal returns* is related to the scattering coming from the base of the NPLD, which nature gives a diffuse scattering especially in correspondence of the so-called basal unit [72]. Fig. 2.4 highlights such classes on the test radargram of Fig. 2.3.

The analysis has been carried out on 7 SHARAD radargrams of the NPLD of Mars. The radargrams were stored in the Reduced Data Record (RDR) format [73], and have been downloaded from the the Geosciences Node of NASA's PDS [48]. We extracted the amplitude information and aligned in time the echoes using the information contained in the RDRs. As the data are highly oversampled, we applied a downsampling factor of

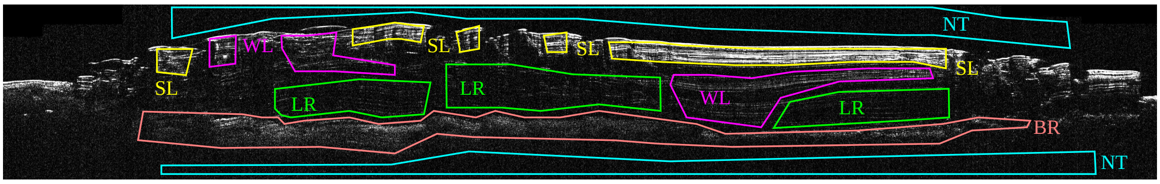

Figure 2.4: Target classes used in the statistical analysis highlighted on the radargram showed in Fig. 2.3.

Table 2.2: SHARAD radargrams used in the analysis and number of samples per target class collected for each radargram.

Radargram number	NT	SL	WL	LR	BR
0371502	212,311	9,443	18,233	18,017	50,905
0385902	166,832	4,425	6,284	13,289	21,417
0681402	209,416	41,459	22,264	44,829	130,687
0794703	209,057	14,586	27,004	46,207	71,387
1292401	113,768	4,701	11,173	12,049	37,082
1312901	148,651	9,173	17,596	51,218	26,684
1319502	195,748	14,688	18,952	33,448	72,582

15. No multilooking has been performed in order to maintain the original statistics of the signals. The acquisitions have been cut in order to consider only the NPLD area. The resulting radargrams are made of a number of samples between 1,071,869 and 2,582,624. On each radargram we selected manually the areas corresponding to the defined classes. In Tab. 2.2 we report for each analyzed acquisition its identification number and the number of samples per class we collected. It is worth noting that a very high number of samples for each class in each radargram is considered in order to have a reliable statistical analysis.

2.4.2 Procedure for the Estimation of pdf Parameters

In order to estimate the parameters of the theoretical statistical distributions different approaches have been suggested in the literature. As an example, an interesting approach based on *second kind statistics* has been proposed by Nicolas [74] for the analysis of SAR images. In this thesis we estimated the parameters of the Rayleigh, Nakagami and K distributions for each class type using a Maximum Likelihood (ML) estimation approach. For the Rayleigh distribution the ML estimate $\tilde{\mu}_{\xi^2}$ of the only parameter μ_{ξ^2} is given by the sample mean power [67]:

$$\tilde{\mu}_{\xi^2} = \frac{1}{n_{\mathrm{smp}}} \sum_{q=1}^{n_{\mathrm{smp}}} \xi_q^2, \tag{2.5}$$

where ξ_q depicts an amplitude sample, and n_{smp} is the number of considered samples.

For the Nakagami distribution, the estimate $\tilde{\mu}_{\xi^2}$ is obtained as for the Rayleigh distribution, and is given by (2.5). The calculation of $\tilde{v}_N$ has been performed using the classical estimator proposed by Greenwood and Durand [75], which is considered in the literature an accurate estimator for the shape parameter of the Nakagami distribution [76]. Therefore, $\tilde{\upsilon}_N$ has been derived by:

$$\tilde{\upsilon}_N = \begin{cases} (0.5000876 + 0.1648852\upsilon - 0.0544274\upsilon^2)/\upsilon & \text{if } 0 < \upsilon \leq 0.5772 \\ \dfrac{8.98919 + 9.059950\upsilon + 0.9775373\upsilon^2}{\upsilon(17.79728 + 11.968477\upsilon + \upsilon^2)} & \text{if } 0.5772 < \upsilon < 17, \end{cases} \tag{2.6}$$

where

$$\upsilon = \ln\left(\frac{\tilde{\mu}_{\xi^2}}{F}\right) \tag{2.7}$$

and

$$F = \left(\prod_{q=1}^{n_{\text{smp}}} \xi_q^2\right)^{\frac{1}{n_{\text{smp}}}}. \tag{2.8}$$

The ML estimation of the K distribution has been obtained retrieving the $\tilde{\upsilon}_K$ and $\tilde{\mu}_{\xi^2}$ estimated values by the numerical maximization of the log-likelihood function, according to [77], i.e.,

$$(\tilde{\upsilon}_K, \tilde{\mu}_{\xi^2}) = \arg \max_{(\upsilon_K, \mu_{\xi^2})} \left\{\ln\left[l_{n_{\text{smp}}}(\upsilon_K, \mu_{\xi^2}; \xi_1, \xi_2, \ldots, \xi_{n_{\text{smp}}})\right]\right\}, \tag{2.9}$$

where

$$\ln\left[l_{n_{\text{smp}}}(\upsilon_K, \mu_{\xi^2}; \xi_1, \xi_2, \ldots, \xi_{n_{\text{smp}}})\right] = \upsilon_K \sum_{q=1}^{n_{\text{smp}}} \ln \xi_q + \sum_{q=1}^{n_{\text{smp}}} \ln\left\{K_{\upsilon_K - 1}\left[2\xi_q\sqrt{\frac{\upsilon_K}{\mu_{\xi^2}}}\right]\right\} + n_{\text{smp}}\left\{\frac{\upsilon_K + 1}{2}\ln\left(\frac{\upsilon_K}{\mu_{\xi^2}}\right) + \ln 4 - \ln\Gamma(\upsilon_K)\right\}, \tag{2.10}$$

and $l_{n_{\text{smp}}}(\upsilon_K, \mu_{\xi^2}; \xi_1, \xi_2, \ldots, \xi_{n_{\text{smp}}})$ is the likelihood function for the K distribution. Due to numerical constraints, the range of values of υ_K has been limited between 0.1 and 50. However, this does not affect the generality of our analysis. Indeed, on the one hand, the characteristics of the signals never require values of υ_K lower than 0.1. On the other hand, for $\upsilon_K \geq 50$ the K distribution becomes nearly Rayleigh [77]. Therefore, the use of values greater than 50 for υ_K is not significant for the comparison between the fitting performance of the two pdfs. For the parameter μ_{ξ^2} we only imposed a lower limit at 0.1, which is well below the typical noise mean power of the SHARAD data.

2.4.3 Results

Tab. 2.3 and Tab. 2.4 report the results obtained for the different classes of targets for each analyzed radargram. The fitting performances of the distributions are shown in Tab. 2.3. These performances have been evaluated in terms of root mean square error (RMSE) and Kullback-Leibler divergence (KL) between the normalized histogram of the data and the histogram obtained by the fitting of each distribution. The KL divergence is defined as [78]:

$$\text{KL}(\text{pdf}, \text{pdf}_{\text{fit}}) = \sum_{\xi_q} \text{pdf}(\xi_q) \log \frac{\text{pdf}(\xi_q)}{\text{pdf}_{\text{fit}}(\xi_q)}, \tag{2.11}$$

where pdf and pdf_{fit} represent the probability distribution of the samples and of the theoretical fit, respectively. The values of ξ_q depend on the size of the bins used for the computation of the histograms. This size has been calculated for each target class according to the method proposed in [79], which is suited for unknown distribution data values, and has already been used for the computation of histograms of SAR images [80]. Tab. 2.4 reports the parameters derived for each fitting distribution. The parameter $\tilde{\mu}_{\xi^2}$ obtained for the Rayleigh distribution is not reported, as it is equal to the corresponding one of the Nakagami distribution. As an example, Fig. 2.5 shows the histogram and the ML estimates for each target class for the test radargram of Fig. 2.3.

The results point out that the best fitting distribution is in almost all the cases the K distribution. Such results agree with the physical basis of the K distribution, which can describe effectively the cases where the scatterers are bunched (see Sec. 2.3). The Nakagami distribution provides almost always a more accurate fit than the Rayleigh distribution except for the case of the *no target* class. For the *no target* case, as expected from the theory, the Rayleigh distribution is an effective estimate as it provides accurate estimations using only one parameter. The Nakagami distribution has approximately the same fitting performance using two parameters, but $\tilde{v}_N$ is always nearly 1, i.e., it approximates the Rayleigh pdf. The K distribution shows lower fitting performances for the *no target* case. This is due to the numerical limit imposed to $\tilde{v}_K$. However, as previously mentioned, the higher $\tilde{v}_K$ the more the distribution approximates the Rayleigh pdf. The Rayleigh pdf can thus be considered the best fitting distribution for the *no target* areas. This confirms that the background noise of the SHARAD data can be modeled as a zero mean AWGN in both the in-phase and quadrature components.

Let us now focus on the computational complexity of the ML estimation for the three considered distributions. Such issue becomes relevant when the statistical analysis of the signals is propaedeutic to other processing steps, e.g., filtering or feature-extraction algorithms. The calculations of the ML estimates for the Rayleigh and Nakagami pdfs are performed analytically and their computational time is negligible on a standard workstation. Instead, the maximization of (2.10) for the estimation of the parameters of the K distribution must be performed numerically. Although the computational time in our tests is still in the order of less than one minute, it may become not negligible when analyzing a large series of radargrams. When the computational time becomes a limit in practical analysis scenarios, one may consider to use the Nakagami distribution for the modeling of the signal statistics in order to speed up the processing, at the cost of slightly lower accuracy.

Table 2.3: Fitting performances of the Rayleigh, Nakagami and K distributions to the sample amplitude data for each scattering class. The best results are highlighted in bold.

Radargram number	**Distribution**	**NT**		**SL**		**WL**		**LR**		**BR**	
		RMSE	KL	RMSE	KL	RMSE	KL	RMSE	KL	RMSE	KL
0371502	Rayleigh	0.0031	0.0067	0.0074	0.0381	0.0133	0.0516	0.0125	0.0108	0.0106	0.0243
	Nakagami	**0.0031**	**0.0067**	0.0032	0.0108	0.0075	0.0186	0.0085	0.0043	0.0079	0.0146
	K	0.0041	0.0068	**0.0028**	**0.0060**	**0.0018**	**0.0021**	**0.0046**	**0.0028**	**0.0024**	**0.0033**
0385902	Rayleigh	0.0032	**0.0029**	0.0118	0.1035	0.0147	0.0475	0.0161	0.0293	0.0108	0.0313
	Nakagami	**0.0031**	0.0030	0.0068	0.0418	0.0103	0.0249	0.0121	0.0153	0.0092	0.0214
	K	0.0047	0.0031	**0.0026**	**0.0067**	**0.0046**	**0.0056**	**0.0059**	**0.0042**	**0.0045**	**0.0058**
0681402	Rayleigh	0.0034	**0.0045**	0.0085	0.0707	0.0222	0.1258	0.0177	0.0247	0.0193	0.0675
	Nakagami	**0.0034**	0.0045	0.0054	0.0285	0.0141	0.0503	0.0139	0.0136	0.0149	0.0362
	K	0.0048	0.0046	**0.0014**	**0.0031**	**0.0044**	**0.0054**	**0.0054**	**0.0033**	**0.0060**	**0.0064**
0794703	Rayleigh	0.0041	0.0062	0.0027	0.0089	0.0188	0.0732	0.0122	0.0131	0.0155	0.0462
	Nakagami	**0.0040**	**0.0060**	0.0021	0.0052	0.0120	0.0293	0.0090	0.0068	0.0126	0.0283
	K	0.0052	0.0062	**0.0014**	**0.0033**	**0.0039**	**0.0028**	**0.0031**	**0.0036**	**0.0052**	**0.0048**
1292401	Rayleigh	0.0046	**0.0041**	0.0052	0.0288	0.0213	0.1016	0.0152	0.0108	0.0157	0.0343
	Nakagami	**0.0045**	0.0043	0.0043	0.0225	0.0140	0.0456	0.0116	0.0060	0.0124	0.0190
	K	0.0062	0.0042	**0.0034**	**0.0110**	**0.0051**	**0.0074**	**0.0087**	**0.0025**	**0.0053**	**0.0058**
1312901	Rayleigh	0.0058	0.0048	0.0039	0.0623	0.0253	0.1093	0.0174	0.0272	0.0178	0.0357
	Nakagami	**0.0058**	**0.0047**	0.0043	0.0500	0.0164	0.0452	0.0149	0.0157	0.0125	0.0189
	K	0.0068	0.0048	**0.0035**	**0.0252**	**0.0057**	**0.0061**	**0.0072**	**0.0065**	**0.0038**	**0.0026**
1319502	Rayleigh	**0.0053**	0.0091	0.0029	0.0135	0.0157	0.0540	0.0210	0.0202	0.0178	0.0585
	Nakagami	0.0053	**0.0089**	**0.0022**	0.0105	0.0079	0.0151	0.0166	0.0109	0.0140	0.0346
	K	0.0065	0.0091	0.0025	**0.0082**	**0.0027**	**0.0029**	**0.0073**	**0.0035**	**0.0056**	**0.0070**

2.5 Proposed Technique for the Generation of Subsurface Feature Maps

The results presented in the previous section can be used to study the RS signals and analyze the scattering signatures of different types of targets. However, they also open to a wide range of applications for the automatic analysis of the radargrams. As mentioned in the introduction of this thesis, planetary radar sounding missions have provided and are still providing a large amount of data, which have been studied mostly by means of manual investigations. In this framework, the automatic detection of radargrams containing subsurface features from the whole available set of radargrams, and the automatic identification of the subsurface areas containing relevant features within each radargram become important tasks that can greatly support scientific investigations. In this section we propose a novel automatic method for the generation of maps of the subsurface areas containing relevant features within a radargram by analyzing the statistical distributions of local parcels of the radargram.

2.5.1 Proposed Technique

As discussed in Sec. 2.4, the background noise of SHARAD radargrams is Rayleigh distributed. The noise characteristics can be simply measured using the samples belonging to the free space region of the radargram, i.e., before any surface echo. Therefore, the statistical distribution of the noise can be determined precisely and in an automatic way. By measuring the statistical difference between the histograms of subsurface parcels and the noise distribution it is thus possible to discriminate in an unsupervised way the areas containing only noise from the regions which contain subsurface features. Several statistical indicators can be used to measure the difference between two distributions. Here, we propose the use of the KL divergence between the histogram of the samples S and the theoretical noise distribution N, i.e., $\mathrm{KL}_{SN} = \mathrm{KL}(S, N)$. The noise characteristics can vary significantly between different acquisitions (see Tab. 2.4). This is mainly due to different conditions of acquisition, e.g., in terms of solar activity or spacecraft attitude, which may raise the background noise level. The proposed algorithm takes into account this issue and adapts its behavior to the variations of the background noise level by automatically detecting and measuring the statistical characteristics of the free space region for each radargram.

A block scheme of the proposed technique is shown in Fig. 2.6. The main steps of the technique are explained in the following using as reference example the SHARAD radargram of Fig. 2.3.

1. *First return detection*: this step aims at automatically identifying the returns from the surface for then discriminating in the radargram the parts belonging to the free space and those associated with the subsurface. The former is used to estimate the radargram background noise signal distribution in the next step. For each frame (column) i of the radargram the algorithm detects the position of the first sample which is statistically different from the frame background noise. We denote such a

Table 2.4: Parameters of the fitted distributions for each test radargram.

Radargram number	**Target class**	**Nakagami** $\tilde{v}_N$	**Nakagami** $\tilde{\mu}_{\xi^2}$	**K** $\tilde{v}_K$	**K** $\tilde{\mu}_{\xi^2}$
0371502	NT	0.999	3.379	50.000	3.381
	SL	0.766	94.201	2.687	94.834
	WL	0.742	33.159	2.313	33.152
	LR	0.896	5.691	7.074	5.689
	BR	0.860	9.769	4.535	9.719
0385902	NT	1.003	3.545	50.000	3.547
	SL	0.673	97.087	1.702	95.763
	WL	0.778	29.970	2.705	29.847
	LR	0.834	6.647	3.958	6.615
	BR	0.856	9.454	4.370	9.374
0681402	NT	1.000	2.897	50.000	2.899
	SL	0.721	85.028	2.121	84.101
	WL	0.643	27.466	1.539	26.781
	LR	0.854	5.454	4.363	5.430
	BR	0.755	10.954	2.524	10.753
0794703	NT	0.997	2.565	50.000	2.567
	SL	0.921	86.080	8.735	86.045
	WL	0.711	26.598	1.999	26.379
	LR	0.901	4.451	6.676	4.446
	BR	0.804	10.831	3.178	10.695
1292401	NT	1.006	2.390	50.000	2.392
	SL	0.872	77.220	4.833	76.931
	WL	0.680	18.658	1.803	18.276
	LR	0.908	3.360	7.192	3.357
	BR	0.830	6.405	3.860	6.357
1312901	NT	0.999	1.933	50.000	1.934
	SL	0.850	87.901	4.297	86.165
	WL	0.665	18.927	1.681	18.537
	LR	0.867	3.143	4.766	3.125
	BR	0.810	8.426	3.325	8.373
1319502	NT	0.998	1.930	50.000	1.931
	SL	0.921	90.057	9.705	89.947
	WL	0.725	29.366	2.115	29.538
	LR	0.874	3.297	5.000	3.288
	BR	0.782	7.747	2.908	7.609

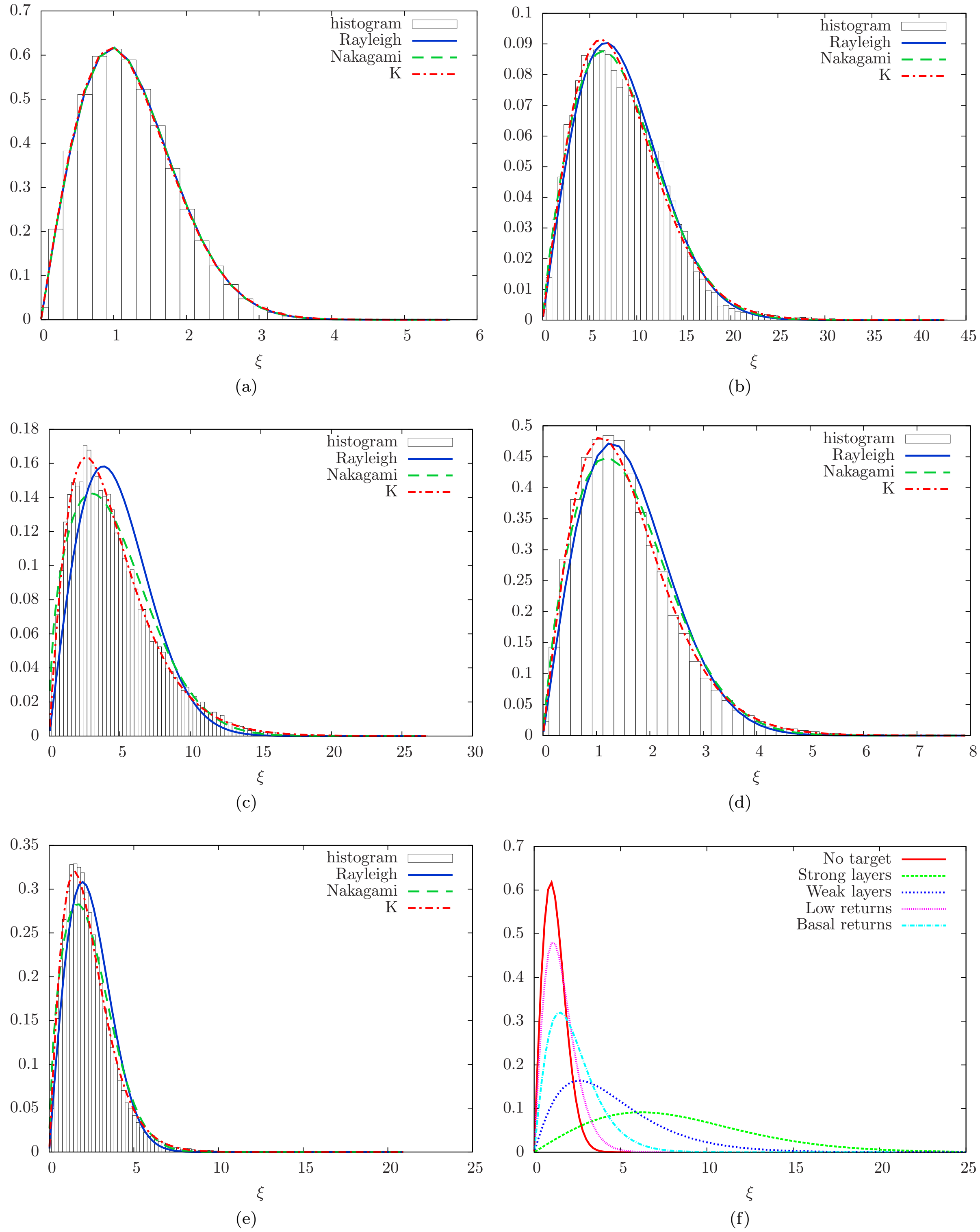

Figure 2.5: Empirical and ML distributions for each target class for the SHARAD radargram 1319502 (see Fig. 2.3): (a) *no target*, (b) *strong layers*, (c) *weak layers*, (d) *low returns*, (e) *basal returns*, (f) summary of the fitted K distributions for each target class.

position as $j_0(i)$ and calculate it as follows:

$$j_0(i) = \min\{j : \xi(i,j) > \mu_N + \varrho_1 s_N\} \qquad \forall j, \tag{2.12}$$

where $\xi(i,j)$ is the amplitude of the sample of the frame i at the time step j; μ_N and s_N are the estimated frame noise mean amplitude and standard deviation, respectively; ϱ_1 is a multiplicative factor. The detected samples are in the ideal case representative of the nadir surface return. This is not true when lateral clutter echoes arrive to the receiver before the nadir return. The local statistics of the noise is estimated for each frame using its last 50 samples, which are in general free from subsurface features as the signal loss is very high at the corresponding depth. If no sample fulfills the condition, the value of ϱ_1 is decreased and the procedure is repeated. At each iteration e the value of ϱ_e is calculated using a positive damping factor df < 1, according to:

$$\varrho_e = \mathrm{df} \cdot \varrho_{e-1} \qquad \forall e = 2, \ldots, E, \tag{2.13}$$

where E is the maximum number of iterations. E, the initial value ϱ_1 and the damping factor df are specified by the user. Note that from (2.12) the minimum signal level necessary to perform a detection cannot be lower than the frame noise mean μ_N. In the case that after E trials no sample fulfills the condition yet, the first return position of the considered frame is estimated using the average position of the first adjacent frames for which the detection was successfully. After the frame-based detection, a smoothing function is applied in order to reduce the effects of both outliers and missing detections. The smoothing function performs local regression using weighted linear least squares and a first-degree polynomial model. Using this approach, for each frame the algorithm detects the most reliable first return at the first iteration (according to a user-defined minimum signal level dependent on ϱ_1). The reliability of the detection decreases increasing the number of iterations. By properly setting E and df the user can thus tune the reliability of the first return detection. The result of the first return detection applied to the test radargram using $E = 3$, $\varrho_1 = 4.5$, and df $= 0.9$ is shown in Fig. 2.7a.

2. *Estimation of the noise statistics*: in this step the algorithm uses all the samples of the radargram belonging to the free space region R_{fs} to estimate the parameter μ_{ξ^2} of a Rayleigh distribution, according to the ML approach (see Sec. 2.4.2). R_{fs} is defined as the upper part of the radargram delimited by the line representing the first returns identified in the previous step, i.e.,

$$R_{fs} = \{(i,j) : 0 < j < j_0(i) - w_G\}, \tag{2.14}$$

where w_G is a positive constant used in order to introduce a guard interval to take into account possible uncertainty in the detection of the first returns. The selection of the value of w_G should be made according to the level of reliability achieved by the first return detection. However, in our experiments the choice of the value of w_G has never been a critical issue. $w_G = 10$ has been used in all our tests.

3. *Calculation of KL_{SN}*: a map of KL_{SN} is generated using a sliding window of $w_a \times w_r$ samples (along-track $\times$ range), and a step of δw_a and δw_r samples in the along-track

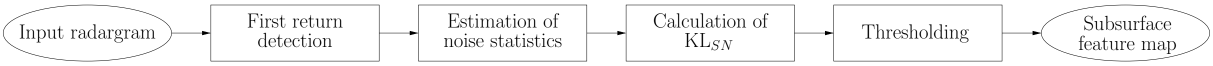

Figure 2.6: Block scheme of the proposed technique for the generation of subsurface feature maps.

and range direction, respectively. The distribution of N is the one estimated in the previous step. The value of KL_{SN} is averaged in the intersections of overlapping windows. This process is applied only to the subsurface part of the radargram, which is defined as the bottom part of the radargram delimited by the first return line. The choice of the size and of the steps of the sliding window should be driven by the characteristics of the considered targets, which are generally extended in the azimuth direction but can present sharp variations in the range direction. Fig. 2.7b shows the values of KL_{SN} obtained on the test radargram using $w_a = 40$, $w_r = 10$, $\delta w_a = 8$, and $\delta w_r = 10$.

4. *Thresholding*: in this step the algorithm produces a binary map which discriminates between the presence and the absence of subsurface features by thresholding the image of KL_{SN} using the threshold thr_{KL}. The value of thr_{KL} can be chosen either manually or automatically [81]. Fig. 2.7c shows the binary map obtained from Fig. 2.7b by using $thr_{\mathrm{KL}} = 0.13$.

2.5.2 Results and Discussion

The results presented in Fig. 2.7b show a description of the characteristics of the subsurface in the radargram of Fig. 2.3 in terms of statistical difference from the background noise computed according to the values of the KL_{SN} distance. Such a difference may vary within the same scattering class. As an example, the statistical characteristics of the scattering coming from the basal area are not uniform. Fig. 2.7c shows the map of the subsurface features of the aforementioned radargram. A qualitative comparison between Fig. 2.3 and Fig. 2.7c points out the high accuracy obtained by the proposed technique in the detection of subsurface features. In order to measure quantitatively the performance of the proposed algorithm, for each tested radargram we selected randomly 3000 reference samples from the regions where it was possible to state clearly whether subsurface features were present or absent. Using such samples, we evaluated the number of missed and false detections yielded by the proposed algorithm with the parameters reported in the previous subsection. The obtained results (see Tab. 2.5) point out that most of the subsurface features present in the radargrams are correctly detected. As it is visible in Fig. 2.7c, the areas corresponding to the target classes *strong layers*, *weak layers* and *basal returns* are mostly correctly detected by the algorithm, whereas the class *low returns* is only partially detected. This can be explained by the simple sliding window and averaging model adopted in this thesis. This acts as a low pass filtering and averages the statistical characteristics of the classes *low returns* and *no target*, which are similar from the statistical point of view (see Tab. 2.4). The choice of the parameters of the algorithm should be driven by both the sensitivity needed for the detection and the type of features which have to be detected.

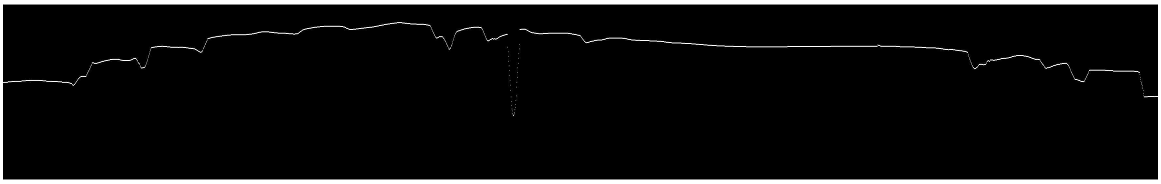

(a)

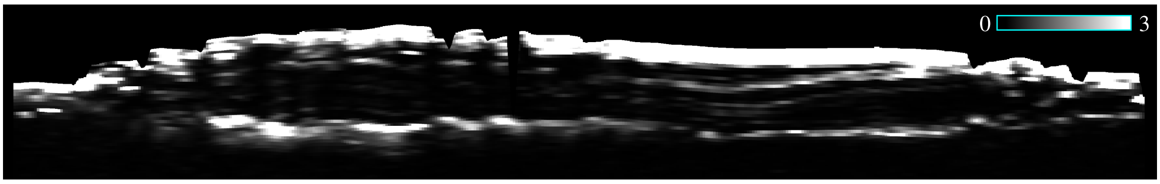

(b)

(c)

Figure 2.7: (a) Detected first returns on SHARAD radargram 1319502 (see Fig. 2.3). (b) Map of KL_{SN} obtained on the same radargram. Values of $\mathrm{KL}_{SN} > 3$ have been saturated to 3 for visualization purposes. (c) Binary map obtained from (b) by thresholding KL_{SN} at $thr_{\mathrm{KL}} = 0.13$.

The results of the proposed algorithm can be a starting point for a subsequent more detailed analysis of the detected targets, which can be achieved by estimating the statistical parameters of the local distributions, according to a given fitting model, e.g., the K distribution.

From a more general point of view, the performance obtained by the proposed technique allows one to assess with very high reliability whether a radargram contains or does not contain subsurface features. Thus, the technique can be effectively exploited to discriminate from the huge set of acquisitions the radargrams with significant subsurface features (which should be object of further analysis) from those that do not have subsurface features.

A possible extension of the proposed technique is to derive maps of the subsurface features by calculating the KL divergence between a theoretical distribution fitted to the local histogram (e.g., the K distribution) and the theoretical noise distribution. The use of the fitted distribution in place of the sample histogram can be seen as an implicit filtering of the signal aimed at discarding outliers.

It is worth noting that the presented approach cannot detect the difference between real subsurface features and clutter returns coming from the surface topography. The detection of clutter returns from single radargrams cannot be done automatically without the use of topographic data or clutter simulations. However, the proposed method can be simply integrated in a processing chain including a clutter detection step which masks the clutter areas in the radargram according to available clutter simulations. In Chapter

Table 2.5: Accuracy provided by the proposed technique for the generation of subsurface feature maps.

Radargram number	Feature samples	Missed alarms	% missed alarms	Non-feature samples	False alarms	% false alarms	Total error	% total error
0371502	492	28	5.69	2,508	240	9.57	268	8.93
0385902	515	50	9.71	2,485	189	7.61	239	7.97
0681402	830	44	5.30	2,170	305	14.06	349	11.63
0794703	718	8	1.11	2,282	362	15.86	370	12.33
1292401	491	9	1.83	2,509	277	11.04	286	9.53
1312901	625	21	3.36	2,375	304	12.80	325	10.83
1319502	657	34	5.18	2,343	318	13.57	352	11.73

4 we address this problem by presenting a technique for the automatic detection of clutter returns through simulation matching.

2.6 Proposed Technique for the Automatic Detection of Basal Returns

In this section we propose an algorithm aimed at detecting the deepest scattering area of a radargram. We applied such a technique to the detection of the basal returns coming from the base of the NPLD in SHARAD radargrams. However, after proper tuning, it can be adapted to other operational conditions (e.g., to the detection of the bedrock returns in data acquired by airborne sounders on Earth's polar regions). As mentioned in Sec. 2.4, basal returns in the NPLD include the scattering from the so-called basal unit. The basal unit is often described as sandy with varying amounts of volatiles [72]. Different hypotheses about its origin have been proposed in the literature [82]. SHARAD is able to penetrate the basal unit only to a certain extent. As shown in Sec. 2.4, the returns coming from the basal unit in SHARAD radargrams are mostly diffuse. The mean amplitude of the signals varies spatially depending on the local geology of both the basal unit and the overlying ice stratigraphy. However, the results obtained in the following demonstrate that the statistical behavior of the signals is in average stationary at least in single SHARAD acquisitions.

2.6.1 Proposed Technique

A block scheme of the proposed technique is shown in Fig. 2.8. The technique is based on the statistical analysis carried out in Sec. 2.4. It composes the basal scattering area using a region-growing approach. The obtained regions are kept or discarded according to the statistical distribution of their samples, which has to be similar to the expected distribution of the basal returns. The latter is estimated automatically by the algorithm. The technique is made up of two main phases: i) definition of an initial map of the basal scattering area, and ii) iterative refinement of the initial map. The two phases are described in detail in the following along with example images showing the main outputs (see Fig. 2.9). As test case we use the radargram shown in Fig. 2.3.

Definition of an initial map of the basal scattering area

The algorithm selects seed regions that have a high probability to belong to the basal scattering area. Then, it uses a region-growing approach which exploits a KL_{SN} map (calculated using the concepts introduced in Sec. 2.5) in order to produce a first initial map of the basal returns. In the following we describe in detail each step of this phase of the algorithm.

- *First return detection and calculation of KL_{SN}*: the radargrams are cut on the area of interest and the procedure described in Sec. 2.5 is applied in order to detect the surface line, estimate the noise statistics, and calculate the KL distance between the local signal histogram and the estimated noise statistical distribution. The calculated image of KL_{SN} is used as basis for the next steps.

- *KL_{SN} thresholding*: the goal of this step is to extract the regions which have a statistical distribution significantly different from that for the noise distribution. Such regions will be used by the algorithm to select the seeds of the basal scattering area in the next step. Therefore, the map of KL_{SN} is thresholded using a threshold thr_1 in order to produce a binary image KL_1, defined as:

$$\mathrm{KL}_1(i,j) = \begin{cases} 1 & \text{if } \mathrm{KL}_{SN}(i,j) \geq thr_1 \\ 0 & \text{otherwise.} \end{cases} \tag{2.15}$$

  The value chosen for thr_1 should be high enough to identify only few small regions of the basal scattering area, besides strong scattering areas belonging mostly to the *strong layers* and *weak layers* classes. In our experiments a value equal to 1.2 fulfilled this condition. The image of KL_1 for the test radargram is shown in Fig. 2.9a.

- *BR seed selection*: the binary image KL_1 contains a set $R_{1,0}$ of disjoint regions. Only those which are likely to be related to the basal returns are kept. The selection is performed on the basis of geometrical criteria, which take into account the usual position of the basal returns in the radargrams, i.e., i) the regions should correspond to the maximum ranges (depths); ii) the regions must not belong to the neighborhood of the surface. Condition i) is verified by the subset of regions $R'_{1,0}$ defined as:

$$R'_{1,0} = \left\{q : q \in R_{1,0} \ \wedge \ \exists i : (i,j) \in q \ \wedge \ j = \max\left\{\tilde{j} : \mathrm{KL}_1(i,\tilde{j}) = 1\right\}\right\}. \tag{2.16}$$

  The subset $R''_{1,0}$ of regions of $R_{1,0}$ which fulfill condition ii) is defined as:

$$R''_{1,0} = \left\{q : q \in R_{1,0} \wedge q \cap R_s = \emptyset\right\}, \tag{2.17}$$

  where R_s is the subsurface neighborhood region of the first returns considering a distance w_{ss} from the first returns. Formally, it is given by:

$$R_s = \left\{(i,j) : j_0(i) < j < j_0(i) + w_{ss}\right\}. \tag{2.18}$$

The selection of the value of w_{ss} should take into account the expected thickness of the area of the NPLD that is investigated. The final set of selected regions R_1 is composed by the regions of $R'''_{1,0} = R'_{1,0} \cap R''_{1,0}$ which fulfill the condition:

$$R_1 = \left\{ q : q \in R'''_{1,0} \ \wedge \ \bar{j}_{R'''_{1,0}} - w_{\text{up}} < \bar{j}_q < \bar{j}_{R'''_{1,0}} + w_{\text{down}} \right\}, \tag{2.19}$$

where $\bar{j}_{R'''_{1,0}}$ is the weighted mean range position of the regions contained in $R'''_{1,0}$ (using the areas of the regions as weights), $\bar{j}_q$ is the mean range position of the region q, and w_{up} and w_{down} are tolerance thicknesses used to define the width of the range of the expected basal position. w_{up} is referred to the thickness toward the surface, while w_{down} represents the thickness towards the bottom of the subsurface. On the one hand, the choice of w_{down} is in general not critical as usually no returns are observed after the basal scattering area. On the other hand, similarly to the discussion about w_{ss}, the value of w_{up} should be chosen according to the expected thickness of the investigated NPLD region. The output of this step for the test radargram is shown in Fig. 2.9b.

- *Region growing*: the regions selected in the previous step are used as seeds for a level-set algorithm. Such an algorithm stretches their contour to fit the basal scattering area using the KL_{SN} image. The algorithm describes the contour as the zero-level set of the function given by the following differential equation:

$$\frac{d}{dt}\iota = \left[-\beta_1 P(i,j) + \beta_2 \vartheta\right] |\nabla \iota|, \tag{2.20}$$

where $\beta_1 P(i,j)$ drives the expansion of the contour, and the term $\beta_2\vartheta$ affects its curvature (and thus the "smoothness" of the detection). ϑ is calculated as the mean curvature of the contour, and β_1 and β_2 are scalar values which define the weight of each term of the equation. In the proposed approach, the term $P(i,j)$ is calculated as

$$P(i,j) = \begin{cases} \text{KL}_{SN}(i,j) - thr_L & \text{if } \text{KL}_{SN}(i,j) < \frac{thr_U - thr_L}{2} + thr_L \\ thr_U - \text{KL}_{SN}(i,j) & \text{otherwise,} \end{cases} \tag{2.21}$$

where thr_U and thr_L define the upper and the lower thresholds of KL_{SN}, respectively, which limit the expansion of the contour. Using the definition in (2.21) the propagation term $P(i,j)$ is positive (expansion) only when $\text{KL}_{SN}(i,j) \in (thr_U, thr_L)$. More details on level sets can be found in [83]. The choice of the values of thr_U and thr_L depends on the limit values of KL_{SN} associated with the basal returns. The most important parameter is thr_L, as it defines the minimum statistical difference to the background noise which makes the contour expand.

At the end of the region growing step, the algorithm has produced an initial map of the basal scattering area composed by a set of regions $R_{1,\text{grow}}$.

Iterative refinement of the initial map

An $(m_{\max} - 1)$-step iterative procedure is started, which is aimed at detecting the weak scattering areas of the basal returns and refining the previous detection. The steps of the iterative loop performed for each iteration m ($m = 2, \ldots, m_{\max}$) are as follows.

- *Estimation of BR statistics*: in this step the algorithm uses the amplitudes of the samples belonging to the regions of $R_{m-1,\text{grow}}$ to estimate the parameters of a K distribution. The estimation is performed using an ML approach (see Sec. 2.4). In this way, the algorithm estimates the statistical distribution of the basal returns, which will be exploited in the next steps.

- *KL_{SN} thresholding*: a binary map is produced by considering only the samples of KL_{SN} which belong to the range $[thr_m, thr_{m-1})$. For each iteration m, the binary image KL_m is thus created according to:

$$\text{KL}_m(i,j) = \begin{cases} 1 & \text{if } thr_m \leq \text{KL}_{SN}(i,j) < thr_{m-1} \\ 0 & \text{otherwise.} \end{cases} \tag{2.22}$$

  The binary map contains a set $R_{m,0}$ of regions. The value of each thr_m and the number of iterations $m_{\max}$ should ensure that for each iteration the binary map contains regions with significant areas. Moreover, the value of $thr_{m_{\max}}$ must be greater than thr_L to assure that the level-set algorithm can expand the region contours also in the last iteration ($m = m_{\max}$).

- *Selection of BR seeds and region growing*: similarly to the previous steps, the binary maps are used to select seed regions, which are likely to belong to the basal scattering area, and the level-set algorithm is run starting from such seeds. The subset of seed regions R_m is selected by means of geometrical constraints, i.e., the regions must belong to a range neighborhood of the estimated basal mean range. This is formally translated in a condition similar to (2.19):

$$R_m = \left\{q : q \in R_{m,0} \ \wedge \ \bar{j}_{R_{m-1,\text{grow}}} - w_{\text{up}} < \bar{j}_q < \bar{j}_{R_{m-1,\text{grow}}} + w_{\text{down}}\right\}, \tag{2.23}$$

  where $\bar{j}_{R_{m-1,\text{grow}}}$ is the weighted mean range position of the regions contained in $R_{m-1,\text{grow}}$ (using their areas as weights), $\bar{j}_q$ is the mean range position of the region q, and w_{up} and w_{down} are the same tolerance thicknesses as those used in (2.19).

- *Region selection*: a subset of the regions obtained in the previous step is selected. The selection is made mainly on a statistical basis. For each region the histogram is computed and if its KL distance to the estimated basal return distribution is smaller than an user-defined threshold thr_G the region is kept, otherwise it is discarded. This step is performed to discard the regions which grew on areas which are not related to the basal scattering area. Therefore, the value of thr_G should be small (e.g., on the order of 0.1). Once the selection is performed, the provisional set of the basal return regions $R_{m-1,\text{grow}}$ is merged with the new regions obtaining the new set $R_{m,\text{grow}}$. Such a set will be the input for the next iteration.

The result of the iterative phase is thus a binary map composed by the merging of the whole set of regions produced during the different iterations.

Finally, small isolated regions are deleted and the final basal return map is created. The resulting basal return area detected on the test radargram is shown in Fig. 2.9c.

2.6.2 Results and Discussion

Fig. 2.10 reports the detected basal return areas of three radargrams. A qualitative analysis of the results points out that the proposed technique is able to detect with high accuracy the scattering areas related to the basal returns both in azimuth and in range direction. The worst performance is related to the detection of the NPLD base interface when layering is visible at close depths. As the subsurface layering is very close to the basal scattering area, the statistics of the two target types are very similar; thus, the algorithm may fail to discard the layered areas.

In order to measure quantitatively the performance of the algorithm, we followed an approach similar to that used in Sec. 2.5. For each of the 7 radargrams analyzed in this chapter, we considered 3000 reference samples randomly taken in the areas of the radargrams for which it was possible to assess clearly the presence (or the absence) of basal returns. The results regarding the detection performance are reported in Tab. 2.6 in terms of number of missed and false alarms calculated using the selected samples. Taking into account that the proposed algorithm is automatic and unsupervised, the overall accuracy can be considered high.

An additional note should be made about the choice of the parameters of the proposed algorithm. As already discussed in the previous subsection, the algorithm is stable with respect to several parameters as their choice is not critical and the same values can be used for a large set of radargrams. The most sensitive parameters are thr_1 and thr_L. Indeed, thr_1 affects the definition of the initial seeds of the algorithm, while thr_L defines the minimum statistical difference that the basal returns must have with respect to the background noise. Therefore, such parameters should be chosen taking into account the average SNR of the analyzed radargram. This depends on the noise level, on the state of the subsurface materials (which affects the signal propagation), and on the spacecraft attitude (e.g., in certain configurations called *rolled acquisitions* the SHARAD antenna gain is greater than that for standard spacecraft attitude). From the practical viewpoint, this means that if the algorithm is run with the same parameters on a set of radargrams with similar SNR characteristics, its performances are almost constant on the whole set of radargrams. In addition, it is worth noting that almost all the parameters involved in the algorithm have a clear physical meaning that represents a guide for a proper tuning. For all the test radargrams considered in this chapter we used the following algorithm parameters: $w_{ss} = 20$, $m_{\max} = 3$, $thr_1 = 1.2$, $thr_2 = 0.7$, $thr_3 = 0.2$, $thr_U = 100$, $thr_L = 0.13$, $\beta_1 = 50$, $\beta_2 = 10$, $w_{\text{up}} = 50$, $w_{\text{down}} = 100$, $thr_G = 0.10$.

The output of the proposed algorithm can be used in scientific analysis for many purposes. A first application is the estimation of the NPLD thickness (assuming a reasonable dielectric constant for the icy materials of the NPLD) using a large set of acquisitions. Given the resolution of SHARAD radargrams, it is possible also to extrapolate from the detected basal topography local buried basins or impact craters. Another possible application is the measurement of the mean power scattered by the basal unit at a certain 3D position, which is useful to study local geology and radar bright (or dark) areas. Finally, the proposed technique can also be used to study seasonal variations of the signal propagation loss within the NPLD. This can be achieved by analyzing the amount of power scattered by the basal area during different seasons on the same areas, and relating such

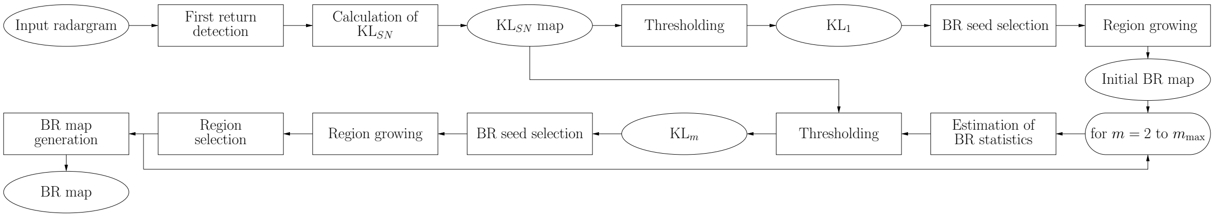

Figure 2.8: Block scheme of the proposed technique for the automatic detection of the NPLD basal returns.

Table 2.6: Accuracy provided by the proposed technique for the detection of the NPLD basal returns.

Radargram number	**Feature samples**	**Missed alarms**	**% missed alarms**	**Non-feature samples**	**False alarms**	**% false alarms**	**Total error**	**% total error**
0371502	250	30	12.00	2,750	37	1.35	67	2.23
0385902	281	51	18.15	2,719	30	1.10	81	2.70
0681402	340	61	17.94	2,660	59	2.22	120	4.00
0794703	282	19	6.74	2,718	71	2.61	90	3.00
1292401	124	9	7.26	2,876	90	3.13	99	3.30
1312901	240	5	2.08	2,760	93	3.37	98	3.27
1319502	271	25	9.23	2,729	80	2.93	105	3.50

measurements to the absorption experienced by the signal within the NPLD.

2.7 Conclusions

In this chapter we presented both a study on the statistical properties of the sounder signals and two novel automatic techniques for the extraction of subsurface features from radargrams. In the study of the properties of sounder signals we analyzed different statistical models from a theoretical point of view and then empirically tested them on different real SHARAD data acquired on the NPLD of Mars. The obtained results show that the statistical distributions of the amplitude signals related to different types of targets can be modeled precisely using the K distribution, while, as expected, the background noise follows a Rayleigh distribution. Exploiting the results of the aforementioned study, we have then proposed two novel techniques for the automatic analysis of radargrams aimed at: i) producing maps of the subsurface areas showing relevant features; and ii) identifying and mapping the deepest scattering areas visible in the radargrams. The former is based on the comparison of the distributions of local subsurface parcels with that of noise adaptively estimated on each radargram. The latter exploits a specifically defined region-growing method implemented in an iterative technique based on the level-set algorithm. The results obtained by both the developed techniques are accurate and thus promising for operational applications.

(a)

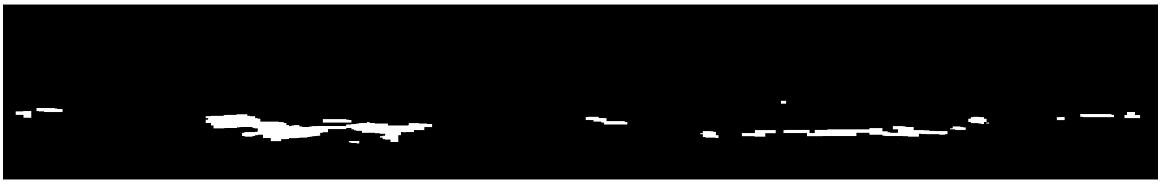

(b)

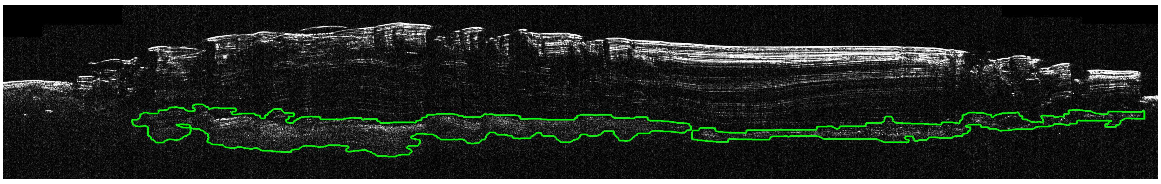

(c)

Figure 2.9: Example of application of the proposed algorithm for the detection of the basal returns to SHARAD radargram 1319502 (see Fig. 2.3). (a) Areas remaining after the first thresholding ($thr_1 = 1.2$). (b) Selected starting seed regions. (c) Final detection.

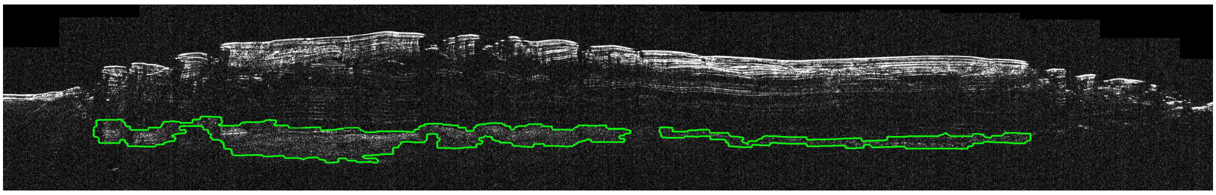

(a)

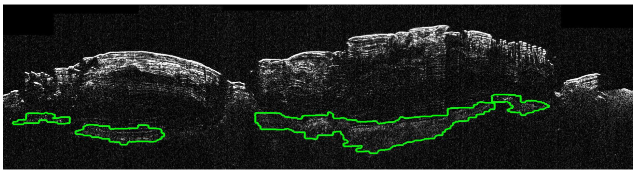

(b)

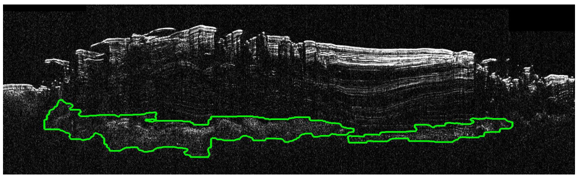

(c)

Figure 2.10: Detected basal scattering area on SHARAD radargrams (a) 0371502, (b) 1292401, and (c) 1312901.

Chapter 3

Extraction and Analysis of Ice Layering

In this chapter[1] *we propose a novel method for the automatic detection of subsurface linear features from RS data acquired in icy regions showing extended layering. The proposed method allows the estimation of the position of the linear features with sub-pixel accuracy. Moreover, each detected linear interface is treated as a single object which is completely described by the position of its points, the estimated local width and the contrast. This allows the direct measurement of geometrical and radiometric parameters (e.g., slope angle, intensity) without the need of further post-processing steps. The chapter also proposes some measurements for deriving from the output of the proposed technique important variables that can characterize quantitatively the properties of the detected linear features (e.g., mean depth, mean intensity) and their distribution (e.g., number and density of layers). The effectiveness of the proposed method is confirmed by the results obtained on several radargrams acquired by the SHARAD instrument on the North Pole of Mars.*

3.1 Introduction on Automatic Analysis of Ice Layering

One of the most important applications of RSs is the analysis of the subsurface in icy regions (e.g., Greenland, Antarctica, poles of Mars). Indeed, ice is one of the most transparent materials at the aforementioned frequencies, thus making the penetration of the signals into the subsurface feasible even for several kilometers [41]. A salient characteristics of icy regions is the presence of extended layering due to the deposition and subsequent solidification of snow in different periods. The study of the structure of the ice stratigraphy (e.g., position and density of the ice layers) is very important for many reasons. Primarily, the analysis of the ice stratigraphy allows the estimation of ice age and accumulation rate, and is necessary for constraining ice flow models [32, 33]. All the aforementioned factors are key parameters for the study of the past history and for the prediction of the evolution of icy environments. Focusing on the Earth, nowadays this

[1]Part of this chapter appears in:
[84] A. Ferro and L. Bruzzone, "Automatic detection and characterization of subsurface linear features in radar sounder data acquired on icy areas," in *Synthetic Aperture Radar (EUSAR), 2012 9th European Conference on*, 2012.

is of primary importance in the framework of the assessment of the impact of climate changes on the Earth's system.

On this topic, related works presenting automatic methods are mainly devoted to the analysis of data acquired by surface-mounted GPRs showing linear and hyperbolic returns [55, 58, 59, 85, 86]. Linear features are often detected by means of the Hough transform or modeled as the limit of hyperbolas with no slope. These approaches are suited for GPR radargrams containing clear straight lines, but they are not appropriate for RS data in which linear features are not straight and change slope locally. In fact, orbiting RS radargrams cover a much longer track than GPR acquisitions usually with a much worse along-track sampling, thereby showing the large scale shape of subsurface linear interfaces (e.g., due to topography). An attempt to the automatic detection of shallow linear features in SHARAD radargrams was made by Freeman *et al.* [87]. In their work the authors used a combination of image filterings followed by a threshold operation. The goal of the filterings is to reduce background noise and highlight almost-horizontal linear features. Prior to image filterings, a coordinate transformation is applied in order to flatten the surface topography, and thus reduce the induced layer slopes. The output of the processing is a binary image where the pixels belonging to linear interfaces are highlighted.

In this chapter we propose a novel technique for the automatic detection of subsurface linear features in layered media which allows the estimation of the position of the linear features with sub-pixel accuracy. Moreover, each detected linear interface is treated as a single object which is completely described by the position of its points, and its estimated local width and contrast, thus allowing the direct measurement of geometrical or radiometric parameters (e.g., slope angle, intensity) without the need of further post-processing steps (as necessary for simpler techniques based on image filtering and thresholding). The chapter also proposes some measurements for deriving from the output of the proposed technique variables that characterize quantitatively the properties of the detected linear features (mean depth, mean intensity, relative mean contrast) and their distribution (number of features, density of layers). Despite the proposed technique is general, in this chapter we evaluate its effectiveness by considering SHARAD radargrams of the NPLD of Mars. The results show the effectiveness of the proposed method.

The remainder of the chapter is organized as follows. Sec. 3.2 defines the notation regarding linear features used throughout the chapter. Sec. 3.3 presents the proposed method for the automatic detection of linear features in RS radargrams. Sec. 3.4 shows the experimental results obtained on real SHARAD radargrams of the NPLD of Mars. Finally, Sec. 3.5 draws the conclusions of the chapter.

3.2 Definition of Linear Feature

A generic linear feature γ_p in a radargram acquired on a icy region will be described as a set of four-element tuples as follows:

$$\gamma_p = \left\{(i,j,w,c) : (i,j) \in \Phi_p \ \wedge \ w = \Omega_{\gamma_p}(i,j) \ \wedge \ c = C_{\gamma_p}(i,j)\right\}, \tag{3.1}$$

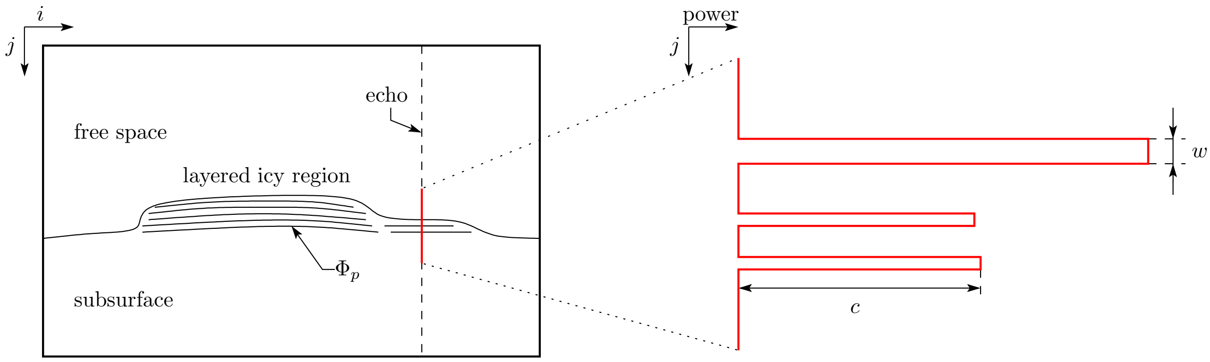

Figure 3.1: Definitions of linear feature parameters on a simplified qualitative radargram.

where Φ_p is the representation of γ_p in the image reference system, and Ω_{γ_p} and C_{γ_p} are operators which calculate the local width and contrast of γ_p at a given point (i, j), respectively. The line contrast is defined as the difference between the line intensity and its surrounding, assuming the simplifying assumption that each line section has a bar shape. Note that Φ_p includes only the axis points of a linear feature, and does not provide any information on its thickness. We define as Φ_p^w the area of the radargram that is described by the tube having as axis Φ_p. The local width of the tube is defined locally for each point $(i, j) \in \Phi_p$ as $w = \Omega_{\gamma_p}(i, j)$. Fig. 3.1 shows graphically the definitions given in this paragraph.

It is worth noting that the definition of γ_p allows one to calculate for each linear feature a set of derived measures which can be computed also locally by selecting a subset of the elements composing γ_p (e.g., line total length, mean width, local mean contrast). For the analysis of actual subsurface reflections, such measures can be then straightforwardly translated in physical quantities (e.g., geographical length of a linear interface, mean intensity of the reflection). In order to give the most general definition, in this chapter we will use as unit for linear feature width and length the number of pixels of the radargrams. In fact, radargrams of different sensors have different resolutions, both in range and along-track. Moreover, even radargrams from the same instrument can be focused at different resolutions. Therefore, the relation between the physical length and width of a reflection and their representations in the image domain are not unique. Using physical quantities for the definition of the parameters of the proposed technique would be thus not general, but linked to a certain instrument and focusing approach.

3.3 Automatic Detection and Characterization of Linear Features in Radar Sounder Data

In this section we describe the proposed automatic technique for the detection and characterization of linear features in RS data. The proposed method is a four-step procedure made up of: i) radargram denoising and enhancement, ii) line detection, iii) removal of first returns, and iv) extraction of measures of interest. Fig. 3.2 shows a block scheme of the proposed method. In the following we describe in detail each step of the algorithm and propose examples of derived measurements that can be calculated after the detection.

3.3.1 Radargram Denoising and Enhancement

The goal of this step is to reduce the background noise of the radargrams and enhance the signature of linear features. Noise reduction and line enhancement are performed jointly by exploiting the intrinsic correlation that linear features show on adjacent frames. As an example, a linear feature covering several adjacent frames is expected to appear at adjacent j positions. This holds independently from its intensity. A linear feature characterized by low intensity can thus be masked by noise peaks in some echoes. However, as noise is uncorrelated among the different frames, the linear feature can be preserved whereas noise is reduced. To this end, we propose for the joint radargram denoising and linear feature enhancement the use a non-local filtering technique. Different methods for non-local filtering of optical and radar images have been recently proposed [88–90]. In this thesis we propose to use the BM3D filter developed by Dabov *et al.* [88]. Fig. 3.3 summarizes the operations performed by the filter. The first step is aimed at producing a so-called basic estimate of the true image (i.e., the image with no noise). This is done by operating in a non-local way. The filter searches the radargram space for similar parcels by means of a block-matching procedure based on a square sliding window. The retrieved blocks are then stacked together to form a 3D group, which is filtered by means of hard-thresholding operated on the coefficients of a 3D transform applied to the group (for instance based on Discrete Cosine Transform or Walsh-Hadamard). The inverse 3D transform is then applied to the thresholded coefficients. Finally, the output block estimates are aggregated together using weights calculated from the thresholded coefficients. Thus, at the end of the first step a basic estimate of the denoised image is produced. Such image is used as input to the second step. In the second step, the filter performs a procedure which is similar to the one of the first step. The main difference is the use of a Wiener filter which denoises the original input image using as reference the basic estimate derived in the first step. For more details on the processing performed by the filter the reader is referred to [88].

The BM3D filter has been originally developed for optical images affected by AWGN noise, and for this type of images it represents the state of the art. The main parameter of the BM3D filter is the estimated variance of the image background AWGN noise. Other parameters tune the size of the blocks and the maximum number of blocks per group. In the case of RS data the AWGN assumption is not valid. As shown in Chapter 2, noise in amplitude radargrams appears as an additive and Rayleigh-distributed contribution (when no multilooking is performed). Moreover, in correspondence of any reflection, the speckle effect appears because of the coherent nature of a radar acquisition (see Chapter 1). The BM3D filter can be properly defined also for non-AWGN noise [88, 91]. It has been also used with good results for despeckling of log-transformed SAR images [92]. As it will be described later, in our experiments we applied the original BM3D filter for AWGN[2] to stretched dB-power radargrams. In fact, the filter performance as a step prior to line detection on this type of data is very good even using its original implementation. It is worth noting that modified versions of the BM3D filter specifically devoted to the

[2]The implementation of the BM3D filter used in this thesis is that available at `http://www.cs.tut.fi/~foi/GCF-BM3D/`.

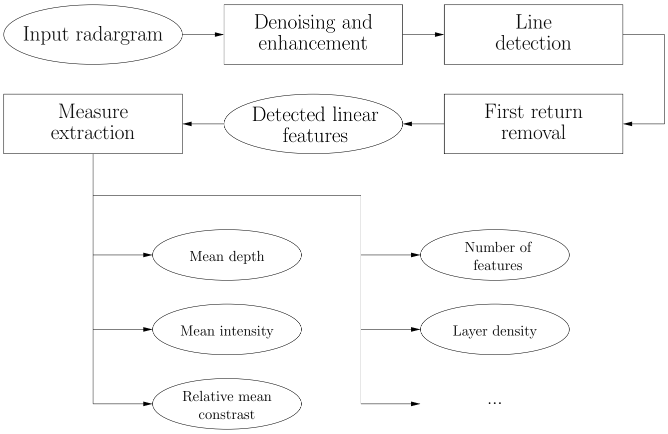

Figure 3.2: Block scheme of the proposed method for the detection and characterization of linear features in RS data.

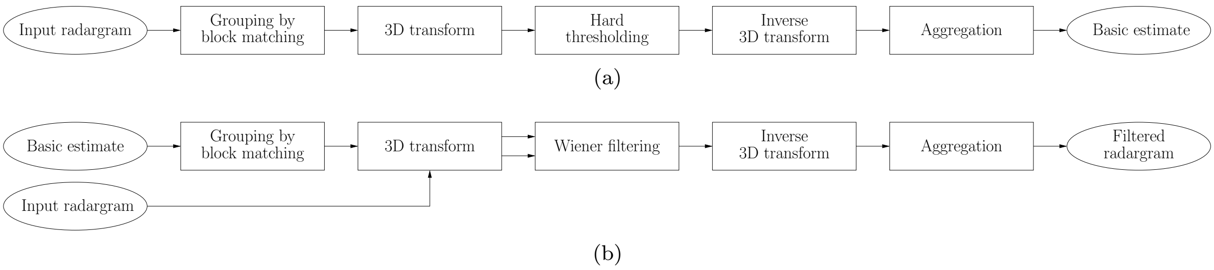

Figure 3.3: Block scheme of the BM3D filter: (a) generation of the basic estimate, (b) generation of the filtered image through Wiener filtering (scheme adapted from [88]).

joint image denoising and edge sharpening have been proposed [88]. In our experiments such methods exhibited good performance. However, the edge sharpening resulted in a subsequent higher number of false line detections due to filtering artifacts. Moreover, edge sharpening changes the line intensity, making thus more difficult to select the parameters of the line detector according to values directly measurable on the original radargram. For these reasons, in this thesis we use the BM3D filter without edge sharpening.

3.3.2 Line Detection

In order to extract linear features from the denoised radargrams we propose to use the Steger filter [93]. The Steger filter has been originally developed for the detection of linear features in optical images and exhibited good performance also on images affected by significant noise [94]. Moreover, it has been successfully applied as a tool for primitive segmentation aimed at building detection in VHR SAR images [24, 95].

The Steger filter assumes for linear features a bar-shape profile (see Fig. 3.1) and the detection of lines is performed by analyzing the second derivative of the convolution of such profile with a Gaussian smoothing kernel. In the 1-dimensional case, the function

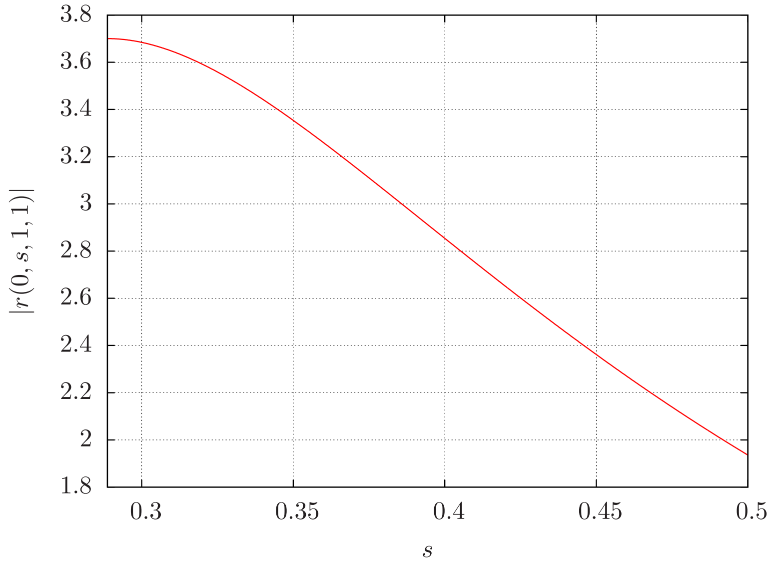

Figure 3.4: Example of response of the Steger filter. Value of $|r(0,s,w,c)|$ calculated using $w = 1$ and $c = 1$, and by varying s in the range $\left[\frac{w}{2\sqrt{3}}, \frac{w}{2}\right]$.

evaluated by the filter is:

$$r(j,s,w,c) = a_s''(j) * \Phi(j) = c\left[a_s'\left(j+\frac{w}{2}\right) - a_s'\left(j-\frac{w}{2}\right)\right], \tag{3.2}$$

where

$$a_s(j) = \frac{1}{\sqrt{2\pi}s}e^{-\frac{j^2}{2s^2}} \tag{3.3}$$

is the Gaussian convolution kernel. $a_s'(j)$ and $a_s''(j)$ are its first and second derivatives, respectively, and $\Phi(j)$ is the line representation in the 1-dimensional space. The line response to the filter is calculated as $|r(0,s,w,c)|$, given by:

$$|r(0,s,w,c)| = \frac{wc}{\sqrt{2\pi}s^3}e^{-\frac{w^2}{8s^2}}. \tag{3.4}$$

According to [93], the value of s should belong to the range $\left[\frac{w}{2\sqrt{3}}, \frac{w}{2}\right]$. However, the maximum line response is obtained using the minimum value allowed for s, which is $s = \frac{w}{2\sqrt{3}}$. Therefore, in our experiments we will use this value for s. As an example, Fig. 3.4 shows the value of $|r(0,s,w,c)|$ for the case $w = 1$ and $c = 1$ with s spanning its domain range.

The mathematical description of the filter allows the unbiased calculation of the line position with sub-pixel accuracy also in the case in which the line has background with asymmetric intensities on its sides. This is important as it allows a precise estimation of the position of the linear feature independently on the fixed pixel spacing. Moreover, width and contrast can be estimated locally for each detected linear feature γ_p by properly defined Ω_{γ_p} and C_{γ_p} operators [93].

For a given w (and thus s), the main parameter of the Steger filter which has to be set is r_{up}. r_{up} is the minimum response to the filter that triggers the detection of a line point. The algorithm also includes the possibility to link the detected line points into lines. This is performed by searching the neighborhood of line points and adding new points which have a second derivative greater than a third parameter r_{low}. The choice of r_{up} can be made by calculating the response of an ideal bar-shaped line with given width w and contrast c_{up} using (3.4) and choosing $s = \frac{w}{2\sqrt{3}}$. This results in:

$$r_{\text{up}} = 24\sqrt{\frac{3}{2\pi}}\frac{e^{-\frac{3}{2}}}{w^2}c_{\text{up}}. \tag{3.5}$$

Similarly, the value of r_{low} can be calculated using in (3.5) a value c_{low} which represents the minimum contrast allowed for the linking of the detected line points.

3.3.3 First Return Removal

The output of the previous step is a set Λ of detected linear features γ_p. As the line detector has been applied to the whole radargram, Λ contains linear features which are caused by both surface and subsurface reflections. Therefore, in this step the algorithm removes the linear features corresponding to the first returns and preserves only the lines which are likely to belong to the subsurface. The detection of the first returns is carried out by means of the algorithm proposed in Chapter 2. It is worth noting that in this step only the surface reflections appearing as first returns in the radargrams are removed. In order to completely remove surface clutter reflections that appear at the same range of the subsurface it would be necessary to match the line detection with clutter simulations and develop a finer line selection. To this end, the technique presented in Chapter 4 of this thesis could be applied. Then, starting from registered simulations proper criteria should be defined for the cancellation of the detected linear features which are likely to be due to surface clutter. Such fine selection based on clutter simulations is a procedure that deviates from the scope of this chapter. However, the development of such post-processing step will be subject of future work.

3.3.4 Extraction of Measures of Interest

As described in the previous subsections, the output of the proposed method is a set of detected linear features described as defined in (3.1). This description already provides useful information, such as the linear feature position, thickness and contrast. As an example, the contrast can be analyzed to extract from the detected features those which have a significant intensity difference with their background. Further parameters associated with the detected linear features can be also estimated. Such parameters can be computed locally for each feature, or can be related to sets of features covering a certain geographical area or belonging to the same depth range. For instance, measurements that can be estimated independently for each detected linear feature are the mean intensity and the mean depth. This type of parameters can be associated to a vector for each detected linear feature, i.e., by extending the definition of (3.1) with new values calculated by proper operators. In the following we propose a set of measurements which can be used to extrapolate further information from the detected linear features.

Mean depth

The mean depth of a linear feature is defined as:

$$\bar{j}_{ss}(\gamma_p) = \frac{1}{|\Phi_p|} \sum_{(i,j)\in\Phi_p} [j - j_0(i)]\,, \tag{3.6}$$

where $j_0(i)$ is the position of the first return in the frame i, as detected by the first return detection described in the previous subsection, and the notation $|.|$ indicates the cardinality of a set.

Mean intensity

We define the mean intensity of a linear feature in the following way:

$$\mu(\gamma_p) = \frac{1}{\left|\Phi_p^w\right|} \sum_{(i,j)\in\Phi_p^w} \xi(i,j), \tag{3.7}$$

where Φ_p^w has been defined in Sec. 3.2, and $\xi(i,j)$ is the radargram intensity at the position (i,j).

Relative mean contrast

The relative mean contrast $\bar{c}_r$ of a linear feature γ_p is defined as the ratio between its mean intensity and the mean intensity of its surrounding. The latter can be extracted exploiting the feature contrast, which is estimated by the line detector. This results in:

$$\bar{c}_r(\gamma_p) = \frac{\mu(\gamma_p)}{\mu(\gamma_p) - \bar{c}(\gamma_p)}, \tag{3.8}$$

where

$$\bar{c}(\gamma_p) = \frac{1}{|\Phi_p|} \sum_{(i,j)\in\Phi_p} C_{\gamma_p}(i,j) \tag{3.9}$$

is the mean contrast of γ_p.

Number of detected features

This measure can be defined locally to a certain range of frames and samples. We define as number of detected features the value

$$n(\Delta I, \Delta J) = |\Lambda(\Delta I, \Delta J)|\,, \tag{3.10}$$

where

$$\Lambda(\Delta I, \Delta J) = \{\gamma_p : (i,j) \in \Phi_p \ \wedge\ \exists (i,j) : i \in \Delta I \wedge j \in \Delta J\}\,. \tag{3.11}$$

$\Delta I = [i_{\min}, i_{\max}]$ and $\Delta J = [j_{\min}, j_{\max}]$ define the range of frames and samples to be considered, respectively. The calculation of $n(\Delta I, \Delta J)$ can be performed by means of a sliding window approach on the whole radargram portion related to the subsurface. This gives a 2D map of the distribution of the linear features within the radargram. If the computation is performed frame-by-frame (i.e., $|\Delta I| = 1$) on the whole J range, the output is a 1D graph describing the number of detected subsurface linear features versus the along-track direction. This is useful for detecting the portions of the track containing the highest number of layers.

Layer density

The layer density is defined as:

$$\Theta(\Delta I, \Delta J) = \frac{n(\Delta I, \Delta J)}{|\Delta J|}. \tag{3.12}$$

Similarly to the case of $n(\Delta I, \Delta J)$, $\Theta(\Delta I, \Delta J)$ can be computed using a sliding window approach. This measure expresses the number of linear features per sample in the range direction. The definition takes into account the intrinsic correlation that linear features show between adjacent frames. Indeed, the size of the window in the along-track direction is not used in the denominator. The result is thus a 2D map of the density of the layers in the range direction. The size of the sliding window should be determined depending on the resolution of the data and on the size of the structures that have to be highlighted. In general, large windows produce density maps with low detail but that are useful to infer the general distribution of the features. On the contrary, small windows can highlight better local feature patches at the cost of more visible blocking artifacts.

It is worth noting that mean depth, number of features, and density are defined in the radargram image space. However, they can be related to geographic and time scales by applying the appropriate conversion factors.

3.4 Experimental Results

In this section we present the results obtained by the proposed technique on real RS data. First, we present the dataset used in the experiments. Second, we show the output of the BM3D filter on sample radargrams and frames in order to discuss its denoising capabilities. Third, we study qualitatively the influence of the parameters of the line detector on its detection performance. Then, we measure quantitatively the detection performance of the proposed method for a fixed set of parameters. Finally, we show examples of measures extracted automatically from the radargrams.

3.4.1 Dataset Description

In order to assess the performance of the proposed technique we used many different SHARAD radargrams taken on the NPLD of Mars. Since we obtained very similar results, in the following we focus the attention on two radargrams. It is worth noting that the presented method is general and can be applied to any radargram with a proper tuning

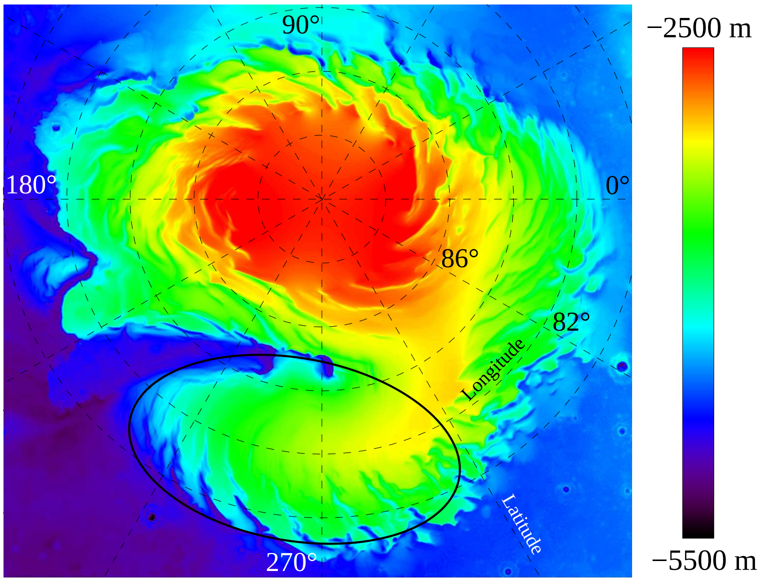

Figure 3.5: DEM of the North Pole of Mars derived from MOLA data. The Gemina Lingula region is highlighted with a black ellipse.

of parameters. The considered radargrams refer to the Gemina Lingula region of the NPLD of Mars, which is mostly flat [30] (see Fig. 3.5). Therefore, surface clutter is very limited and this allows us to focus on the detection of actual subsurface linear features. We will consider only the upper part of the radargrams (i.e., the first 11 μs after the first detected return for each frame), corresponding to a densely layered shallow subsurface. The radargrams have been focused using the FPB processor [96] hosted at the Southwest Research Institute of Boulder, CO, USA. The data have been converted to dB and thresholded in the range $[\mu_{N,\mathrm{dB}}-3, \mu_{N,\mathrm{dB}}+32]$ dB, where $\mu_{N,\mathrm{dB}}$ is the mean noise power measured on the radargram and expressed in dB. Finally, the radargrams have been stretched in the range [0,255]. The spatial resolution of the radargrams is approximately 450 m $\times$ 3 km (along $\times$ across track) with an along-track sampling of about 115 m. The range sampling is of 37.5 ns, corresponding to 5.63 m in free space and slightly more than 3 m in an icy subsurface ($\varepsilon_{\mathrm{ss}} = 3.15$). However, as described in Sec. 1.2.5, the range resolution of SHARAD is about 10 m in ice.

3.4.2 Radargram Denoising and Enhancement

The two test radargrams and the relative output of the BM3D filter are presented in Fig. 3.6 and Fig. 3.7. The vertical dimension has been exaggerated by a factor 1.3 for better visualization. The figures show the capability of the filter to flatten the noise background while preserving, and enhancing, the linear features present in the radargrams. These effects can be appreciated more in detail in Fig. 3.8. The figure shows one echo taken from the test radargram of Fig. 3.6 before and after the application of the BM3D filter. It is worth noting that the filter mostly preserves the actual intensity value of the linear features, thus making the choice of the parameters of the line detector directly related to the intensity of the features in the original radargram. In our experiments we fixed the

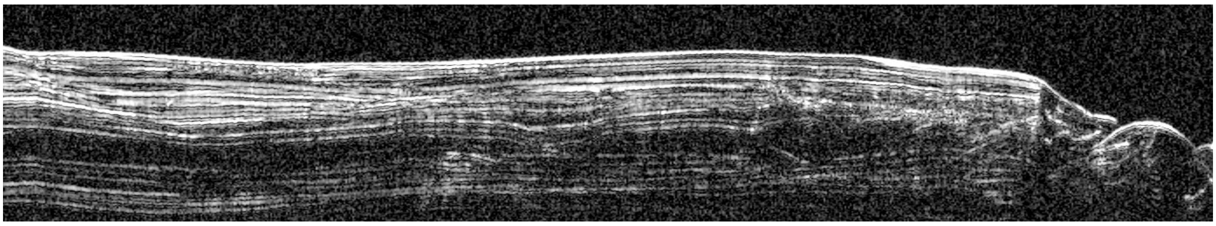

(a)

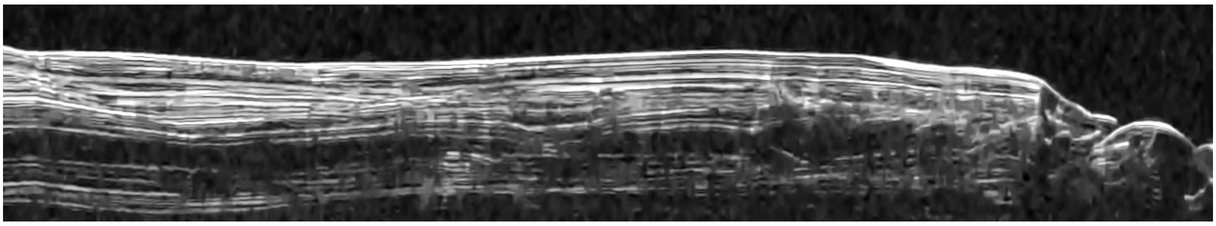

(b)

Figure 3.6: SHARAD radargram 0520501 (a) before and (b) after the application of the BM3D filter.

size of the blocks used by the BM3D filter to 32 × 32, and set the maximum number of blocks per group to 16. We obtained the best trade-off between denoising and feature enhancing by setting the AWGN standard deviation parameter of the filter equal to the background noise dynamic measured on the radargrams, which is on the order of 60 in the considered dataset.

3.4.3 Selection of the Parameters of the Line Detector

In order to select the best parameters to be used as input to the proposed technique and to understand the dependence of the results on the parameter values, we analyzed the results obtained by the method with different input parameters. In particular, we studied the dependence of the results on the choice of w and c_{up}. The value of c_{low} has been fixed to 2 for all the experiments. Lines shorter than 10 pixels have been discarded both in the reference and in the detected maps. In fact, the proposed technique is suited for the analysis of subsurface areas showing extended layering where linear interfaces usually appear for long distances. It is worth noting that our goal is to detect significant layers. Thus, small lines are discarded as they can be associated with other features of ice. Lines with a horizontal inclination greater than 45° have been also discarded. Such constraint comes from the fact that standard RS focusing processing makes it difficult to detect returns from surfaces with high slopes. Thus, inclined features have high probability to be false alarms.

Dependence on w

Fig. 3.9 and Fig. 3.10 show the output of the proposed technique using three different values of w (2, 4 and 6) on the test radargrams of Fig. 3.6 and Fig. 3.7. The value of $c_{\max}$ has been fixed to 3. On the one hand, as expected the results show that increasing w results in a lower sensitivity of the technique to thin linear features. On the other hand, in

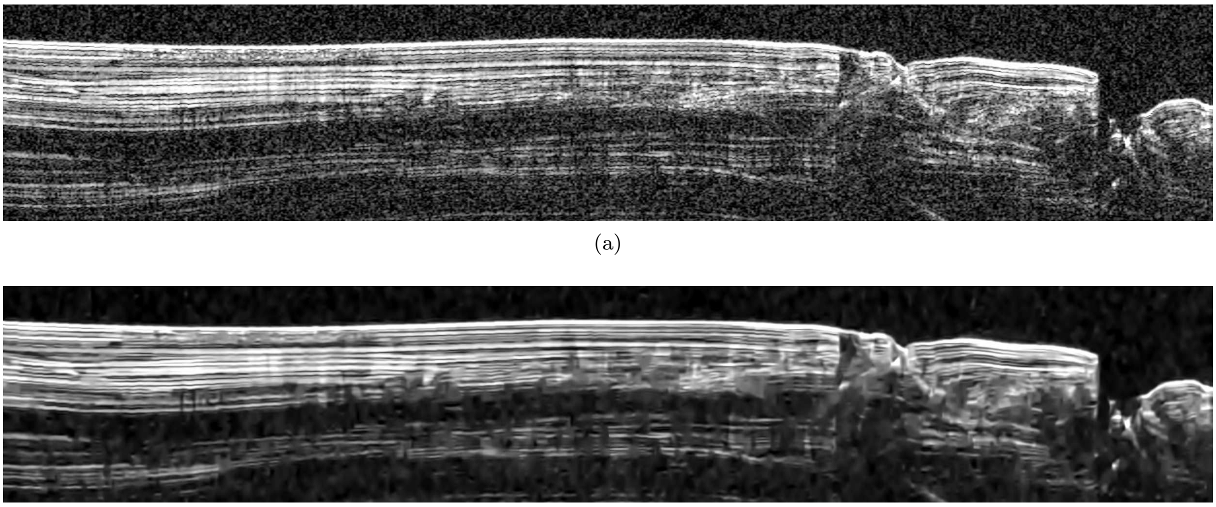

(a)

(b)

Figure 3.7: SHARAD radargram 0528401 (a) before and (b) after the application of the BM3D filter.

the radargrams linear features thicker than the selected value of w are still well detected. The number of false alarm is in overall low and the detection accuracy of the algorithm is high. A slightly greater number of false alarms is associated to higher values of w. This can be explained by analyzing (3.5). Indeed, for a given value of $c_{\max}$ the maximum line response $\rho_{\max}$ decreases by increasing w, thus increasing the probability of false alarms.

Dependence on $c_{\max}$

In this tests we fixed the values of w to 2. The value of $c_{\max}$ has been set to 3, 10 and 20. Fig. 3.11 and Fig. 3.12 show the related results on the test radargrams. As expected, by increasing the value of $c_{\max}$ the proposed technique detects only the most salient lines, whereas linear features with low contrast are not detected. For the aim of this thesis low contrast features are important. Therefore, low values of $c_{\max}$ will be considered in the following.

3.4.4 Quantitative Performance Analysis

The qualitative analysis of the dependence of the results obtained by the proposed technique on its parameters allowed us to define a range of values that are appropriate for the application of the technique to the test dataset. In particular, the values which gave the best results are $w = 2$ and $c_{\max} = 3$. This has been confirmed by applying the proposed technique to other radargrams. Fig. 3.13 and Fig. 3.14 show the results obtained on two additional tracks. Using those parameters, in this section we thus analyze quantitatively the performance of the proposed method on the two SHARAD radargrams used for the qualitative analysis. Each radargram contains a large number of lines with different lengths and widths. The detection performance is assessed by measuring i) the number of correctly detected linear features and false alarms, and ii) the quality of the detections in terms of length of detected linear features versus their actual length. In order to measure

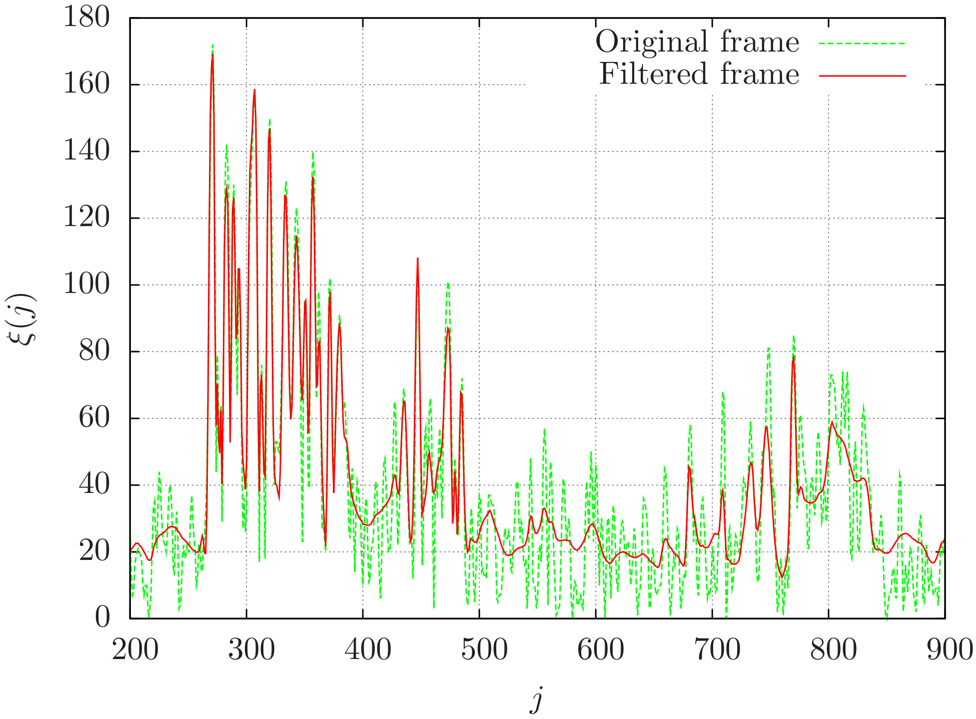

Figure 3.8: Sample frames taken from the radargram of Fig. 3.6 before (dotted green curve) and after (solid red curve) the application of the BM3D filter.

such quantities we defined manually reference maps of the linear features present in the radargrams and compared them to the results of the proposed method. The reference maps drawn from the test radargrams are shown in Fig. 3.15. The reference maps do not contain lines shorter than 10 pixels in order to be comparable to the output of the proposed method.

Detection and false alarm rate

The number of lines present in the reference maps, the number of detected lines and the number of false alarms produced by the proposed technique are summarized in Tab. 3.1 for the two test radargrams. We consider a line detected if it overlaps with a line produced by the algorithm. Similarly, we consider a line produced by the algorithm as a false alarm if it does not overlap with any line contained in the reference map. The analysis of the results points out that the proposed technique has good performance, especially considering that it is automatic. In order to have a more detailed understanding of the detection rate of the method, we studied the relation between the number of missed, detected and false alarms and the line lengths. The results are reported in Fig. 3.16, which shows the histograms representing the number of detected (green), missed (red) and false (yellow) lines versus their length for the two test radargrams. The last column of the histograms includes the lines that have a length equal or greater than 195 pixels. The histograms show that the proposed method detected approximately all the linear features with a length greater than about 30 pixels. For shorter lines the detection performance decreases, and false alarms

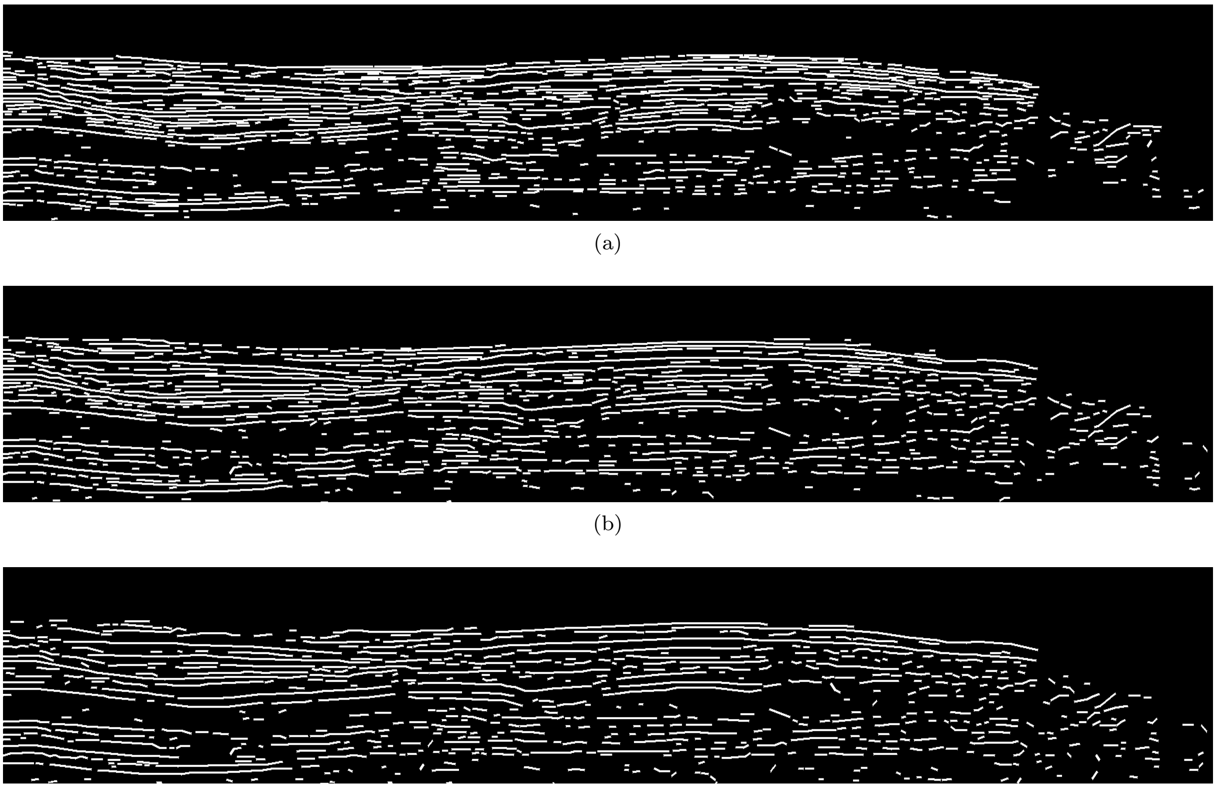

(a)

(b)

(c)

Figure 3.9: Results obtained by the proposed technique on SHARAD radargram 0520501 by varying the parameter w. The value of $c_{\max}$ has been fixed to 3. (a) $w = 2$, (a) $w = 4$, (a) $w = 6$.

arise. It is worth noting that this behavior is not an issue for the goal of the proposed technique, which is the automatic analysis of subsurface areas showing extended layering. It is expected that in such areas significant linear features have a long extension in the radargram domain.

Quality of detection

In order to quantify the quality of the detection performed by the proposed method, we measured for each retrieved line the length of the detected part. This measure has been compared to the actual length of the line. Fig. 3.17 summarizes the results obtained on the two test radargrams. The figure shows for each test radargram a histogram representing

Table 3.1: Accuracy provided by the proposed technique for the detection of linear features in RS data on two SHARAD radargrams.

Radargram number	Number of lines	Detected lines	False alarms
0520501	777	636	63
0528401	768	601	52

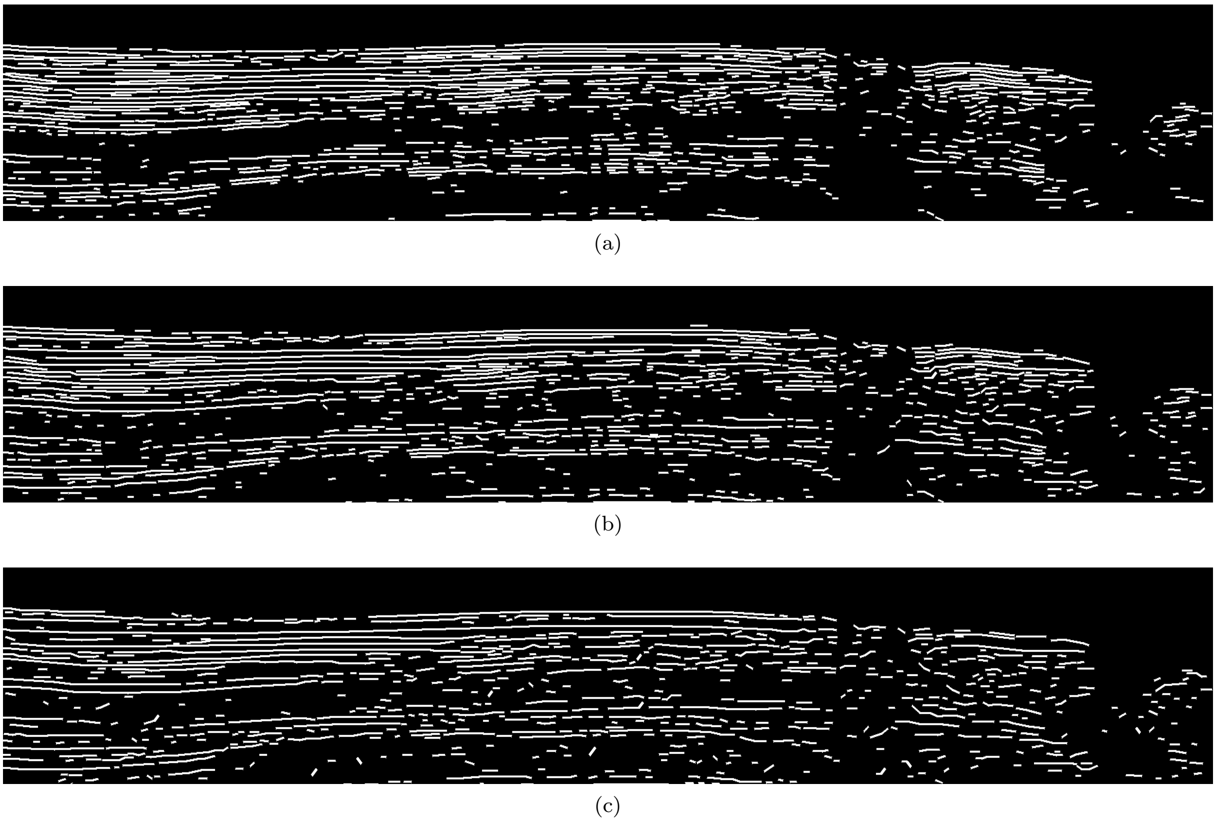

Figure 3.10: Results obtained by the proposed technique on SHARAD radargram 0528401 by varying the parameter w. The value of $c_{\max}$ has been fixed to 3. (a) $w = 2$, (b) $w = 4$, (c) $w = 6$.

the number of detected lines versus the ratio between detected length and actual length. The results point out that in most cases the algorithm is able to detect up to the 60-90% of the length of the linear features.

3.4.5 Extraction of Measurements of Interest

In Sec. 3.3.4 we defined several measurements that can be derived from the output of the linear feature detection. In this section we focus on the calculation of the number of detected lines and their density in a given radargram area. Indeed, such measurements are interesting as they can give a quick overview of the presence of subsurface linear features and of their distribution, and become important when 3D maps of these parameters should be obtained by interpreting radargrams acquired on parallel adjacent tracks in global mapping applications. Fig. 3.18 shows the measured number of lines per frame for the test radargrams of Fig. 3.6 and Fig. 3.7. Both the number of layers present in the reference map and in the detected set are shown. The values have been averaged using a 10-wide moving window in order to reduce the effect of outliers. The graphs show that the output of the proposed technique well approximates the values given by the reference maps. In general the proposed technique slightly underestimates the number of linear features. The largest gaps between the output of the algorithm and the reference map are

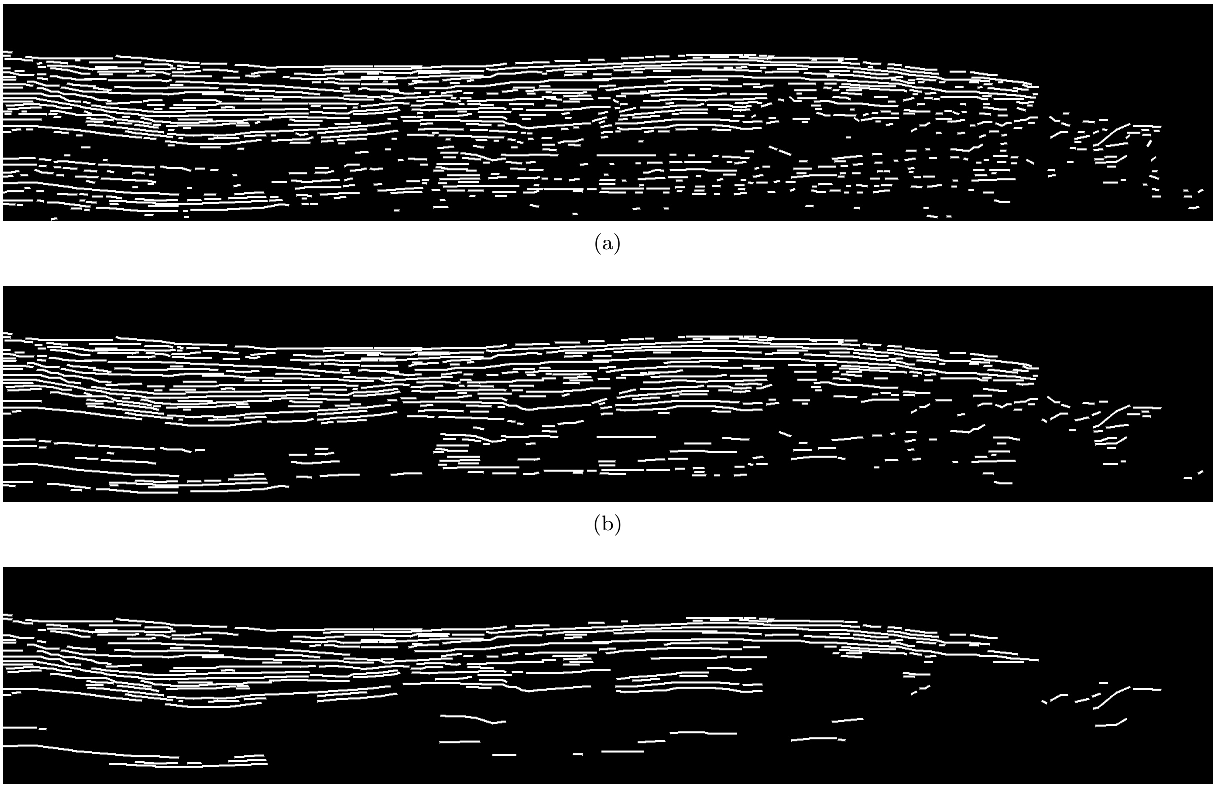

(a)

(b)

(c)

Figure 3.11: Results obtained by the proposed technique on SHARAD radargram 0520501 by varying the parameter $c_{\max}$. The value of w has been fixed to 2. (a) $c_{\max} = 3$, (b) $c_{\max} = 10$, (c) $c_{\max} = 20$.

due to low contrast linear features (low power at the interface) which are not detected.

Fig. 3.19 and Fig. 3.20 show the layer densities maps obtained for the two test radargrams. Both the map obtained from the layer reference map and the detected map are shown for each radargram. The densities have been calculated using a sliding window of size 5 $\times$ 20 pixels (along-track $\times$ range) with a step of 1 pixel in both along-track and range directions. The measures obtained from overlapping windows have been averaged. The layer density is represented in terms of number of lines per samples. By considering the range sampling of the considered SHARAD radargrams (which is 37.5 ns), this means that the values shown in Fig. 3.19 and Fig. 3.20 correspond approximately to a range of 0 to 0.63 lines every 10 meters (using $\varepsilon_{ss} = 3.15$). The choice of the size of the sliding window has been driven by the much different resolution of the data in the along-track and range direction. As commented in Sec. 3.3.4, the choice of a larger window would have produced smoothed versions of the density maps. The density maps of Fig. 3.19 and Fig. 3.20 present clearly how the linear features are distributed within the radargrams. A visual comparison between the reference density maps and the detected density maps shows that the proposed technique is able to approximate the reference map with good accuracy in a completely automatic way.

(a)

(b)

(c)

Figure 3.12: Results obtained by the proposed technique on SHARAD radargram 0528401 by varying the parameter $c_{\max}$. The value of w has been fixed to 2. (a) $c_{\max} = 3$, (b) $c_{\max} = 10$, (c) $c_{\max} = 20$.

3.5 Conclusions

In this chapter we presented a novel technique for the automatic detection and characterization of subsurface linear features in RS data. The method is suited to the analysis of regions showing extended layering. The experimental results obtained on real planetary RS data confirmed the effectiveness of the proposed method both qualitatively and quantitatively.

In order to extract further information from the radargrams, we also proposed a set of measurements which can be derived from the detected linear features. Such measures can describe locally the properties of the single linear features and provide information about their distribution within the radargram (and thus the geographical area of interest).

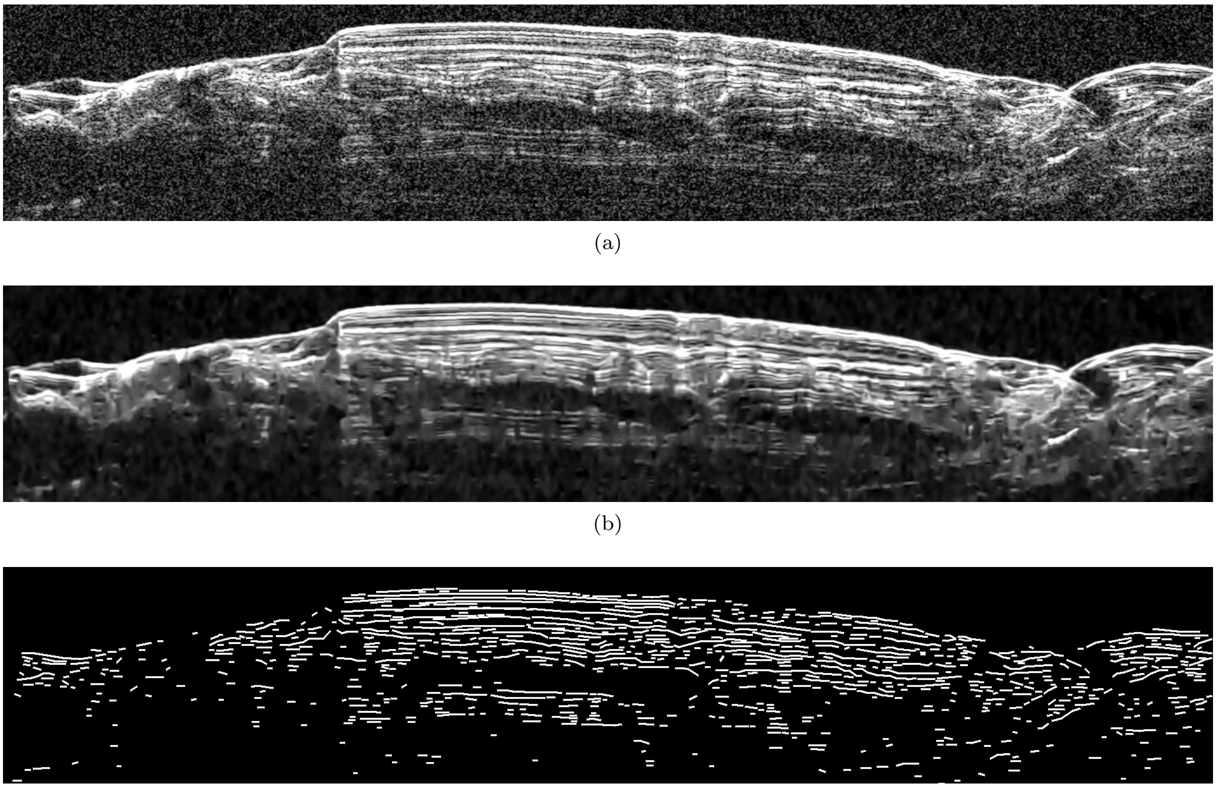

(a)

(b)

(c)

Figure 3.13: Denoising and detection results obtained on the SHARAD radargram 0519701 using the parameters $w = 2$ and $c_{\max} = 3$. (a) original radargram, (b) denoised radargram, (c) detection result.

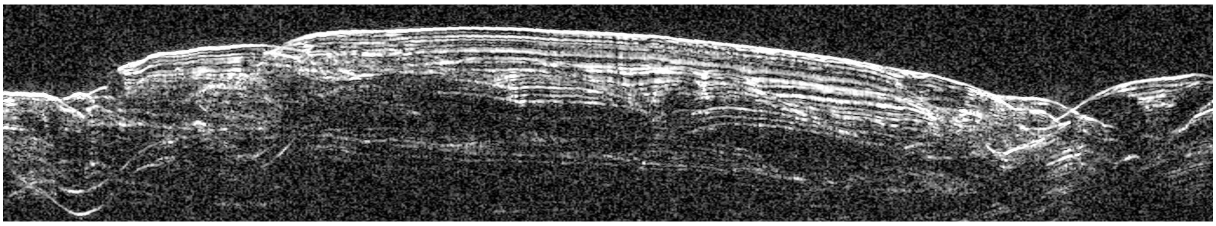

(a)

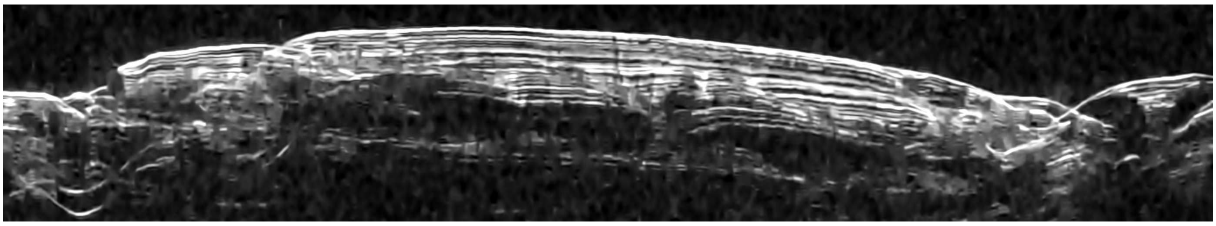

(b)

(c)

Figure 3.14: Denoising and detection results obtained on the SHARAD radargram 1591701 using the parameters $w = 2$ and $c_{\max} = 3$. (a) original radargram, (b) denoised radargram, (c) detection result.

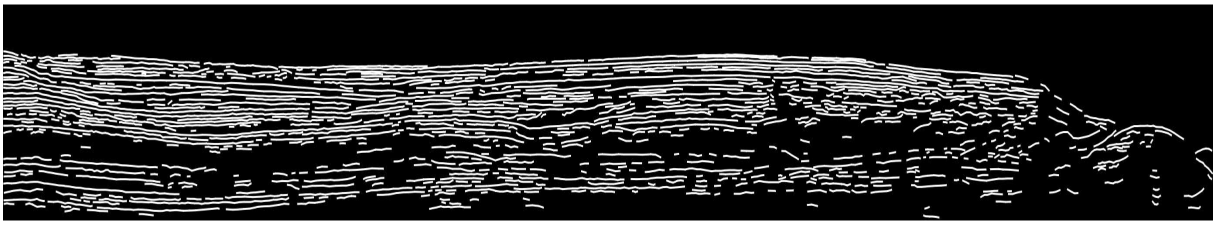

(a)

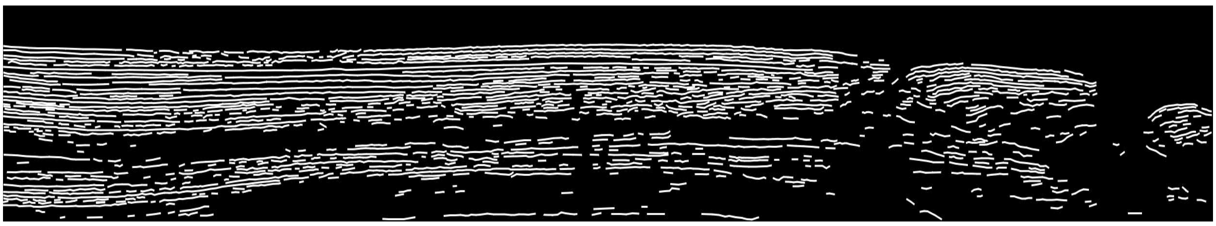

(b)

Figure 3.15: Reference maps used for the quantitative performance analysis: (a) radargram 0520501, (a) radargram 0528401.

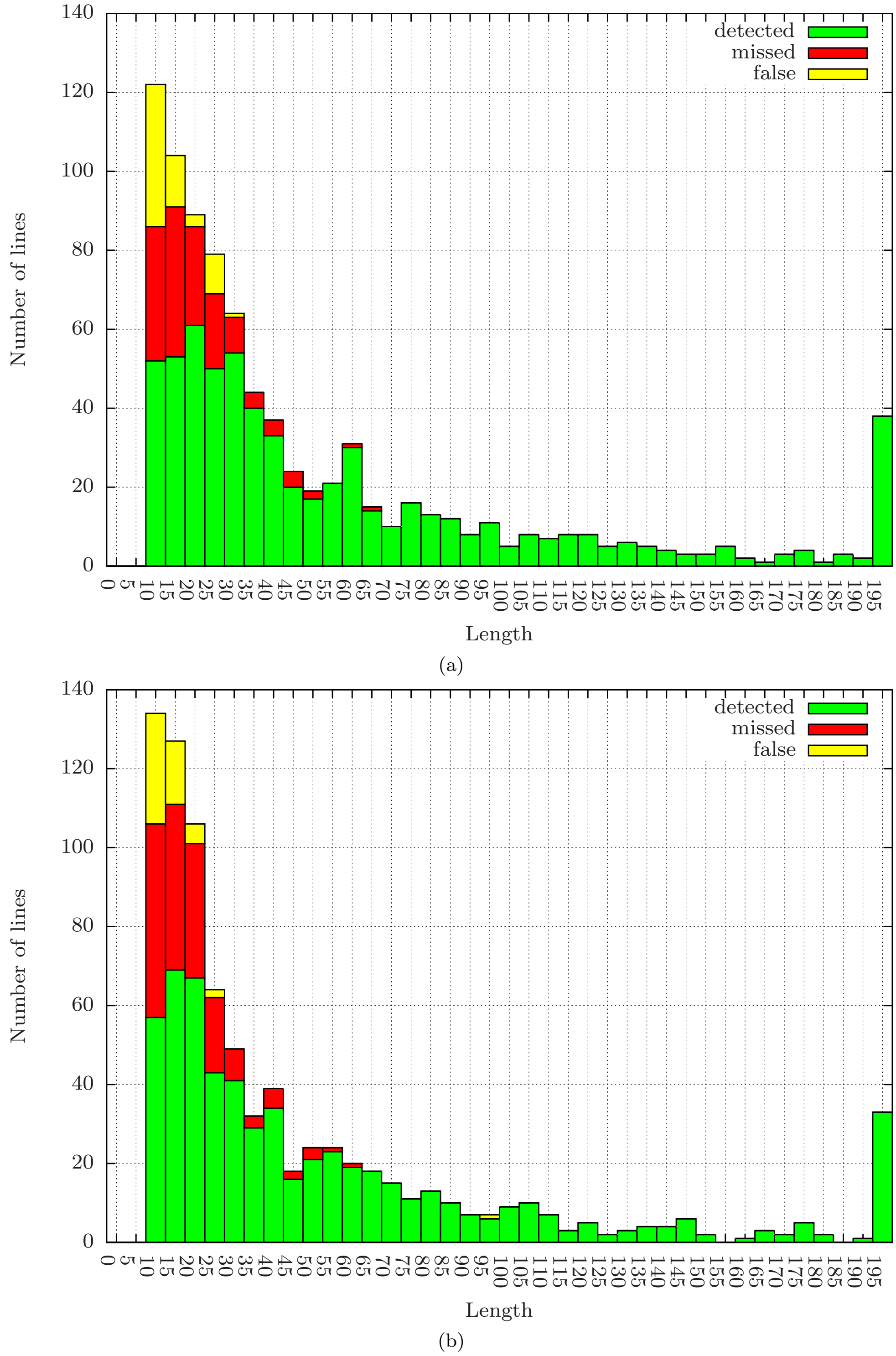

Figure 3.16: Histograms representing the number of detected (green), missed (red) and false (yellow) lines versus their length for the two test radargrams. (a) SHARAD radargram 0520501, (b) SHARAD radargram 0528401.

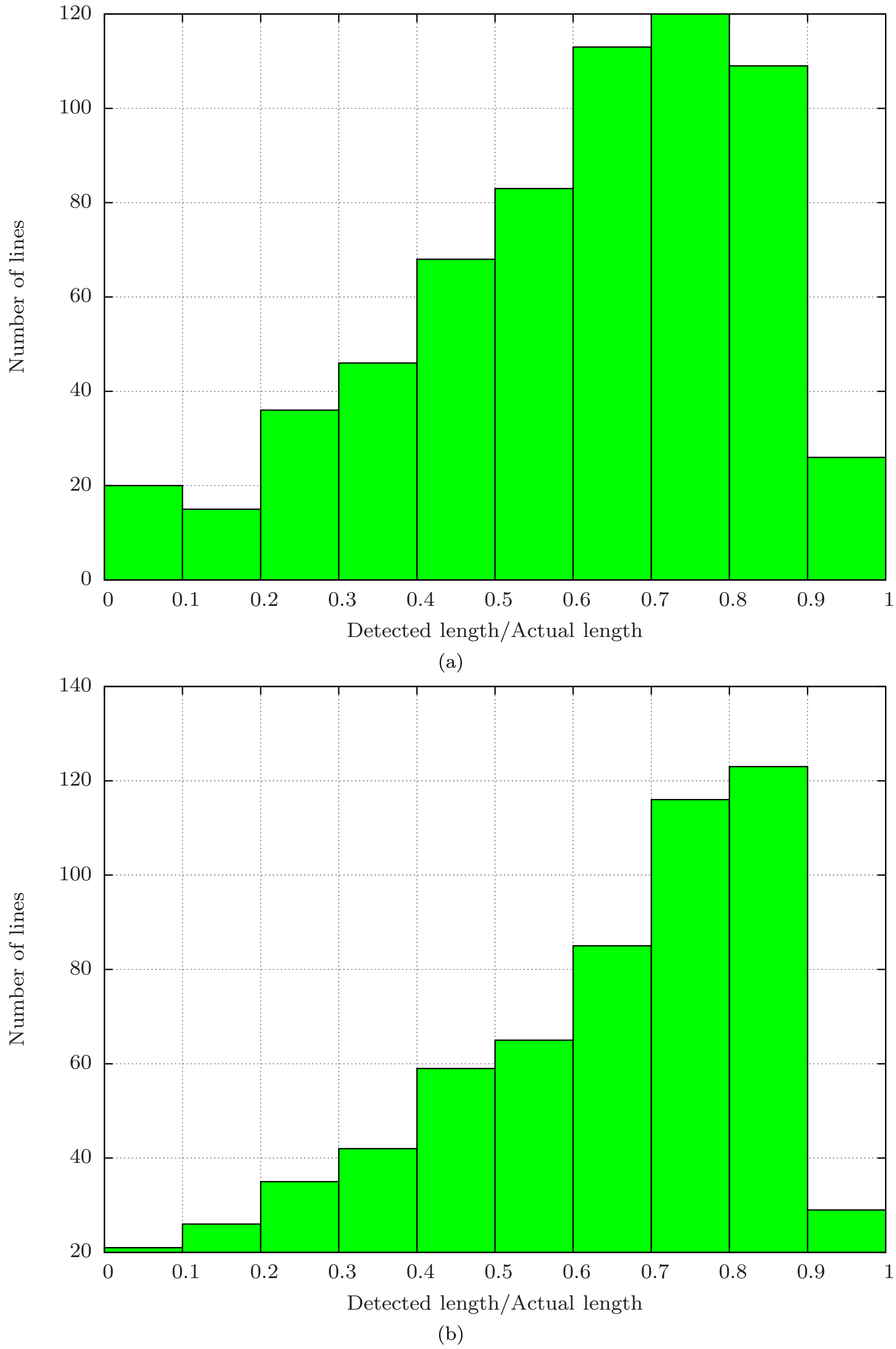

Figure 3.17: Histograms representing the number of detected lines versus the ratio between their detected and actual lengths for the two test radargrams. (a) SHARAD radargram 0520501, (b) SHARAD radargram 0528401.

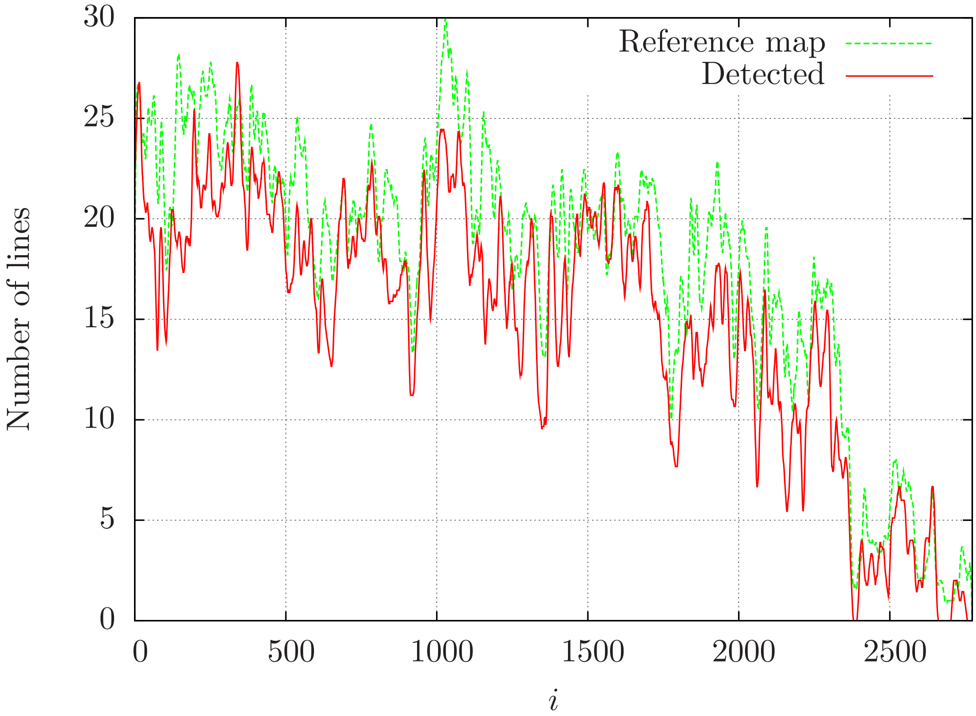

(a)

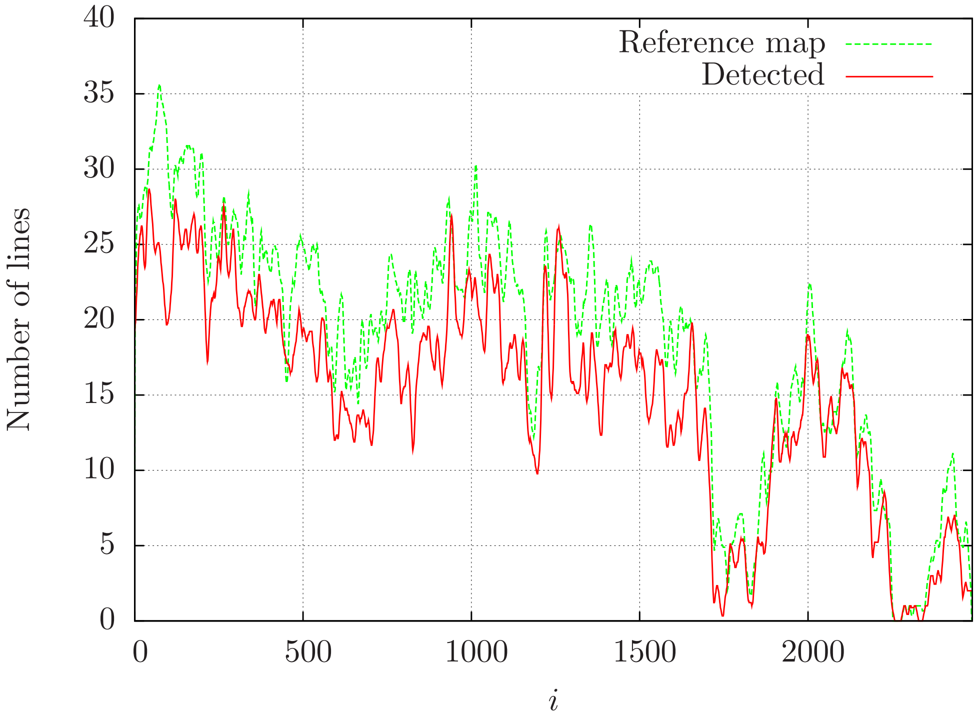

(b)

Figure 3.18: Number of detected lines per frame for the SHARAD test radargrams (a) 0520501, and (b) 0528401. The measured values have been averaged using a moving window of width equal to 10 frames.

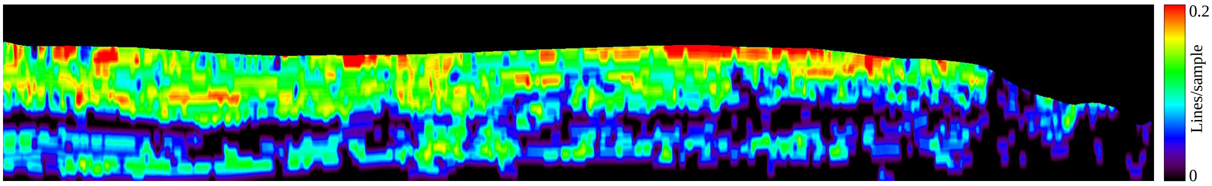

(a)

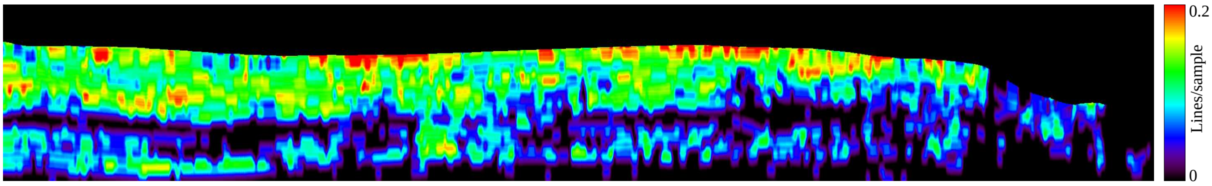

(b)

Figure 3.19: Layer density measured using a sliding window of 5 × 20 pixels (along-track × range) with a step of 1 pixel in both along-track and range directions on (a) the reference map, and (b) the detected linear features of SHARAD radargram 0520501. The measured values have been averaged on overlapping windows.

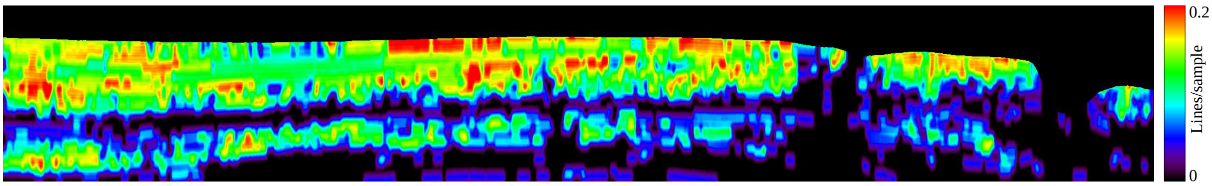

(a)

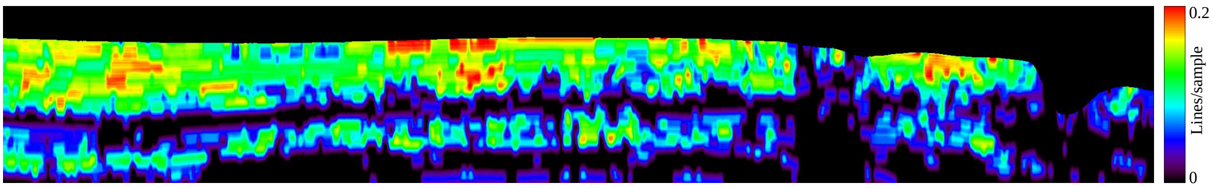

(b)

Figure 3.20: Layer density measured using a sliding window of 5 × 20 pixels (along-track × range) with a step of 1 pixel in both along-track and range directions on (a) the reference map, and (b) the detected linear features of SHARAD radargram 0528401. The measured values have been averaged on overlapping windows.

Chapter 4

Detection of Surface Clutter Returns through Clutter Simulation Matching

One of the most critical and time-consuming tasks related to the analysis of orbiting RS data is the detection of surface clutter returns, which is usually carried out manually. In this chapter we address this problem by proposing a novel technique for the automatic detection of surface clutter returns in RS data. The proposed method is made up of three steps: i) simulation of surface clutter returns using available digital elevation models, ii) automatic coregistration between radargrams and simulations, and iii) extraction of surface clutter returns from the coregistered radargrams. The coregistration step is performed in two phases: i) a coarse registration based on the detection of the first return line on both input radargrams, and ii) a fine registration based on B-spline deformation. The proposed technique is robust to radargram deformations (e.g., due to ionosphere effects) and allows the generation of different types of outputs (e.g., coregistered simulations, binary clutter maps, false-color compositions) that can both greatly support the scientific community in manual analysis of RS data and drive the development of reliable automatic methods. The effectiveness of the proposed method is proven on two large datasets acquired on different areas of Mars by the SHARAD instrument.

4.1 Introduction

One of the most critical problems which affects both manual and automatic analysis of radargrams is the presence of surface clutter. Surface clutter has been introduced in Chapter 1. Briefly, it is due to off-nadir returns caused by both surface topography and roughness, which are detected by the radar at the same time of subsurface returns. These produce in radargrams apparent false subsurface features that show similar characteristics to real subsurface structures. Therefore, an operator (or a general automatic method) who is not aware of the presence of such spurious scattering may extract information which is biased by clutter returns. To our knowledge, the problem of the automatic detection of surface clutter in detected radargrams has not been yet addressed in the literature.

As reported in Chapter 1, although different techniques have been proposed to perform clutter reduction [7,46], radargrams acquired by orbiting RSs usually show strong residual clutter returns. When DEMs of the surface of the area of interest are available, a widely used approach for the detection of surface clutter is the comparison of radargrams to surface clutter simulations [34,35,97,98]. This is performed manually for each radargram, thus limiting the reliable analysis of datasets composed by many acquisitions, which would require a very large amount of time.

In this chapter we address the above-mentioned problem by proposing a novel automatic technique for the detection of surface clutter in radar sounding data. The proposed method is made up of three steps: i) simulation of surface clutter returns, ii) automatic coregistration between radargrams and simulations, and iii) extraction of surface clutter returns from the coregistered radargrams. In order to simulate clutter returns we developed a fast clutter simulator suited to both user-oriented real-time investigations and batch processing. The coregistration is performed in two phases: i) a coarse registration based on the detection of the first return line on both the input radargrams, and ii) a fine registration based on B-spline deformation. Such procedure can be used also for the coregistration of multitemporal radargram series. The proposed technique is robust to radargram deformations (e.g., due to critical variations of ionospheric delays) and allows the generation of different types of outputs (e.g., coregistered simulations, binary clutter maps, false-color compositions), which can both greatly support the scientific community in manual analysis of RS data and drive the development of reliable automatic methods for information extraction. The effectiveness of the proposed method is proven on two large datasets acquired on different areas of Mars by the SHARAD instrument.

The remainder of the chapter is organized as follows. Sec. 4.2 presents the general architecture of the proposed technique for the automatic detection of surface clutter returns in RS data. The following sections illustrate the main steps of the proposed method in greater detail. Sec. 4.3 presents the algorithm developed for simulating surface clutter returns. Sec. 4.4 describes in detail the proposed automatic technique for the coregistration of radargrams and clutter simulations. Sec. 4.5 addresses the problem of the extraction of the clutter returns from coregistered radargrams and simulations. In Sec. 4.6 the results of the experiments carried out on real SHARAD data are presented and discussed. Finally, the conclusions of the chapter are drawn in Sec. 4.7.

4.2 Proposed Method for the Automatic Detection of Surface Clutter Returns

The proposed method for the automatic detection of surface clutter returns in RS data is made up of three main steps: i) simulation of surface clutter returns, ii) automatic coregistration of radargrams and simulations, and iii) extraction of surface clutter returns from the coregistered radargrams. Fig. 4.1 shows the block scheme of the proposed processing chain. The main inputs of the method are a real radargram and a DEM of the area of interest. The input radargram should be correlated with ancillary information describing the spatial position of the radar for each frame of the radargram. As it will be described in greater detail in Sec. 4.3, the characteristics of the DEM should be

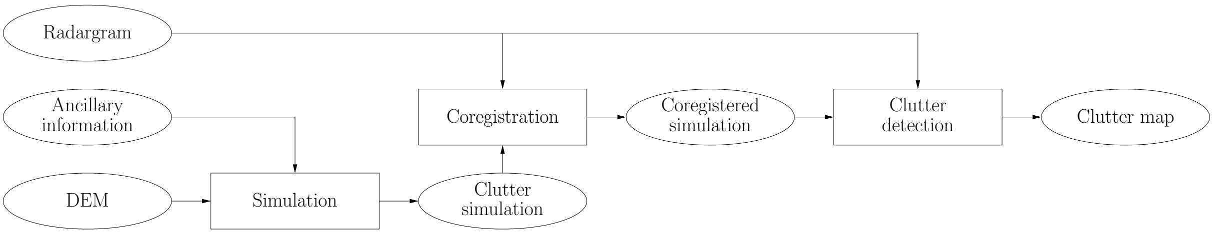

Figure 4.1: Block scheme of the proposed method for the automatic detection of surface clutter returns in RS data.

compatible with the spatial resolution of the RS in order to generate meaningful clutter simulations.

The main output of the proposed method is a binary map indicating which features appearing in the subsurface part of the input radargram have high probability to be due to surface clutter. As it will described in Sec. 4.4, the proposed method for the coregistration of radargrams and simulations is capable to correct for geometrical distortions due to external factors (e.g., variations of ionospheric delay) which may affect the radargram acquisition, and thus the clutter detection. The intermediate outputs of the method can be also used for relevant scientific purposes. In particular, the coregistered simulations given by the second step can be used as a starting point for further visual analyses (e.g., false-color compositions with the real radargram). Moreover, the transformation performed on the simulation in order to match it with the real radargram is known. This can be used to generate further simulations with different parameters (e.g., roughness values, scattering model) which can be straightforwardly coregistered with real data and previous simulations without performing the coregistration process from the beginning.

In the following sections we describe more in detail the three steps of the proposed method.

4.3 Simulation of Surface Clutter Returns

In this section we firstly give an overview of the literature on the topic of RS surface clutter simulation. Then, we describe in detail the characteristics of the clutter simulator used in this thesis.

4.3.1 Background

The simulation of surface clutter returns needs the knowledge of the surface topography of the area under investigation. In order to generate accurate simulations, the topography should be known at least at the scale defined by the Rayleigh criterion [99]. This allows one to properly estimate the characteristics of surface roughness at the working wavelength and to simulate its effect. However, this is not possible in many situations, especially in the case of planetary RSs, where the knowledge of surface topography is limited or not available at such high sampling rate. In the literature some works addressed the topic of the development of clutter simulators for radar sounding applications, mainly focusing on the analysis of RS data acquired on Mars. The most common approach exploited for clutter simulation is the so-called facet method [34]. The basic principle is to locally approximate surface topography with flat facets and calculate scattering from such facets using a proper surface scattering model. In [34] this approach was introduced for the analysis of MARSIS data. The method allows one to simulate coherently the signal, taking into account also the radiation pattern of each facet. In [97] an incoherent simulator that also considers the azimuth SAR processing is proposed and used for the analysis of SHARAD radargrams. A fast numerical model used for simulating SHARAD radargrams is discussed in [98]. Such a model works in the frequency domain in order to speed-up the required intensive calculations. Another approach to clutter simulation is reported in [35]. The authors show examples of radargrams acquired at Antarctica by an airborne sounder and discuss in detail the use of simulations for the discrimination of clutter in data taken from an orbital RS with focus on Mars.

4.3.2 Fast Surface Clutter Simulation

In order to apply the techniques proposed in this chapter, we developed a fast imaging simulator which is suited to the implementation of both user-oriented real-time analysis and batch automatic processing chains. In the following we describe the basic principles of such a simulator. However, it is worth noting that the techniques proposed in this chapter are general and can work with any type of simulation.

The developed simulator generates surface clutter simulations frame-by-frame in the time domain. It uses as input a DEM of the investigated region and the spatial position of the radar for each frame that has to be simulated. In order to produce simulations that match as much as possible with real radargrams, in our experiments we extracted the radar position from the ancillary data which are distributed along with the considered radargrams. However, the developed simulator can be used also as a tool to predict the surface clutter behavior for any radar position even if no radargram has been actually acquired. Fig. 4.4 shows the main steps involved in the clutter simulation. For each frame that has to be simulated, the algorithm firstly determines the position of the radar using the input ancillary data. Starting from such a position, the simulator calculates the local radar ground footprint on the DEM according to the illuminated area that is expected to give relevant surface reflections (which depends on the instrument characteristics and can be automatically estimated or set manually by the user). This is carried out by locally converting the DEM coordinates into a Universal Transverse Mercator (UTM) projection, if necessary. Such a conversion makes the computations performed in the following steps general, as they do not depend on the particular projection used for the DEM. Moreover, in a UTM projection real distances are preserved and can be straightforwardly calculated according to the Pythagoras' theorem.

The goal of the developed simulator is to generate simulated radargrams showing the main geometrical features due to clutter. Thus, simulations are suited for the comparison with real radargrams and can be used as a starting point for the automatic detection of surface clutter. Surface scattering is simulated through incoherent summation of the contributions coming from each DEM resolution cell belonging to the considered ground footprint. For every frame i to be simulated, the backscattered simulated power ξ_S in time t can be modeled using two simple power laws with increasing complexity:

$$\xi'_{\mathrm{S}}(i,t) = K \sum_{(x,y)\in A_i} \frac{\delta[t-2R(x,y)]}{R(x,y)^4}, \tag{4.1}$$

$$\xi''_{\mathrm{S}}(i,t) = K \sum_{(x,y)\in A_i} \rho(\theta(x,y),\varepsilon_r(x,y)) \cos(\theta(x,y))^{\kappa} \cdot \frac{\delta[t-2R(x,y)]}{R(x,y)^4}. \tag{4.2}$$

The law of (4.2) differs from that of (4.1) for the fact that it takes into account the dielectric contrast of the ground and the effective local incidence angle at every illuminated position. The term A_i is the area on the ground which is expected to produce surface clutter returns when considering the frame i. K is a constant which goal is to increase the dynamic of the simulated intensity values. In this thesis, K is calculated in order to rescale the 99.9% of the histogram of the intensity of the simulation in the range 0-255. The function $\delta(.)$ indicates a Dirac impulse (which will be coded as a single pixel in the simulated radargram through a proper conversion from time t to sample position j for the considered frame i). The term $R(x,y)$ represents the distance between the radar and the ground position (x,y) (see Chapter 1). For the sake of completeness, we recall that $R(x,y)$ is calculated as:

$$R(x,y) = \sqrt{(x-x_0)^2 + (y-y_0)^2 + [h_0 - h(x,y)]^2}, \tag{4.3}$$

where (x_0, y_0, h_0) and $[x, y, h(x,y)]$ are the 3D position of the radar and of a ground point, respectively. For each considered ground point (x,y), its elevation $h(x,y)$ is given by the input DEM. In order to produce correct simulations, it is important that the altitude of the radar and of the ground (given by the DEM) have the same zero-reference point. The factor $\rho(\theta(x,y),\varepsilon_r(x,y))$ depicts the relative Fresnel coefficient of the surface, given by [12]:

$$\rho(\theta(x,y),\varepsilon_r(x,y)) = \left| \frac{\cos\theta(x,y) - \sqrt{\varepsilon_r(x,y) - \sin^2\theta(x,y)}}{\cos\theta(x,y) + \sqrt{\varepsilon_r(x,y) - \sin^2\theta(x,y)}} \right|^2 . \tag{4.4}$$

$\rho(\theta(x,y),\varepsilon_r(x,y))$ is thus a function of the local incidence angle $\theta(x,y)$ and the surface dielectric constant $\varepsilon_r(x,y)$. The local incidence angle is estimated by using the neighborhood DEM resolution cells [34]. The value of $\varepsilon_r(x,y)$ can be set according to available dielectric maps of the surface of the area under investigation. If such maps are not available, it can be set to a fixed value indicating the expected dielectric constant of the surface. Finally, the term κ is a user-defined constant which modulates the effect of the local incidence angle on the simulated intensity. Fig. 4.2 and Fig. 4.3 show the comparison between two simulations obtained with both (4.1) and (4.2), and the corresponding real SHARAD radargrams related to two different areas of Mars.

The models of (4.1) and (4.2) do not allow a precise estimation of the scattered power and do not take into account the SAR processing usually applied for improving the along-track resolution of radargrams. The effect of SAR processing can be approximated by setting the size of the illuminated area on ground in the along-track direction according to the expected focused radar resolution. More complex scattering models (e.g., fully coherent approach, PO [99], fractal [100]) can be used for the computation of the intensity of the

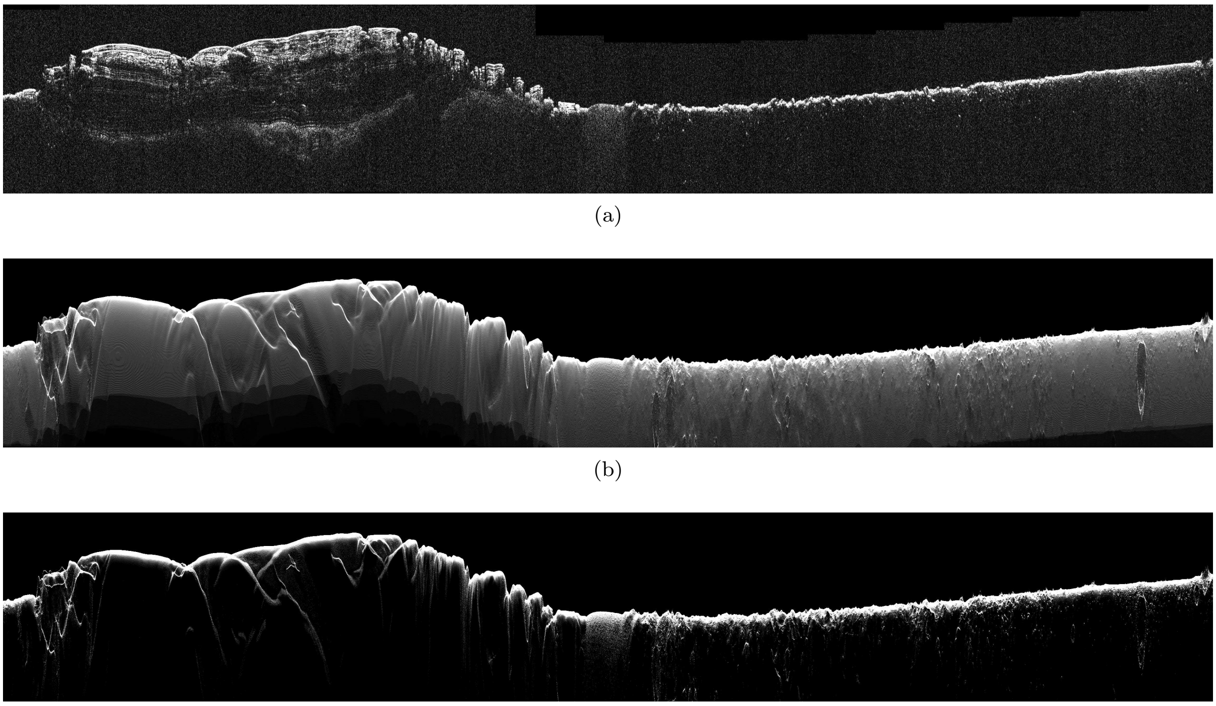

(a)

(b)

(c)

Figure 4.2: (a) SHARAD radargram 0921802 acquired on the North Pole of Mars and the related simulations obtained with (b) law (4.1), and (c) law (4.2) using a fixed $\varepsilon_r = 3.15$ and $\kappa = 3000$.

simulation instead of (4.1) and (4.2). However, such models would introduce dependence on more parameters, in particular surface roughness. This poses additional constraints on the input DEM in order to assure their validity, and increases the computational effort required for simulation. As we will show in Sec. 4.6, the use of simple power laws as those defined in (4.1) and (4.2) does not represent a limitation for the goal of detecting surface clutter on real radargrams. Indeed, the simulations obtained according to such laws are usually very conservative [for the case of (4.2) the conservativity depends on the factor κ], showing surface clutter features at long ranges which are not visible in the corresponding radargrams. The risk that clutter returns are underestimated due to wrong scattering model parameters is thus reduced. Simulated features that do not appear in real data can be detected by proper cross-comparison (see Sec. 4.5).

4.4 Automatic Coregistration of Radargrams and Clutter Simulations

In this section the proposed method for the automatic coregistration of radargrams and clutter simulations is presented. After an overview of the technique, its main steps are discussed in detail.

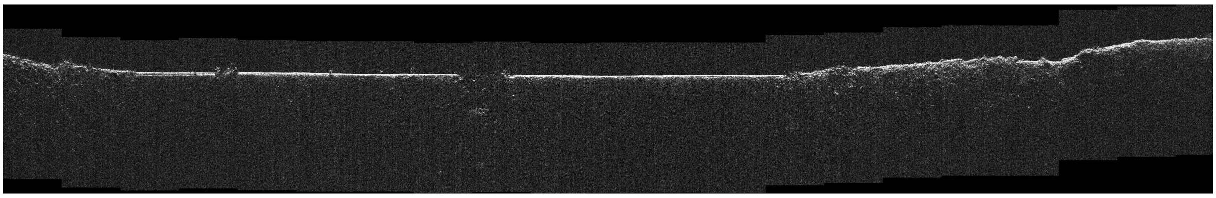

(a)

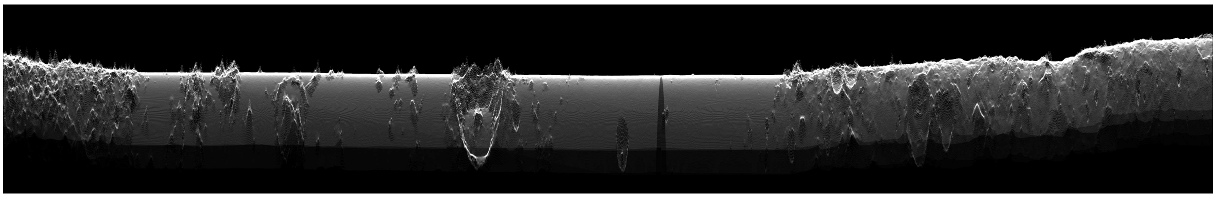

(b)

(c)

Figure 4.3: (a) SHARAD radargram 0365601 acquired on the Elysium Planitia on Mars and the related simulations obtained with (b) law (4.1), and (c) law (4.2) using a fixed $\varepsilon_r = 5$ and $\kappa = 3000$.

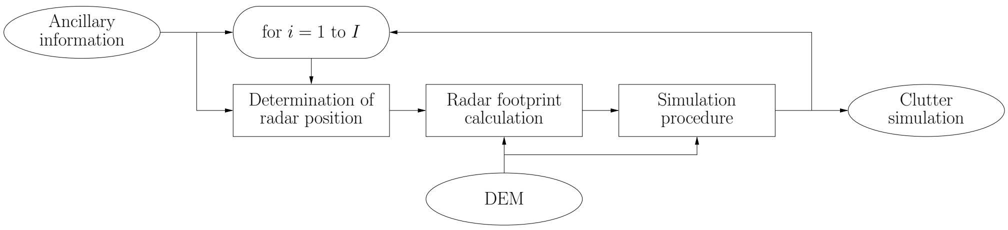

Figure 4.4: Block scheme of the developed simulator.

4.4.1 Method Overview

The coregistration method proposed in this thesis is designed for the alignment between radargrams and related clutter simulations. However, the method is more general and can be used for the coregistration of multitemporal radargram series. As the topic of this chapter is the automatic detection of clutter returns, in the following the focus will be on the coregistration between radargrams and clutter simulations.

As mentioned before, orbital RS data can be affected by geometrical and radiometric distortions due to external factors, such as the influence of ionosphere. The effect of such distortions may be different within a single acquisition. As a result, the coregistration between radargrams and simulations is a difficult task that needs both a proper definition of the initial parameters and the use of deformable transformations.

The proposed technique for the automatic coregistration of radargrams is made up of

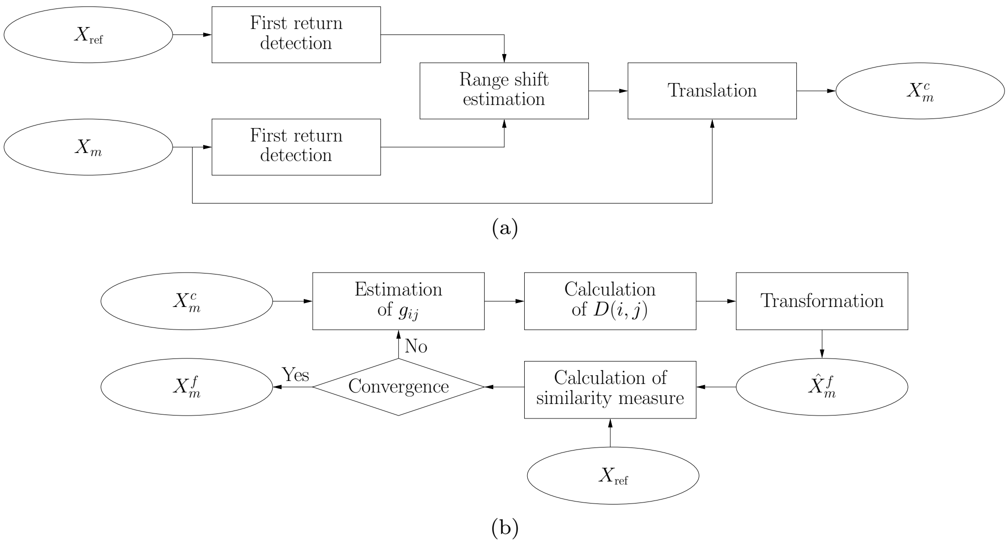

Figure 4.5: Block scheme of the proposed method for the automatic coregistration of radargrams and clutter simulations: (a) coarse registration, (b) fine registration.

two steps: i) a feature-based coarse registration based on the detection of the first return line on both input radargrams, and ii) an area-based fine registration using B-spline deformation (see Fig. 4.5). This procedure allows the technique to match roughly the two input radargrams in the first step and to refine the coregistration in the second step. The proposed two-step approach thus mitigates the problem of the sensitivity to initial conditions intrinsic of area-based registration techniques [101]. One of the two radargrams acts as *reference radargram* and is not modified during the registration process. The second radargram (*moving radargram*) is deformed in order to match with the reference radargram. We denote the reference and moving radargrams with X_{ref} and X_m, respectively. Note that in the case of the coregistration between a real radargram and a clutter simulation $X_{\text{ref}} = X$ and $X_m = X_{\text{S}}$, where X and X_{S} identify the real and the simulated radargram, respectively. This allows to keep unaltered the radargram and to apply all the processing related to the coregistration to the simulation. The method requires that the input radargrams represent the same ground track, with the same extension and sampling. This means that the number of frames I is the same for both radargrams. This condition can be met by properly cutting the input radargrams or, in the case the moving radargram is a clutter simulation, by simulating surface clutter using the ancillary data provided along with the real radargram. In the following the two steps of the proposed method will be described in greater detail.

4.4.2 Feature-based Coarse Registration

The coarse registration is a feature-based approach aimed at reducing the impact of unpredictable vertical (range) shifts present in the input radargrams which may hamper their correct coregistration. When the moving radargram is a clutter simulation, the correct range alignment with the reference radargram can be obtained by simulating clutter using the orbital parameters of the reference radargram. Indeed, orbital parameters include the spatial position of the orbiter for each radargram frame and this can be given as input to the simulation process. However, in some cases the orbit knowledge is not precise or other factors introduce delays in the real data which may be different even within a same track (e.g., ionosphere effects in night/day transitions in polar regions). The coarse registration step is thus aimed at estimating and removing these shifts globally from the moving radargram. This is performed in three main steps (see Fig. 4.5a): i) first return detection, ii) shift estimation, and iii) translation of the moving radargram.

The first step detects the first return line as reference to coarsely align the input radargrams. Indeed, the most reliable feature in a radargram (and in a simulation) is the first return line, which appears as a strong feature. Ideally, the first return line is the nadir surface return. In practice this is not true when lateral clutter echoes arrive to the receiver before the nadir return. However, if a radargram and a simulation have been produced in the same conditions, no changes are expected in the shape of the first return line (unless major ground changes occurred between the two acquisitions). The detection of the first return line on real radargrams is performed according to the method proposed in Chapter 2.

The position of the first return in the simulated radargram is known during the simulation process. Therefore, no specific technique is needed in order to perform its detection.

In the second step of the coarse registration process the range shift between the input radargrams is calculated. Let us denote with $j_{0,\text{ref}}(i)$ and $j_{0,m}(i)$ the first return position detected on the reference and the moving radargram, respectively. The range shift Δj is thus calculated as follows:

$$\Delta j = \frac{1}{I} \sum_{i=1}^{I} \left[j_{0,m}(i) - j_{0,\text{ref}}(i) \right]. \tag{4.5}$$

In the last step, the moving radargram is translated in the range direction by a quantity of pixels equal to Δj. As Δj is calculated with sub-pixel accuracy, interpolation of the moving radargram is required in order to perform the coarse translation. Depending on the nature of the moving radargram, different approaches can be applied (e.g., nearest neighbor, linear interpolation, spline interpolation) [102]. However, in the case X_m is a clutter simulation, according to our experiments, linear interpolation is sufficient for an initial alignment and also allows one to preserve the properties of the moving radargram. This holds also for the fine registration step. We denote the moving radargram after applying the coarse registration with X_m^c.

In the case the moving radargram is a clutter simulation, the coarse registration process may be biased due to simulation conservativity. Indeed, simulations often show lateral surface returns which are not visible in real data. These are usually related to lateral relief, which appears in simulations but may correspond to (almost) flat areas in actual radargrams. This is due to the fact that clutter simulators often overestimate the scattering contribution of off-nadir slopes not directly facing the radar. Fig. 4.6 shows an example of simulation conservativity. In order to deal with this problem, when the moving radargram is a clutter simulation the coarse registration is performed by considering only the flat regions of both the reference and moving radargram. This is carried out by applying (4.5) only to a subset of the frame set composed by the frames i_f which fulfill

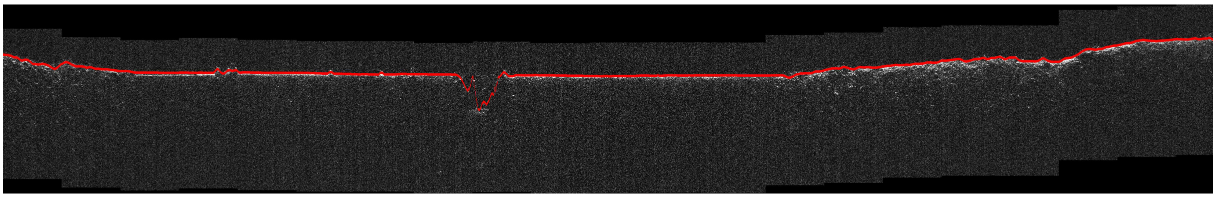

(a)

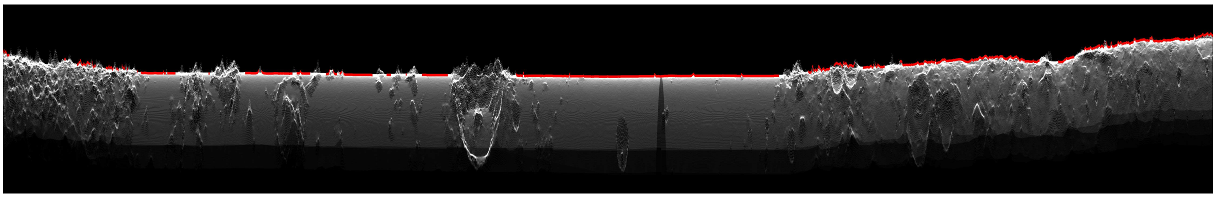

(b)

Figure 4.6: Result of the first return detection on (a) the SHARAD radargram 0365601 acquired on Elysium Planitia and (b) the related simulation obtained using the law of (4.1). For the simulation, the detected first returns have been downselected according to the criterion of (4.6).

the following condition:

$$s(i_f, w) \leq s_t, \tag{4.6}$$

where $s(i_f, w)$ is the standard deviation of the first return positions calculated on the simulated radargram within a sliding window of width w centered on i_f, and s_t is a user-defined threshold. In Fig. 4.6b the result of such a selection is shown on a SHARAD simulation. In our experiments the results of the coarse registration (and thus also of the whole registration process) demonstrated to be weakly dependent on the selection of w and s_t.

4.4.3 Area-based Fine Registration

The fine registration step aims at generating the final coregistered moving radargram starting from the output of the coarse registration. For the fine registration an area-based method is used. This choice comes from the fact that in radargrams (and clutter simulations) it is difficult to identify automatically features which detection can be sufficiently reliable to assure a precise sub-pixel coregistration. This is true especially if the moving radargram is a clutter simulation. Indeed, a feature-based coregistration approach exploiting the presence of particular subsurface structures is not applicable to clutter simulations as they only show surface clutter returns. For these reasons, the use of an area-based coregistration approach preserves the generality of the proposed technique.

In order to deal with the aforementioned problem of local distortions, a registration technique capable to deform locally the moving radargram has to be applied. We propose the use of a deformable transformation based on B-splines [103]. A rectangular coarse grid spanning the whole moving radargram space (B-spline grid) is defined. The grid is made up of a set of control points $g_{i'j'}$ uniformly distributed in both the along-track and range directions. The total number of control points is equal to $G = G_I \cdot G_J$, where G_I and G_J are the number of points in the along-track and range direction, respectively.

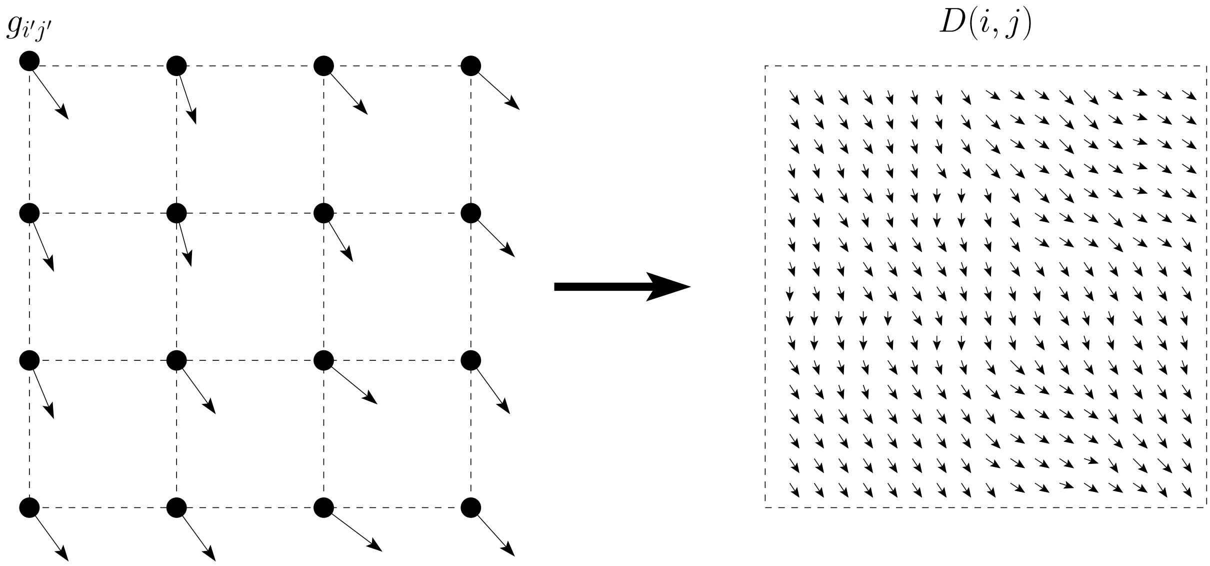

Figure 4.7: Schematic representation of the B-spline grid including the deformation vectors, and of the resulting deformation field $D(i, j)$.

Each point $g_{i'j'}$ represents a deformation vector. The deformation field $D(i, j)$ defined for all radargram points (i, j) is then calculated and applied to the moving radargram (see Fig. 4.7). $D(i, j)$ is obtained through B-spline interpolation [103] as follows:

$$D(i,j) = \sum_{p_1=0}^{3} \sum_{p_2=0}^{3} B_{p_1}(u_1) B_{p_2}(u_2) g_{i''+p_1, j''+p_2}, \tag{4.7}$$

where $i'' = \lfloor i/G_I \rfloor - 1$, $j'' = \lfloor j/G_J \rfloor - 1$, $u_1 = i/G_I - \lfloor i/G_I \rfloor$, and $u_2 = j/G_J - \lfloor j/G_J \rfloor$. The functions $B_p(\cdot)$ represent the basis functions of the B-spline and are given by:

$$\begin{aligned} B_0(u) =& (1-u)^3/6 \\ B_1(u) =& (3u^3 - 6u^2 + 4)/6 \\ B_2(u) =& (-3u^3 + 3u^2 + 3u + 1)/6 \\ B_3(u) =& u^3/6. \end{aligned} \tag{4.8}$$

The process is repeated iteratively, obtaining at each iteration a different deformed moving radargram $\hat{X}_m^f$. Fig. 4.5b summarizes schematically the fine registration process. For each iteration a new deformation field is computed with the goal to optimize a similarity measure $\Upsilon(X_{\text{ref}}, \hat{X}_m^f)$, calculated between the reference radargram X_{ref} and the deformed moving radargram $\hat{X}_m^f$. The process stops when the similarity measure converges, and the final deformed moving radargram X_m^f is returned. Convergence is obtained when

$$\left| \Upsilon(X_{\text{ref}}, \hat{X}_{m,p}^f) - \Upsilon(X_{\text{ref}}, \hat{X}_{m,p-1}^f) \right| < \varsigma, \tag{4.9}$$

where $\hat{X}_{m,p}^f$ and $\hat{X}_{m,p-1}^f$ are the deformed moving radargram at iteration p and $p-1$, respectively; and ς is a user-defined value. At each iteration a number $2G$ of parameters has to be estimated, where the factor 2 accounts for the fact that deformation vectors have two components (as we are dealing with 2D radargrams). The problem described by (4.9) can be solved using several optimization approaches. Due to the high number of parameters involved in the coregistration process, in our experiments we used a limited-memory bound-constrained Broyden-Fletcher-Goldfarb-Shanno (L-BFGS-B) optimizer [104].

Different similarity measures can be used for the coregistration of radargrams and clutter simulations. Due to the synthetic simulation process and to the approach adopted, the radiometry of the simulated signals are much different from that of real data. For this reason, covariance-like measurements are not suited to be used as similarity measures between real radargrams and simulations [25]. Thus, we propose to use as measure mutual information (MI). Indeed, MI can model complex mappings between two images when their radiometry has no direct dependency relations. As a result, MI is widely used as similarity measure for multi-modal coregistration [102, 105, 106] and, recently, was introduced also for the coregistration between SAR real and simulated images [25]. The MI between X_{ref} and X_m is calculated as follows [25]:

$$\text{MI}(X_{\text{ref}}, X_m) = H(X_{\text{ref}}) + H(X_m) - H(X_{\text{ref}}, X_m), \tag{4.10}$$

where $H(X_{\text{ref}})$ and $H(X_m)$ are the entropies of X_{ref} and X_m, respectively, and $H(X_{\text{ref}}, X_m)$ is their joint entropy. The entropies can be computed as:

$$H(X_{\text{ref}}) = -\sum_{\xi_{\text{ref}}} p_{X_{\text{ref}}}(\xi_{\text{ref}}) \cdot \log p_{X_{\text{ref}}}(\xi_{\text{ref}}) \tag{4.11}$$

$$H(X_m) = -\sum_{\xi_m} p_{X_m}(\xi_m) \cdot \log p_{X_m}(\xi_m) \tag{4.12}$$

$$H(X_{\text{ref}}, X_m) = -\sum_{\xi_{\text{ref}},\xi_m} p_{X_{\text{ref}},X_m}(\xi_{\text{ref}}, \xi_m) \cdot \log p_{X_{\text{ref}},X_m}(\xi_{\text{ref}}, \xi_m), \tag{4.13}$$

where ξ_{ref} and ξ_m denote the intensity values in the reference and moving radargram, respectively; $p_{X_{\text{ref}}}(\xi_{\text{ref}})$ and $p_{X_m}(\xi_m)$ are the marginal probability functions, and $p_{X_{\text{ref}},X_m}(\xi_{\text{ref}}, \xi_m)$ is the joint probability function. These functions can be estimated in an approximate way by:

$$p_{X_{\text{ref}},X_m}(\xi_{\text{ref}}, \xi_m) = \frac{hist(\xi_{\text{ref}}, \xi_m)}{\sum_{\xi_{\text{ref}},\xi_m} hist(\xi_{\text{ref}}, \xi_m)} \tag{4.14}$$

$$p_{X_{\text{ref}}}(\xi_{\text{ref}}) = \sum_{\xi_{\text{ref}}} p_{X_{\text{ref}},X_m}(\xi_{\text{ref}}, \xi_m) \tag{4.15}$$

$$p_{X_m}(\xi_m) = \sum_{\xi_m} p_{X_{\text{ref}},X_m}(\xi_{\text{ref}}, \xi_m), \tag{4.16}$$

where $hist(\xi_{\text{ref}}, \xi_m)$ is the joint histogram of X_{ref} and X_m.

As we will show in Sec. 4.6, the use of the B-spline deformable transform can effectively overcome the problem of local misalignment between reference and moving radargrams due to, e.g., variations of the ionospheric delay along the same track. It is noteworthy that in the case no local distortions are present in the considered data, a simpler rigid

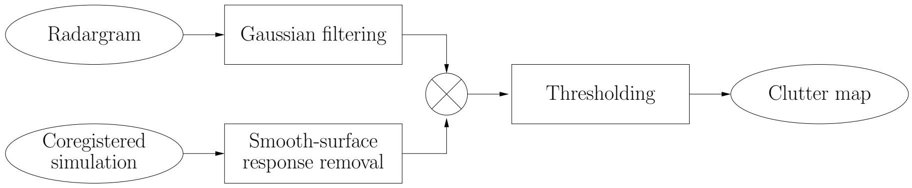

Figure 4.8: Block scheme of the proposed method for the automatic generation of clutter binary maps from coregistered radargrams and simulations.

transform (e.g., translation, affine) could be sufficient to correctly align reference and moving radargrams. However, the only advantage of using such rigid transformations is the reduced computation time.

The main parameters to be set for the B-spline transformation are the number of points of the B-spline grid to be used in the along-track and range directions of the moving radargram. On the one hand, geometric distortions on radargrams usually vary in the along-track direction in the form of changing range offsets. On the other hand, in the range direction no local distortions within single frames are usually visible once the radargram has been properly focused. For this reason, in the range direction only a small number of B-spline grid points is sufficient. Instead, in the along-track direction a number of grid points proportional to the along-track size of the radargram should be set. In Sec. 4.6 we report the number of grid points used in our experiments.

4.5 Automatic Detection of Surface Clutter Returns

The technique presented in the previous section allows the coregistration of radargrams and clutter simulations. Once the coregistration has been performed, radargrams and simulations can be combined in order to generate binary maps of the clutter returns automatically. The block scheme of the proposed technique for the automatic generation of surface clutter binary maps is reported in Fig. 4.8. The method is made up of three steps: i) smooth-surface response removal from the simulation, ii) multiplication of radargram and filtered simulation, and iii) thresholding. In order to reduce the noise contribution on the radargram (and thus also on the final clutter map), this is previously filtered with a Gaussian filter. In the following the main steps of the proposed method are explained in greater detail. In order to simplify the notation, in this section the symbol X_{S} will denote a clutter simulation which is already coregistered with the relative radargram.

4.5.1 Smooth-surface Response Removal

The simulator presented in Sec. 4.3 does not consider the effect of surface roughness. This is done to simplify and speed up the simulation process. Moreover, in many cases no reliable *a priori* information on surface roughness is available from the DEM of the region of interest, thus making it difficult to set the parameters of a more complex clutter simulators. For this reason, it is possible that simulations are quite conservative, showing long scattering tales also in regions where the surface can be considered smooth. As an example, Fig. 4.9 shows the surface impulse simulated with the simulator presented in

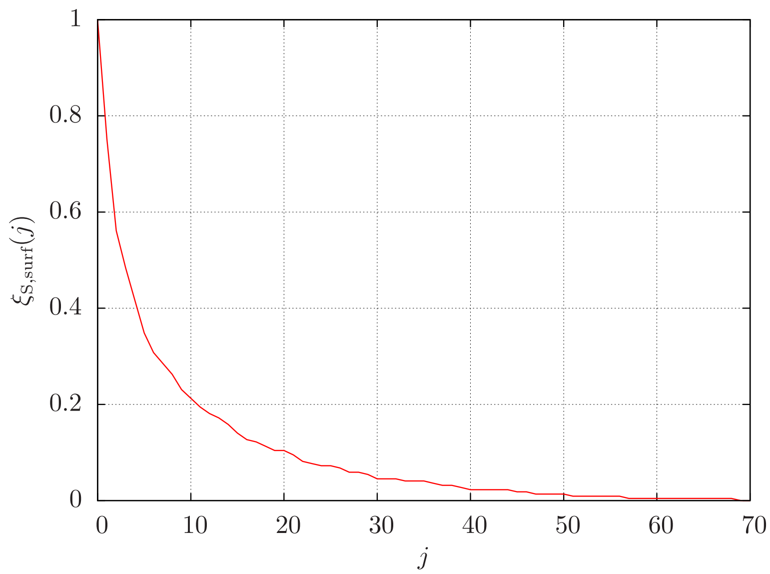

Figure 4.9: Normalized smooth-surface impulse given by the simulator described in Sec. 4.3.

Sec. 4.3 on a smooth area through the power law of (4.2) ($\varepsilon_r = 3.15$, $\kappa = 3000$). For the considered simulator, such a profile is constant for all smooth surfaces. However, as it is visible in Fig. 4.2 and Fig. 4.3, real radargrams usually show much sharper surface returns. This difference makes it difficult to combine radargrams and simulations following a pixel-wise approach, as actual subsurface features may be identified as surface clutter due to the long surface response present in the simulations.

In order to mitigate this problem and to simplify the detection of clutter returns in the shallow subsurface range, we defined a smooth-surface response removal procedure. The goal of this step is to subtract the smooth-surface response $\xi_{\mathrm{S,surf}}(j)$ from the region of the simulation X_{S} related to the shallow subsurface. The knowledge of such a response is needed. The user is thus requested to select interactively a smooth region in order to tune the algorithm. The algorithm detects the surface response and stores its shape normalized between 0 and 1 starting from the nadir return [i.e., $\xi_{\mathrm{S,surf}}(0)$ is equal to 1 and corresponds to the nadir return]. It is worth noting that, as mentioned before, if the parameters of the simulator are constant the surface response does not change. Therefore, only one profile is sufficient to allow the filtering of all the simulations obtained with the same parameter set.

The smooth-surface response is subtracted from the simulation according to the following equation:

$$\xi_{\mathrm{S},f}(i,j) = \begin{cases} \xi_{\mathrm{S}}(i,j) - \hat{\xi}_{\mathrm{S,surf}}[i, j - j_{\mathrm{nadir}}(i)] & \text{if } \xi_{\mathrm{S}}(i,j) \geq \hat{\xi}_{\mathrm{S,surf}}[i, j - j_{\mathrm{nadir}}(i)] \\ 0 & \text{if } \xi_{\mathrm{S}}(i,j) < \hat{\xi}_{\mathrm{S,surf}}[i, j - j_{\mathrm{nadir}}(i)] \end{cases}$$
$$\forall i, \forall j \geq j_{\mathrm{nadir}}(i) + j_{\mathrm{tol}}, \quad (4.17)$$

where $\xi_{\mathrm{S},f}(i,j)$ are the samples of the filtered simulation $X_{\mathrm{S},f}$, $j_{\mathrm{nadir}}(i)$ indicates the sample position of the nadir return of the frame i, and $\hat{\xi}_{\mathrm{S,surf}}(i,j) = \xi_{\mathrm{S}}(i, j_{\mathrm{nadir}})\xi_{\mathrm{S,surf}}(j)$ is the smooth-surface response modulated on the intensity of the nadir return of the frame i.

The parameter j_{tol} has the goal to preserve the first samples related to the nadir return, which is a feature that usually appears as a thick strong line in real radargrams. The choice of the value of j_{tol} depends on the range resolution and on the sampling of the considered data. According to (4.17) the simulated returns stronger than the smooth-surface response are reduced by a quantity equal to the modulated ideal smooth-surface contribution. This is in agreement with the simulation process, which generates a frame as the summation of independent contributions coming from different resolution cells.

4.5.2 Fusion of Radargram and Filtered Simulation

The goal of this step is to generate an image which highlights the surface clutter returns present in the radargram, using the simulation filtered in the previous step and the real radargram. In order to reduce the effect of the background noise on the final map, the real radargram X is filtered with a Gaussian filter, obtaining the filtered radargram X_f. The size of the filter depends on the resolution and sampling of the radargram. It has to be chosen in order to reduce noise while preserving the visible subsurface structures. For the considered application, the latter issue is more important than noise reduction. The two filtered input radargrams X_f and $X_{\text{S},f}$ are thus combined using a pixel-wise multiplication as follows:

$$\Pi = X_f \cdot X_{\text{S},f}. \tag{4.18}$$

This operation has the advantage to highlight the samples which have high intensity in both the real radargram and the clutter simulation. The strength of the returns present in the simulation which are not visible in the real radargram is thus reduced. Indeed, they are multiplied with noise, which has a lower intensity with respect to actual returns visible in the real radargram. This contributes to mitigate the residual conservativity of simulations and simplifies the threshold operation performed in the following step.

4.5.3 Thresholding

In this step the product image Π is thresholded in order to create a binary map Π_{bin} representing the samples which have high probability to be affected by surface clutter returns. This is performed according to:

$$\pi_{\text{bin}}(i,j) = \begin{cases} 0 & \text{if } \pi(i,j) < \pi_{\text{thr}} \\ 1 & \text{if } \pi(i,j) \geq \pi_{\text{thr}} \end{cases} \qquad \forall i, \forall j, \tag{4.19}$$

where $\pi(i,j)$ and $\pi_{\text{bin}}(i,j)$ are the samples of Π and Π_{bin}, respectively; and π_{thr} is a user-defined threshold. As mentioned in the previous subsection, the product operation has the advantage to highlight simulated surface clutter returns which also appear in the real radargram. As we will show in Sec. 4.6, this effect is visible in the histogram of Π, where most of the values belong to the range in proximity of zero and the useful information (actual clutter returns) corresponds to the tail of the histogram. In order to obtain the final binary map it is thus sufficient to threshold the histogram at high values. This can be done manually by the user, depending on the considered dataset and the desired level of conservativity of the final binary map. Automatic approaches to the histogram thresholding can be also applied [81].

The final binary map can be used to generate false-color compositions using on different color channels the original radargram and the binary map itself. Such an approach can be also applied using as input the other intermediate outputs of the technique. In this way, it is possible to generate images that allow a quick visual representation of actual and false subsurface features by means of a color code. As an example, false-color compositions can be obtained through RGB compositions where the green channel corresponds to the amplitude of the reference radargram and the red and blue channels show the coregistered clutter simulation. According to this color table, green pixels correspond to features which are visible only in the radargram, whereas magenta pixels are associated with returns which are visible only in the simulation. Finally, white pixels correspond to features which are visible (and matched) in both radargram and clutter simulation, and thus should not be considered in the radargram as they are artifacts due to clutter. This representation will be used in Sec. 4.6.2 as a mean to evaluate qualitatively the performance of the proposed method.

4.6 Experimental Results

In this section we show the results obtained by the proposed method on two real large datasets acquired by the SHARAD instrument at Mars. After a brief description of the considered datasets, qualitative results and quantitative measurements will be discussed.

4.6.1 Experimental Setup

The radargrams used in this chapter have been downloaded from the Geosciences Node of NASA's PDS [48]. We selected more than one hundred radargrams and extracted the amplitude information. Echoes have been aligned in time using the information contained in the RDRs [73]. As the data are highly oversampled, we applied a downsampling factor of 15 in the along-track direction. No multilooking has been performed. The selected radargrams can be divided in two datasets corresponding to two different areas: the NPLD and Elysium Planitia. As shown in Fig. 4.10, the two regions have different characteristics. On the one hand, the NPLD has a relevant topography due to the ice deposits of the North Pole. On the other hand, the Elysium Planitia is an almost flat region including some craters. The subsurface of the two regions is also characterized by different features. As it is visible in Fig. 4.2a and Fig. 4.3a, the subsurface of the NPLD shows extended layering due to ice stratigraphy, whereas in the subsurface of Elysium Planitia only a single linear reflector in the shallow subsurface is visible in many tracks. Moreover, the acquisitions taken on the NPLD usually cross the night/day limit. As it will be shown later, this implies that the ionospheric delay changes during the orbit causing distortions in the radargram.

In the experiments, for the coregistration step we used simulations obtained with (4.1). For the generation of the final binary clutter map we used simulations created using (4.2), which have been previously deformed using the same transformation derived in the coregistration step. Indeed, in our experiments we obtained the best coregistration performance using conservative simulations, while the generation of the final clutter maps benefits from the use of less conservative power laws. The input DEM was derived by MOLA data and has a resolution of 128 pixels per degree of latitude and longitude. These data are also available from the PDS. The grid used for the B-spline deformation coefficients had a fixed size of $G_J = 5$ in the range direction. The along-track size of the grid G_I has been defined adaptively depending on the number of frames of the radargrams, according to:

$$G_I = 6 + \left\lceil \frac{I - 3000}{2000} \right\rceil . \tag{4.20}$$

4.6.2 Qualitative Results

The performance of the proposed method can be evaluated qualitatively by superimposing the reference radargram to the outputs of the different steps of the technique by means of false-color compositions. Here we adopt the color code proposed in Sec. 4.5.2 and present in detail the results obtained on two radargrams, one for each considered dataset. The results for the other processed radargrams are similar.

Radargram of the NPLD

Fig. 4.11 shows the intermediate and final outputs of the proposed method for a radargram of the NPLD dataset. The considered radargram shows a deformation on the right side. Indeed, the corresponding part of the orbit was approaching the day side of Mars. As a result, the delay introduced on the signal by the ionosphere increased during the orbit. This produced a deformation of the radargram, and the surface return appears shifted towards the bottom of the radargram. This effect is not present in the simulation as it would be very difficult to model precisely the variability of the ionosphere. Therefore, it is not possible to align the radargram and the simulation without deforming the simulation accordingly. The output of the coarse registration minimizes the mean range shift between the radargram and the simulation. This is visible in Fig. 4.11a, where the simulation appears slightly mismatched on both the left and right side of the radargram. As a reference, in Fig. 4.11b we report the results obtained with a simple rigid translation transform (applied to the output of the coarse registration). The result of the iterative procedure converges to an unsatisfactory alignment between the inputs. In particular, it is possible to note that there is a good alignment in the right side of the radargram, while the left part is completely mismatched. This problem is due to the aforementioned variation of the ionospheric delay. Such a problem is solved by using the proposed approach. Fig. 4.11c shows the coregistration obtained by the proposed method, where radargram and simulation are aligned with high precision and the simulation has been deformed by the B-spline transform according to the distortion occurred on the radargram. Fig. 4.11d illustrates the same situation of Fig. 4.11c but using a less conservative simulation [obtained with the law of (4.2) using $\varepsilon = 3.15$, and $\kappa = 3000$]. In Fig. 4.11e the effect of the smooth-surface removal procedure is shown. Finally, Fig. 4.11f illustrates the RGB composition obtained using the clutter binary map generated after the thresholding of the product image (as explained in Sec. 4.5.2). From Fig. 4.11c to Fig. 4.11f it is thus possible to note the reduction of the conservativity of the clutter simulation and how this allows the generation of a final clutter map which shows only the clutter returns which are actually visible in the real radargram. A detail of Fig. 4.11 is shown in Fig. 4.12. A detailed analysis of Fig. 4.11 and Fig. 4.12 shows the potential of the technique combined with false-color compositions. Such products can represent for scientists a fast visual way to study radargrams and discriminate between actual and false subsurface features due to clutter. Indeed, the former correspond to green features, while the latter are represented in white.

Radargram of Elysium Planitia

An example of coregistration between a real radargram and the relative simulation, and of clutter detection for a radargram of the Elysium Planitia is shown in Fig. 4.13. Differently from the NPLD case, this type of radargrams are not affected by geometrical distortions. Therefore, the clutter simulator reproduces with good accuracy the geometry of surface clutter returns as it appears also in real radargrams. The result of the coarse registration is reported in Fig. 4.13a, where the residual misalignment between the radargram and the simulation is visible. The outputs of the rigid translation transform and of the proposed method are shown in Fig. 4.13b and Fig. 4.13c, respectively. Visually, the two results are comparable. This is expected, as no deformation affects the radargram. Fig. 4.13d illustrates the same situation of Fig. 4.13c but using a less conservative simulation [obtained with the law of (4.2) using $\varepsilon = 5$, and $\kappa = 3000$]. The output of the smooth-surface removal procedure is shown in Fig. 4.13e. Finally, Fig. 4.13f reports the RGB composition obtained using the clutter binary map generated after the thresholding of the product image. The final map correctly shows as clutter returns only those related to the nadir surface and to the area of a crater.

4.6.3 Quantitative Results

In order to measure quantitatively the coregistration performance of the proposed method, we selected a subset of 6 and 5 radargrams for the NPLD and Elysium Planitia datasets, respectively. For each radargram we defined manually a set of $n_{\mathrm{RP}} = 10$ reference points (RPs) on both the radargram and the corresponding clutter simulation. Finally, we measured the distance between the RPs of the radargram and the corresponding RPs on the clutter simulation coregistered by the coarse registration, by the rigid translation transform and by the proposed method. We report the measured distances in terms of mean shift error (Δd), mean shift error in the along-track and range direction (Δd_{alt} and Δd_z, respectively), and root mean square error (Δd_{RMSE}). These parameters are calculated as follows:

$$\Delta d = \frac{1}{n_{\mathrm{RP}}} \sum_{p=1}^{n_{\mathrm{RP}}} \sqrt{(i_p^{\mathrm{ref}} - i_p^m)^2 + (j_p^{\mathrm{ref}} - j_p^m)^2} \tag{4.21}$$

$$\Delta d_{alt} = \left| \frac{1}{n_{\mathrm{RP}}} \sum_{p=1}^{n_{\mathrm{RP}}} (i_p^{\mathrm{ref}} - i_p^m)^2 \right| \tag{4.22}$$

$$\Delta d_r = \left| \frac{1}{n_{\mathrm{RP}}} \sum_{p=1}^{n_{\mathrm{RP}}} (j_p^{\mathrm{ref}} - j_p^m)^2 \right| \tag{4.23}$$

$$\Delta d_{\mathrm{RMSE}} = \sqrt{\frac{1}{n_{\mathrm{RP}}} \sum_{p=1}^{n_{\mathrm{RP}}} \left[(i_p^{\mathrm{ref}} - i_p^m)^2 + (j_p^{\mathrm{ref}} - j_p^m)^2 \right]}, \tag{4.24}$$

where $(i_p^{\mathrm{ref}}, j_p^{\mathrm{ref}})$ and (i_p^m, j_p^m) indicate the coordinates of the p-th RP on the real and the simulated radargram, respectively. In the following we present the results obtained for the two considered datasets.

Radargrams of the NPLD

The quantitative results obtained for the subset of radargrams of the NPLD are reported in Tab. 4.1, Tab. 4.2, Tab. 4.3, and Tab. 4.4. All the measurements carried out confirm that the proposed method is capable to register with high precision real radargrams to the relative clutter simulations despite geometrical distortions. Both the mean shift and root mean square errors are below 2 pixels in most of the tests. Such values are smaller than the expected tolerance of the clutter simulation and thus no significant clutter artifacts are missed. The comparison between the results obtained with rigid transformations (only coarse, translation) and the results given by the proposed method shows the better performance of the latter. In particular, the rigid translation transform gives the worst results, also with respect to the coarse registration only. This is due to the presence of geometrical distortions which make the iterative process of the translation fine registration converge to a position which matches only one side of the radargram.

Radargrams of Elysium Planitia

The results related to the radargrams of Elysium Planitia are reported in Tab. 4.5, Tab. 4.6, Tab. 4.7, and Tab. 4.8. Also for this dataset the proposed technique shows a good registration performance and outperforms the other methods. However, differently from the results obtained on the NPLD dataset, the rigid translation transform gives good results. This confirms what has been observed qualitatively in Sec. 4.6.2. As the clutter simulator reproduces with good precision the geometry of the surface returns due to the absence of time-variant delays of the ionosphere, the registration process mainly corrects only for along-track and range misalignments.

Table 4.1: Mean shift error Δd in pixels for the NPLD dataset.

Radargram number	Coarse	Rigid translation	Proposed method
0794703	6.09	14.13	1.81
0879602	8.65	14.47	1.37
0921802	9.83	17.44	1.59
1041902	11.46	19.49	0.83
1592001	8.65	17.38	2.16
1743601	7.22	7.15	1.72

Table 4.2: Mean shift error the along-track direction Δd_{alt} in pixels for the NPLD dataset.

Radargram number	Coarse	Rigid translation	Proposed method
0794703	1.68	8.58	0.63
0879602	2.65	8.25	0.65
0921802	2.67	9.60	0.48
1041902	7.05	14.55	0.27
1592001	5.35	8.15	0.27
1743601	5.87	2.87	0.53

Table 4.3: Mean shift error in the range direction Δd_z in pixels for the NPLD dataset.

Radargram number	Coarse	Rigid translation	Proposed method
0794703	2.36	10.55	0.48
0879602	2.88	10.42	0.30
0921802	4.05	11.87	0.68
1041902	4.94	11.30	0.12
1592001	0.90	14.37	0.77
1743601	1.58	6.08	0.18

Table 4.4: RMSE Δd_{RMSE} in pixels for the NPLD dataset.

Radargram number	Coarse	Rigid translation	Proposed method
0794703	7.11	15.08	1.88
0897602	9.27	15.76	1.48
0921802	11.43	18.38	1.67
1041902	11.99	20.21	1.06
1592001	9.70	18.36	2.20
1743601	7.36	7.86	1.89

Table 4.5: Mean shift error Δd in pixels for the Elysium Planitia dataset.

Radargram number	Coarse	Rigid translation	Proposed method
0365601	4.38	2.45	1.43
0394601	12.18	2.98	1.39
0486901	4.81	1.94	1.89
0566001	6.65	1.87	1.53
0914802	6.50	2.21	1.71

Table 4.6: Mean shift error in the along-track direction Δd_{alt} in pixels for the Elysium Planitia dataset.

Radargram number	Coarse	Rigid translation	Proposed method
0365601	0.78	1.65	0.48
0394601	7.53	1.03	0.55
0486901	0.78	0.60	0.30
0566001	2.53	0.68	0.43
0914802	4.73	0.43	0.18

Table 4.7: Mean shift error in the range direction Δd_z in pixels for the Elysium Planitia dataset.

Radargram number	Coarse	Rigid translation	Proposed method
0365601	4.14	1.00	0.58
0394601	4.89	0.80	0.31
0486901	4.53	0.05	0.33
0566001	6.13	0.28	0.18
0914802	3.93	0.70	0.10

Table 4.8: RMSE Δd_{RMSE} in pixels for the Elysium Planitia dataset.

Radargram number	Coarse	Rigid translation	Proposed method
0365601	4.54	2.63	1.70
0394601	19.70	3.30	1.47
0486901	5.17	2.21	2.13
0566001	6.92	2.13	1.78
0914802	6.82	2.35	1.97

4.7 Conclusion

In this chapter we presented a novel technique for the automatic detection of surface clutter returns from RS data. The technique is based on the automatic coregistration between real radargrams and surface clutter simulations. The main output of the proposed method is a binary map representing the areas of the radargram which have high probability to be affected by clutter returns. In addition, the intermediate outputs of the method (e.g., coregistered clutter simulations) can be also used to support manual investigations. The chapter also presented a fast clutter simulator suited to both user-oriented real-time analyses and batch processing.

The qualitative and quantitative experimental results obtained on two large datasets acquired by the SHARAD instrument at Mars confirm the effectiveness of the proposed method. In particular, the technique is capable to align with good precision clutter simulations to radargrams. This was observed also when radargrams are affected by geometrical distortions due to variations of the ionospheric delay during the same acquisition.

The proposed method represents a valuable contribution to the analysis of planetary RS data. Indeed, the detection of surface clutter through the comparison with clutter simulations is nowadays performed manually by scientists. This process is time-consuming and subjective. In this context, if suitable DEMs of the area of interest are available, the proposed technique can be included in the basic processing chain of RS data in order to generate matched simulations and clutter maps which can be distributed along with radargrams as higher level products. Such products would greatly help the community and increase the scientific return of the analysis of the data.

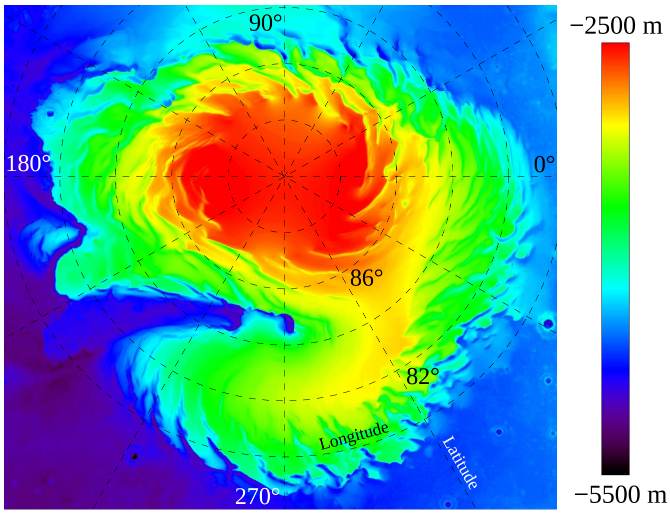

(a)

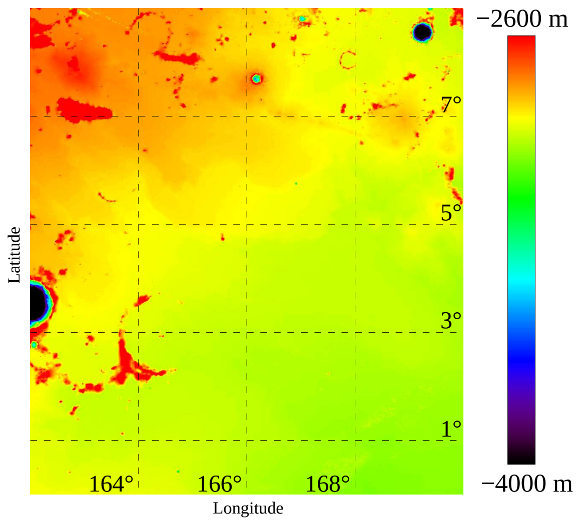

(b)

Figure 4.10: Digital elevation models of (a) the NPLD, and (b) Elysium Planitia on Mars derived from MOLA data.

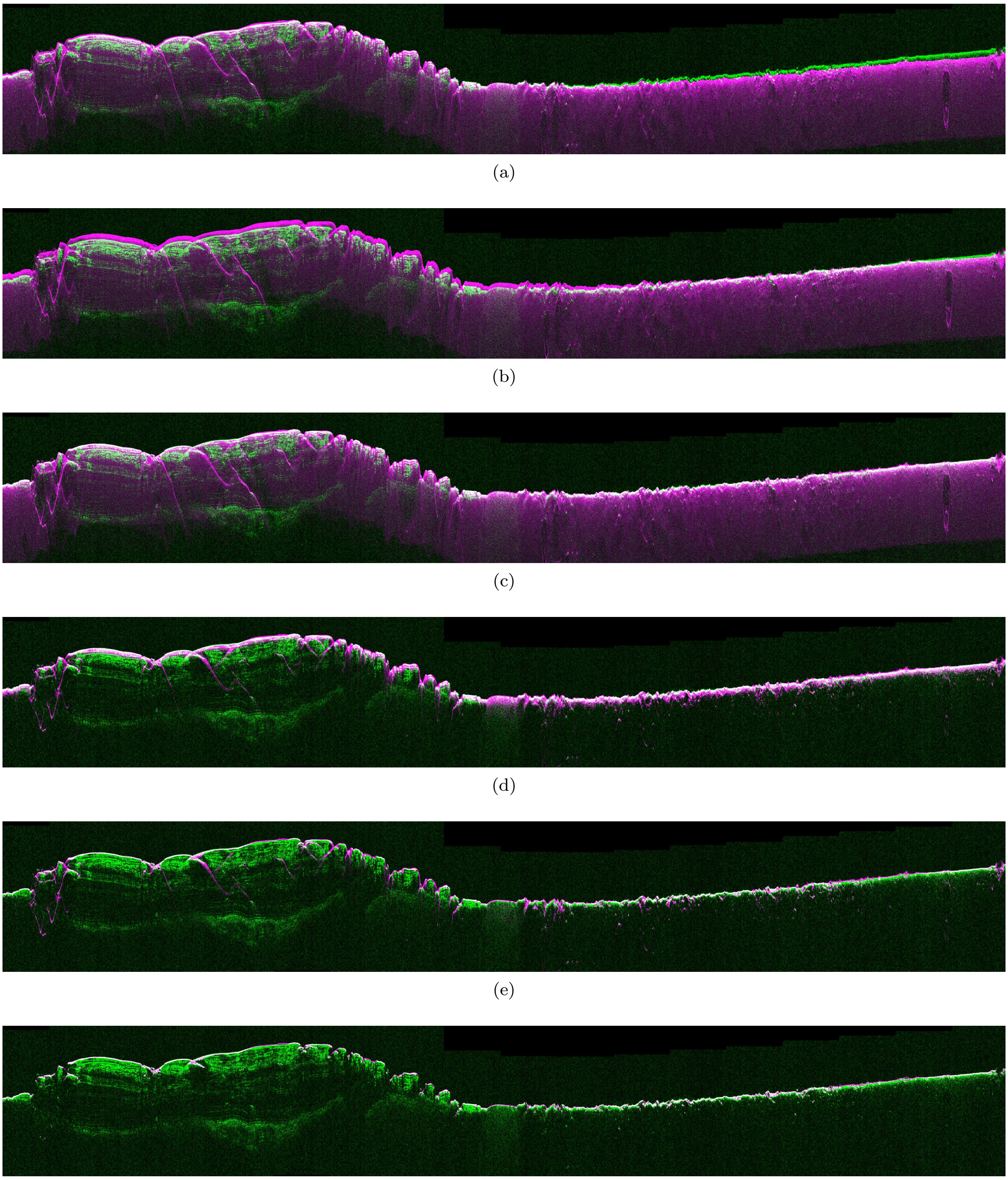

(a)

(b)

(c)

(d)

(e)

(f)

Figure 4.11: RGB compositions obtained according to the method proposed in Sec. 4.5.2 by the combination of the SHARAD radargram 0921802 acquired on the North Pole of Mars and the related clutter simulations (see Fig. 4.2) after the different steps of the proposed method. (a) Coarse registration; (b) rigid translation transform; (c) proposed method; (d) final transformation applied to a less conservative simulation obtained using (4.2) and $\varepsilon_r = 3.15$ and $\kappa = 3000$; (e) result of the smooth-surface impulse removal; (f) final binary clutter map.

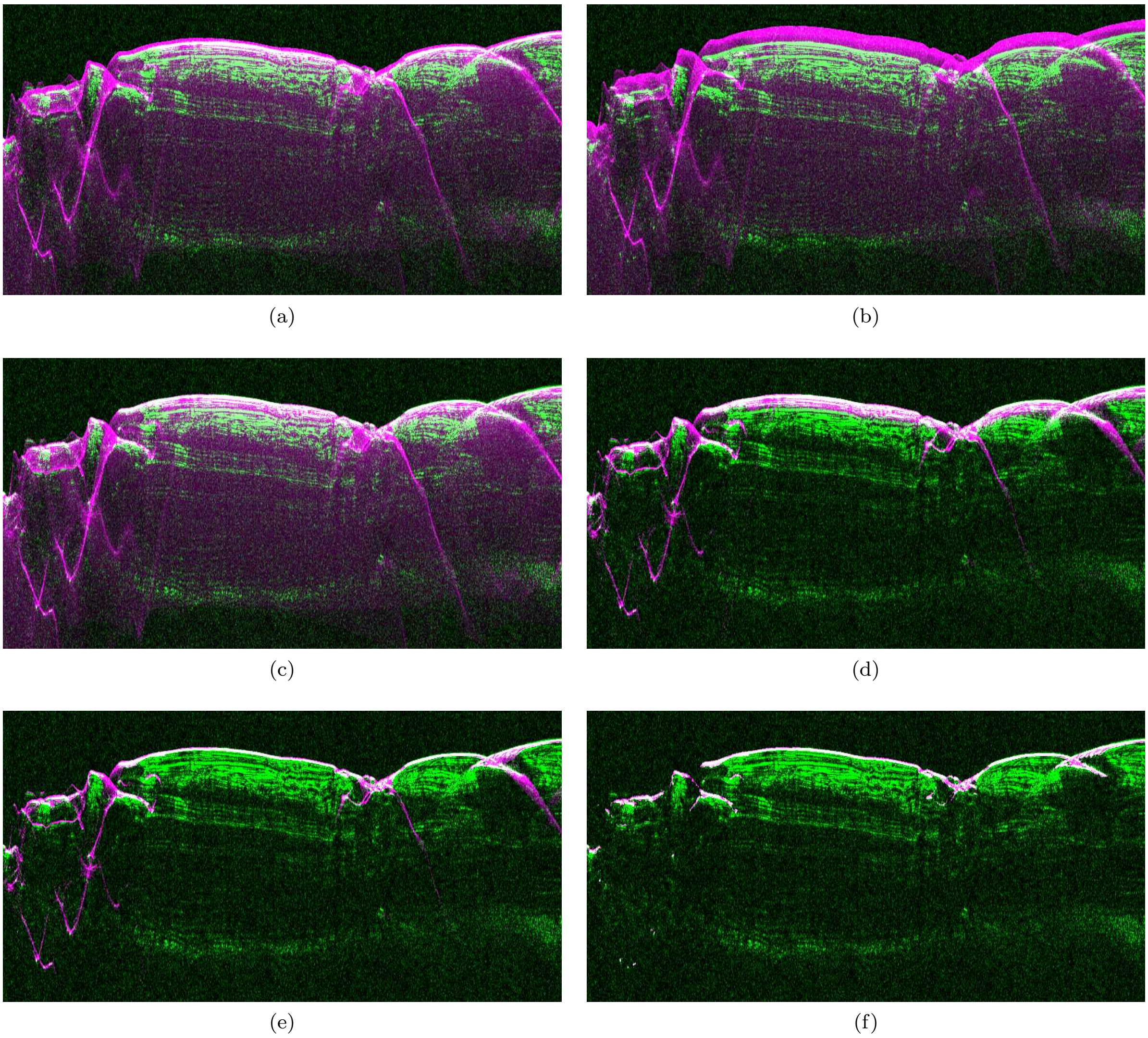

(a) (b) (c) (d) (e) (f)

Figure 4.12: Detail of Fig. 4.11. (a) Coarse registration; (b) rigid translation transform; (c) proposed method; (d) final transformation applied to a less conservative simulation obtained using (4.2) and $\varepsilon_r = 3.15$ and $\kappa = 3000$; (e) result of the smooth-surface impulse removal; (f) final binary clutter map.

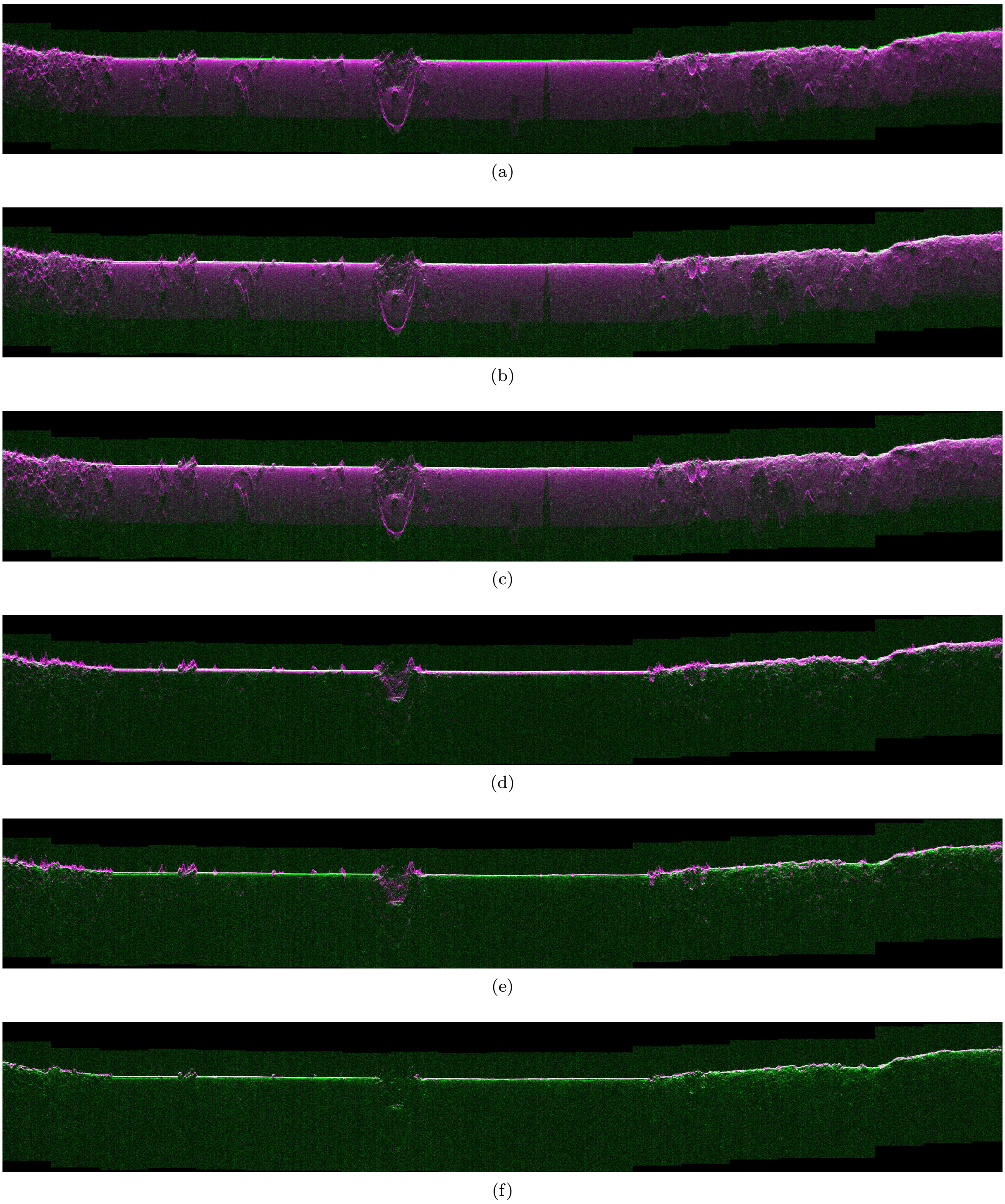

Figure 4.13: RGB compositions obtained according to the method proposed in Sec. 4.5.2 by the combination of the SHARAD radargram 0365601 acquired on the region of Elysium Planitia of Mars and the related clutter simulations (see Fig. 4.3) after the different steps of the proposed method. (a) Coarse registration; (b) rigid translation transform; (c) proposed method; (d) final transformation applied to a less conservative simulation obtained using the law of (4.2) and $\varepsilon_r = 5$ and $\kappa = 3000$; (e) result of the smooth-surface impulse removal; (f) final binary clutter map.

Part II

Analysis of VHR SAR Images for the Automatic Building Extraction

Chapter 5

A Study on the Relationship between Double Bounce and the Orientation of Buildings in VHR SAR Images

In this chapter[1] *we study empirically the relation between the double-bounce effect of buildings in VHR SAR images and the orientation angle for two different ground materials (i.e., asphalt and grass), by analyzing two different TerraSAR-X VHR spaceborne SAR images. Furthermore, we compare our empirical results with simulations obtained using theoretical electromagnetic models. In order to deal with slightly rough surfaces, we also present a novel model for double-bounce scattering based on the SPM. We show that the double-bounce effect results in different power signatures depending on the type of the building and the surrounding ground properties. Finally, we discuss the reliability of theoretical models for predicting the double-bounce power for the analyzed datasets. The models can predict the general behavior of the double bounce, but lack in calculating the accurate double-bounce RCS reliably.*

5.1 Introduction

Among the different scattering contributions present in meter-resolution VHR SAR (e.g., COSMO-SkyMed and TerraSAR-X) data from urban areas, the double-bounce effect of buildings (which is caused by the corner reflector assembled by the front wall of the building and its surrounding ground area) is an important scattering characteristic [36,37]. It

[1] This chapter appears in:

[38] D. Brunner, L. Bruzzone, A. Ferro, J. Fortuny, and G. Lemoine, "Analysis of the double bounce scattering mechanism of buildings in VHR SAR data," in *Proc. SPIE Conf. on Image and Signal Processing for Remote Sensing XIV*, vol. 7109, 2008, pp. 71 090Q–71 090Q–12.

[107] D. Brunner, L. Bruzzone, A. Ferro, and G. Lemoine, "Analysis of the reliability of the double bounce scattering mechanism for detecting buildings in VHR SAR images," in *Proc. IEEE Radar Conf*, 2009.

[108] A. Ferro, D. Brunner, L. Bruzzone, and G. Lemoine, "On the relationship between double bounce and the orientation of buildings in VHR SAR images," *IEEE Geosci. Remote Sens. Lett.*, vol. 8, no. 4, pp. 612–616, 2011.

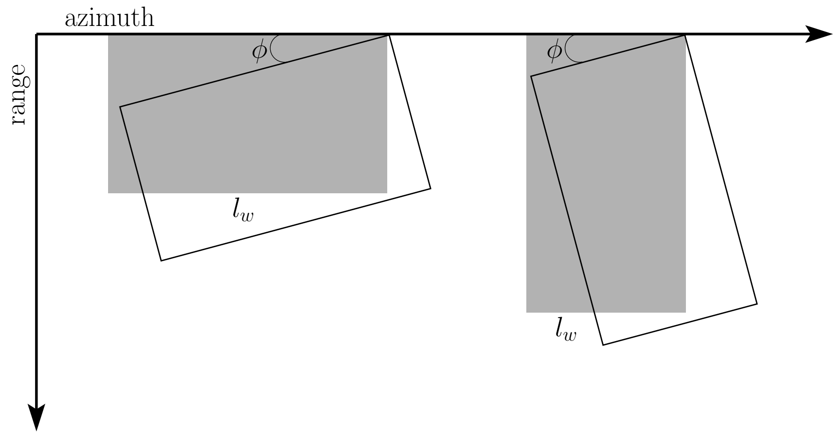

Figure 5.1: Definition of the orientation angle of a building.

indicates the presence of a building because it appears as a linear feature in correspondence with its front wall. The double bounce has been exploited for the development of automatic methods for the detection and reconstruction of buildings from multi-aspect [23] and interferometric SAR (InSAR) data [24]. However, the relation between the double-bounce effect and the SAR illumination conditions, and thus its reliability as a feature for building detection purposes, has not yet been investigated to a sufficient extent in real VHR SAR images.

The effect of the orientation angle ϕ of a building on the power signature of the double bounce is important. The orientation angle is defined as the angle between the front wall of the building and the azimuth direction (see Fig. 5.1). As an example, we show in Fig. 5.2 a meter-resolution TerraSAR-X image and the corresponding aerial photo of a flat-roof building that has two main axis, i.e., it has two walls which are oriented towards the sensor but with different orientation angles. The smaller axis of the building (A) shows a stronger double bounce than the larger axis (B). Since we are investigating the same building, which has similar structures for the two front walls (as shown in Fig. 5.2b), the deviations in the strength of the double bounce cannot be attributed to differences in either the material properties or the facade structure. Nevertheless, observing the orientation angles with which the two walls were imaged, we find that they are quite different ($\phi = 2.4°$ for A and $\phi = 29.2°$ for B). Another factor that affects the double-bounce scattering is the ground material, which properties are difficult to retrieve without any *a priori* information about the scene.

As buildings are imaged with different orientation angles in different surroundings, the relation between the orientation angle, the ground material and the double-bounce strength implies the limits of detection techniques which are based on the double-bounce effect. In this context, the understanding of this behavior both on theoretical models and on real VHR SAR images can be exploited for developing novel optimized detection techniques based on single SAR images (see Chapter 6), and refined tools for the interpretation of the scattering in urban areas [109]. This is of special interest for operational monitoring tasks with stringent limitations on the timely availability of the data (e.g., for emergency response), where the acquisition of a pair of images for building detection

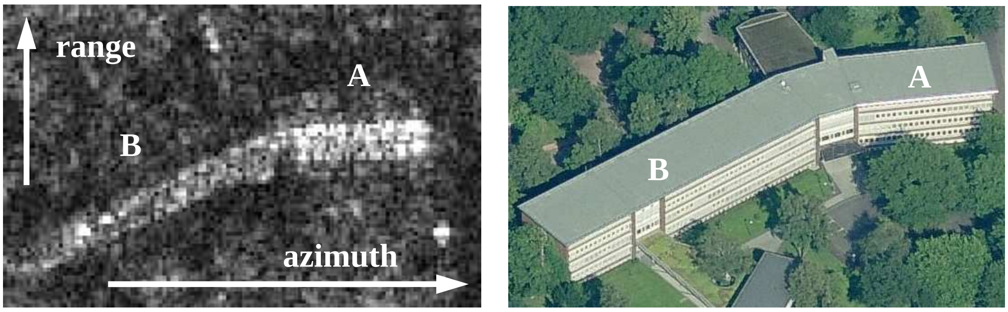

(a) (b)

Figure 5.2: (a) Building with two axes in VHR TerraSAR-X data. Illumination from bottom to top (© Infoterra). (b) Corresponding optical image (© Microsoft).

cannot be considered.

In this chapter we extend and refine the findings from [38], presenting a detailed study of the relation between the double-bounce effect and the orientation angle. First, we investigate empirically a set of industrial and residential buildings with two different ground materials (grass and asphalt) in ascending and descending spaceborne meter-resolution TerraSAR-X images. Then we compare these findings with state of the art theoretical models in order to assess to which extent they can predict the double-bounce behavior. This is important to consider if these models are employed for information extraction purposes (e.g., building detection and reconstruction). In order to deal with slightly rough surfaces such as asphalt, we developed a novel model for double-bounce scattering based on SPM.

The remainder of the chapter is organized as follows. In Sec. 5.2 the main scattering effects related to buildings and the literature regarding the double-bounce effect are reviewed. In Sec. 5.3 we report the double-bounce RCS measurements performed on real data, while in Sec. 5.4 we compare such results with theoretical models. Finally, Sec. 5.5 we draw the conclusions of this study.

5.2 Background

In this section we provide background information related to the scattering of buildings in VHR SAR images and on the modeling of the double-bounce effect. In the first subsection we illustrate the typical scattering behavior of flat- and gable-roof buildings. Then, we review the theoretical models developed in the literature for the modeling of the double-bounce scattering mechanism. Finally, we also report the main empirical works present in the state of the art regarding the analysis of the double-bounce effect in real data.

5.2.1 Modeling of Building Radar Footprints in Single Detected VHR SAR Images

The side-looking and ranging properties of SAR sensors cause peculiar geometrical distortions in VHR SAR imagery. A review of the main general effects visible in SAR images

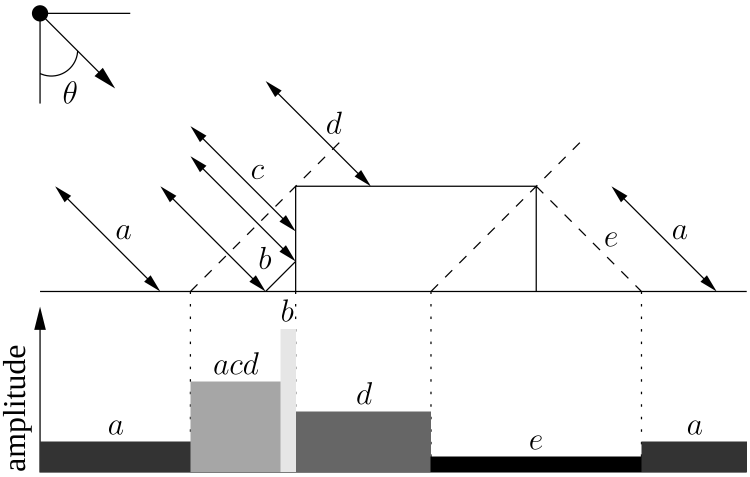

Figure 5.3: Scattering model for a flat roof building with viewing direction from left. The different gray areas at the bottom of the figure symbolize the amplitudes.

has been provided in Chapter 1. In this context, the key characteristics of buildings in SAR are the layover, double-bounce, and shadowing effects. To illustrate this, Fig. 5.3 shows a schematic view of the scattering profile of a simplified flat-roof building model. In this figure, the building in the middle, which is modeled as a rectangular box, is imaged by a sensor with incidence angle θ. The annotations a refers to backscattering from the ground surface surrounding (in this 2D figure before/behind) the building. acd denotes the layover area where scattering from the ground, from the vertical building front wall and from parts of the flat roof are superimposed since these parts have the same distance to the sensor. The vertical front wall and the surface area in front of the building compose a corner reflector resulting in the bright double-bounce effect b. The scattering area that is only characterized by scattering from the roof is denoted by d. The elevated building occludes parts of the surface behind the building from the radar beam, resulting in the shadow area e. This backscattering profile is flexible with respect to a number of parameters [110]. For instance, for very high buildings there is typically no area d as the part of the roof is entirely included in the layover area. An example of radar footprint of an industrial flat-roof building is shown in Fig. 5.4. The main scattering mechanisms are visible (i.e., layover, double bounce, scattering from roof and shadow). However, additional features appear (e.g., bright spots on the roof due to metallic structures). The figure also shows examples of interference due to other targets, in this case tall trees. In fact, both the layover and the shadow areas of the footprint are partially masked by the trees that surround the building.

For gable-roof buildings the theoretic scattering signature is slightly different [111,112]. As shown in Fig. 5.5, the signature has a second bright scattering feature acd at the sensor-close side resulting from direct backscattering from the roof. The extent and the strength of this feature depends on the relationship between θ and the roof inclination angle θ_{roof}. For $\theta_{\mathrm{roof}} = \theta$ the strength of this feature is maximum, whereas its extent is smallest. Moreover, we found that in actual 1 m resolution TerraSAR-X and COSMO-SkyMed data this second bright scattering area is also detectable for buildings with a

(a) (b)

Figure 5.4: Example of a flat-roof building. (a) Building in 1 m resolution TerraSAR-X data with viewing direction from left (© Infoterra). The double-bounce line is highlighted with a red arrow. (b) The same building in an optical image (© Microsoft).

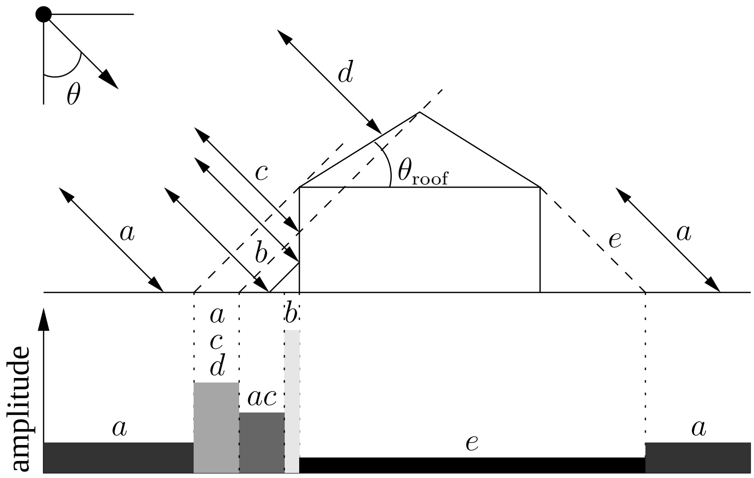

Figure 5.5: Scattering model for a gable-roof building with viewing direction from left. Here, the roof inclination angle θ_{roof} is smaller than θ. The different gray areas at the bottom of the figure symbolize the amplitudes.

high orientation angle. This is illustrated in Fig. 5.6 and Fig. 5.7, where we show actual scattering signatures from gable-roof buildings with small and large orientation angles, respectively.

5.2.2 Theoretical Models

In order to model the double-bounce effect of a building, the theory of dihedral corner reflectors has been extended to simplified building models, which are generally constituted by rectangular parallelepipeds with smooth walls surrounded by a homogeneous ground surface [36,37]. These models are considered isolated in the electromagnetic sense, i.e., no interactions with other structures in the scene are taken into account. In particular, [36] presents a fully analytical electromagnetic model for urban environments that also includes a study on the double-bounce contribution from buildings based on Geometric Optics (GO) and Physical Optics (PO) [99], according to the surface roughness.

(a) (b)

Figure 5.6: Examples of gable-roof buildings with small orientation angles. (a) Buildings in 1 m resolution TerraSAR-X data with viewing direction from left (© Infoterra). The double-bounce and roof scattering lines are highlighted with red and yellow arrows, respectively. (b) The same buildings from (a) in an optical image (© Microsoft).

(a) (b)

Figure 5.7: Examples of gable-roof buildings with large orientation angles. (a) Buildings in 1 m resolution TerraSAR-X data with viewing direction from left (© Infoterra). The scattering lines due to the roofs are highlighted with yellow arrows. (b) The same buildings from (a) in an optical image (© Microsoft).

However, the choice of the adequate roughness parameters, i.e., the RMS height h_{RMS} and the correlation length l_c, and dielectric parameters of a surface is non-trivial. RCS measurements made directly on SAR images can differ considerably with theoretical predictions using literature material parameters, e.g., due to the effect of the moisture content or the temperature of the material. Furthermore, surfaces in urban areas are not homogeneous, even at the scale of a single meter-resolution cell. For instance, a paved street in a city may have small structures elements (e.g., manhole covers), causing local variations in the actual surface roughness. Moreover, they are also made of metal, which is a different material with respect to the surrounding asphalt. Hence, using only the dielectric constant and surface roughness parameters of asphalt to calculate the RCS of a street in urban areas is a significant simplification. In addition, in dense urban environments scattering effects coming from adjacent objects can interfere and therefore invalidate the assumption of isolated buildings. As a result, the theoretical models currently reported in literature can only be considered as a tool for making preliminary predictions of the scattering behavior of buildings in urban environments imposing the need for empirical studies.

5.2.3 Empirical Studies

The effect of the orientation angle on the scattering from urban areas (the so-called cardinal effect) has already been reported for medium resolution SAR data [113]. Furthermore, [114] demonstrated the influence of the polarization and the incidence angle on the double-bounce effect, which showed that the corner reflector has generally a higher return in HH polarization. Instead, VV polarization is more sensitive to variations in the incidence angle. This analysis was conducted only on buildings parallel or perpendicular to the azimuth direction. In [37] the authors discussed the influence of both incidence and orientation angles on the scattering from urban environments using actual SAR airborne data. They observed that buildings which are parallel to the azimuth direction have a stronger double-bounce contribution than buildings facing away from the radar. Their study was conducted on a small set of residential and commercial buildings.

Some preliminary experimental studies on the double-bounce effect have been conducted acquiring SAR measurements on scaled building models under controlled conditions. In [115], the results of an experiment developed by means of an outdoor Inverse SAR (ISAR) facility on corner reflector models made from different real world materials are presented. In [38], we presented a detailed experimental study using polarimetric laboratory ISAR measurements, which were taken on a scaled building model. In addition we discussed preliminary results for a meter-resolution airborne image which was a simulation of a spaceborne acquisition. Both studies confirmed that the double-bounce effect gives a strong power signature to buildings with walls almost parallel to the SAR azimuth direction, but decays rapidly in a narrow range of orientation angles.

5.3 Analysis of Real VHR Spaceborne SAR Data

The data that we analyze in this chapter is a pair of ascending and descending high-resolution spotlight TerraSAR-X images acquired in HH polarization in December 2007 and January 2008 from the city of Dorsten, Germany. Their geometric resolution is 1.1 m $\times$ 1.2 m (azimuth $\times$ slant range). The two images were acquired with similar incidence angles (50.7° for the ascending and 53.8° for the descending image).

This study aims at analyzing the actual double-bounce effect of buildings which are minimally affected by the scattering from other structures present on walls (e.g., metal pipes, porch roofs). For complex building facades the backscattering depends rather on the elements on the facades than on the double-bounce effect itself. In fact, such elements may interfere with the double wall-ground and ground-wall reflections. Therefore, we selected a set of candidate buildings which presented simple walls (i.e., no windows and balconies) with asphalt or grass ground surfaces in the surroundings using the bird's eye view data from Bing™ maps [116]. We estimated their planar and height dimensions from the optical images in order to predict their scattering behavior. These estimates were then confirmed by measuring the return of the buildings on the SAR image. The expected scattering behavior of a building permitted to locate the position of the double-bounce stripe, the layover and shadow areas, and the eventual single-bounce stripe due to an inclined building roof.

The data set included 55 buildings suitable for the extraction of the mean RCS value of the expected double-bounce area: 17 residential buildings surrounded by asphalt terrain (*residential/asphalt*), 19 industrial buildings surrounded by asphalt terrain (*industrial/asphalt*) and 19 residential buildings surrounded by grass covered soil (*residential/grass*). We considered buildings with different orientation angles in the range between 0° and 42°. For larger orientation angles the double-bounce areas of suitable buildings were not well distinguishable from the surroundings; thus we did not consider these buildings in the study. In single polarized images, single-bounce backscattering from the building roofs complicates the extraction of the double-bounce stripes, as in many cases this contribution is superimposed with the double-bounce stripe itself. In our observations this occurs mainly when the roof is not facing the SAR sensor and appears to be related to the roof tile coverage. Buildings showing a single-bounce stripe overlapping with the expected double-bounce region have not been considered in our analysis. The RCS of the double bounce is dependent on the area of the building wall, and thus also on its height. The higher the building, the stronger the double bounce. This needs to be taken into account when the RCSs of different buildings are compared to each other. As the empirical measurements refer to buildings with different heights, we considered as reference a building height of 6.5 m, which is the mean height of the buildings in the data set, and normalized the RCS values accordingly. The normalization has been performed taking into account the quadratic and linear dependence of the double-bounce RCS on the building height for coherent and incoherent scattering, respectively [36, 37]. As the azimuth resolution is smaller than the building length, we did not consider the length in the normalization step [36]. The difference of the incidence angles between the two scenes is about 3°. Based on theoretical models, we confirmed that this variation in incidence angle only implies a marginal change of the double-bounce RCS, which can be assumed to be smaller than the error introduced by the analysis process. Hence, we considered the buildings in the two scenes as they were in a single scene.

The results of the analysis are shown in Fig. 5.8 (crossed points), which show the relation between the RCS of the corner reflector and the orientation angle per building/terrain category. The graphs show that buildings with similar orientation angles can have double-bounce stripes that differ by several dBs. This behavior reflects the fact that in real SAR data many variables (which are mainly unknown) affect the scattering behavior of surfaces, as mentioned in Sec. 5.2. Therefore, our goal was to analyze the overall trend of the double-bounce effect for each class of buildings, rather than the double-bounce stripe of individual buildings.

Fig. 5.8a shows the behaviour of the RCS versus the orientation angle for the *residential/asphalt* case. The graph shows that, on the one hand, the double bounce is significant in the first 10° orientation angle range, with values in the order of 30 dBs, and then decreases considerably. The strong part of the double bounce is caused by a strong coherent scattering. On the other hand, for larger orientation angles, the relevance of incoherent scattering due to the surface roughness increases and the double-bounce effect is less pronounced. The results of the analysis of the *industrial/asphalt* class are reported in Fig. 5.8b. The trend is similar to that for the *residential/asphalt* class, but with generally higher power values. The difference is in the order of 10 dBs. Moreover, the double bounces of the buildings in the *industrial/asphalt* class present a sparser distribution.

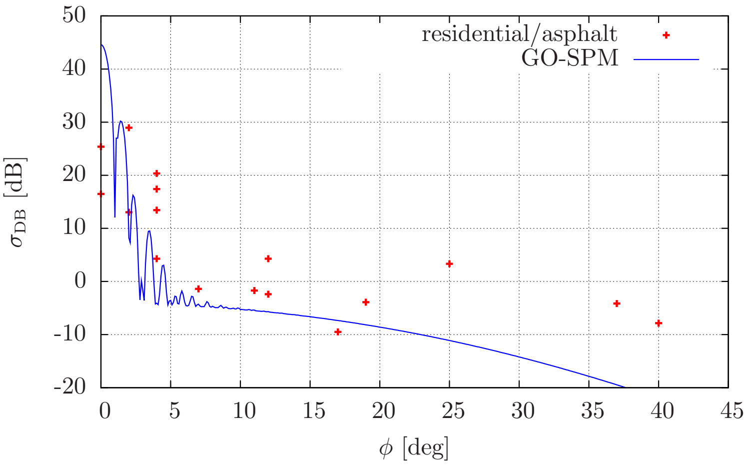

(a)

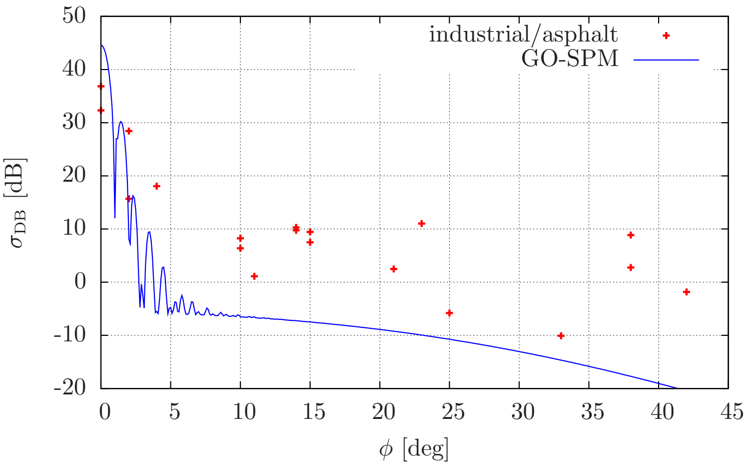

(b)

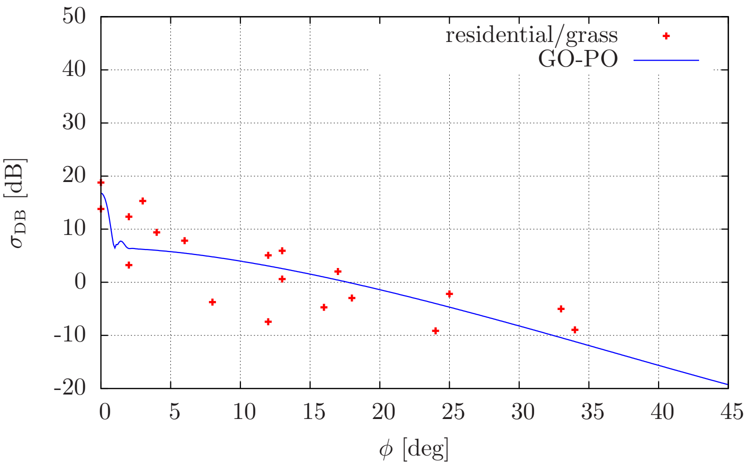

(c)

Figure 5.8: Relation between double-bounce RCS and orientation angle: collected data (crosses), theoretical model (solid line). (a) *residential/asphalt* category. (b) *industrial/asphalt* category. (c) *residential/grass* category.

These two effects can be explained by the variable and inhomogeneous materials used for industrial buildings, and by the presence of more metal parts that are not as common as for residential buildings. Finally, Fig. 5.8c depicts the distribution of the double-bounce RCS for the *residential/grass* class. Due to the impact of the roughness of the grass surrounding the buildings (which is expected to be higher than for asphalt grounds) the contrast between the double-bounce peak at near 0° orientation angles and the remaining part of the graph is lower than for buildings which are surrounded by asphalt. The peak power is about 10 dBs lower compared to the *residential/asphalt* class, while the RCS decreases with increasing orientation angles in a smoother way, suggesting a pronounced relevance of incoherent scattering.

5.4 Comparison between Empirical Results and Theoretical Models

In this section we compare the empirical measurements retrieved in Sec. 5.3 with theoretical models. First, we illustrate the used theoretical models and describe the developed GO-SPM formulation. Then, after a discussion on the proper selection of the model parameters, we present and discuss the obtained results.

5.4.1 Theoretical Models

In order to assess whether the trends shown in Sec. 5.3 are in agreement with theoretical models, we compared the actual data to simulated data obtained with analytic models. The models approximate the building wall as a smooth surface in order to apply standard GO rules for the estimation of the scattering from the wall. This allows the calculation of the area which is illuminated at the ground in closed form by considering a plane wave reflected by the wall. Hence, no roughness parameters need to be defined for the wall. The area surrounding the building wall is considered as a rough surface. On the one hand, the roughness parameters of grass allows for the considered frequency the estimation of the double-bounce scattering power for the *residential/grass* class using the GO-PO approximation proposed in [36]. On the other hand, the analytic models currently reported in the literature are not valid for slightly rough surfaces like asphalt. Therefore, we derived a novel model for double-bounce scattering based on GO-SPM. The single backscattering contribution of the ground and its eventual variations are not taken into account as they are expected to be negligible compared with the double-bounce power for the considered incidence angle [36].

For the double bounce modeling, both formulations are composed of two contributions: a coherent ($\sigma_{\mathrm{DB},c}$) and an incoherent term ($\sigma_{\mathrm{DB},i}$). The double-bounce RCS σ_{DB} is obtained by the sum of these two contributions. For the proposed GO-SPM model, the coherent term corresponds to the scattering from a smooth dihedral corner reflector on an infinite surface:

$$\sigma_{\mathrm{DB},c} = \left(\frac{k^2}{\pi}\right) A_w^2 |\rho_{hh}|^2 \mathrm{sinc}^2[kl_w \sin(\theta)\sin(\phi)] \mathrm{sinc}^2 \left[kh_w \frac{\sin^2(\theta)\sin^2(\phi)}{\cos(\theta)}\right] \tag{5.1}$$

where $k = 2\pi/\lambda$; $\mathrm{sinc}(x) = \sin(x)/x$; h_w and l_w are the height and length of the wall, respectively; $A_w = hl\tan(\theta)\cos(\phi)$. The term ρ_{hh} is defined by:

$$\rho_{hh} = 2\rho_\perp(\theta)\cos(\theta)\cos(2\phi)A_h + [\sin^2(\theta)\sin(2\phi) + \rho_\parallel(\theta)\left(1+\cos^2(\theta)\right)\sin(2\phi)]B_h \quad (5.2)$$

$$A_h = -\cos^2(\theta)\cos^2(\phi)\rho_{\perp w}(\theta_w) + \sin^2(\phi)\rho_{\parallel w}(\theta_w) \quad (5.3)$$

$$B_h = \cos(\theta)\cos(\phi)\sin(\phi)\left[\rho_{\perp w}(\theta_w) + \rho_{\parallel w}(\theta_w)\right], \quad (5.4)$$

and $\rho_\perp(\theta)$, $\rho_\parallel(\theta)$, $\rho_{\perp w}(\theta_w)$, $\rho_{\parallel w}(\theta_w)$ depict the Fresnel coefficients for the ground and the wall, respectively. $\theta_w = \cos^{-1}[\sin(\theta)\cos(\phi)]$ is the local incidence angle on the building wall. The incoherent scattering is given by:

$$\sigma_{\mathrm{DB},i} = 32A_w|\varpi_{hh} + \varpi_{hv}|^2\cos^4(\theta)k^4h^2_{\mathrm{RMS}}W\left\{k\sin(\theta)\left[1-\cos(2\phi)\right], -k\sin(\theta)\sin(2\phi), l_c\right\} \quad (5.5)$$

where $W(k_x, k_y, l_c)$ represents the roughness spectrum using a Gaussian correlation function and is given by:

$$W(k_x, k_y, l_c) = \frac{l_c^2}{2}\exp\left[-\frac{l_c^2}{4}(k_x^2 + k_y^2)\right]. \quad (5.6)$$

The factors ϖ_{hh} and ϖ_{hv} are given by:

$$\varpi_{hh} = -A_h\frac{(\varepsilon_{r,g}-1)\cos(2\phi)}{(\cos(\theta)+\varpi_C)^2} \quad (5.7)$$

$$\varpi_{hv} = B_h\frac{(\varepsilon_{r,g}-1)\sin(2\phi)\varpi_C}{(\cos(\theta)+\varpi_C)(\varepsilon_{r,g}\cos(\theta)+\varpi_C)}, \quad (5.8)$$

where $\varpi_C = \sqrt{\varepsilon_{r,g} - \sin^2(\theta)}$ and $\varepsilon_{r,g}$ is the relative dielectric constant of the ground surface.

Both the GO-PO and GO-SPM models do not consider the effects of the azimuth aperture of the SAR sensor in order to achieve a simple analytical solution [117]. These contributions are expected to be negligible for the scope of this study [36].

5.4.2 Dielectric and Roughness Parameters

To compare the results from the empirical analysis with theoretical models, we first collected the information about the roughness parameters and the dielectric characteristics of the materials (asphalt, grass, and concrete) from the literature (see Tab. 5.1) [118–122]. Starting from these values we calculated the theoretical curves which give the minimum RMSE with respect to the data from the real SAR images for each of the three categories. The fitting has been performed in the validity ranges of the considered theoretical models [99]. The calculated best-fit parameters are reported in Tab. 5.2.

5.4.3 Analysis of Results

The solid lines in the graphs in Fig. 5.8 show the theoretical RCSs as a function of the orientation angle in comparison to the measured data from the actual SAR scenes. In Tab. 5.2 the mean absolute error (MAE) between empirical and theoretical dB RCSs is

Table 5.1: Roughness parameter and dielectric constant ranges used for the fitting of the theoretical models to the measured data ($\varepsilon_r = \varepsilon_r' - j\varepsilon_r''$).

Materials	ε_r'	ε_r''	h_{RMS}	l_c
Asphalt	3–8	0–0.5	0.3–1.4 mm	0.4–2 cm
Grass	3–20	0–7	5–20 mm	0.5–10 cm
Concrete	3–8	0–0.5	-	-

reported. Considering the graph for the *residential/asphalt* category (Fig. 5.8a) the range in which the coherent term prevails matches correctly with the points characterized by high RCS values for small orientation angles. However, for large orientation angles the theoretical model underestimates the double-bounce power. Considering the orientation angles between 11° and 45°, the empirical mean dB power is −2.74 dB and the MAE is 8.40 dB. The prediction error of the theoretical model is thus considerable. Note that the best-fit curve is obtained using the upper limits of the parameter ranges for the dielectric constants and for h_{RMS} (see Tab. 5.2). Using higher values for these parameters results in a better fit. However, this would imply that the materials are not realistic. Moreover, higher h_{RMS} values do not fulfill the SPM validity conditions [99]. The *industrial/asphalt* category (Fig. 5.8b) shows characteristics similar to the *residential/asphalt* case. The prediction error for large orientation angles is higher than for small orientation angles. In fact, the MAE for orientation angles greater than 10° is equal to 15.17 dB while the empirical mean dB power in the same range is 3.80 dB. Considering the *residential/grass* category (Fig. 5.8c), the theoretical curve has a good agreement with the empirical data. The contribution of the coherent scattering term is reduced to the first orientation angles and its strength is much lower than for the *residential/asphalt* and *industrial/asphalt* classes, as expected due to the increased surface roughness of grass with respect to asphalt.

For asphalt surfaces the use of the literature values in the theoretical models did not reflect the behavior of the empirical measurements sufficiently, especially for high orientation angles. This can be explained by the presence of metal objects or other small structures resulting in a relatively strong scattering also at larger orientation angles. For the grass surfaces the GO-PO model can predict the scattering behavior of the selected buildings more accurately. However, the range of valid model parameters for grass is very large (see Tab. 5.1), hampering a precise *a priori* choice of reasonable general values. This confirms that, as mentioned in Sec. 5.2, the scattering in urban areas depends on many variables. Literature values for one material are too specific to describe an extended surface in an urban area precisely. Therefore, material properties can only be used in an approximate way in the currently reported analytical electromagnetic models to infer the rough scattering behavior in an urban area in practical situations.

5.5 Conclusion

In this chapter we presented an empirical study on the behavior of the double-bounce scattering mechanism of buildings in VHR SAR. We focused on the analysis of the strength of the double bounce with respect to the orientation angle. The study investigated three

Table 5.2: Material properties and MAE between empirical and theoretical RCS per category.

	residential/asphalt	*industrial/asphalt*	*residential/grass*
Building wall	$\varepsilon_r = 8.0 - j0.5$	$\varepsilon_r = 8.0 - j0.5$	$\varepsilon_r = 4.0 - j0.05$
Ground surface	$\varepsilon_r = 8.0 - j0.5$ $h_{\mathrm{RMS}} = 1.4$ mm $l_c = 1.8$ cm	$\varepsilon_r = 8.0 - j0.5$ $h_{\mathrm{RMS}} = 1.4$ mm $l_c = 1.5$ cm	$\varepsilon_r = 14.0 - j1.0$ $h_{\mathrm{RMS}} = 10$ mm $l_c = 5.5$ cm
MAE			
0° - 10°	16.40 dB	14.06 dB	4.73 dB
11° - 45°	8.40 dB	15.17 dB	3.91 dB
0° - 45°	12.18 dB	14.79 dB	4.25 dB

classes of buildings in two TerraSAR-X images and compared these results with theoretical electromagnetic scattering models. In this context, we presented a novel model for predicting the double-bounce power based on SPM, which is suitable for urban surfaces like asphalt.

The results pointed out that the double-bounce effect has a strong power signature for buildings which have the wall on the sensor close side almost parallel to the SAR azimuth direction. Furthermore, the strength of the double bounce decays rapidly in a narrow range of orientation angles, while it decays moderately for larger angles. The exact characteristic of the decay depends on the material and surface parameters, making the double bounce a variable feature within the same scene. Therefore, the double-bounce feature can only be used for reliable building detection and reconstruction by taking into account its non-linear relation with the orientation angle.

The comparison between the predictions from the theoretical electromagnetic models based on SPM and PO and the real data showed the general behavior of the double bounce can be derived with theoretical models. However, the complexity of the actual scene hampers the reliable calculation of the double-bounce RCS. In particular, in complex environments such as urban areas, many scattering contributions from small structures with possibly different materials interfere, which is not considered in the currently reported theoretical models. In order to improve their reliability, more complex models need to be developed, including these additional contributions. Nonetheless, although the development of these models is very important from a theoretical viewpoint, the increased number of parameters required by more complex models would make it impossible to use them in real building detection/reconstruction applications.

The study presented in this chapter demonstrated that the correct behavior of the double-bounce effect with respect to the orientation angle of buildings can be derived empirically considering a few real world cases. As it will be shown in Chapter 6, this result can be integrated easily in practical feature extraction application scenarios, e.g., for the development of building detection/reconstruction techniques from meter-resolution SAR images.

Chapter 6

A Novel Method for the Automatic Detection and Reconstruction of Building Radar Footprints from Single VHR SAR Images

In this chapter[1] *we present a novel method for the automatic detection of buildings from VHR SAR scenes, which also reconstructs the 2D radar footprints of the detected buildings. Unlike most of the literature methods, the proposed approach can be applied to single images. The method is based on the extraction of a set of low-level features from the images and on their composition to more structured primitives using a production system. Then, the concept of semantic meaning of the primitives is introduced and used for both the generation of building candidates and the radar footprint reconstruction. The semantic meaning represents the probability that a primitive belongs to a certain scattering class (e.g., double bounce, roof, facade) and has been defined in order to compensate for the lack of detectable features in single images. Indeed, it allows the selection of the most reliable primitives and footprint hypotheses on the basis of fuzzy membership grades. The efficiency of the proposed method is demonstrated by processing a 1 m resolution TerraSAR-X spotbeam scene containing flat- and gable-roof buildings at various settings. The results show that the method has a high overall detection rate and that radar footprints are reconstructed accurately.*

[1] Part of this chapter appears in:

[123] A. Ferro, D. Brunner, and L. Bruzzone, "An advanced technique for building detection in VHR SAR images," in *Proc. SPIE Conf. on Image and Signal Processing for Remote Sensing XV*, vol. 7477, 2009, pp. 74 770V–74 770V–12.

[124] A. Ferro, D. Brunner, and L. Bruzzone, "Detection and reconstruction of building footprints from single VHR SAR images," in *Synthetic Aperture Radar (EUSAR), 2010 8th European Conference on*, 2010.

[95] A. Ferro, D. Brunner, and L. Bruzzone, "Building detection and radar footprint reconstruction from single VHR SAR images," in *Proc. IEEE Int. Geoscience and Remote Sensing Symp. (IGARSS)*, 2010, pp. 292–295.

6.1 Introduction on Building Detection in VHR SAR Images

As mentioned in the introduction of this thesis, in the last few years VHR spaceborne SAR sensors acquiring data with meter resolutions became widely available. To a greater extent, optical imagery at meter and submeter resolution is now also available (e.g., QuickBird, Worldview-2). All these data have the potential to be employed for various important application scenarios, such as the monitoring of changes in urban areas [125, 126], the characterization of urban areas (e.g., slum mapping) [127, 128], the surveillance of the effects of violent conflicts [29], and the crisis management after natural disasters (e.g., earthquakes) [28, 129]. For the latter application scenario, spaceborne VHR SAR sensors, such as COSMO-SkyMed and TerraSAR-X, are of particular interest, due to their independence on the solar illumination and the relative insensitivity to the weather conditions.

One of the main drawbacks of VHR SAR is the complexity of the images, mainly owing to the speckle effect and the side-looking geometry of the SAR sensor, hampering the interpretation of the data by non-SAR experts. This is especially true for urban areas, where the data are mainly characterized by layover, multi-bounce and shadowing effects of the buildings (see Chapter 5). Therefore, to support the widespread usage of VHR SAR, robust automatic information extraction methods are essential.

Different techniques for building detection and reconstruction from VHR SAR images have been presented in literature. For instance, Soergel *et al.* [130] proposed an iterative technique for building reconstruction from InSAR data, which is based on the detection of the combined occurrence of a strong scatter line and a shadow area in correspondence of an elevated region. Cellier *et al.* [131] presented a building reconstruction technique for InSAR data based on building hypothesis management. The developed method uses a tree of hypotheses, which is simplified according to a set of semantic rules. Thiele *et al.* [24] proposed an approach to building detection which uses orthogonal multi-aspect InSAR images. The approach is based on the detection of edges and their combination to building footprints. A method for the extraction of buildings and the estimation of their height from stereoscopic airborne radar images was presented by Simonetto *et al.* in [132], while in [133] a building extraction method using dual-aspect SAR data was presented. An algorithm for building reconstruction from multi-aspect polarimetric SAR (PolSAR) images was presented by Xu and Jin [23]. The polarimetric information is exploited by employing an edge detector effective on polarimetric images. The retrieved edges are then parameterized by means of the Hough transform to generate the building footprint hypotheses. Wang *et al.* [134] developed a method for the detection of buildings from single-aspect PolSAR data combining edge and area features with Markov random fields. Hill *et al.* [135] presented a semi-supervised method for the estimation of building dimensions in VHR SAR temporal scenes based on the analysis of the shape of building shadows. Another method based on shadow analysis which exploits InSAR data and is suitable for high or isolated buildings was proposed by Tison *et al.* [136]. A building detection method using an orthophoto and an InSAR image based on conditional random fields is presented in [137]. Techniques for the 3D reconstruction of buildings using VHR optical data for the 2D building footprint reconstruction and a single VHR SAR scene for the building height extraction were presented in [110] and [138]. Finally, recently a technique for the fusion of high resolution optical and SAR images for the updating of building databases has been proposed in [139]. Such a method exploits a framework based on Dempster-Shafer evidence theory for the evaluation of the detected building footprints.

All the aforementioned works addressed the problem of building detection and reconstruction in VHR SAR images by relying on the availability of ancillary or multi-sensor data (e.g., optical imagery), polarimetric SAR, interferometric SAR, or multi-dimensional airborne data which implies that the area under investigation is imaged more than once with different viewing configurations (changed incidence and/or aspect angle). This represents a limitation for application scenarios with stringent timing restrictions which do not allow the acquisition of multi-dimensional SAR data (e.g., emergency response). For these reasons, research on the detection and extraction of buildings from single VHR SAR data is important. To our knowledge, only very few papers addressed the problem of building detection with one single meter-resolution SAR images only. One of the few related works using single VHR SAR images was presented by Quartulli and Datcu [140], and was based on a stochastic geometrical model and *a posteriori* probability maximization (MAP). Recently, a method for L-shape building footprint extraction from single SAR images was proposed in [141]. This method fails in the detection of buildings if they do not show L-shaped returns. Moreover, it considers only bright lines and discards other relevant features, such as bright areas and shadows.

In this chapter we propose a novel method for building detection and radar footprint reconstruction from detected VHR SAR images. Unlike most of the literature methods, it can be applied to single images. Moreover, it is suitable to be used with data acquired by currently operational spaceborne SAR sensors. In this context, radar footprint refers to the characteristic scattering signature of buildings in SAR. The method integrates the concepts of basic feature extraction and their composition to more structured primitives using a production system [142, 143]. In order to compensate for the lack of detectable features in single images, the concept of semantic meaning of the primitives is introduced and used to generate building candidates and reconstruct radar footprints. The semantic meaning represents the probability that a primitive belongs to a certain scattering class (e.g., facade, double bounce) and allows the selection of the most reliable primitives and footprint hypotheses on the basis of fuzzy membership grades.

The main novelties and advantages of the proposed method are: i) the capability to accurately detect individual buildings using only one SAR scene without the need for ancillary data, ii) the possibility to estimate the reliability of the detected features and footprint hypotheses through a set of fuzzy functions, iii) the flexibility to handle gable- and flat-roof buildings at different sizes and at various settings, and iv) the expansibility of the approach, which allows the definition of new scattering classes and rules according to specific image characteristics or user requirements. These characteristics make the approach valuable for different application scenarios, e.g., damage assessment after crisis events and change detection in urban areas. In addition, as shown later in the chapter, the method is suited to the implementation on computer clusters, thereby making it possible almost-real-time applications.

Some steps in our proposed method have similarities with existing work. For instance, the method presented in [131] is based on hypothesis management. Since their approach relies on submeter-resolution InSAR data the hypothesis are based on different information (combination of height and topology) compared to ours (presence and semantic meaning of scattering features). Moreover, we introduce a way to quantitatively evaluate the hypotheses to automatically select the best one, which is missing in [131]. Similar to our approach, the method in [140] uses the layover and double-bounce features for the reconstruction of buildings. However, this method is based on a global MAP estimation using Monte Carlo methods, while the approach proposed in this thesis exploits also the shadow information and introduces the concept of semantic meaning and membership grade for each primitive and footprint hypothesis. Moreover, such a work was intended as a tool for the investigation of the limits and merits of information extraction from single images, and was not optimized for building reconstruction purposes.

The radar footprint map extracted with the proposed method can be used to derive different information, such as the build-up presence index. It can also be used as a feature in the classification of the build-up areas (e.g., according to residential and commercial areas). Indeed, radar footprints in single SAR images lack the information about the exact dimensions (length, width, height) and the location of the 2D footprint of buildings. In order to derive them, the method could be combined with an iterative simulation and matching scheme as presented for instance in [110] for the building height extraction. In this context, the capability of the proposed method to extract the individual scattering contributions of a building in the SAR image could be used to improve the matching function as the simulator is also able to distinguish between the different contributions.

The remainder of this chapter is structured as follows. In Sec. 6.2, we present the proposed methodology in detail, while Sec. 6.3 discusses the processing of full VHR SAR scenes using a grid computing infrastructure. In Sec. 6.4 we demonstrate the performance and the properties of our approach by processing and analyzing a large meter-resolution TerraSAR-X spotlight mode scene from Dorsten, Germany, which is characterized by different types of buildings at various settings. Finally, in Sec. 6.5, we draw some conclusions.

6.2 Proposed Technique for the Automatic Detection and Reconstruction of Building Radar Footprints

The proposed technique for the automatic detection and reconstruction of building radar footprints from single VHR SAR images is suited for meter-resolution data. Buildings are assumed to be approximately regular parallelepipeds, with rectangular base, or compositions of parallelepipeds. The minimum building size which can be handled by the algorithm depends on the specific building characteristics. As a reference, buildings with a base with a main side shorter than 10 m and a height lower than 5 m with no relevant scattering centers are likely to be not detected in meter-resolution images. The radar footprints corresponding to very tall buildings have a high probability to be detected. However, additional features and rules would be necessary (with respect to the algorithm specifications reported in this chapter) in order to handle properly those situations. The algorithm does not require the buildings to be isolated. However, it may provide better results on isolated buildings. In fact, such buildings usually show a clear shadow feature,

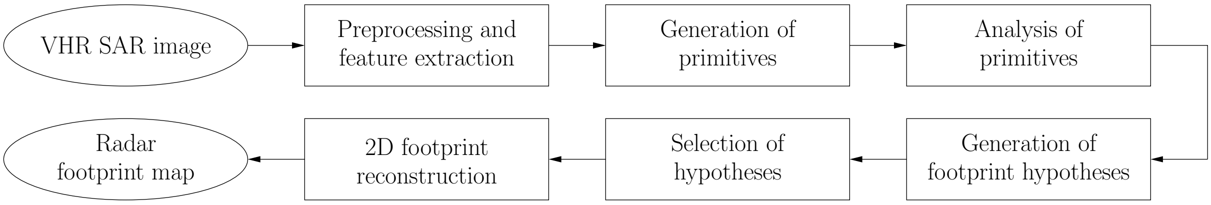

Figure 6.1: Block scheme of the processing chain of the proposed technique for the automatic detection and reconstruction of building radar footprints in single VHR SAR images.

which is exploited by the algorithm to improve the detection performance. Very close buildings may be detected as single structures, as we will show in Sec. 6.4.

The proposed technique is composed of six main steps: i) preprocessing and feature extraction, ii) generation of primitives, iii) analysis of primitives, iv) generation of building radar footprint hypotheses, v) selection of hypotheses, vi) 2D radar footprint reconstruction. Fig. 6.1 shows a block scheme representing the proposed processing chain. In the following we describe in detail each step. In this thesis we present the algorithm optimized for the application to meter-resolution SAR images. However, the general structure of the algorithm is suitable to handle also higher resolution data. We highlight throughout the chapter the modifications which would be necessary to apply the algorithm to submeter-resolution images.

6.2.1 Preprocessing and Feature Extraction

In the preprocessing, the input image is first radiometrically calibrated. Although this step is not strictly necessary, it permits to define the algorithm parameters to be used with SAR images of different datasets and data products acquired by either the same or different sensors. Afterwards, the image is filtered with a Gamma MAP filter [144] in order to reduce the signal variability due to speckle. Both the unfiltered and filtered images are used by the algorithm. The basic features composing building radar footprints in VHR SAR images are extracted from the calibrated image. According to the aforementioned assumptions on building shapes, these are bright linear features with different thicknesses, and dark areas. The former are usually related to double-bounce scattering or, as the line thickness increases, to layover areas, where the roof or the facade scattering may be dominant depending on the building characteristics. The latter are due to building shadows and low-return areas (e.g., roads, rivers, lakes). These features are sufficient to describe the main parts of a building radar footprint in meter-resolution images. However, as far as resolution increases, other scattering effects due to small structures become visible (e.g., point scatterers due to pipes on walls) and other types of features may be extracted to increase the detection performance of the algorithm. In the following, the techniques used for the extraction of bright linear features and dark areas are described in detail.

Extraction of bright linear features

The extraction of bright linear features is performed on the unfiltered image by means of the line detector proposed by Tupin *et al.* in [145]. This detector is based on a three-region

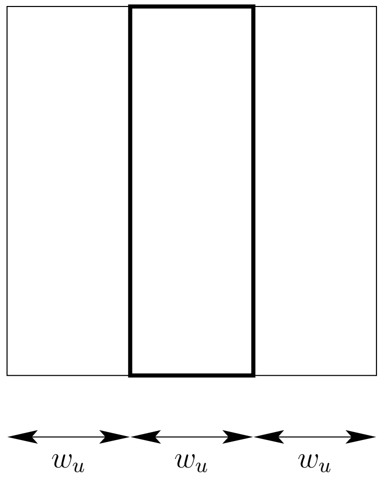

Figure 6.2: Definition of the window used by line detector.

sliding-window approach and is a well-known algorithm specifically developed for SAR images. Here we use as reference for the window size the dimension of the central region, and assume that the lateral regions have the same width and length (see Fig. 6.2). The length has been set to ten times the resolution of the image and 16 directions have been considered for the window. As we are interested in both thin and thick linear features, the detector is applied T times with different increasing window sizes w_u ($u = 1, \ldots, T$). Each filtering is performed independently. The result of each filtering is a detection map, which is then thresholded, obtaining binary linear regions which thickness is related to w_u. Such regions are vectorized using a rectangular approximation. This is performed by approximating the region skeletons with lines and using such lines as the axis of rectangles of width w_u. The region skeletons are extracted according to [146]. In Fig. 6.3 we show an example of the detection on a meter-resolution SAR image of an urban area using $w_u = 5$ m. The intermediate results are also shown. For each rectangle, the local contrast value C_r is calculated on the filtered image as:

$$C_r = \left[\frac{1}{|A_{\text{in}}|} \sum_{p \in A_{\text{in}}} \bar{\xi}_p \right] \cdot \left[\frac{1}{|A_{\text{out}}|} \sum_{p \in A_{\text{out}}} \left(1 - \bar{\xi}_p\right) \right], \tag{6.1}$$

where A_{in} and A_{out} are the inner region of the rectangle and an outer thick border surrounding it, respectively. The thickness of A_{out} is defined as $\frac{w_u}{2}$. $|A_{\text{in}}|$ and $|A_{\text{out}}|$ represent the number of pixels contained in the regions A_{in} and A_{out}, respectively; and $\bar{\xi}_p$ depicts the pixel amplitude value normalized between 0 and 1. For the normalization the image amplitude dynamic range has been thresholded to cover the 99.5th percentile of the original image histogram in order to reduce the effect of very bright point scatterers. C_r is a measure of the contrast between the pixels contained in the rectangles and their surrounding. The higher the difference between the mean amplitude of the two regions, the higher the value of C_r. This measure has been proposed in [147] and has been used in [132] for the case of binary images.

As a result of the T filterings we obtain T vector maps containing rectangles corre-

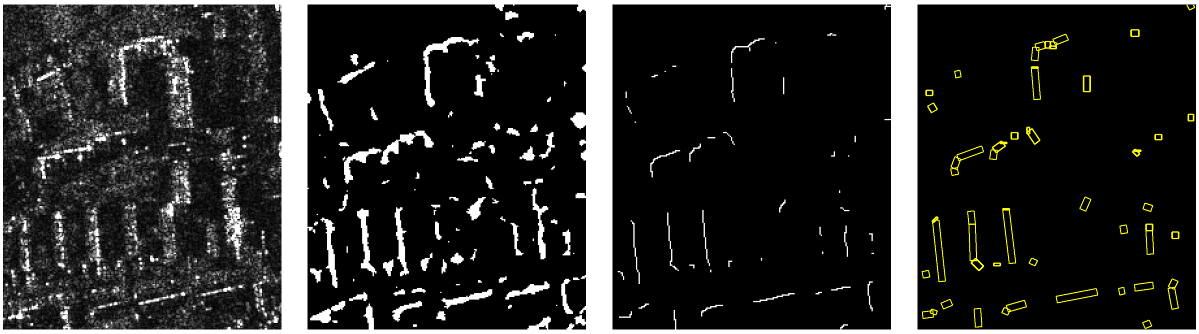

(a) (b) (c) (d)

Figure 6.3: (a) Meter-resolution TerraSAR-X image of an urban area (© Infoterra). (b) Result of the line detection using $w_u = 5$ m. (c) Skeletons of the binary regions shown in (b). (d) Rectangles generated using the skeletons shown in (c).

sponding to bright linear features with different thicknesses. These maps are thus merged in one map. It is possible that the same real bright objects are detected independently for different w_u, resulting in overlapping rectangles in the merged map. In order to reduce the number of rectangles, a downselection step is performed by means of a production net. For each combination of two rectangles (p, q) the net tests the following conditions: i) the width of the two rectangles is similar, and ii) the two rectangles overlap. Condition i) is met when:

$$|w_p - w_q| < \delta w_{\max} \tag{6.2}$$

where w_p and w_q are the widths of the rectangles, and $\delta w_{\max}$ is a user-defined threshold (see Fig. 6.4). Condition ii) is fulfilled when:

$$A_\cap > A_p \cdot A_t \ \wedge \ A_\cap > A_q \cdot A_t \tag{6.3}$$

where A_p and A_q are the areas of the rectangles, $A_\cap = A_p \cap A_q$ (see Fig. 6.4), and A_t is a value belonging to the range $(0, 1)$ set by the user. When conditions (6.2) and (6.3) are fulfilled, the net discards the rectangle with the lowest contrast, which is the rectangle associated to the lowest value of C_r.

For the choice of the values of $\delta w_{\max}$ and A_t, values on the order of 3 m and 0.5 are suggested, respectively. Moreover, in our experiments a number of $T = 7$ filterings using equally spaced w_u between 3 and 15 m has given a good detection of the linear bright features in the test images using a fixed threshold equal to 0.4 for all the considered w_u.

It is worth noting that this downselection step is not strictly necessary for the correct operation of the proposed technique. However, it greatly reduces the number of extracted bright linear features, thus improving the overall performance in terms of execution time and memory requirements of the technique.

Extraction of dark areas

Dark areas are extracted from the unfiltered image by means of mean shift clustering followed by a threshold operation, according to the approach proposed in [148]. This operation selects only the clusters with amplitude values lower than an user-defined threshold

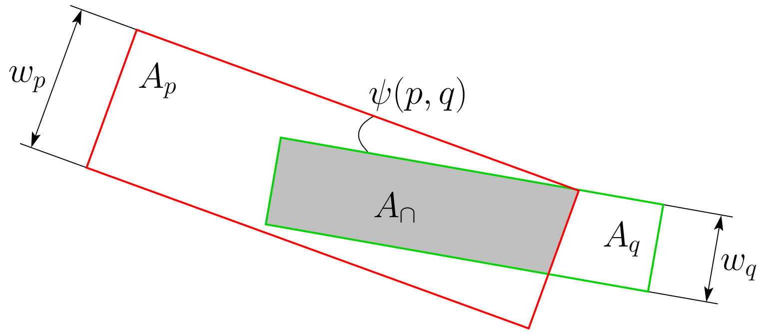

Figure 6.4: Measures involved in the rectangle downselection described in the feature extraction step, and in the primitives generation step.

ξ_S. The extracted clusters are then vectorized and a simplification procedure is applied in order to reduce the number of vertexes describing their shape. Such simplification is not strictly necessary, but it allows the algorithm to work with simpler objects reducing the needed amount of memory. In order to select only the dark regions which are likely to be related to building shadows, the algorithm removes the regions which are not located in the sensor-far side of any bright linear feature (previously extracted). This is done by keeping only the dark areas which overlap with the predicted shadow area of the bright features. The predicted shadow area is determined by taking into account the viewing configuration of the SAR. The maximum range size l_S of the expected shadow area is set by the user. The parameters of the mean shift clustering and the value of ξ_S have to be selected by analyzing the amplitude of sample pixels belonging to shadow regions in the SAR image. In our experiments, reasonable values for ξ_S were in the order of -13 – -11 dB.

6.2.2 Generation of Primitives

The goal of this step is to generate the primitives that will be used in the following steps as basis for the composition of building radar footprint hypotheses. Starting from the set of simple extracted bright linear features and dark areas, the algorithm merges adjacent features in order to compose bigger objects. This is done by a production system applied to the vector domain, after a conversion from slant range to ground range, and is aimed at compensating for errors in the feature extraction step. The conversion from slant to ground range allows us to define the parameters of the method in the ground domain, which is independent on the incidence angle and thus simpler to handle for an end-user. After their generation, composed objects are given as input to the production system. Therefore, multiple compositions with other simple or composed objects are possible. The set of objects and productions involved in the generation of primitives is shown in Fig. 6.5. The composition of dark areas is based only on an adjacency criterion, represented by productions P_1 and P_2. For the case of bright linear features, merged features are generated as new rectangles which have as principal axis the conjunction of the two farthest points of the principal axes of the original features. The width of the new rectangles is calculated as the weighted average of the widths of the original

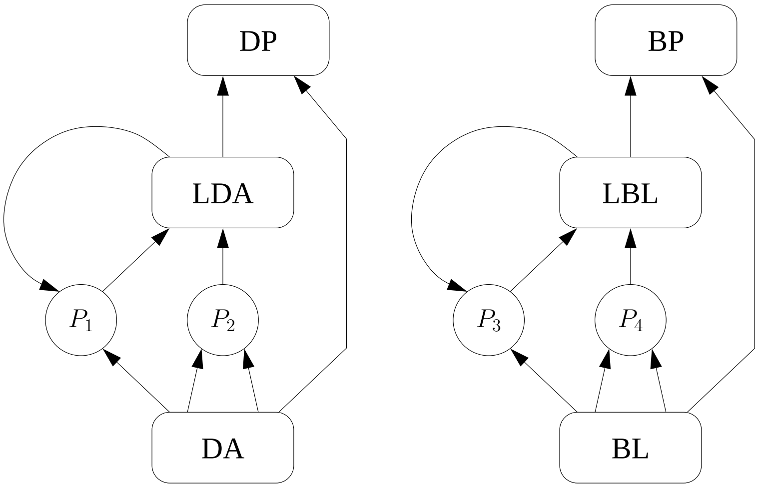

Figure 6.5: Production net for the generation of dark primitives (DP) and bright primitives (BP). The inputs of the process are dark areas (DA) and bright linear features (BL), which are composed to large dark areas (LDA) and large bright linear features (LBL), respectively. The whole set of DA, LDA, BL and LBL are selected as primitives.

features, using as weights their length. The algorithm merges two bright features when the following conditions are fulfilled (P_3 and P_4): i) the features have similar widths, ii) their orientation is approximately the same, iii) the composed object has an orientation that is approximately the same of the original features. Condition i) is equivalent to (6.2). Condition ii) is fulfilled when $\psi(p,q) < \delta\psi_{\max}$, where $\psi(p,q)$ is the angle between the two linear bright features represented by the rectangles p and q (see Fig. 6.4), and $\delta\psi_{\max}$ is user-defined and indicates the maximum angle allowed between two features for which they are considered parallel. The value of $\delta\psi_{\max}$ should be on the order of 20°. Condition iii) is satisfied when:

$$\psi(\chi,p) < \delta\psi_{\max} \ \wedge \ \psi(\chi,q) < \delta\psi_{\max}, \tag{6.4}$$

where χ is the rectangle corresponding to the composed bright linear feature. It is probable that in this step many bright primitives are generated. In order to reduce their number, a selection procedure as the one described in the previous subsection for bright linear features can be applied.

At the end of this step, for the whole set of simple and composed objects the algorithm stores a set of attributes regarding their size and position, and the amplitude features of the composing pixels (i.e., mean value, standard deviation). The set of simple and composed objects (with the related attributes) will be considered as set of primitives for the following steps.

6.2.3 Analysis of Primitives

This step aims at evaluating the semantic meaning of the primitives. Here we use the term semantic meaning to describe the membership grade of a certain primitive to belong to a predefined scattering class. Different scattering classes are related to different parts of building radar footprints. The choice of the set of semantic classes is related to the

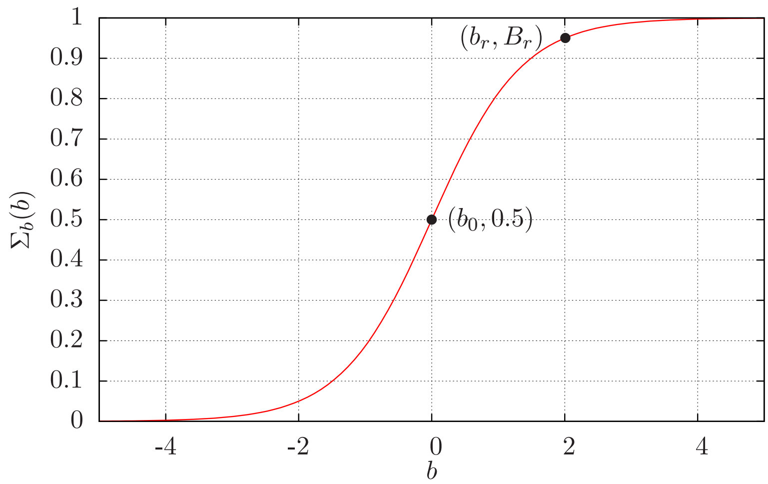

Figure 6.6: Example of sigmoid function $\Sigma_b(b)$ defined according to (6.5). $b_r = 2$, $b_0 = 0$, $B_r = 0.95$.

types of features extracted from the image and, thus, to the image resolution. For the bright primitives (i.e., the primitives obtained from bright linear features) we define four semantic classes: *general line*, *double bounce*, *roof*, and *facade*. For dark primitives (i.e., the primitives obtained from dark areas) only the class *shadow* has been defined. The membership grade of each primitive to belong to a certain semantic class is calculated on the filtered image according to membership functions (MFs) derived empirically for each semantic class. The MFs are functions of the primitive attributes and describe the membership grade of a primitive as a number in the range (0,1). The membership grades to belong to the different semantic classes are calculated independently. Thus, one primitive can have high membership grade for different classes at the same time. The different semantic meanings are managed by the proposed technique in the later stages of the processing chain.

The MFs are defined as a product of sigmoid functions. Each sigmoid factor depends on a specific attribute of the primitives. A generic sigmoid function is defined as follows [149]:

$$\Sigma_b(b) = \frac{1}{1 + e^{-\alpha_b(b-b_0)}} \tag{6.5}$$

$$\alpha_b = -\frac{\ln(1/B_r - 1)}{b_r - b_0}, \tag{6.6}$$

where b indicates the attribute which constrains the function (e.g., the coefficient of variation of the amplitude of the pixels contained in the primitive), $\Sigma(b_0) = 0.5$ and $\Sigma(b_r) = B_r$. The function $\Sigma_b(b)$ gives values in the range (0,1). For each sigmoid function two parameters needs to be specified: the value of b for which the sigmoid returns a high likelihood B_r (b_r), and the value corresponding to the center of the sigmoid (b_0), implicitly setting the slope of the function. Fig. 6.6 shows an example of sigmoid function.

The MFs which relate bright primitives to the relative semantic classes are defined according to the tree shown in Fig. 6.7. The number of sigmoid functions composing the MF for a semantic class is smaller or equal to the number of branches which connect the root to the final leaf. In the following we describe in detail the MFs of each semantic class

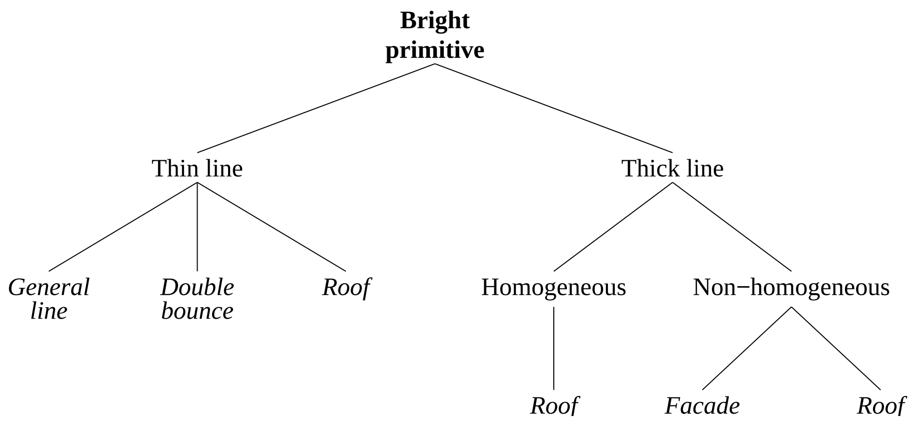

Figure 6.7: Tree representing the semantic classes used in this thesis for bright primitives.

for both bright and dark primitives, by also suggesting the range of parameters which is most suited for the related scattering class. Unless otherwise stated, such values have been estimated by analyzing the scattering properties of a set of samples of the considered scattering classes manually selected on the meter-resolution TerraSAR-X input images used in this chapter. As the images are calibrated, the suggested values related to pixel amplitude can be considered generally valid. In the case of images acquired at different resolution and/or with a sensor with different characteristics, some of the values should be estimated again. In Sec. 6.4.5 the choice of the parameters is discussed more in detail.

Bright primitives

General line The membership grade of a primitive to the class *general line* depends only on its width. The MF is thus defined as

$$\mathrm{MF}_{\mathrm{GL}} = \Sigma_w^{\mathrm{thin}}(w), \tag{6.7}$$

where $\Sigma_w^{\mathrm{thin}}(w)$ gives a measure of the membership of the primitive to the high-level class *thin line*, which depends on the primitive width w. According to the definitions of (6.5) and (6.6), $\Sigma_w^{\mathrm{thin}}(w)$ is controlled by the parameters w_r^{thin} and w_0^{thin}. The values of these parameters are chosen to give high values when w is small (e.g., $w_r^{\mathrm{thin}} = 5$ m, $w_0^{\mathrm{thin}} = 7$ m for meter-resolution images).

Double bounce As shown in Chapter 5, the double-bounce effect appears in VHR SAR images as relatively thin bright lines and is more evident when the building wall is parallel to the azimuth direction, i.e., its orientation angle is close to zero. The MF of the class *double bounce* is thus defined as follows

$$\mathrm{MF}_{\mathrm{DB}} = \Sigma_w^{\mathrm{thin}}(w)\Sigma_\phi^{\mathrm{DB}}(\phi), \tag{6.8}$$

where the term ϕ is the primitive orientation angle, and $\Sigma_\phi^{\mathrm{DB}}(\phi)$ takes into account the dependence of the double-bounce effect on ϕ. $\Sigma_\phi^{\mathrm{DB}}(\phi)$ has high values when ϕ is close to zero. In such a case, the MFs of the classes *general line* and *double bounce* give very similar values. Proper values for ϕ_r^{DB} and ϕ_0^{DB} are on the order of 10° and 30°, respectively. Such values have been chosen according to the results discussed in Chapter 5.

Roof The class *roof* is the most specific, as it appears as leaf for every branch combination. This is due to the intrinsic uncertainty given by the fact that we are using only one VHR SAR image and that we are considering meter-resolution images. Indeed, the signature of a building roof could be either a thin line (e.g., in the case of gable-roof buildings with high orientation angle), or a homogeneous rectangular area (e.g., flat roof buildings), or a non-homogeneous rectangular area (e.g., flat roof buildings with metal structures on the roof, which are common for industrial buildings). Therefore, for the class *roof* the final membership grade is calculated as the maximum of the membership grades given by the three MFs corresponding to the three occurrences of the class in the tree. These are defined as:

$$\mathrm{MF}'_{\mathrm{R}} = \Sigma_w^{\mathrm{thin}}(w) \tag{6.9}$$

$$\mathrm{MF}''_{\mathrm{R}} = \Sigma_w^{\mathrm{thick}}(w)\Sigma_\zeta^{\mathrm{hom}}(\zeta) \tag{6.10}$$

$$\mathrm{MF}'''_{\mathrm{R}} = \Sigma_w^{\mathrm{thick}}(w)\Sigma_\zeta^{\mathrm{non\text{-}hom}}(\zeta). \tag{6.11}$$

Finally, we obtain:

$$\mathrm{MF}_{\mathrm{R}} = \max\left\{\mathrm{MF}'_{\mathrm{R}}, \mathrm{MF}''_{\mathrm{R}}, \mathrm{MF}'''_{\mathrm{R}}\right\}. \tag{6.12}$$

The definition of $\Sigma_w^{\mathrm{thick}}(w)$ is complementary to that of $\Sigma_w^{\mathrm{thin}}(w)$. As a requirement, to cover the whole possible range of primitive thicknesses it is necessary that $w_r^{\mathrm{thin}} = w_r^{\mathrm{thick}}$. This assures that any value of w is mapped either in the *thin line* or *thick line* classes with high membership grade (greater than B_r). Fig. 6.8 shows the behaviors of the complementary MFs $\Sigma_w^{\mathrm{thin}}(w)$ and $\Sigma_w^{\mathrm{thick}}(w)$ that are used in this thesis. The same considerations hold for the definition of $\Sigma_\zeta^{\mathrm{hom}}(\zeta)$ and $\Sigma_\zeta^{\mathrm{non\text{-}hom}}(\zeta)$, which indicate the degree of membership of a primitive to the classes *homogeneous* and *non-homogeneous*, respectively. These refer to the homogeneity of the pixels contained in the primitive. The homogeneity is measured using as parameter the coefficient of variation ζ of the pixels. Reasonable values for w_0^{thick}, $\zeta_r^{\mathrm{hom}} = \zeta_r^{\mathrm{non\text{-}hom}}$, ζ_0^{hom} and $\zeta_0^{\mathrm{non\text{-}hom}}$ are on the order of $2-3$ m, $0.3-0.35$, $0.45-0.55$, and $0.15-0.3$, respectively. Thanks to these constraints, the tree representing the semantic classes covers all the possible combinations of attributes taken into account in this thesis. In the specific case of the class *roof*, (6.12) shows that the membership grade is always greater or equal to B_r^2. This is in line with the aforementioned issue of the uncertainties related to the radar signature of building roofs.

Facade As reported in the tree of Fig. 6.7, the semantic class *facade* includes primitives with a relevant width and which pixels have non-homogeneous values. This is the general scattering behavior of building facades, where returns coming from structures like windows or balconies (often made of metal) give a strong textured signature in the radar footprint. As a further constraint, the orientation angle of the building should not be too high (i.e., the building should not be perpendicular to the azimuth direction). Indeed, the facade scattering area in the radar footprint becomes smaller with increasing orientation angles.

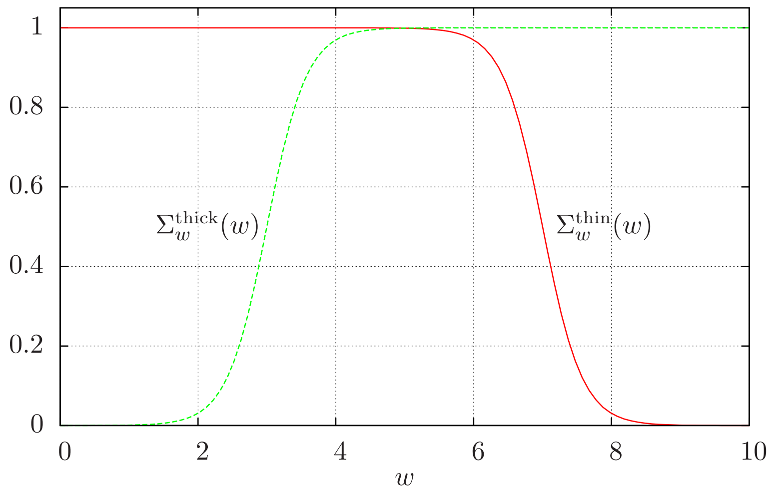

Figure 6.8: Complementary MFs $\Sigma_w^{\text{thin}}(w)$ and $\Sigma_w^{\text{thick}}(w)$ used in this chapter. $w_r^{\text{thin}} = w_r^{\text{thick}} = 5$, $w_0^{\text{thin}} = 7$, $w_0^{\text{thick}} = 3$, $B_r = 0.999$.

These factors are taken into account in the definition of the *facade* MF as follows:

$$\text{MF}_\text{F} = \Sigma_w^{\text{thick}}(w)\Sigma_\zeta^{\text{non-hom}}(\zeta)\Sigma_\phi^{\text{F}}(\phi), \tag{6.13}$$

where $\Sigma_\phi^{\text{F}}(\phi)$ models the effect of the building orientation angle ϕ by penalizing primitives with high orientation angles (e.g., $\phi_r^{\text{F}} = 70°$ and $\phi_0^{\text{F}} = 80°$). As mentioned at the beginning of this section, we do not include in our analysis very high buildings, for which the facade scattering area can have different characteristics.

Dark primitives

For dark primitives only the semantic class *shadow* has been defined. The MF of this class takes into account the mean and the coefficient of variation of the pixels contained in the primitive. It is defined as:

$$\text{MF}_\text{S} = \Sigma_{\tilde{\mu}}^{\text{S}}(\tilde{\mu})\Sigma_\zeta^{\text{hom}}(\zeta), \tag{6.14}$$

where $\Sigma_{\tilde{\mu}}^{\text{S}}(\tilde{\mu})$ is the sigmoid functions depending on the pixel mean $\tilde{\mu}$. The MF is tuned in order to penalize dark primitives with high mean value and high coefficient of variation. Our experiments pointed out that reasonable values for $\Sigma_{\tilde{\mu}}^{\text{S}}(\tilde{\mu})$ are $\tilde{\mu}_r^{\text{S}} \in (-14, -12)$ dB and $\tilde{\mu}_0^{\text{S}} \in (-9, -8)$ dB.

6.2.4 Generation of Building Radar Footprint Hypotheses

In this step the algorithm creates building radar footprint hypotheses starting from the set of primitives. The hypotheses are generated according to a set of rules and the process is performed by means of a production system. Fig. 6.9 summarizes the generation process. A footprint hypothesis is generated when i) two bright primitives, or ii) two bright primitives and one dark primitive, or iii) one bright primitive and one dark primitive are close each other and have a relative position compatible with the viewing configuration of

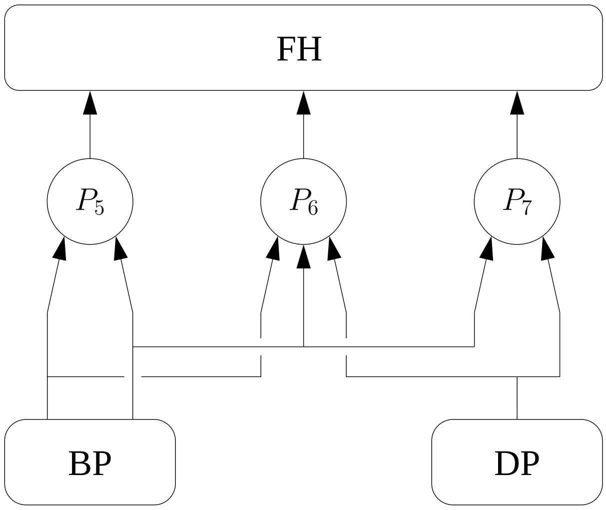

Figure 6.9: Production net for the generation of building radar footprint hypotheses (FH) starting from the set of bright primitives (BP) and dark primitives (DP).

the SAR sensor (i.e., dark primitives are located in the sensor-far side of bright primitives). The three cases are described by the productions P_5, P_6 and P_7 of Fig. 6.9. The generation is thus based only on the vicinity criterion, and many hypotheses are usually created for the same actual building radar footprint. The vicinity is checked by measuring the minimum distance between the primitives. A proper value for the maximum distance allowed between two primitives is the value δd_0 used in the selection of hypotheses (see Sec. 6.2.5). As it will be shown in Sec. 6.2.5, on the one hand if two primitives have a distance greater than δd_0 they produce footprint hypotheses which are associated to low scores by the algorithm. On the other hand, a distance threshold shorter than δd_0 would discard hypotheses which may be associated to high scores.

The order in which the bright primitives are aggregated is also taken into account, i.e., at least two hypotheses will be generated for each pair of bright primitives. The choice of using a maximum number of two bright primitives depends on the image resolution and on the types of features used in this thesis. In meter-resolution images an average building radar footprint can be usually described effectively by the combinations considered in this thesis. In the case more types of features are extracted from the image or decimeter-resolution images are used, more combinations of primitives become relevant.

6.2.5 Selection of Hypotheses

As mentioned in the previous subsection, many hypotheses are generated by aggregating the primitives. At this stage the algorithm selects only the most reliable hypotheses, which will be used in the next step as starting point for the 2D radar footprint reconstruction. Therefore, the output of this step is a map containing the detected (but not reconstructed) building radar footprints. This means that the output map is composed by footprint hypotheses which are still not refined.

The reliability of each hypothesis is evaluated on the basis of a score. The score is computed from the membership grades of the primitives composing each hypothesis. The general form of the score equation for a building radar footprint hypothesis $\tilde{h}$ is given by:

$$S_{\tilde{h}} = n_{\tilde{h}} \max_{p,q} \{\Xi_{\tilde{h}}(p,q) M_{\tilde{h}}(p,q)\} Z_{\tilde{h}}, \tag{6.15}$$

where $n_{\tilde{h}}$ depends on the number of primitives composing the hypothesis, $\Xi_{\tilde{h}}(p,q)$ and $M_{\tilde{h}}(p,q)$ are related to the relative position and to the membership grades of the bright primitives, respectively, and $Z_{\tilde{h}}$ depends on the membership grade and position of the dark primitive. (p,q) indicates the combination of the semantic class p of the first bright primitive and the class q of the second bright primitive. All these factors belong to the range [0,1]. The overall value of $S_{\tilde{h}}$ thus belongs to the same range. In the following we describe in detail each term of the equation:

- $n_{\tilde{h}}$: for the case presented in this thesis, when the hypothesis $\tilde{h}$ includes three primitives (i.e., the maximum number allowed), then $n_{\tilde{h}} = 1$. In the case one primitive is missing, it takes the value $n_{\tilde{h}} = n'_{\tilde{h}} < 1$, which is set by the user. This term is thus related to the reliability assigned by the user to the candidates composed by a non-complete set of primitives.

- $\Xi_{\tilde{h}}(p,q)$: this term depends on the relative position of the bright primitives in the radar footprint hypothesis. In this thesis, only the classes *general line* and *double bounce* are considered for the first bright primitive, and the classes *roof* and *facade* for the second bright primitive. It is worth noting that the technique also considers the case in which the bright primitives are switched, as in the hypotheses generation step different hypotheses are created taking into account also the order in which the bright primitives are aggregated. If only one bright primitive is present the value of $\Xi_{\tilde{h}}(p,q)$ is 1. When two bright primitives are included in the hypothesis and the first bright primitive is closer to the SAR flight path than the second primitive, its value is 0. Indeed, for the considered cases, scattering from double bounce or any other linear scattering feature of a building (associated to the first bright primitive) cannot precede in range the scattering from the roof and from the facade (which are associated to the second bright primitive). At most, the scattering area of double bounce and other lines are contained in that of roof and facade. When this condition is fulfilled, the value of $\Xi_{\tilde{h}}(p,q)$ is calculated differently depending on the combination (p,q). In detail, $\Xi_{\tilde{h}}(p,q)$ is calculated as follows:

$$\Xi_{\tilde{h}}(p,q) = \begin{cases} \Sigma_{\delta d}^{\text{close}}(\delta d_{\text{fs}}) \Sigma_{\delta\psi}^{\text{parallel}}(\delta\psi_{\text{pa}}) & \text{if } p\text{=}\textit{double bounce}, q\text{=}\textit{facade} \\ \Sigma_{\delta d}^{\text{close}}(\delta d) \Sigma_{\delta\psi}^{\text{parallel}}(\delta\psi_{\min}) & \text{otherwise}, \end{cases} \tag{6.16}$$

where δd_{fs} is the distance between the first bright primitive and the sensor-far side of the second bright primitive oriented in its principal direction, and $\delta\psi_{\text{pa}}$ is the angle between them (see Fig. 6.10). δd is the distance between the two bright primitives. Distances are measured in terms of minimum distance between the considered objects. The distance to the sensor is calculated considering an infinite line located outside the image with a position and angle compatible with the viewing configuration of the SAR. If one bright primitive overlaps with the other, $\delta d = 0$. $\delta\psi_{\min}$ is defined as:

$$\delta\psi_{\min} = \min\{\delta\psi_{\mathrm{pa}}, \delta\psi_{\mathrm{sa}}\} \tag{6.17}$$

where $\delta\psi_{\mathrm{sa}}$ is the angle between the first bright primitive and the secondary axis of the second bright primitive (see Fig. 6.10). The functions $\Sigma^{\mathrm{close}}_{\delta d}(\delta d)$ and $\Sigma^{\mathrm{parallel}}_{\delta\psi}(\delta\psi)$ give values close to 1 when their argument is small. The definition of $\Xi_{\tilde{h}}(p,q)$ thus assures that its value is close to 1 when the bright primitives are both close and oriented parallel or perpendicularly to each other. For the combination *double bounce/facade* the condition is more strict and requires that the two primitives have their principal axis oriented in the same direction, and that the supposed double-bounce line is located at the sensor-far side of the facade scattering area (see Chapter 5). Proper values for δd_r and δd_0 are on the order of 3 m and 10 m, respectively. Regarding $\delta\psi_r$ and $\delta\psi_0$, values on the order of 10° and 30° are suggested.

- $M_{\tilde{h}}(p,q)$: this factor depends on the membership grades of the bright primitives composing the footprint hypothesis and on their size. When only one bright primitive is present, it reduces to $M_{\tilde{h}}(p)$ and its value is equal to the membership grade of the primitive to the class p. If two bright primitives are present, it is calculated in the following way:

$$M_{\tilde{h}}(p,q) = \frac{M'_{\tilde{h}}(p,q) + M''_{\tilde{h}}(p,q)}{2} \tag{6.18}$$

$$M'_{\tilde{h}} = \mathrm{MF}_{1,p} \cdot \mathrm{MF}_{2,q} \tag{6.19}$$

$$M''_{\tilde{h}} = \frac{A_1 \cdot \mathrm{MF}_{1,p} + A_2 \cdot \mathrm{MF}_{2,q}}{A_1 + A_2}, \tag{6.20}$$

  where $\mathrm{MF}_{1,p}$ indicates the membership grade of the first bright primitive to the class p, and $\mathrm{MF}_{2,q}$ is the membership grade of the second bright primitive to the class q. A_1 and A_2 are the areas of the first and of the second bright primitives, respectively. The definition of $M_{\tilde{h}}(p,q)$ permits to obtain reliable scores also for particular combinations of bright primitives. For instance, if one of the two bright primitives has a very low membership grade, the term $M'_{\tilde{h}}(p,q)$ becomes very small and the overall value of $M_{\tilde{h}}(p,q)$ will be low (in the limit, $M_{\tilde{h}}(p,q) = \frac{M''_{\tilde{h}}(p,q)}{2} \leq 0.5$). Instead, the term $M''_{\tilde{h}}(p,q)$ takes into account the area of the bright primitives. As a result, the value of $M''_{\tilde{h}}(p,q)$ depends more on the larger bright primitive.

- $Z_{\tilde{h}}$: this term is function of the membership grade to the class *shadow* of the dark primitive, and on its position in the radar footprint hypothesis with respect to the bright primitives. It is calculated as:

$$Z_{\tilde{h}} = \mathrm{MF}_{\mathrm{S}} \cdot \Sigma^{\mathrm{close}}_{\delta d}(\min\{\delta d_{1,\mathrm{S}}, \delta d_{2,\mathrm{S}}\}), \tag{6.21}$$

  where $\delta d_{1,\mathrm{S}}$ and $\delta d_{2,\mathrm{S}}$ are the distances of the dark primitive from the first and the second bright primitive, respectively (see Fig. 6.10).

On the basis of the value of $S_{\tilde{h}}$, the algorithm deletes all the radar footprint hypotheses for which $S_{\tilde{h}} < S_{\tilde{h},\min}$, where $S_{\tilde{h},\min}$ is an user-defined threshold. After this first selection,

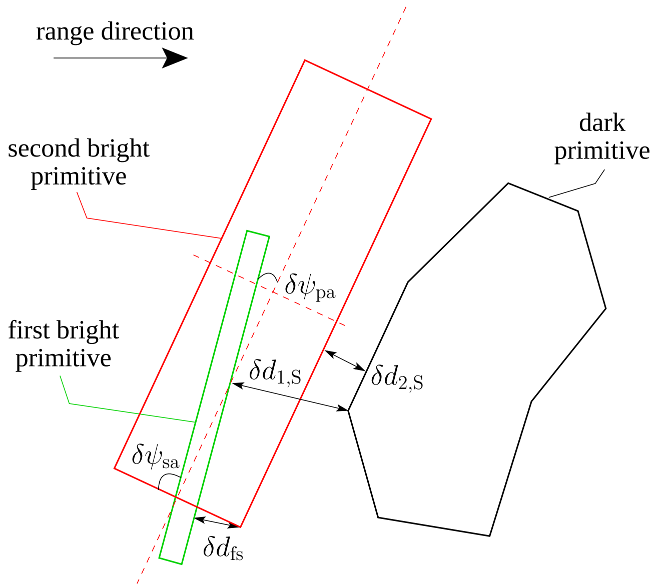

Figure 6.10: Measures involved in the calculation of the term $\Xi_{\tilde{h}}(p,q)$.

many hypotheses with high values of $S_{\tilde{h}}$ may still overlap in correspondence of actual building radar footprints (e.g., composed by different combinations of primitives). Therefore, the algorithm selects amongst the overlapping hypotheses only the one with the highest value of $S_{\tilde{h}}$.

6.2.6 2D Radar Footprint Reconstruction

The 2D radar footprint reconstruction aims at refining the detection of both, the bright part and the dark part (if present) of the footprint hypotheses selected in the previous step. This is performed in order to reduce the effect of imprecisions coming from the feature extraction and primitive generation steps, and to provide reliable outputs which can be used to estimate parameters of the buildings, such as their length, width and height (with the limitations imposed by the fact that only a single image is available). The result of this procedure is thus the final map of the building radar footprints detected and reconstructed from the input VHR SAR image.

As a first step, the algorithm generates for each footprint hypothesis a best-fit rectangle which includes its bright primitives. If only one bright primitive is present, the best-fit rectangle and the bright primitive match. The local contrast C_r of the rectangle is calculated according to (6.1). Then, the rectangle is translated, rotated, expanded and shrunk with the goal to maximize C_r. The maximization is carried out using a Particle Swarm Optimization approach (PSO) [150], which is a well-known iterative method suited for the optimization of problems without *a priori* assumptions. A similar approach was applied in [132] for binary images and using a different optimization strategy. The rectangles which become smaller than the minimum sizes set in the previous steps of the algorithm are deleted. Moreover, it is possible that some rectangles move and overlap. Therefore, the algorithm deletes overlapping rectangles, and thus the corresponding footprint hypothesis, keeping only the rectangles associated to the hypotheses with the highest scores.

A refinement procedure is carried out also for the dark part of the footprint hypothesis, when it is present. In fact, a good knowledge of the size of the shadow area of a building can be exploited for the retrieval of the building height [110]. The refinement aims at expanding the dark primitive on pixels with amplitude values similar to those of shadows in the sensor-far side area of the reconstructed bright primitive. To this end, the center of the dark primitive is used as seed for a region growing algorithm which, starting from an initial circular contour, stretches its border to fit the dark area around the seed. The chosen implementation is a level-set algorithm [83] which moves the contour by including the pixels which have amplitude values in the range $[0, \tilde{\mu}_r^{\mathrm{S}}]$ ($\tilde{\mu}_r^{\mathrm{S}}$ has been defined in Sec. 6.2.3). The resulting regions are cut in the azimuth direction in order to match the extension of the reconstructed bright part of the footprint hypothesis. Indeed, the reconstructed regions are associated to building shadow areas, which cannot be larger than the corresponding buildings in the azimuth direction. The size of the reconstructed dark areas in the range direction depends only on the radiometric measurements in the image. As the proposed technique uses as input only one VHR SAR image and no *a priori* information is available, it is not possible to detect the end of the shadow region by other means. This may lead to shadow areas which are longer than real shadows because of low scattering areas behind the buildings (e.g., roads, parking lots). This problem can be partially mitigated by imposing a maximum shadow range size l_{S} set by the user as in Sec. 6.2.1. Shadows longer than l_{S} are cut to l_{S}, and a flag is set to notice the user about the lower reliability of the reconstructed shadow.

6.3 Analysis of Large VHR SAR Scenes

The technique proposed in this chapter can be used in many application scenarios, e.g., the detection of changes in urban areas aimed at the quick assessment of damages after a natural disasters. For these applications it is important to process entire scenes in a fast manner. However, the processing chain described in the previous section is demanding both in terms of computation effort and memory requirements. This reduces the size of the input images that can be analyzed to a small subset of an actual VHR SAR scene, thus limiting the potential application of the method in real scenarios. In particular, the amount of resources required by the proposed technique depends directly on: i) the size of the input image, mainly for the parts of the algorithm based on image filtering and feature extraction (i.e., despeckling and line detection); and ii) the number of primitives and hypotheses generated through the processing chain. The latter is the most relevant factor that defines the complexity of the method. Indeed, the amount of required resources shows a non-linear dependence on the number of objects inserted in the production systems used in the processing chain. Although the number of primitives and hypotheses depends on the size of the input image, it also depends on the type of imaged area. As an example, two images of the same size covering a urban area and a rural area will produce a different number of primitives, with the greater number of primitives from the urban area.

In order to face these problems, we extended the algorithm to operate in a computer

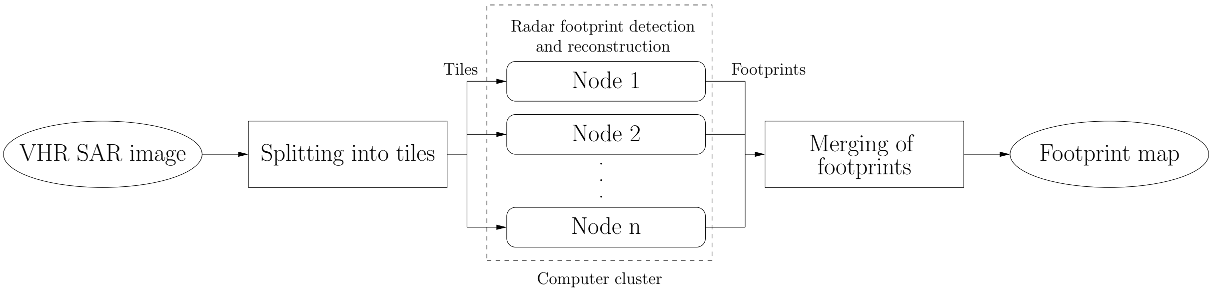

Figure 6.11: Proposed computing architecture to perform the building detection and reconstruction method on large VHR SAR scenes.

cluster infrastructure. In such a framework, the nodes in the cluster process different subsets of the input image in parallel. Each subset contains only few primitives, and thus also a reduced number of footprint hypotheses. This enables us to apply the proposed technique on large scenes in a fast way on state-of-the-art hardware. In Fig. 6.11 a block scheme of the considered simple architecture is presented. As a first step, the VHR SAR image is split into tiles. Every tile overlaps with its neighbors to assure that buildings located at the tile borders are detected and reconstructed properly at least in one tile. Then, the tiles are distributed across the nodes which independently execute the proposed method. Finally, the results for each tile are merged in order to generate the final radar footprint map for the entire input scene. When footprint hypotheses coming from different tiles overlap on tile borders, the algorithm selects the ones with the highest score.

6.4 Experimental Results

In this section we show the results obtained by applying the proposed methodology to a real meter-resolution large SAR image. After a brief description of the used dataset, we show and analyze qualitatively the results obtained on the whole image following the grid-computing approach described in Sec. 6.3. Then, we focus on two subsets of the image in order to assess quantitatively the accuracy of the method.

6.4.1 Dataset Description

The effectiveness of the proposed method has been tested on the ascending spotlight TerraSAR-X image of the city of Dorsten, Germany, used also in Chapter 5. The image has a geometrical resolution of approximately 1.1 m $\times$ 1.2 m (azimuth $\times$ slant range). The incidence angle varies between 50.3° and 51.0°. The original scene has been cut to a subset of 2800 $\times$ 3712 pixels, covering an area of approximately 10 km^2. The cut includes both urban and rural areas. Urban areas are characterized by both flat- and gable-roof buildings at various settings. Fig. 6.12 shows the SAR test image and an optical image corresponding to the same area taken from Google™ Maps [151].

(a)

(b)

Figure 6.12: (a) TerraSAR-X image used for assessing the effectiveness of the proposed technique (© Infoterra). (b) Optical image taken from Google™ Maps of the investigated area (© Google).

6.4.2 Results on the Entire Scene

The proposed method has been run using the parameters reported in Tab. 6.1, Tab. 6.2 and Tab. 6.3. The values of such parameters have been chosen according to the guidelines given in Sec. 6.2. The results obtained are shown in Fig. 6.13. The method shows in overall a high detection rate. False alarms are mostly related to the scattering from objects different from buildings (e.g., trees, garages) that show radar footprints similar to those of buildings. A particular case is represented by bridges, which have been also detected. Such structures can be easily masked, either using *a priori* information about the presence of rivers, or by extracting the rivers directly from the SAR scene [152].

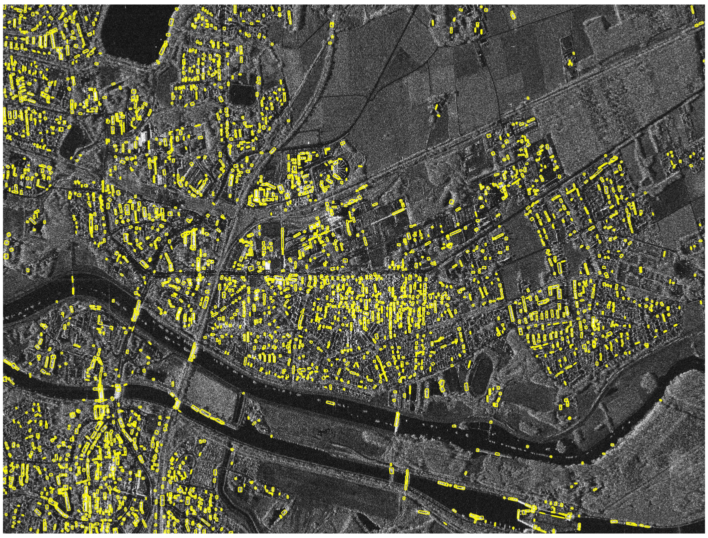

Figure 6.13: Building detection and radar footprint reconstruction obtained by the proposed technique on the SAR image of Fig. 6.12a. Only the bright parts of the reconstructed building radar footprints are shown.

Table 6.1: Parameters used in the feature extraction and primitive generation steps in the experiments carried out with the proposed technique.

Parameter	Value
T	7
$w_1, \ldots, w_7$	3,5,...,15
$\delta w_{\max}$	3
A_t	0.5
ξ_S	-12.2 dB
l_S	30 m
$\delta\psi_{\max}$	20°

The radar footprints of complex buildings which do not correspond to the rectangular model used in this thesis are mostly detected with some reconstruction errors (e.g., the radar footprint has been split in more parts). In general, the proposed method detected and reconstructed quite precisely the radar footprints of medium- and big-size buildings that fulfill the rectangular model. Radar footprints of small adjacent buildings aligned in regular patterns are also detected, but in some cases are considered as belonging to a single building. Small buildings which do not show clear features are not detected by the method. However, considering the use of a single SAR image, the results can be considered qualitatively very satisfactory. Moreover, it is worth noting that if the proposed method is applied in order to derive indexes of the presence of buildings, reconstruction errors (i.e., split and merged buildings) do not represent a critical issue. In order to analyze quantitatively and in greater detail the results achieved by the proposed method, in the following we focus on two subsets of the test image.

Table 6.2: Parameters used in the analysis of primitives step in the experiments carried out with the proposed technique.

Parameter	Value
B_r	0.999
$w_r^{\text{thin}}, w_0^{\text{thin}}$	5 m, 7 m
$w_r^{\text{thick}}, w_0^{\text{thick}}$	5 m, 3 m
$\phi_r^{\text{DB}}, \phi_0^{\text{DB}}$	10°, 30°
$\zeta_r^{\text{hom}}, \zeta_0^{\text{hom}}$	0.3, 0.5
$\zeta_r^{\text{non-hom}}, \zeta_0^{\text{non-hom}}$	0.3, 0.2
$\phi_r^{\text{F}}, \phi_0^{\text{F}}$	70°, 80°
$\tilde{\mu}_r^{\text{S}}, \tilde{\mu}_0^{\text{S}}$	-13.6 dB, -8.6 dB

Table 6.3: Parameters used in the selection of hypotheses and 2D radar footprint reconstruction steps in the experiments carried out with the proposed technique.

Parameter	Value
$n'_{\tilde{h}}$	0.8
$\delta d_r, \delta d_0$	3 m, 10 m
$\delta\psi_r, \delta\psi_0$	10°, 30°
$S_{\tilde{h},\min}$	0.7

6.4.3 Results on the Subset 1

Fig. 6.14 shows the area corresponding to the subset 1 in both the SAR and optical images. This area is characterized by both flat- and gable-roof buildings with different sizes and orientations. In particular, the upper part of the image contains mainly medium to large buildings, while the bottom part includes smaller buildings, which are also often joined together and surrounded by gardens with other man-made structures or trees. In order to assess the performance of the proposed technique, we consider the correct/missed and false building detection rates and correlate such results with the size of the buildings. The number of split or merged buildings is also counted. The planar area of the buildings (length $\times$ width) has been estimated using the optical image. The set of buildings present in the investigated area has been divided into three subsets: *small*, *medium* and *large*. Each subset corresponds to a different range of planar areas. Buildings are considered to be small if their planar area is smaller or equal to 200 m^2, medium if the area is between 200 and 400 m^2, and large if it is greater than 400 m^2. Tab. 6.4 reports the number of buildings for each size class in the subset 1 and the number of buildings correctly detected given by the proposed technique. As it is difficult to measure numerically the accuracy of the reconstruction of the building radar footprints, here we only evaluate the detection performance of the algorithm in terms of footprints detected in correspondence of actual buildings. The detections have been checked manually by comparing the SAR image, an optical image of the same area, and the positions of the footprints extracted by the algorithm. A building is considered detected if the algorithm extracted a footprint in correspondence of the actual building footprint. Fig. 6.14e shows the correct and missed detection on the optical image. The results point out that the overall detection rate of the

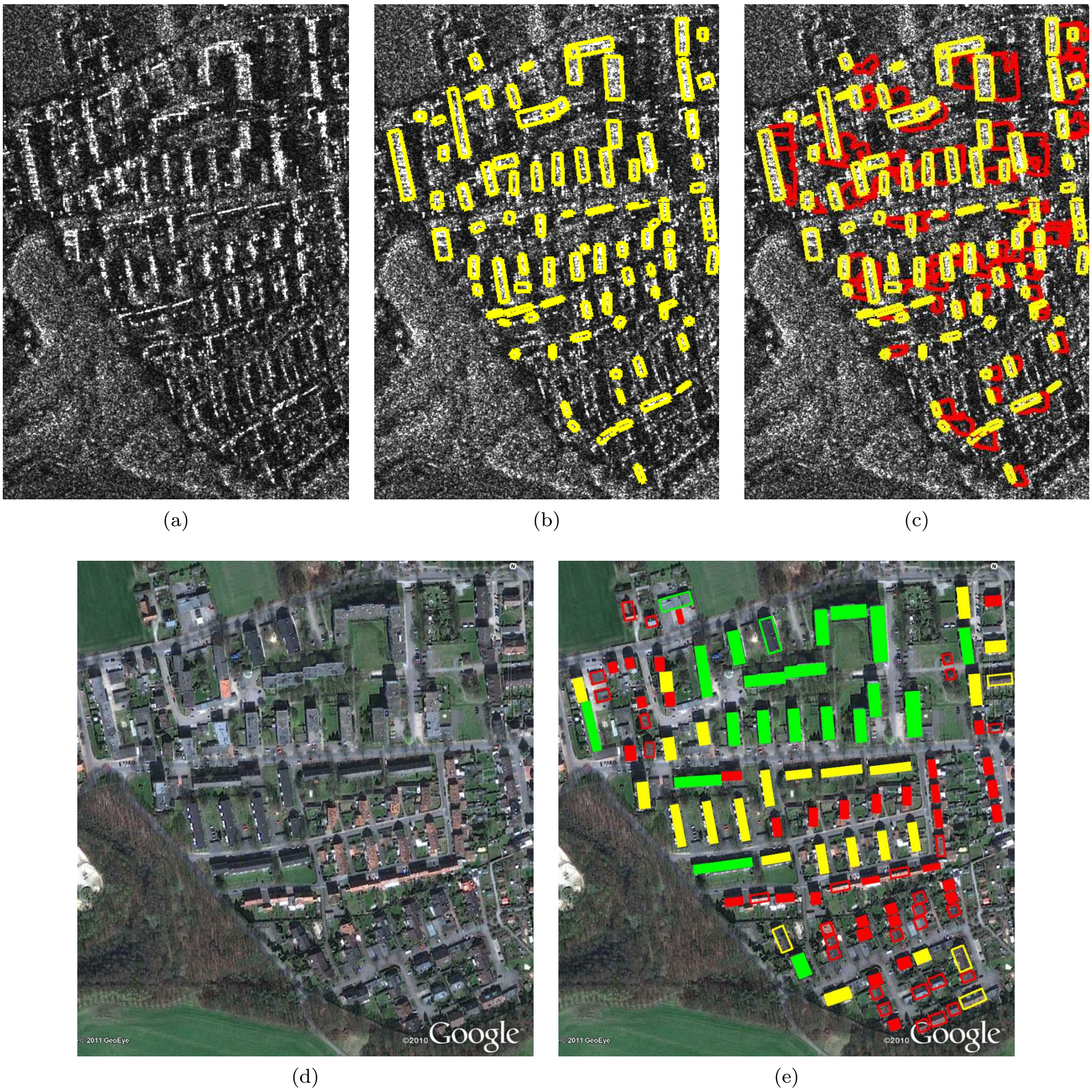

Figure 6.14: Subset 1: (a) original TerraSAR-X image of the considered area, viewing direction from left (© Infoterra); (b) reconstructed bright parts of the detected building radar footprints on the SAR image; (c) reconstructed building radar footprints on the SAR image: (yellow) bright parts, (red) dark parts; (d) optical image (© Google); (e) optical image with detected and missed buildings for each building size class: (green) *large*, (yellow) *medium*, and (red) *small*. Detected and missed buildings are highlighted with filled and empty rectangles, respectively.

proposed technique is high, especially considering that the method is unsupervised and works on a single meter-resolution VHR SAR image. The performance of the technique is very good for medium and large buildings, while small buildings result in a higher number of missed alarms. This expected result is due to the fact that small buildings in meter-resolution images often do not show the scattering features used by the proposed technique. On the one hand, the number of split buildings is 1, 4 and 2 for the classes

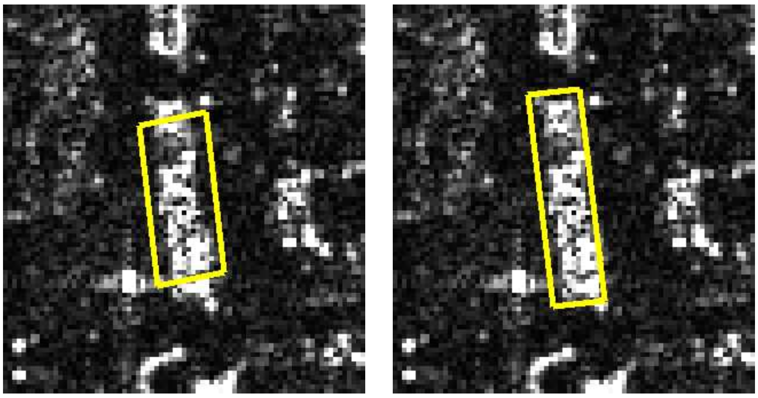

(a) (b)

Figure 6.15: Example of bright part of a radar footprint hypothesis (a) before, and (b) after the 2D footprint reconstruction step.

small, *medium* and *large*, respectively. Therefore, as far as building size increases, the probability that the technique splits the radar footprints in more parts increases. On the other hand, as far as building size decreases, the probability that the radar footprints of adjacent buildings are detected as a single one increases. In fact, the number of merged buildings is 9 for the class *small*, 3 for the class *medium* and 1 for the class *large*. The number of false alarms in building detection is 11. The size of the bright part of the false building radar footprints has been measured on the SAR image and false alarms have been divided in *small*, *medium* and *large* according to the same rules used for building planar sizes. Although the two measurements considered (i.e., area of false building radar footprints and planar area of real buildings) are different, the use for false alarms of the same classes as for real buildings allows us to give an indication on the types of false alarms produced by the proposed method. As shown in Tab. 6.4, false alarms are mostly related to small radar footprints. By comparing the SAR image to the optical image it is clear that false alarms usually correspond to other man-made structures (e.g., garages) or trees which show radar signatures that are very similar to those of buildings. Such false alarms are also difficult to be detected by an expert human interpreter without other sources of information (e.g., a reference optical image). The footprints reconstructed by the proposed technique are usually accurate for medium and large buildings. As an example, Fig. 6.15 shows the refinement of the bright part of a footprint hypothesis after the 2D footprint reconstruction step. For small buildings the radar footprints are often reconstructed with lower accuracy. Fig. 6.14c shows also the detected (and reconstructed) building shadows. The proposed technique extracted with good accuracy most of the shadow areas related to the detected building radar footprints. This result can be used for further estimations on the building sizes, e.g., for estimating building heights [110]. However, it is worth noting that in many cases shadow areas are limited by adjacent buildings, thus reducing their usefulness for height extraction purposes.

Table 6.4: Algorithm performance for Subset 1, Subset 2 and Subset 1 + Subset 2 in terms of number of detected buildings, false alarms, split and merged buildings per building class.

	Building size	**Number of buildings**	**Detected**	**False alarms**	**Split**	**Merged**
Subset 1	Large	21	19	0	2	1
	Medium	26	22	2	4	3
	Small	66	35	9	1	9
Subset 2	Large	12	12	0	4	0
	Medium	27	23	2	4	3
	Small	53	34	9	1	8
Subsets 1+2	Large	33	31	0	6	1
	Medium	53	45	4	8	6
	Small	119	69	18	2	17

6.4.4 Results on the Subset 2

The area corresponding to the subset 2 is shown in Fig. 6.16. This area is characterized by a large number of trees located along the streets (in Fig. 6.16d it is possible to see their shadows). Such trees often mask the radar returns also from medium-sized buildings. Moreover, small buildings are usually quite irregular, and show many structures on their walls. This subset is thus a challenging benchmark for the proposed technique. Tab. 6.4 reports the results obtained for the subset 2, and Fig. 6.16e shows the correct and missed detections on the optical image. As for the subset 1, the detection rate for the classes *large* and *medium* is very good. For the class *small* performance are less satisfactory. The number of split buildings is 1 for the class *small*, 4 for the class *medium* and 4 for the class *large*; while the number of merged buildings is 8 for the class *small* and 3 for the class *medium*. The total number of false alarms is 11. As for subset 1, the most of them are related to small false building radar footprints. In overall, considering the issues mentioned at the beginning of this paragraph and the limited amount of information used by the proposed technique, the results can be considered very good. In order to provide a more general view of the results obtained by the proposed method, Tab. 6.4 also reports the overall results computed by summing the results of the subsets 1 and 2. The total statistic confirms the trend highlighted for the single subsets, i.e., the algorithm has a high detection rate for medium and large buildings, with a limited amount of false alarms, whereas its performance decreases in the case of small buildings, which are associated to most of the total number of false alarms. It is worth noting that it is possible to mitigate this problem by imposing a rule for discarding the footprints smaller than an user-defined minimum footprint size. As a consequence, the number of false alarms would be considerably reduced and the detection of small buildings would not be a target of the method anymore. This is a reasonable strategy to adopt for tuning the proposed technique only on the detection of medium and large buildings.

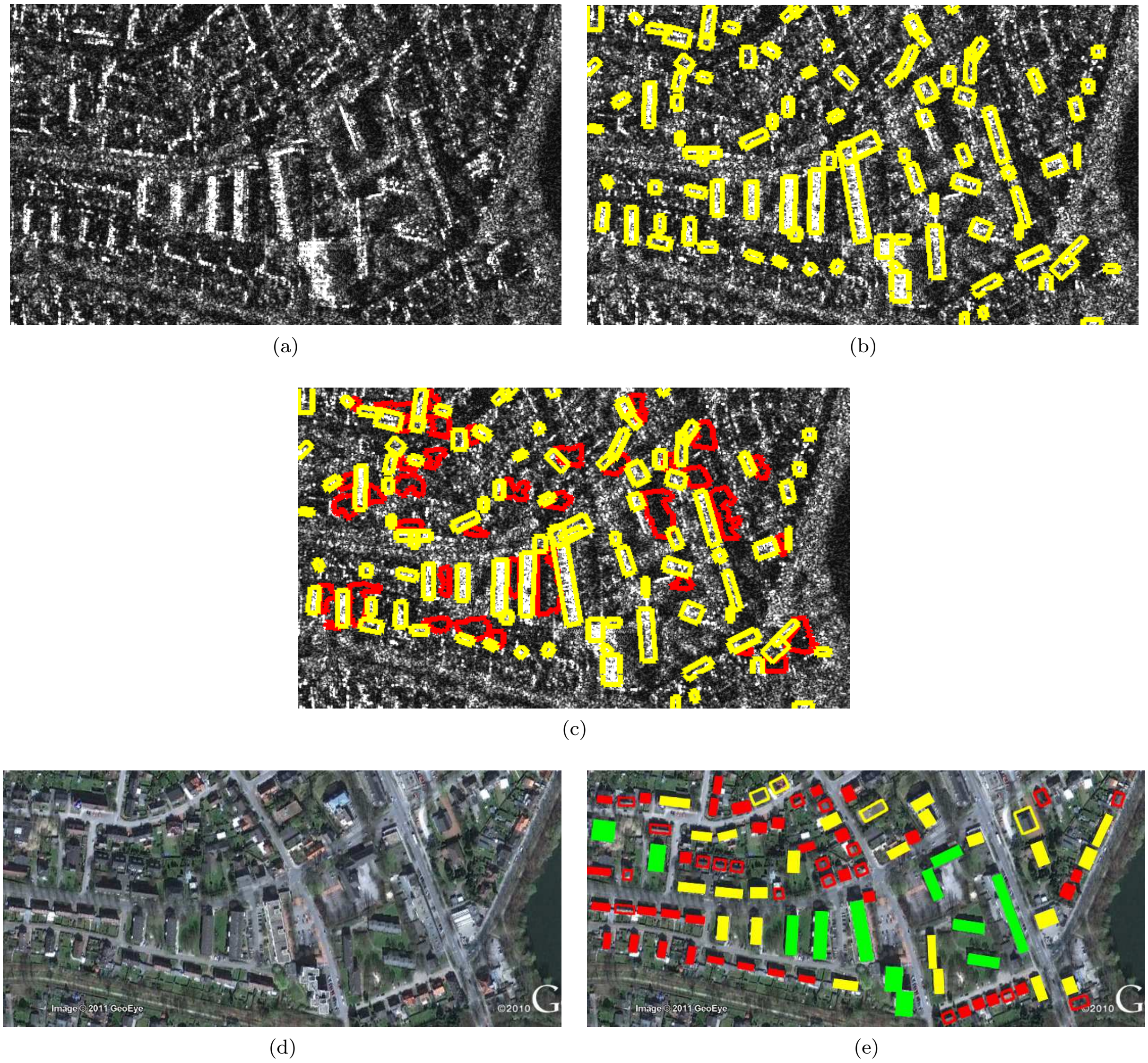

Figure 6.16: Subset 2: (a) original TerraSAR-X image of the considered area, viewing direction from left (© Infoterra); (b) reconstructed bright parts of the detected building radar footprints on the SAR image; (c) reconstructed building radar footprints on the SAR image: (yellow) bright parts, (red) dark parts; (d) optical image (© Google); (e) optical image with detected and missed buildings for each building size class: (green) *large*, (yellow) *medium*, and (red) *small*. Detected and missed buildings are highlighted with filled and empty rectangles, respectively.

6.4.5 Selection of Algorithm Parameters

The tuning of the parameters has been performed according to the scene investigated. However, some parameters are not strictly related to the image analyzed, and can be set *a priori* following general rules. Moreover, many of the considered parameters have a clear physical meaning that helps the user to include its prior knowledge on the scene in the detection algorithm. In addition to the guidelines already provided in Sec. 6.2, in this section we analyze more in detail the role of the parameters of the proposed method.

Feature extraction and primitive generation

In these steps the main parameters of the proposed technique are related to the detection and generation of bright rectangles, and to the extraction of the shadows. The possible range of values for the window of the line detector w_u should be set between the expected thickness of thin linear features and the maximum size of the buildings which has to be extracted. The sampling of the range of w_u, given by the number of filterings T, should assure that most of the linear features can be effectively modeled with the considered values of w_u. The minimum value for $\delta w_{\max}$ has to be greater than the width sampling resulting from the definition of the values of w_u. On the one hand, a value smaller than this quantity would not allow the algorithm to downselect effectively the rectangles produced in the feature extraction step. Moreover, the procedure for the generation of primitives would combine only rectangles with approximately the same width. On the other hand, a value much greater than the width sampling would make the algorithm to downselect too many rectangles, and combine features with much different widths. According to our tests, a good choice for the value of $\delta w_{\max}$ is 1.5 times the width sampling used in the line detection. Regarding the parameters A_t and $\delta\psi_{\max}$, high values for A_t and low angles for $\delta\psi_{\max}$ make conditions (6.3) and (6.4) too stringent, respectively. By setting $A_t = 0.5$ and $\delta\psi_{\max} = 20°$ we obtained the best results in our experiments. Note that these settings are general and do not depend on the image under analysis.

As mentioned in Sec. 6.2.1, the choice of the value of ξ_{S} depends on the characteristics of the shadow regions in the SAR image. The results obtained with different values for ξ_{S} showed that the detection and reconstruction of the shadows is not sensitive to slight variations of the parameter. The choice of l_{S} depends on the maximum expected height of the buildings present in the scene (and thus of their shadows). Thus, this parameter should be set according to the acquisition incidence angle and to prior information on the scene. However, if no *a priori* information is available, a large value can be set. This does not affect significantly the detection of the radar footprints. In fact, footprint hypotheses including dark primitives which are not close to bright primitives (which have been kept in the feature extraction due to a large l_{S}) are penalized by the term (6.21) in the selection of hypotheses. Thus, only the reconstruction step is affected by the choice of l_{S}, as shadows can grow further.

Analysis of primitives

In this step the main parameters to be set are those related to the membership functions defined for the different scattering classes. The choice of the value of B_r is not critical, and $B_r = 0.999$ can be considered as a fixed value. The parameters $w_r^{\mathrm{thin}} = w_r^{\mathrm{thick}}$, w_0^{thin}, and w_0^{thick} used in this chapter can also be considered general. Indeed, they are given in meters, so that they do not depend on the resolution of the system. According to our tests, by setting $w_r^{\mathrm{thin}} = w_r^{\mathrm{thick}}$ to a value 2-3 m greater than the expected thickness of the linear signatures due to the double-bounce effect give the best results, as the procedure which creates rectangles from the output of the line detector may overestimate their actual thickness.

The values of the parameters ϕ_r^{DB}, ϕ_0^{DB}, ϕ_r^{F}, and ϕ_0^{F} are defined on the basis of our experience in analyzing VHR SAR images. These values are also general, and can be considered valid for most images of urban areas. The main studies carried out specifically on the relation between the double-bounce effect and the orientation angle of buildings has been described in Chapter 5.

The choice of the values $\zeta_r^{\text{hom}} = \zeta_r^{\text{non-hom}}$, ζ_0^{hom}, and $\zeta_0^{\text{non-hom}}$ depends on the characteristics of speckle in the considered image. As the membership functions are evaluated on the GMAP filtered image, different parameters applies for different filterings. Similarly, these parameters depend on the image resolution, as speckle develops differently on the same target depending on resolution. For these reasons, the correct choice of these values in terms of capability to model effectively homogeneous and non-homogeneous areas comes after a proper optimization of the GMAP filtering parameters.

The last parameters used in this step are $\tilde{\mu}_r^{\text{S}}$ and $\tilde{\mu}_0^{\text{S}}$. As for ξ_{S}, these values depend on the characteristics of shadows in the SAR image. According to our experiments, $\tilde{\mu}_r^{\text{S}}$ and $\tilde{\mu}_0^{\text{S}}$ should be set about 1.5 dB lower and 3-4 dB greater than ξ_{S}, respectively. This allows one to obtain a quite smooth term $\Sigma_{\tilde{\mu}}^{\text{S}}(\tilde{\mu})$ in (6.14). Indeed, the mean amplitude of a dark region corresponding to a shadow may be biased by the interference of surrounding structures which increases its value. Thus, using a sharp $\Sigma_{\tilde{\mu}}^{\text{S}}(\tilde{\mu})$ would make the algorithm to discard possible real shadows.

Selection of hypotheses and 2D radar footprint reconstruction

As mentioned in Sec. 6.2.5, the parameter $n'_{\tilde{h}}$ is related to the reliability assigned by the user to the footprint hypotheses composed by only two primitives. In our tests, by setting this parameter to higher values resulted in detection maps with less hypotheses composed by three primitives, as expected. This does not affect significantly the detection rate of the proposed method, but it increases the probability that the extracted footprints are not well-reconstructed (e.g., shadows are missing even though they were detected). On the contrary, by setting $n'_{\tilde{h}}$ to low values would increase the number of missed detections. Therefore, the choice of $n'_{\tilde{h}}$ should be done by the user as a trade-off between reliability of the reconstruction and detection performance.

The pair of parameters $(\delta d_r, \delta d_0)$ and $(\delta\psi_r, \delta\psi_0)$ are related to the vicinity and relative orientation of the primitives, respectively. The values proposed in this chapter can be considered general for the defined scattering classes. Note that using these values the sigmoid functions present in (6.16) and (6.21) are quite smooth, thus mitigating the effect of possible errors in feature extraction.

The last parameter to be discussed is $S_{\tilde{h},\min}$. This parameter gives the trade-off between false and missed detections. According to our tests, the use of high $S_{\tilde{h},\min}$ results in a greater number of missed detections, as expected. However, the number of false alarms is not reduced significantly. Indeed, these are usually related to footprints of other man-made structures, or trees, which actually appear as related to buildings. For this reason, values in the order of 0.6-0.7 are suggested.

6.4.6 Computational Load

The test image described in Sec. 6.4.1 has been processed using a cluster composed by 16 AMD® Opteron™ 6172 CPUs, for a total of 192 cores, with 4 GB of RAM per core. The image has been split on tiles of 300 × 300 pixels with an overlapping offset of 30 pixels with the neighbors. The total number of tiles was thus 154, and each tile was processed by one core. The total processing time was about 45 minutes. With the same infrastructure it is thus possible to process a whole spotlight image of about 6000 × 10.000 pixels in less than 3 hours. We also tested the proposed technique using a smaller cluster composed by 8 commercial workstations equipped with Intel® Core™ i7-870 quad-core processors and 8 GB of RAM. The total processing time for the test image on this smaller architecture was about 1 hour and 30 minutes, which is a good performance in terms of operational application of the algorithm.

6.5 Discussion and Conclusion

In this chapter the problem of the detection and reconstruction of building radar footprints in VHR SAR images has been addressed. Unlike many other methods presented in the literature, the proposed technique can be applied to single VHR SAR images. It extends state-of-the-art feature extraction and composition steps to more structured primitives using a production system and by introducing the concept of semantic meaning. This has been done in order to compensate for the lack of information due to the fact that only one VHR SAR image is used as input. The semantic meaning represents the probability that an object belongs to a certain scattering class (e.g., facade, double bounce), and is calculated via fuzzy membership functions. Therefore, it allows the technique to select the most reliable primitives and footprint hypotheses during its processing steps. As a further refinement, the proposed technique also reconstructs the detected radar footprints. The goal of this step is to provide as output a map which can be used for further calculations, e.g., the estimation of building widths and lengths. Moreover, by exploiting the reconstruction of the shadow areas, height retrieval techniques can be also applied to estimate building heights. In order to make it possible to use the proposed technique on large VHR SAR images in near real-time, we also proposed and implemented an infrastructure based on a computer cluster for the processing of large VHR SAR scenes.

The proposed method is suited for meter-resolution SAR images. However, it can be extended and tuned for higher-resolution airborne data by introducing new types of primitives, composed objects and rules. Moreover, new semantic classes for the primitives should be defined, as finer scattering mechanisms become visible in submeter data.

The experimental results obtained on a large meter-resolution SAR image confirmed the effectiveness of the proposed technique. In particular, the method shows very high detection rates in the case of medium and large buildings, exhibiting also a good capability to reconstruct their radar footprints. The number of false alarms is limited, and these are mostly related to other man-made structures or trees which show radar signatures similar to those of buildings. For small buildings the proposed technique shows worse detection and reconstruction performance, and an increased number of false alarms. This is mainly due to the low number of features related to small buildings visible in single meter-resolution SAR images. Nonetheless, this is an expected problem, which is mainly related to the need to use submeter-resolution images for a proper detection of these buildings, rather than to a limitation of the proposed technique. In order to mitigate this problem, it is possible to include a simple rule in the proposed technique for discarding the radar footprints smaller than an user-defined threshold, thereby reducing the number of false alarms and avoiding the detection of small buildings. This is a reasonable strategy to adopt for tuning the proposed method only on the detection of medium and large buildings, on which performances are very accurate.

The proposed approach needs the user to set some parameters which depend on the product under analysis. After this, the method is automatic and can be applied with the same set of parameters to similar products. Guidelines for the selection of the parameters were given throughout the chapter. It is worth noting that many relevant parameters have been already selected on calibrated SAR images so that they can be applied to different VHR SAR scenes without the need to be changed.

The proposed technique is promising for addressing problems in real operative scenarios which exploit the available spaceborne meter-resolution SAR systems (e.g., COSMO-SkyMed, TerraSAR-X, and TanDEM-X). As an example, it can be used for a fine estimation of the density of urban areas even from single images or it can be used for the analysis of multitemporal series, e.g., for the detection of changes in urban areas. It is worth noting that the method is independent of the viewing configuration of the SAR sensor, as it works in the vector domain. This makes it possible to potentially combine the results obtained from SAR acquisitions taken with different viewing angles, or also maps derived from optical images. This would allow a finer detection of buildings and a more accurate estimation of building properties. However, the problem of the correct geolocalization of buildings in the different acquisitions should be faced e.g., for the correct merging of the single radar and/or optical footprint maps.

Conclusions

This chapter concludes this thesis by providing a summary of the novel contributions and the related experimental results presented in the document. Finally, future developments of the proposed methods are discussed.

Summary and Discussion

In this thesis we have presented novel methods for the automatic analysis of RS and VHR SAR signals. Such methods represent a valuable contribution for the analysis of the data provided by new generation radars mounted onboard of orbiting platforms. Indeed, in order to effectively exploit both the amount of data provided by new missions and their properties, automatic information extraction methods are essential to support both scientific studies and practical application scenarios.

In the first part of the thesis we presented novel automatic methods for the analysis of RS data. This topic has been only marginally addressed in the literature so far. As a first step, we carried out a statistical analysis of RS signals aimed at the development of automatic methods for the detection and characterization of subsurface features. Then, we proposed a technique for the automatic extraction and analysis of ice layering. Finally, a method for the automatic detection of surface clutter returns through clutter simulation matching has been developed.

In the study of the properties of sounder signals we analyzed different statistical models from a theoretical point of view and then empirically tested them on different real SHARAD data acquired on the NPLD of Mars. The obtained results show that the statistical distributions of the amplitude signals related to different types of targets can be modeled precisely using the K distribution, while, as expected, the background noise follows a Rayleigh distribution. Exploiting the results of the aforementioned study, we have then proposed two novel techniques for the automatic analysis of radargrams aimed at: i) producing maps of the subsurface areas showing relevant features; and ii) identifying and mapping the deepest scattering areas visible in the radargrams. The former is based on the comparison of the distributions of local subsurface parcels with that of noise adaptively estimated on each radargram. The latter exploits a specifically defined region-growing method implemented in an iterative technique based on the level-set algorithm. The results obtained by both the developed techniques are accurate and thus promising for operational applications.

The proposed novel method for the automatic detection and characterization of subsurface linear features in RS data is suited to the analysis of regions showing extended layering. The method is based on the joint radargram denoising and enhancement, followed by a line detection step which operates with sub-pixel accuracy. In order to extract further information from the radargrams, we also proposed a set of measurements which can be derived from the detected linear features. Such measures can describe locally the properties of the single linear features and provide information about their distribution within the radargram (and thus the geographical area of interest). The technique and the measurements proposed in this thesis are relevant for the automatic analysis and combination of many RS acquisitions over large areas. Indeed, they can provide in a fast way information on subsurface layering which can be used to derive high level products in a global mapping perspective, or to drive further manual analysis on interesting areas.

The novel technique for the automatic detection of surface clutter returns from RS data is based on the automatic coregistration between real radargrams and surface clutter simulations. The coregistration is performed by a two-step procedure. The first step aims at performing a coarse registration of the inputs, while the final coregistration is carried out in the second step using a deformable transformation. The main output of the proposed method is a binary map representing the areas of the radargram which have high probability to be affected by clutter returns. In addition, the intermediate outputs of the method (e.g., coregistered clutter simulations) can be also used to support manual investigations. In this framework, we also presented a fast clutter simulator suited to both user-oriented real-time analyses and batch processing. The qualitative and quantitative experimental results obtained on two large datasets acquired by the SHARAD instrument at Mars confirm that the technique is capable to align with good precision clutter simulations to radargrams affected by geometrical distortions (e.g., due to variations of the ionospheric delay during the same acquisition). The proposed method represents an important contribution to the analysis of planetary RS data. Indeed, the detection of surface clutter through the comparison with clutter simulations is nowadays performed manually by scientists, thus introducing subjectivity and wasting time and resources.

The methods developed in this thesis are suited to be included in the basic processing chain of RS data. In this way, it is possible to generate high-level products that can be distributed along with radargrams (e.g., maps of subsurface features, detected basal returns, extracted layering, clutter maps). The joint analysis of radargrams and such products would greatly help the community and increase the scientific return of the data.

The second part of this dissertation presented the main contributions on the analysis of VHR SAR images of urban areas. In particular, we described in detail the empirical and theoretical study carried out on the relation between the double-bounce effect of buildings and their orientation angle. Then, a novel approach to the automatic detection of building radar footprints from single VHR SAR images has been illustrated.

The presented study on the strength of the double-bounce scattering mechanism with respect to the orientation angle of buildings in VHR SAR investigated three classes of buildings in two TerraSAR-X images and compared these results with theoretical electromagnetic scattering models. In this context, we presented a novel model for predicting the double-bounce power based on SPM, which is suitable for urban surfaces like asphalt.

The results pointed out that the double-bounce effect has a strong power signature for buildings which have the wall on the sensor close side almost parallel to the SAR azimuth direction. Furthermore, the strength of the double bounce decays rapidly in a narrow range of orientation angles, while it decays moderately for larger angles. The exact characteristic of the decay depends on the material and surface parameters, making the double bounce a variable feature within the same scene. As a result, the double-bounce feature can only be used for reliable building detection and reconstruction by taking into account its non-linear relation with the orientation angle. The comparison between the predictions from the theoretical electromagnetic models based on SPM and PO and the real data showed that the general behavior of the double bounce can be derived with theoretical models. However, the complexity of the actual scene hampers the reliable calculation of the double-bounce RCS. The presented study demonstrated that the correct behavior of the double-bounce effect with respect to the orientation angle of buildings can be derived empirically considering a few real world cases. This result can be integrated easily in practical feature extraction application scenarios (e.g., for the development of building detection/reconstruction techniques from meter-resolution SAR images).

The proposed method for the automatic detection of building radar footprints can be applied to single VHR SAR images. This is a major innovation, as most of the methods presented in the literature that address this topic rely on multi-dimensional data. The technique extends state-of-the-art feature extraction and composition steps to more structured primitives using a production system and by introducing the concept of semantic meaning. This has been done in order to compensate for the lack of information due to the fact that only one VHR SAR image is used as input. The semantic meaning represents the probability that an object belongs to a certain scattering class (e.g., facade, double bounce), and is calculated via fuzzy membership functions. Therefore, it allows the technique to select the most reliable primitives and footprint hypotheses during its processing steps. As a further refinement, the proposed technique also reconstructs the detected radar footprints. The goal of this step is to provide as output a map which can be used for further calculations, e.g., the estimation of building widths and lengths. Moreover, by exploiting the reconstruction of the shadow areas, height retrieval techniques can be also applied to estimate building heights. In order to make it possible to use the proposed technique on large VHR SAR images in near real-time, we also proposed and implemented an infrastructure based on a computer cluster for the processing of large VHR SAR scenes. The experimental results obtained on a large meter-resolution SAR image confirmed the effectiveness of the proposed technique. In particular, the method shows very high detection rates in the case of medium and large buildings, exhibiting also a good capability to reconstruct their radar footprints. For small buildings the proposed technique shows worse detection and reconstruction performance, and an increased number of false alarms. This is mainly due to the low number of features related to small buildings visible in single meter-resolution SAR images. Nonetheless, this is an expected problem, which is mainly related to the need to use submeter-resolution images for a proper detection of these buildings, rather than to a limitation of the proposed technique. Despite this limitation, the proposed technique is promising for addressing problems in real operative scenarios which exploit the available spaceborne meter-resolution SAR systems (e.g., COSMO-SkyMed, TerraSAR-X, and TanDEM-X).

Concluding Remarks and Future Work

The studies, the techniques and the results described in this thesis regarding planetary radar sounding are a first step to the definition of a general framework for the analysis of RS data. The goal of such a framework is to extend the low-level processing chain currently applied to the downlinked data with high-level information extraction steps. To this end, additional automatic techniques for the extraction of features and parameters from radargrams should be developed with respect to what presented in this document. This should be done by taking into account indications provided from scientists expert of the considered application and of the related requirements. The framework could be also extended to the use of input data coming from other sensors (e.g., optical images of the investigated area). Although human interpretation cannot be fully replaced by automatic algorithms, automatic methods can significantly help to overcome the subjectivity intrinsic in manual investigations by providing in a fast way numerical results obtained with predefined and fixed metrics. These results can then drive further manual refinements.

At the present time, the techniques developed for the automatic extraction of information from RS signals are important especially for the analysis of the data provided by the currently operating RSs at Mars. However, the development of automatic methods such as the ones proposed in this thesis becomes important also for future spaceborne missions exploring other planetary bodies or the Earth's polar regions. In the latter case, it is expected that a RS orbiting the Earth will provide a huge amount of high-precision data, allowing also multi-temporal studies. All these factors make automatic methods suitable for a fast and objective analysis of the data, which can help to provide information for the assessment of the impact of climate changes on the Earth's system.

Future developments regarding the methods related to the analysis of RS data illustrated in this thesis should focus on their full automatization and generalization in order to make them suited for the analysis of a wider set of RS data with different characteristics. In particular, future work should address the following points:

- Definition of a procedure for the unsupervised and adaptive selection of the parameters of the presented techniques.
- Development of novel methods for the generation of subsurface feature maps based on the local statistics using context-sensitive techniques for the adaptive determination of the local parcel size.
- Test of the proposed method for the extraction of ice layering on datasets acquired at different frequencies and resolutions on Mars, and on the Earth's polar regions by airborne RSs.
- Test the proposed method for the automatic detection of surface clutter with other clutter simulators and with different real datasets (e.g., focused with different parameters or acquired by other instruments, including airborne RSs operating in the polar regions of the Earth).

Regarding the part of the thesis related to the analysis of VHR SAR data of urban areas, future developments should be devoted to the definition of a (semi-) automatic procedure for the setting of the parameters of the proposed method for the automatic detection of building radar footprints. Moreover, although the method is suited for meter-resolution SAR images, it can be extended and tuned for higher-resolution airborne data by introducing new types of primitives, composed objects and rules. To this aim, new semantic classes for the primitives should be defined, as finer scattering mechanisms become visible in submeter data. The proposed technique can be also extended to both the analysis of multi-aspect acquisitions (e.g., images acquired on ascending and descending orbits) and the integration of interferometric height information in the steps of the processing chain. In this way it is possible to develop a flexible framework for building detection and radar footprint extraction requiring as minimum only a single SAR scene, but making best use of additional input data if available. The integration of the presented method with state-of-the-art change detection algorithms can be also investigated in order to develop novel reliable approaches to change detection in urban areas using VHR SAR multi-temporal series.

List of Publications

Journal Papers

[1] A. Ferro, D. Brunner, L. Bruzzone, and G. Lemoine, "On the relationship between double bounce and the orientation of buildings in VHR SAR images," *IEEE Geosci. Remote Sens. Lett.*, vol. 8, no. 4, pp. 612–616, 2011.

[2] L. Bruzzone, G. Alberti, C. Catallo, A. Ferro, W. Kofman, and R. Orosei, "Subsurface radar sounding of the Jovian Moon Ganymede," *Proc. IEEE*, vol. 99, no. 5, pp. 837–857, 2011.

[3] A. Ferro and L. Bruzzone, "Analysis of radar sounder signals for the automatic detection and characterization of subsurface features," *IEEE Trans. Geosci. Remote Sens.*, Submitted for publication in January 2011.

[4] A. Ferro, D. Brunner, and L. Bruzzone, "Automatic detection and reconstruction of building radar footprints from single VHR SAR images," *IEEE Trans. Geosci. Remote Sens.*, Submitted for publication in April 2011.

[5] A. Ferro and L. Bruzzone, "Automatic extraction and analysis of ice layering in radar sounder data," *IEEE Trans. Geosci. Remote Sens.*, Submitted for publication in August 2011.

[6] A. Ferro, A. Pascal, and L. Bruzzone, "A novel technique for the automatic detection of surface clutter returns in radar sounder data," *IEEE Trans. Geosci. Remote Sens.*, Submitted for publication in November 2011.

International Conferences

[1] D. Brunner, L. Bruzzone, A. Ferro, J. Fortuny, and G. Lemoine, "Analysis of the double bounce scattering mechanism of buildings in VHR SAR data," in *Proc. SPIE Conf. on Image and Signal Processing for Remote Sensing XIV*, vol. 7109, 2008, pp. 71 090Q–71 090Q–12.

[2] D. Brunner, L. Bruzzone, A. Ferro, and G. Lemoine, "Analysis of the reliability of the double bounce scattering mechanism for detecting buildings in VHR SAR images," in *Proc. IEEE Radar Conf*, 2009, pp. 1–6.

[3] A. Ferro, D. Brunner, and L. Bruzzone, "An advanced technique for building detection in VHR SAR images," in *Proc. SPIE Conf. on Image and Signal Processing for Remote Sensing XV*, vol. 7477, 2009, pp. 74 770V–74 770V–12.

[4] A. Ferro, D. Brunner, and L. Bruzzone, "Detection and reconstruction of building footprints from single VHR SAR images," in *Synthetic Aperture Radar (EUSAR), 2010 8th European Conference on*, 2010.

[5] G. Alberti, S. Mattei, R. Seu, L. Bruzzone, A. Ferro, R. Orosei, A. Olivieri, and C. Catallo, "Preliminary performance of Sub-Surface Radar for the EJSM/Laplace mission," in *Proc. 13th Int. Ground Penetrating Radar (GPR) Conference*, 2010.

[6] A. Ferro, D. Brunner, and L. Bruzzone, "Building detection and radar footprint reconstruction from single VHR SAR images," in *Proc. IEEE Int. Geoscience and Remote Sensing Symp. (IGARSS)*, 2010, pp. 292–295.

[7] L. Bruzzone, G. Alberti, P. Beck, C. Catallo, A. Ferro, A. Frigeri, E. Heggy, W. Kofman, G. Komatsu, S. Mattei, R. Orosei, J.J. Plaut, and R. Seu, "Sub-surface radar sounding of the Jovian Icy Moons," in *Proc. URSI-F Microwave Signatures Meeting*, 2010.

[8] A. Ferro, L. Bruzzone, E. Heggy, and J.J. Plaut, "Automatic detection and characterization of subsurface features from Mars radar sounder data," in *Proc. AGU Fall Meeting*, 2010.

[9] E. Heggy, J. Boisson, S.M. Clifford, J.J. Plaut, A. Ferro, and Y. Gim, "Constraining the equatorial basins sedimentation chronology from MARSIS tomographic data analysis," in *Proc. AGU Fall Meeting*, 2010.

[10] A. Ferro and L. Bruzzone, "A novel approach to the automatic detection of subsurface features in planetary radar sounder signals," in *Proc. IEEE Int. Geoscience and Remote Sensing Symp. (IGARSS)*, 2011, pp. 1071–1074.

[11] A. Ferro and L. Bruzzone, "Automatic detection and characterization of subsurface linear features in radar sounder data acquired on icy areas," in *Synthetic Aperture Radar (EUSAR), 2012 9th European Conference on*, 2012.

Workshops and others

[1] L. Bruzzone, G. Alberti, C. Catallo, A. Ferro, A. Frigeri, W. Kofman, G. Komatsu, S. Mattei, R. Orosei, J.J. Plaut, A. Safaeinili, and R. Seu, "Sub-Surface Radar for the Jupiter Ganymede Orbiter," *2nd Europa Jupiter System Mission Instrument Workshop*, Jul. 2009.

[2] A. Ferro and L. Bruzzone, "Statistical analysis of SHARAD signals for automatic data processing," *Joint MARSIS-SHARAD Science Team Meeting*, Sep. 2009.

[3] L. Bruzzone, G. Alberti, C. Catallo, A. Ferro, A. Frigeri, E. Heggy, W. Kofman, G. Komatsu, S. Mattei, R. Orosei, J.J. Plaut, and R. Seu, "Sub-Surface Radar

for the Jupiter Ganymede Orbiter," *3rd Europa Jupiter System Mission Instrument Workshop*, Jan. 2010.

[4] A. Ferro and L. Bruzzone, "Study and reduction of the effects of noise on the SHARAD signal for the analysis of sub-surface layers," *Joint MARSIS-SHARAD Science Team Meeting*, Apr. 2010.

[5] L. Bruzzone, G. Alberti, P. Beck, C. Catallo, A. Ferro, A. Frigeri, E. Heggy, W. Kofman, G. Komatsu, S. Mattei, R. Orosei, J.J. Plaut, and R. Seu, "Progress report on study activities on the development of a Sub-Surface Radar for JGO," *EJSM Science Meeting*, May 2010.

[6] A. Ferro and L. Bruzzone, "Statistical analysis of SHARAD signals and its application to the automatic detection of the NPLD basal unit," *Joint MARSIS-SHARAD Science Team Meeting*, Sep. 2010.

[7] A. Ferro, L. Bruzzone, E. Heggy, and J.J. Plaut, "Automatic and integrated analysis of SHARAD and MARSIS data," *Joint MARSIS-SHARAD Science Team Meeting*, Sep. 2010.

[8] G. Alberti, S. Mattei, L. Bruzzone, A. Ferro, A. Olivieri, R. Seu, R. Orosei, and C. Catallo, "Exploring Ganymede's sub-surface with low-frequency radar," *X Congresso Nazionale di Scienze Planetarie*, Jan. 2011.

[9] L. Bruzzone, G. Alberti, A. Ferro, W. Kofman, G. Komatsu, G. Mitri, and R. Orosei, "A Sub-Surface Radar instrument concept for the JUICE mission study," *Jupiter System Mission Science Workshop*, Aug. 2011.

[10] L. Bruzzone, G. Alberti, P. Beck, R. Croci, A. Ferro, A. Frigeri, W. Kofman, G. Komatsu, G. Mitri, R. Orosei, and R. Seu, "Sub-Surface Radar instrument for the JUICE mission," *Jupiter Icy Moons Explorer Instrument Workshop*, Nov. 2011.

Bibliography

[1] C. Oliver and S. Quegan, *Understanding Synthetic Aperture Radar images.* Raleigh, NC, USA: SciTech Publishing, Inc., 2004.

[2] D. J. Daniels, *Ground Penetrating Radar (2nd edition).* London, UK: Institution of Engineering and Technology, 2007.

[3] M. Neumann, L. Ferro-Famil, and A. Reigber, "Estimation of forest structure, ground, and canopy layer characteristics from multibaseline polarimetric interferometric SAR data," *IEEE Trans. Geosci. Remote Sens.*, vol. 48, no. 3, pp. 1086–1104, 2010.

[4] L. Shi, C. T. Allen, J. R. Ledford, F. Rodriguez-Morales, W. A. Blake, B. G. Panzer, S. C. Prokopiack, C. J. Leuschen, and S. Gogineni, "Multichannel coherent radar depth sounder for NASA operation Ice Bridge," in *Proc. IEEE Int. Geoscience and Remote Sensing Symp. (IGARSS)*, 2010, pp. 1729–1732.

[5] J. Dall, S. S. Kristensen, V. Krozer, C. C. Hernandez, J. Vidkjr, A. Kusk, J. Balling, N. Skou, S. S. Sbjrg, and E. L. Christensen, "ESA's POLarimetric Airborne Radar Ice Sounder (POLARIS): design and first results," *IET Radar, Sonar & Navigation*, vol. 4, no. 3, pp. 488–496, 2010.

[6] V. Ciarletti, C. Corbel, D. Plettemeier, P. Cais, S. M. Clifford, and S.-E. Hamran, "WISDOM GPR designed for shallow and high-resolution sounding of the Martian subsurface," *Proc. IEEE*, vol. 99, no. 5, pp. 824–836, 2011.

[7] R. Jordan et al., "The Mars Express MARSIS sounder instrument," *Planetary and Space Science*, vol. 57, pp. 1975–1986, 2009.

[8] R. Croci, R. Seu, E. Flamini, and E. Russo, "The SHAllow RADar (SHARAD) Onboard the NASA MRO Mission," *Proc. IEEE*, vol. 99, no. 5, pp. 794–807, 2011.

[9] T. Ono, A. Kumamoto, Y. Yamaguchi, A. Yamaji, T. Kobayashi, Y. Kasahara, and H. Oya, "Instrumentation and observation target of the Lunar Radar Sounder (LRS) experiment on-board the SELENE spacecraft," *Earth, Planets, and Space*, vol. 60, pp. 321–332, Apr. 2008.

[10] L. J. Porcello, R. L. Jordan, J. S. Zelenka, G. F. Adams, R. J. Phillips, J. Brown, W. E., S. H. Ward, and P. L. Jackson, "The Apollo lunar sounder radar system," *Proc. IEEE*, vol. 62, no. 6, pp. 769–783, 1974.

[11] (2009, Jan.) Europa Jupiter System Mission NASA/ESA joint summary report. [Online]. Available: http://sci.esa.int/ejsm/

[12] L. Bruzzone, G. Alberti, C. Catallo, A. Ferro, W. Kofman, and R. Orosei, "Subsurface radar sounding of the Jovian Moon Ganymede," *Proc. IEEE*, vol. 99, no. 5, pp. 837–857, 2011.

[13] (2009, Jan.) Titan Saturn System Mission NASA/ESA joint summary report. [Online]. Available: http://opfm.jpl.nasa.gov/library/

[14] A. Herique, W. Kofman, P. Bauer, F. Remy, and L. Phalippou, "A spaceborne ground penetrating radar: MIMOSA," in *Proc. IEEE 1999 Int. Geoscience and Remote Sensing Symp. IGARSS '99*, vol. 1, 1999, pp. 473–475.

[15] *CARISMA, Carbon Cycle and Ice Sheet Mapping Mission.* Proposal to ESA's Earth Explorer Opportunity Mission call, 2005.

[16] IGOS, "Cryosphere theme report," 2007. [Online]. Available: http://cryos.ssec.wisc.edu/docs/cryos_theme_report.pdf

[17] L. Bruzzone et al., *GLACIES, Glaciers and Icy Environments Sounding.* Proposal to ESA's Earth Explorer Opportunity Mission call, Jun. 2010.

[18] (2011, Sep.) NASA Mars research helps find buried water on Earth. [Online]. Available: http://www.nasa.gov/topics/earth/features/kuwait20110914.html

[19] M. Skolnik, *Radar Handbook (3rd edition).* New York, US: McGraw-Hill, 2008.

[20] F. Caltagirone, G. De Luca, F. Covello, G. Marano, G. Angino, and M. Piemontese, "Status, results, potentiality and evolution of COSMO-SkyMed, the Italian Earth Observation constellation for risk management and security," in *Proc. IEEE Int. Geoscience and Remote Sensing Symp. (IGARSS)*, 2010, pp. 4393–4396.

[21] R. Werninghaus and S. Buckreuss, "The TerraSAR-X mission and system design," *IEEE Trans. Geosci. Remote Sens.*, vol. 48, no. 2, pp. 606–614, 2010.

[22] G. Krieger, A. Moreira, H. Fiedler, I. Hajnsek, M. Werner, M. Younis, and M. Zink, "TanDEM-X: A satellite formation for high-resolution SAR interferometry," *IEEE Trans. Geosci. Remote Sens.*, vol. 45, no. 11, pp. 3317–3341, 2007.

[23] F. Xu and Y.-Q. Jin, "Automatic reconstruction of building objects from multiaspect meter-resolution SAR images," *IEEE Trans. Geosci. Remote Sens.*, vol. 45, no. 7, pp. 2336–2353, 2007.

[24] A. Thiele, E. Cadario, K. Schulz, U. Thonnessen, and U. Soergel, "Building recognition from multi-aspect high-resolution InSAR data in urban areas," *IEEE Trans. Geosci. Remote Sens.*, vol. 45, no. 11, pp. 3583–3593, 2007.

[25] D. Brunner, G. Lemoine, and L. Bruzzone, "Earthquake damage assessment of buildings using VHR optical and SAR imagery," *IEEE Trans. Geosci. Remote Sens.*, vol. 48, no. 5, pp. 2403–2420, May 2010.

[26] D. Mason, R. Speck, B. Devereux, G.-P. Schumann, J. Neal, and P. Bates, “Flood detection in urban areas using TerraSAR-X,” *IEEE Trans. Geosci. Remote Sens.*, vol. 48, no. 2, pp. 882–894, Feb. 2010.

[27] C. Tison, J.-M. Nicolas, F. Tupin, and H. Maitre, “A new statistical model for Markovian classification of urban areas in high-resolution SAR images,” *IEEE Trans. Geosci. Remote Sens.*, vol. 42, no. 10, pp. 2046–2057, 2004.

[28] S. Voigt, T. Kemper, T. Riedlinger, R. Kiefl, K. Scholte, and H. Mehl, “Satellite image analysis for disaster and crisis-management support,” *IEEE Trans. Geosci. Remote Sens.*, vol. 45, no. 6, pp. 1520–1528, 2007.

[29] D. Brunner, G. Lemoine, F.-X. Thoorens, and L. Bruzzone, “Distributed geospatial data processing functionality to support collaborative and rapid emergency response,” *IEEE Journal of Selected Topics in Applied Earth Observations and Remote Sensing*, vol. 2, no. 1, pp. 33–46, 2009.

[30] R. J. Phillips et al., “Mars North Polar Deposits: Stratigraphy, age, and geodynamical response,” *Science*, vol. 320, pp. 1182–1185, May 2008.

[31] R. Seu et al., “Accumulation and erosion of Mars’ South Polar Layered Deposits,” *Science*, vol. 317, pp. 1715–1718, Sep. 2007.

[32] D. Vaughan, H. Corr, C. Doake, and E. Waddington, “Distortion of isochronous layers in ice revealed by ground-penetrating radar,” *Nature*, vol. 398, pp. 323–326, 1999.

[33] E.D. Waddington et al., “Inference of accumulation-rate patterns from deep layers in glaciers and ice sheets,” *J. of Glaciol.*, vol. 53, no. 183, pp. 694–712, 2003.

[34] J.-F. Nouvel, A. Herique, W. Kofman, and A. Safaeinili, “Radar signal simulation: Surface modeling with the facet method,” *Radio Science*, vol. 39, no. 1, Feb. 2004.

[35] J. W. Holt, M. E. Peters, S. D. Kempf, D. L. Morse, and D. D. Blankenship, “Echo source discrimination in single-pass airborne radar sounding data from the Dry Valleys, Antarctica: Implications for orbital sounding of Mars,” *J. Geophys. Res.*, vol. 111, p. E06S24, 2006.

[36] G. Franceschetti, A. Iodice, and D. Riccio, “A canonical problem in electromagnetic backscattering from buildings,” *IEEE Trans. Geosci. Remote Sens.*, vol. 40, no. 8, pp. 1787–1801, 2002.

[37] Y. Dong, B. Forster, and C. Ticehurst, “Radar backscatter analysis for urban environments,” *Int. Journal of Remote Sensing*, vol. 18, no. 6, pp. 1351–1364, Apr. 1997.

[38] D. Brunner, L. Bruzzone, A. Ferro, J. Fortuny, and G. Lemoine, “Analysis of the double bounce scattering mechanism of buildings in VHR SAR data,” in *Proc. SPIE Conf. on Image and Signal Processing for Remote Sensing XIV*, vol. 7109, 2008, pp. 71 090Q–71 090Q–12.

[39] F. T. Ulaby, R. K. Moore, and A. K. Fung, *Microwave Remote Sensing: Active and Passive.* Addison-Wesley, 1981, vol. 1.

[40] R. Touzi, "A review of speckle filtering in the context of estimation theory," *IEEE Trans. Geosci. Remote Sens.*, vol. 40, no. 11, pp. 2392–2404, 2002.

[41] V. Bogorodsky, C. Bentley, and P. Gudmandsen, *Radioglaciology.* D. Reidel Publishing Co., 1985.

[42] D. Vaughan, H. Corr, F. Ferraccioli, N. Frearson, A. O'Hare, D. Mach, J. Holt, D. Blankenship, D. Morse, and D. Young, "New boundary conditions for the West Antarctic ice sheet: Subglacial topography beneath Pine Island Glacier," *Geophys. Res. Lett.*, vol. 33, p. L09501, 2006.

[43] J.J. Plaut et al., "Subsurface radar sounding of the South Polar Layered Deposits of Mars," *Science*, vol. 316, pp. 92–95, 2007.

[44] L. M. Carter et al., "Shallow radar (SHARAD) sounding observations of the Medusae Fossae Formation, Mars," *Icarus*, vol. 199, no. 2, pp. 295–302, Feb. 2009.

[45] I. G. Cumming and F. H. Wong, *Digital Processing Of Synthetic Aperture Radar Data: Algorithms And Implementation.* Artech House, 2005.

[46] R. K. Raney, "Radar sounder: Cross-track polarimetric selectivity," in *Synthetic Aperture Radar (EUSAR), 2008 7th European Conference on*, 2008.

[47] ASI's Science Data Center. [Online]. Available: http://www.asdc.asi.it

[48] NASA's Planetary Data System. [Online]. Available: http://pds-geosciences.wustl.edu

[49] P. Snoeij, E. Attema, M. Davidson, B. Duesmann, N. Floury, G. Levrini, B. Rommen, and B. Rosich, "Sentinel-1 radar mission: Status and performance," *IEEE Aerospace and Electronic Systems Magazine*, vol. 25, no. 8, pp. 32–39, 2010.

[50] A. R. Brenner and L. Roessing, "Radar imaging of urban areas by means of very high-resolution SAR and interferometric SAR," *IEEE Trans. Geosci. Remote Sens.*, vol. 46, no. 10, pp. 2971–2982, 2008.

[51] O. Ruault du Plessis, J.-F. Nouvel, R. Baque, G. Bonin, P. Dreuillet, C. Coulombeix, and H. Oriot, "ONERA SAR facilities," *IEEE Aerospace and Electronic Systems Magazine*, vol. 26, no. 11, pp. 24–30, 2011.

[52] K. Scipal, M. Arcioni, J. Chave, J. Dall, F. Fois, T. LeToan, C. Lin, K. Papathanassiou, S. Quegan, F. Rocca, S. Saatchi, H. Shugart, L. Ulander, and M. Williams, "The BIOMASS mission – an ESA Earth Explorer candidate to measure the biomass of the Earth's forests," in *Proc. IEEE Int. Geoscience and Remote Sensing Symp. (IGARSS)*, 2010, pp. 52–55.

[53] H. Rott, D. Cline, C. Duguay, R. Essery, C. Haas, C. Haas, G. Macelloni, E. Malnes, J. Pulliainen, H. Rebhan, and S. Yueh, “CoReH2O – A Ku- and X-band SAR mission for snow and ice monitoring,” in *Synthetic Aperture Radar (EUSAR), 2008 7th European Conference on*, 2008.

[54] A. Ferro and L. Bruzzone, “A novel approach to the automatic detection of subsurface features in planetary radar sounder signals,” in *Proc. IEEE Int. Geoscience and Remote Sensing Symp. (IGARSS)*, 2011, pp. 1071–1074.

[55] P. Gamba and S. Lossani, “Neural detection of pipe signatures in ground penetrating radar images,” *IEEE Trans. Geosci. Remote Sens.*, vol. 38, no. 2, pp. 790–797, 2000.

[56] M. Fahnestock, W. Abdalati, S. Luo, and S. Gogineni, “Internal layer tracing and age-depth-accumulation relationships for the northern Greenland ice sheet,” *J. Geophys. Res.*, vol. 106, no. 33, pp. 789–797, 2001.

[57] C.-C. Chen, M. B. Higgins, K. O’Neill, and R. Detsch, “Ultrawide-bandwidth fully-polarimetric ground penetrating radar classification of subsurface unexploded ordnance,” *IEEE Trans. Geosci. Remote Sens.*, vol. 39, no. 6, pp. 1221–1230, 2001.

[58] S. Delbo, P. Gamba, and D. Roccato, “A fuzzy shell clustering approach to recognize hyperbolic signatures in subsurface radar images,” *IEEE Trans. Geosci. Remote Sens.*, vol. 38, no. 3, pp. 1447–1451, 2000.

[59] E. Pasolli, F. Melgani, and M. Donelli, “Automatic analysis of GPR images: A pattern-recognition approach,” *IEEE Trans. Geosci. Remote Sens.*, vol. 47, no. 7, pp. 2206–2217, 2009.

[60] E. Pasolli, F. Melgani, and M. Donelli, “Gaussian process approach to buried object size estimation in GPR images,” *IEEE Geosci. Remote Sens. Lett.*, vol. 7, no. 1, pp. 141–145, 2010.

[61] F. Heliere, C.-C. Lin, H. Corr, and D. Vaughan, “Radio echo sounding of pine island glacier, west antarctica: Aperture synthesis processing and analysis of feasibility from space,” *IEEE Trans. Geosci. Remote Sens.*, vol. 45, no. 8, pp. 2573–2582, 2007.

[62] S. Lauro, E. Mattei, E. Pettinelli, F. Soldovieri, R. Orosei, M. Cartacci, A. Cicchetti, R. Noschese, and S. Giuppi, “Permittivity estimation of layers beneath the northern polar layered deposits, Mars,” *Geophys. Res. Lett.*, vol. 37, p. L14201, 2010.

[63] J. Boisson, E. Heggy, S. Clifford, A. Frigeri, J. Plaut, W. Farrel, N. Putzig, G. Picardi, R. Orosei, P. Lognonne, and D. Gurnett, “Sounding the subsurface of Athabasca Valles using MARSIS radar data: Exploring the volcanic and fluvial hypotheses for the origin of the rafted-plate terrain,” *J. Geophys. Res.*, vol. 114, p. E08003, 2009.

[64] E. Pettinelli, P. Burghignoli, A. R. Pisani, F. Ticconi, A. Galli, G. Vannaroni, and F. Bella, “Electromagnetic propagation of GPR signals in Martian subsurface

scenarios including material losses and scattering," *IEEE Trans. Geosci. Remote Sens.*, vol. 45, no. 5, pp. 1271–1281, 2007.

[65] R. Orosei, R. Bianchi, A. Coradini, S. Espinasse, C. Federico, A. Ferriccioni, and A. Gavrishin, "Self-affine behavior of Martian topography at kilometer scale from Mars Orbiter Laser Altimeter data," *J. Geophys. Res.*, vol. 108, no. E4, p. 8023, 2003.

[66] N. Nakagami, "The m-distribution, a general formula for intensity distribution of rapid fading," in *Statistical Methods in Radio Wave Propagation*, W. G. Hoffman, Ed. Oxford, England: Pergamon, 1960.

[67] A. Papoulis, *Probability, Random Variables, and Stochastic Processes, 2nd ed.* New York, US: McGraw-Hill, 1984.

[68] D. Lewinski, "Nonstationary probabilistic target and clutter scattering models," *IEEE Trans. Antennas Propag.*, vol. 31, no. 3, pp. 490–498, 1983.

[69] K. D. Ward, "Compound representation of high resolution sea clutter," *Electronics Letters*, vol. 17, no. 16, pp. 561–563, 1981.

[70] C. Grima, W. Kofman, A. Herique, and R. Seu, "Physical parameters of the near-surface of Mars derived from SHARAD radar reflectivity: statistical approach," in *38th COSPAR Scientific Assembly*, 2010.

[71] M. Zuber, D. Smith, S. Solomon, D. Muhleman, J. Head, J. Garvin, J. Abshire, and J. Bufton, "The Mars Observer Laser Altimeter investigation," *J. Geophys. Res.*, vol. 97, no. E5, pp. 7781–7797, 1992.

[72] M. Selvans, J. Plaut, O. Aharonson, and A. Safaeinili, "Internal structure of Planum Boreum, from Mars advanced radar for subsurface and ionospheric sounding data," *J. Geophys. Res.*, vol. 115, p. E09003, 2010.

[73] S. Slavney and R. Orosei, "Shallow radar Reduced Data Record software interface specification, ver. 1.0," Jul. 2007. [Online]. Available: http://pds-geosciences.wustl.edu/mro/mro-m-sharad-4-rdr-v1/mrosh_1001/document/rdrsis.pdf

[74] J.-M. Nicolas, "Introduction aux statistiques de deuxième espèce : applications des logs-moments et des logs-cumulants à l'analyse des lois d'images radar," *Traitement du Signal*, vol. 19, no. 3, pp. 139–167, 2002.

[75] J. Greenwood and D. Durand, "Aids for fitting the gamma distribution by maximum likelihood," *Technometrics*, vol. 2, pp. 55–65, 1960.

[76] Q. T. Zhang, "A note on the estimation of Nakagami-m fading parameter," *IEEE Commun. Lett.*, vol. 6, no. 6, pp. 237–238, 2002.

[77] I. R. Joughin, D. B. Percival, and D. P. Winebrenner, "Maximum likelihood estimation of K distribution parameters for SAR data," *IEEE Trans. Geosci. Remote Sens.*, vol. 31, no. 5, pp. 989–999, 1993.

[78] J. Lin, "Divergence measures based on the Shannon entropy," *IEEE Trans. Inf. Theory*, vol. 37, no. 1, pp. 145–151, 1991.

[79] H. Shimazaki and S. Shinomoto, "A method for selecting the bin size of a time histogram," *Neural Computation*, vol. 19, no. 6, pp. 1503–1527, 2007.

[80] U. Stilla and K. Hedman, "Feature fusion based on bayesian network theory for automatic road extraction," in *Radar Remote Sensing of Urban Areas*, ser. Remote Sensing and Digital Image Processing, U. Soergel, Ed. Springer Netherlands, 2010, vol. 15, pp. 69–86.

[81] L. Bruzzone and D. F. Prieto, "Automatic analysis of the difference image for unsupervised change detection," *IEEE Trans. Geosci. Remote Sens.*, vol. 38, no. 3, pp. 1171–1182, 2000.

[82] K. E. Fishbaugh and J. W. H. III, "Origin and characteristics of the Mars north polar basal unit and implications for polar geologic history," *Icarus*, vol. 174, no. 2, pp. 444–474, 2005.

[83] J. Sethian, *Level set methods and fast marching methods: evolving interfaces in computational geometry, fluid mechanics, computer vision, and materials science, 2nd ed.* Cambridge, UK: Cambridge University Press, 1999.

[84] A. Ferro and L. Bruzzone, "Automatic detection and characterization of subsurface linear features in radar sounder data acquired on icy areas," in *Synthetic Aperture Radar (EUSAR), 2012 9th European Conference on*, 2012.

[85] L. Capineri, P. Grande, and J. A. G. Temple, "Advanced image-processing technique for real-time interpretation of ground-penetrating radar images," *Int. Journal of Imaging Systems and Technology*, vol. 9, no. 1, pp. 51–59, 1998.

[86] W. Al-Nuaimy, H. H. Lu, S. Shihab, and A. Eriksen, "Automatic mapping of linear structures in 3-dimensional space from ground-penetrating radar data," in *Proc. Remote Sensing and Data Fusion over Urban Areas IEEE/ISPRS Joint Workshop 2001*, 2001, pp. 198–201.

[87] G. J. Freeman, A. C. Bovik, and J. W. Holt, "Automated detection of near surface Martian ice layers in orbital radar data," in *Proc. IEEE Southwest Symp. Image Analysis & Interpretation (SSIAI)*, 2010, pp. 117–120.

[88] K. Dabov, A. Foi, V. Katkovnik, and K. Egiazarian, "Image denoising by sparse 3-D transform-domain collaborative filtering," *IEEE Trans. Image Process.*, vol. 16, no. 8, pp. 2080–2095, 2007.

[89] C.-A. Deledalle, L. Denis, and F. Tupin, "Iterative weighted maximum likelihood denoising with probabilistic patch-based weights," *IEEE Trans. Image Process.*, vol. 18, no. 12, pp. 2661–2672, 2009.

[90] C.-A. Deledalle, L. Denis, and F. Tupin, "NL-InSAR: Nonlocal interferogram estimation," *IEEE Trans. Geosci. Remote Sens.*, vol. 49, no. 4, pp. 1441–1452, 2011.

[91] S. Parrilli, M. Poderico, C. V. Angelino, G. Scarpa, and L. Verdoliva, "A nonlocal approach for SAR image denoising," in *Proc. IEEE Int. Geoscience and Remote Sensing Symp. (IGARSS)*, 2010, pp. 726–729.

[92] M. Mäkitalo, A. Foi, D. Fevralev, and V. Lukin, "Denoising of single-look SAR images based on variance stabilization and nonlocal filters," in *International Conference on Mathematical Methods in Electromagnetic Theory (MMET)*, Sep. 2010.

[93] C. Steger, "An unbiased detector of curvilinear structures," *IEEE Trans. Pattern Anal. Mach. Intell.*, vol. 20, no. 2, pp. 113–125, 1998.

[94] C. Steger, "Evaluation of subpixel line and edge detection precision and accuracy," in *International Archives of Photogrammetry and Remote Sensing*, 1998, pp. 256–264.

[95] A. Ferro, D. Brunner, and L. Bruzzone, "Building detection and radar footprint reconstruction from single VHR SAR images," in *Proc. IEEE Int. Geoscience and Remote Sensing Symp. (IGARSS)*, 2010, pp. 292–295.

[96] B. A. Campbell, N. E. Putzig, L. M. Carter, and R. J. Phillips, "Autofocus correction of phase distortion effects on sharad echoes," *IEEE Geosci. Remote Sens. Lett.*, vol. 8, no. 5, pp. 939–942, 2011.

[97] F. Russo, M. Cutigni, R. Orosei, C. Taddei, R. Seu, D. Biccari, E. Giacomoni, O. Fuga, and E. Flamini, "An incoherent simulator for the SHARAD experiment," in *Proc. IEEE Radar Conf. RADAR '08*, 2008.

[98] M. Iorio, F. Fois, R. Mecozzi, C. Catallo, G. Picardi, R. Seu, and E. Flamini, "Fast radar signal simulator for SAR ground penetrating applications," in *Proc. IEEE Radar Conf. RADAR '08*, 2008.

[99] F. T. Ulaby, R. K. Moore, and A. K. Fung, *Microwave Remote Sensing: Active and Passive.* Artech House, 1982, vol. 2.

[100] G. Franceschetti, A. Iodice, M. Migliaccio, and D. Riccio, "Scattering from natural rough surfaces modeled by fractional Brownian motion two-dimensional processes," *IEEE Trans. Antennas Propag.*, vol. 47, no. 9, pp. 1405–1415, 1999.

[101] B. Zitov and J. Flusser, "Image registration methods: a survey," *Image and Vision Computing*, vol. 21, pp. 977–1000, oct 2003.

[102] J. P. W. Pluim, J. B. A. Maintz, and M. A. Viergever, "Mutual-information-based registration of medical images: a survey," *IEEE Trans. Med. Imag.*, vol. 22, no. 8, pp. 986–1004, 2003.

[103] D. Rueckert, L. I. Sonoda, C. Hayes, D. L. G. Hill, M. O. Leach, and D. J. Hawkes, "Nonrigid registration using free-form deformations: application to breast mr images," *IEEE Trans. Med. Imag.*, vol. 18, no. 8, pp. 712–721, 1999.

[104] R. H. Byrd, P. Lu, J. Nocedal, and C. Zhu, "A limited memory algorithm for bound constrained optimization," *SIAM Journal on Scientific and Statistical Computing*, vol. 16, no. 5, pp. 1190–1208, 1995.

[105] W. W. III, P. Viola, H. Atsumi, S. Nakajima, and R. Kikinis, "Multi-modal volume registration by maximization of mutual information," *Medical Image Analysis*, vol. 1, no. 1, pp. 35–51, 1996.

[106] X. Fan, H. Rhody, and E. Saber, "A spatial-feature-enhanced MMI algorithm for multimodal airborne image registration," *IEEE Trans. Geosci. Remote Sens.*, vol. 48, no. 6, pp. 2580–2589, 2010.

[107] D. Brunner, L. Bruzzone, A. Ferro, and G. Lemoine, "Analysis of the reliability of the double bounce scattering mechanism for detecting buildings in VHR SAR images," in *Proc. IEEE Radar Conf*, 2009.

[108] A. Ferro, D. Brunner, L. Bruzzone, and G. Lemoine, "On the relationship between double bounce and the orientation of buildings in VHR SAR images," *IEEE Geosci. Remote Sens. Lett.*, vol. 8, no. 4, pp. 612–616, 2011.

[109] R. Guida, A. Iodice, D. Riccio, and U. Stilla, "Model-based interpretation of high-resolution sar images of buildings," *IEEE Journal of Selected Topics in Applied Earth Observations and Remote Sensing*, vol. 1, no. 2, pp. 107–119, 2008.

[110] D. Brunner, G. Lemoine, L. Bruzzone, and H. Greidanus, "Building height retrieval from VHR SAR imagery based on an iterative simulation and matching technique," *IEEE Trans. Geosci. Remote Sens.*, vol. 48, no. 3, pp. 1487–1504, 2010.

[111] A. Thiele, E. Cadario, K. Schulz, U. Thoennessen, and U. Soergel, "Feature extraction of gable-roofed buildings from multi-aspect high-resolution InSAR data," in *Proc. IEEE Int. Geoscience and Remote Sensing Symp. (IGARSS)*, 2007, pp. 262–265.

[112] A. J. Bennett and D. Blacknell, "Infrastructure analysis from high resolution SAR and InSAR imagery," in *Proc. 2nd GRSS/ISPRS Joint Workshop Remote Sensing and Data Fusion over Urban Areas*, 2003, pp. 230–235.

[113] G. Hardaway and G. C. Gustafson, "Cardinal effect on SEASAT images of urban areas," *Photogrammetric Engineering and Remote Sensing*, vol. 48, pp. 399–404, 1982.

[114] Y. A. Hussin, "Effect of polarization and incidence angle on radar return from urban features using L-band aircraft radar data," in *Proc. IEEE Int. Geoscience and Remote Sensing Symp. (IGARSS)*, vol. 1, 1995, pp. 178–180.

[115] T. Kempf, M. Peichl, S. Dill, and H. Süß, "Microwave radar signature acquisition of urban structures," in *Proc. of ITG WFMN07 - Wave Propagation in Communication, Microwave Systems and Navigation*, 2007, pp. 68–73.

[116] Bing Maps. [Online]. Available: http://www.bing.com/maps/

[117] A. S. Khwaja, L. Ferro-Famil, and E. Pottier, “Efficient sar raw data generation for anisotropic urban scenes based on inverse processing,” *IEEE Geosci. Remote Sens. Lett.*, vol. 6, no. 4, pp. 757–761, 2009.

[118] Y. Wang, E. S. Kasischke, J. M. Melack, F. W. Davis, and N. L. C. Jr., “The effects of changes in loblolly pine biomass and soil moisture on ERS-1 SAR backscatter,” *Remote Sensing of Environment*, vol. 49, no. 1, pp. 25–31, 1994.

[119] T. J. Jackson, H. McNairn, M. A. Weltz, B. Brisco, and R. Brown, “First order surface roughness correction of active microwave observations for estimating soil moisture,” *IEEE Trans. Geosci. Remote Sens.*, vol. 35, no. 4, pp. 1065–1069, 1997.

[120] E. S. Li and K. Sarabandi, “Low grazing incidence millimeter-wave scattering models and measurements for various road surfaces,” *IEEE Trans. Antennas Propag.*, vol. 47, no. 5, pp. 851–861, 1999.

[121] E. J. Jaselskis, J. Grigas, and A. Brilingas, “Dielectric properties of asphalt pavement,” *Journal of Materials in Civil Engineering*, vol. 15, no. 5, pp. 427–434, 2003.

[122] H. Al-Mattarneh, D. Ghodgaonkar, and W. Majid, “Microwave sensing of moisture content in concrete using open-ended rectangular waveguide,” *Subsurface Sensing Technologies and Applications*, vol. 2, pp. 377–390(14), October 2001.

[123] A. Ferro, D. Brunner, and L. Bruzzone, “An advanced technique for building detection in VHR SAR images,” in *Proc. SPIE Conf. on Image and Signal Processing for Remote Sensing XV*, vol. 7477, 2009, pp. 74 770V–74 770V–12.

[124] A. Ferro, D. Brunner, and L. Bruzzone, “Detection and reconstruction of building footprints from single VHR SAR images,” in *Synthetic Aperture Radar (EUSAR), 2010 8th European Conference on*, 2010.

[125] S. Marchesi, F. Bovolo, and L. Bruzzone, “A context-sensitive technique robust to registration noise for change detection in VHR multispectral images,” *IEEE Trans. Image Process.*, vol. 19, pp. 1877–1889, 2010.

[126] F. Pacifici and W. J. Emery, “Pulse coupled neural networks for automatic urban change detection at very high spatial resolution,” in *Proc. of the 14th Iberoamerican Conference on Pattern Recognition*, 2009, pp. 929–942.

[127] T. Kemper, A. Wania, and M. Pesaresi, “Supporting slum mapping using very high resolution satellite data,” in *Proc. of 33rd Int. Symp. on Remote Sensing of Environment*, 2009.

[128] I. Baud, M. Kuffer, K. Pfeffer, R. Sliuzas, and S. Karuppannan, “Understanding heterogeneity in metropolitan India: The added value of remote sensing data for analyzing sub-standard residential areas,” *Int. J. Applied Earth Observation and Geoinformation*, vol. 12, no. 5, pp. 359 – 374, 2010.

[129] D. Al-Khudhairy, “Geo-spatial information and technologies in support of EU crisis management,” *Int. J. of Digital Earth*, vol. 3, no. 1, pp. 16 – 30, 2010.

[130] U. Soergel, U. Thoennessen, and U. Stilla, "Reconstruction of buildings from interferometric SAR data of built-up areas," in *ISPRS Conference "Photogrammetric image analysis"*, 2003, pp. 59–64.

[131] F. Cellier, H. Oriot, and J.-M. Nicolas, "Hypothesis management for building reconstruction from high resolution InSAR imagery," in *Proc. IEEE Int. Geoscience and Remote Sensing Symp. (IGARSS)*, 2006, pp. 3639–3642.

[132] E. Simonetto, H. Oriot, and R. Garello, "Rectangular building extraction from stereoscopic airborne radar images," *IEEE Trans. Geosci. Remote Sens.*, vol. 43, no. 10, pp. 2386–2395, 2005.

[133] F. Zhang, Y. Shao, and X. Zhang, "Building extraction using dual-aspect high resolution SAR images," in *Proc. 18th International Conference on Geoinformatics*, 2010.

[134] Y. Wang, F. Tupin, C. Han, and J.-M. Nicolas, "Building detection from high resolution PolSAR data by combining region and edge information," in *Proc. IEEE Int. Geoscience and Remote Sensing Symp. (IGARSS)*, vol. 4, 7-11 July, Boston, MA, USA, 2008, pp. IV–153–IV–156.

[135] R. Hill, C. Moate, and D. Blacknell, "Estimating building dimensions from synthetic aperture radar image sequences," *IET Radar Sonar Navig.*, vol. 2, no. 3, pp. 189–199, 2008.

[136] C. Tison and F. Tupin, "Retrieval of building shapes from shadows in high resolution SAR interferometric images," in *Proc. IEEE Int. Geoscience and Remote Sensing Symp. (IGARSS)*, vol. 3, 2004, pp. 1788–1791.

[137] J. D. Wegner, R. Hansch, A. Thiele, and U. Soergel, "Building detection from one orthophoto and high-resolution InSAR data using conditional random fields," *IEEE Journal of Selected Topics in Applied Earth Observations and Remote Sensing*, vol. 4, no. 1, pp. 83–91, 2011.

[138] H. Sportouche, F. Tupin, and L. Denise, "Extraction and three-dimensional reconstruction of isolated buildings in urban scenes from high-resolution optical and sar spaceborne images," *IEEE Trans. Geosci. Remote Sens.*, vol. 49, no. 10, pp. 3932–3946, 2011.

[139] V. Poulain, J. Inglada, M. Spigai, J.-Y. Tourneret, and P. Marthon, "High-resolution optical and sar image fusion for building database updating," *IEEE Trans. Geosci. Remote Sens.*, vol. 49, no. 8, pp. 2900–2910, 2011.

[140] M. Quartulli and M. Datcu, "Stochastic geometrical modeling for built-up area understanding from a single SAR intensity image with meter resolution," *IEEE Trans. Geosci. Remote Sens.*, vol. 42, no. 9, pp. 1996–2003, 2004.

[141] F. Zhang, Y. Shao, X. Zhang, and T. Balz, "Building L-shape footprint extraction from high resolution SAR image," in *IEEE Proc. Joint Urban Remote Sensing Event*, 2011, pp. 273–276.

[142] E. Michaelsen, U. Soergel, and U. Thoennessen, "Perceptual grouping for automatic detection of man-made structures in high-resolution SAR data," *Pattern Recog. Lett.*, vol. 27, no. 4, pp. 218–225, 2006.

[143] C. L. Forgy, "Rete: A fast algorithm for the many pattern/many object pattern match problem," *Artif. Intell.*, vol. 19, no. 1, pp. 17–37, 1982.

[144] D. Kuan, A. Sawchuk, T. Strand, and P. Chavel, "Adaptive restoration of images with speckle," *IEEE Trans. Acoust., Speech, Signal Process.*, vol. 35, no. 3, pp. 373–383, 1987.

[145] F. Tupin, H. Maître, J.-F. Mangin, J.-M. Nicolas, and E. Pechersky, "Detection of linear features in SAR images: application to road network extraction," *IEEE Trans. Geosci. Remote Sens.*, vol. 36, no. 2, pp. 434–453, 1998.

[146] R. C. Gonzales and R. E. Woods, *Digital Image Processing.* Addison Wesley, 1993.

[147] E. Simonetto, H. Oriot, and R. Garello, "Extraction of industrial structures and DEM from airborne SAR images," in *Proc. Physics in Signal and Image Processing*, Marseille, France, Jan. 2001, pp. 412–417.

[148] F. Cellier, H. Oriot, and J.-M. Nicolas, "Introduction of the mean shift algorithm in SAR imagery: Application to shadow extraction for building reconstruction," in *Proceedings of EARSeL Workshop 3D-Remote Sensing*, 2005.

[149] J.-S. R. Jang, C.-T. Sun, and E. Mizutani, *Neuro-Fuzzy and Soft Computing.* Prentice Hall, 1997.

[150] R. C. Eberhart, Y. Shi, and J. Kennedy, *Swarm Intelligence*, ser. The Morgan Kaufmann Series in Evolutionary Computation. Morgan Kaufmann, 2001.

[151] Google Maps. [Online]. Available: http://maps.google.com

[152] M. Silveira and S. Heleno, "Separation between water and land in SAR images using region-based level sets," *IEEE Geosci. Remote Sens. Lett.*, vol. 6, no. 3, pp. 471–475, 2009.